Hybrid Perovskite Design through Composition and its Impact on Growth and Morphology

Spencer Thomas Williams

A dissertation
submitted in partial fulfillment of the
requirements for the degree of

Doctor of Philosophy

University of Washington
2017

Reading Committee:
Professor Alex Jen, Chair
Professor David Ginger
Professor Fumio Ohuchi

Program Authorized to Offer Degree:
Materials Science & Engineering (Nanotechnology)

© Copyright 2017

Spencer Thomas Williams

University of Washington

Abstract

Hybrid Perovskite Design Through Composition and its Impact on Growth and Morphology

Spencer Thomas Williams

Chair of the Supervisory Committee:
Professor Alex Jen
Materials Science and Engineering

Hybrid perovskite solar cells (PVSCs) have emerged into the academic and industrial communities as a potentially transformative alternative to prevailing silicon technologies. PVSCs have rapidly increased in efficiency in the brief time they have been in the research spotlight, but fundamental material challenges like Pb-toxicity, ionic diffusivity, and stability impede efforts toward commercialization. This has led to significant world-wide investments in the compositional engineering of $CH_3NH_3PbI_3$, one of the most commonly studied hybrid perovskites for photovoltaics. Throughout the course of this effort, a significant amount of work has been directed at modifying each site in the hybrid perovskite lattice, but the complexity inherent to this material system has complicated rational design.

This dissertation presents a series of case studies aimed at elucidating the role that each site in the $CH_3NH_3PbI_3$ lattice plays in mediating material growth and structural evolution. Chapters 2 and 3 present experimental investigations of the role that halide anion and organic cation sites play in transformation, respectively. Chapter 4 presents a conceptual overview that connects this understanding to the many other techniques being developed to control $CH_3NH_3PbI_3$ growth. Chapter 5 expands on this conceptual footing

to mount a survey of the periodic table to identify species with the potential to modify the metal cation site, and Chapter 6 mounts a focused investigation of transition metal inclusion in $CH_3NH_3PbI_3$.

Relationships between composition, growth, morphology, and resulting properties are uniquely complex in this relatively new class of material. As a whole, the work presented in this dissertation provides a framework to untangle this complexity and rationally motivate continued compositional engineering to eventually facilitate technology translation. Chapter 7 summarizes relationships between composition, growth, and structure along with presenting broader perspective to direct continued efforts toward Pb replacement. A selection of key figures from each chapter are reproduced in this concluding chapter to allow a non-specialist reader to draw value out of this dissertation without requiring a close reading of each topic covered.

TABLE OF CONTENTS

LIST OF FIGURES

LIST OF TABLES

LIST OF SCHEMES

ABBREVIATIONS

a-$(MA)_{1+x}PbI_{3+x}$: amorphous $(CH_3NH_3)_{1+x}PbI_{3+x}$

AMX_3: Generalized formula for hybrid perovskites (A^+ = organic; M^{2+} = metal, X^- = halogen)

BIPV: building integrated photovoltaics

CIGS: copper indium gallium selenide

CTL: charge transporting layer

DCB: dichlorobenzene

DLS: dynamic light scattering

DMAc: dimethylacetamide

DMF: dimethylformamide

DMSO: dimethyl sulfoxide

DSSC: dye sensitized solar cell

EDS: energy dispersive spectroscopy

EPBT: energy payback time

ETL: electron transporting layer

FA: formamidinium, $HC(NH_2)_2$

$FAPbI_3$: $HC(NH_2)_2PbI_3$

FB: forward bias

FF: fill factor

FTO: fluorine doped tin oxide

FWHM: full width at half maximum

GBL: gamma butyrolactone

HF: hysteresis factor

High $[MA^0]$ treatment: CH_3NH_2 vapor treatment at high CH_3NH_2 vapor pressure

HTL: hole transporting layer

IPA: isopropanol

ITO: indium tin oxide

J_{SC}: short-circuit current

LACE: levelized avoided cost of electricity

LCA: lifecycle analysis

LCOE: levelized cost of electricity

Low [MA^0] treatment: CH_3NH_2 vapor treatment at low CH_3NH_2 vapor pressure

MA^+: methylammonium, $CH_3NH_3^+$

MA^0: methylamine, CH_3NH_2

$MA_4PbI_6{\cdot}2H_2O$: $(CH_3NH_3)_4PbI_6{\cdot}2H_2O$

MACl: CH_3NH_3Cl

MAI: CH_3NH_3I

$MAPbBr_3$: $CH_3NH_3PbBr_3$

$MAPbCl_3$: $CH_3NH_3PbCl_3$

$MAPbCl_{3-y}I_y$: $CH_3NH_3PbCl_{3-y}I_y$

$MAPbI_2Cl$: $CH_3NH_3PbI_2Cl$

$MAPbI_3$: $CH_3NH_3PbI_3$

$MAPbI_3{\cdot}DMF$: $CH_3NH_3PbI_3{\cdot}DMF$

$MAPbI_3{\cdot}DMSO$: $CH_3NH_3PbI_3{\cdot}DMSO$

$MAPbI_3{\cdot}MA^0$: $CH_3NH_3PbI_3{\cdot}\ CH_3NH_2$

$MAPbI_{3-x}Br_x$: $CH_3NH_3PbI_{3-x}Br_x$

$MAPbI_{3-x}Cl_x$: $CH_3NH_3PbI_{3-x}Cl_x$

$MASnI_3$: $CH_3NH_3SnI_3$

MAX: CH_3NH_3X (X = I or Cl)

OC → SC: open-circuit to short-circuit scan

OPV: organic photovoltaics

$PbI_2{\cdot}MA^0$: $PbI_2{\cdot}\ CH_3NH_2$

PCE: power conversion efficiency

PEDOT:PSS: poly(3,4-ethylenedioxythiophene) polystyrene sulfonate

PET: polyethylene terephthalate

PHJ: planar heterojunction

PL: photoluminescence

PPA: power purchasing agreement

PTFE: polytetrafluoroethylene

PV: photovoltaic

PVSC: hybrid perovskite solar cell

QY: quantum yield

R2R: roll-to-roll

RB: reverse bias

SAED: select area electron diffraction

SAM: self-assembled monolayer

SC → OC: short-circuit to open-circuit scan

SEM: scanning electron microscopy

TEM: transmission electron microscopy

Tr-PL: transient photoluminescence

UV-Vis: ultra violet-visible

VASP: vapor assisted solution process

V_{OC}: open-circuit voltage

VSM: vibrating sample magnetometry

XPS: X-ray photoelectron spectroscopy

XRD: X-ray diffraction

ACKNOWLEDGMENT

I would like to acknowledge the patient and persistent support that my family has given me throughout this work. I deeply thank my advisor Prof. Alex Jen in addition to the many people that have worked to make the Jen Group what it is. I also specifically thank my colleagues Adharsh Rajagopal and Ting Zhao for their direct and invaluable contributions to the work presented in this dissertation.

Chapter 1. INTRODUCTION

**This chapter has been adapted from STW-1, with portions reproduced verbatim (Reproduced from Ref. STW-1 with permission from the American Chemical Society.)*

This dissertation presents a set of work that focuses continued efforts toward hybrid perovskite material design through a series of investigations into the impact of composition on material growth, morphology, functionality, and performance. Chapters 2, 3, and 4 focus on establishing relationships between processing, structure, and performance. Chapters 5 and 6 direct this insight toward the larger compositional challenge of Pb-replacement.

This introductory chapter endeavors to more completely illustrate the motivation behind the development of hybrid perovskite solar cells, challenges that impede commercialization, and the key role that both compositional design and rational control over material growth play in facilitating continued efforts toward technology translation. The following material is adapted from a Perspective article titled *Current Challenges and Prospective Research for Upscaling Hybrid Perovskite Photovoltaics* (STW-1). Figures and portions of the text are reproduced verbatim, but many portions of the text have been amended or removed to preserve relevance to this dissertation.

Materials Science and Engineering, as a field, is built around the investigation of links between a material's processing, structure, properties, and performance. This broad focus on relationships between how a material is created, how it is structured, and how it functions is key in technological development because a material's functionality is not exclusively determined by what it contains. The many different scales at which structural features arise have unique impacts on material functionality, meaning that mechanistically understanding material growth is an inevitably necessary part of fully grasping the potential of any technologically relevant material. This is particularly true in the case of hybrid organic-inorganic perovskites like $CH_3NH_3PbI_3$.

1.1 Introduction to Hybrid Perovskite Photovoltaics (PVSCs)

The rapidly rising efficiencies of solar cells based on hybrid organic-inorganic perovskite absorbers have recently captivated the photovoltaic research community. This relatively new class of material possesses the same essential symmetry as many oxide perovskites, but the lattice of these hybrid organic-inorganic perovskites is built from halogen anions rather than oxygen. Oxide perovskites, like most other oxide materials, require high temperatures for material formation because of the metal-oxygen bonds from which the lattice is built. The metal-halogen bond that builds the essential framework of the hybrid organic-inorganic perovskite lattice requires very different conditions for growth, allowing this unique class of material to be grown at low temperatures *via* solution, vapor, or solid-state deposition. This incredibly flexible processibility combined with the material's inherent optoelectronic and semiconducting quality have made it an attractive platform for a wide variety of applications, especially considering that key properties like bandgap, stability, and emissivity are uniquely tuneable through composition.

Since the first application of $CH_3NH_3PbI_3$ in solar cells,[1] the explosive rise of perovskite photovoltaics has stimulated aggressive development of the hybrid organic-inorganic AMX_3 perovskite material system. In this class of material, each component including the organic cation (A^+), metal cation (M^{2+}), and halogen anion (X^-) play unique and important design roles. While the organic cation doesn't strongly participate directly in electronic structure of conduction or valence bands,[2] it provides cohesion and maintains electroneutrality as an extra halogen builds the three dimensional metal halide framework of $CH_3NH_3PbI_3$. When the composition of the A-site site is varied, it changes the symmetry and nature of cohesion within the lattice. Cs^+ and formamidinium[3,4] are employed on the A-site with the effect of altering symmetry and lattice dimensions as well as changing lattice reactivity toward polar, protic foreign species like water and methylamine vapor.STW-3 Also, dipolar organic species like methylammonium in the lattice allow dynamic responses to conditions that the field is still working to understand, like reorientation under illumination.[5–7] Larger organic cations like butyl ammonium and phenylethyl ammonium break the three dimensional metal halide framework of AMX_3 and create a layered structure.[8] Although the A^+ cation does not generally participate in conduction and valence band structure, its impact on the structure of the lead halide framework affects band structure, absorption, and energetic transport.[5,8]

Since the halogen anion (X^-) is largely responsible for orbitals comprising the valence band of this material system, I^-, Br^-, and to a limited extent Cl^- have been employed to tune band-gap.[8] The variation in size and chemical hardness in this set of halogens makes them useful for tuning lattice symmetry[9] and crystal growth,[STW-2] respectively. The existence of $CH_3NH_3PbI_{3-x}Br_x$[10] and $CH_3NH_3PbBr_{3-x}Cl_x$[11] solid solutions allow continuous tuning of band-gap with the exception of phase separation under illumination in the case of $CH_3NH_3PbI_{3-x}Br_x$.[12] Despite the limited solid solubility of Cl^- in $CH_3NH_3PbI_3$,[13] it is useful for altering defect equilibria[14] and encouraging larger grain growth.[STW-2]

The metal cation site (M^{2+}) has proven much more challenging to modify due to the uniqueness of Pb. The inert pair effect[15] stabilizes the 2+ oxidation state on Pb. Instability of this oxidation state is the intrinsic failing of tin and germanium substitution.[16] Frontier energetic structure is strongly determined by the metal cation, and tin substitution results in a red-shift in band-gap.[17] Additionally, in the larger classes of both oxide and hybrid perovskites, the symmetry surrounding the M-site determines other functional properties like piezoelectricity, ferroelectricity, and magnetism.[18–20]

Chemically, the nature of the metal cation determines the rules governing metal halide complex formation. This tendency is exemplified by the solution chemistry of lead iodide in which PbI_x^{2-x} complex ions play an important role in both solvation and solidification.[STW-2,[21]] This intimately couples material formation with the choice of metal and halogen ions, and it strongly links composition with resulting material growth and morphology.

1.1.1 *Practical look at PVSC implementation*

Organic-inorganic hybrid perovskite photovoltaics (PVSCs) have transfixed researchers in the solar energy field since the first exploration of $CH_3NH_3PbI_3$ as a light harvesting material.[1] While soaring efficiencies[22] and increasingly flexible processability make this technology potentially transformative, there remains measured skepticism[23] about ultimate impact because of intrinsic toxicity and instability.[24]

The implementation of an energy generation technology necessitates a pragmatic balance between energy investment, energy return, and overall impact of implementation. As a technology and societies using it change, this balance shifts. This is partly manifested in the gradually changing experience curve of a photovoltaic (PV) technology: production quality as a function of cost. Currently, the experience curve of silicon PV is daunting to contend with,[23] but it is difficult to fairly compare silicon and perovskite experience curves because of their very different stages of development. Moreover, even with an established technology, accurately analyzing true economic and energetic investment/return is difficult. Changes in commodities, government subsidies, regulations, implementation, environmental factors like insolation, and continued developments at all levels of production complicate the generation of unambiguous price points. To understand cumulative economic and environmental costs of a technology over its entire service life it is common to use lifecycle analysis (LCA), a framework regulated by the International Organization of Standardization. This framework provides structure for analyzing such a wide array of systems and scales that some subjectivity is entailed in approaching specific sets of questions, and resources are available to guide analysis.[25]

As has been noted by the National Renewable Energy Lab, market and policy complexities make prices defining a PV technology's threshold of profitability highly dependent upon the economic performance metric chosen.[26] One of the most holistically meaningful metrics is the levelized cost of electricity (LCOE) which accounts for subsidized and direct capital investment as well as continued investment in facility overhead. LCOE is essentially the cost at which electricity must be generated to completely recoup initial and continued investment averaged over a technology's lifetime. The US Energy Information Administration estimates that the LCOE for photovoltaics in general will be roughly \$125 per megawatt-hour (MW-hr) in 2020 compared to ~\$100 per MW-hr for coal.[27] For perspective on what is becoming realistically achievable, SunEdison, an industry leader in monocrystalline silicon photovoltaics, is building to meet a \$46 per MW-hr power purchasing agreement (PPA) by 2016. More recently, a Nevada utility signed a PPA for ~\$39 per MW-hr power from a thin film solar farm being developed by First Solar. These price points reflect sharp changes from as recently as 2014 when the same Nevada utility paid an average of ~\$140 per MW-hr for renewable energy.[28] Champion PVSCs have reached over 20% power conversion efficiency (PCE) in just a few years compared to the ~40 years of research behind champion 25% PCE monocrystalline silicon devices and 21.5% PCE CIGS and CdTe thin film devices.[22] This combined with relatively low material and fabrication costs[29] makes PVSCs appear viable as on-grid competitors for existing technologies; however, this remains completely dependent on addressing ecotoxicity, J-V hysteresis, and degradation.

Both LCOE and levelized avoided cost of electricity (LACE) are necessary metrics for fairly comparing viability of different generation strategies in real settings, but the sensitivity to economic and regional realities make these mechanics cumbersome for comparing various PV technologies on equal footing. Energy payback time (EPBT) is the service time required for a solar cell to generate net positive energy after accounting for all energy invested in its creation. It has recently been shown that PVSC EPBT can be as low as 0.22 years compared to ~2.4 and ~0.7 years for crystalline silicon and thin film PV technologies respectively.[29] Deleterious impacts on freshwater and human health identified by recent LCAs have been linked to Pb in $CH_3NH_3PbI_3$ and other environmentally expensive materials in PVSCs like FTO/ITO glass and noble metal electrodes.[29] While encapsulation[30] makes Pb escape during PVSC service negligible, disposal[31] is a serious issue. The remarkably low PVSC EPBT may allow greater investment in end-of-life infrastructure for this technology, as well as aggressive device encapsulation to address the most direct impediment to PVSC implementation: $CH_3NH_3PbI_3$ degradation.[32] $CH_3NH_3PbI_3$ is vulnerable to degradation through hydration, but exposure to illumination, bias, and heat accelerate the process in unique ways.[32] Moreover, $CH_3NH_3PbI_3$ is thermodynamically unstable relative to PbI_2 at operating temperatures which makes eventual degradation inevitable regardless of encapsulation.[33] While this issue makes PVSC commercialization potentially prohibitive, compositional engineering[33,34] has shown promise in addressing both thermodynamic instability of $CH_3NH_3PbI_3$ and J-V hysteresis in PVSCs.

Currently, most markets necessitate 15 to 20 year warrantees for competitive residential and commercial PV systems. Depending on how successfully the research community addresses $CH_3NH_3PbI_3$ degradation, this service life may not be possible for some time. While this limits immediate PVSC on-grid potential, the remarkably low EPBT, wide and vivid color tunability,[35] and device flexibility readily enable contributions to the same niche markets organic photovoltaics (OPV) have sought footing in.[36,37] Semitransparent, neutral density[38] and colored PVSCs[35] have demonstrated the technology's potential for building integrated photovoltaics (BIPV) as well.[39] Impediments to PVSC energy grid integration make market contribution more likely via gradual percolation through these niche markets. Thus, scaling up large area, flexible device fabrication allows greater access to the value this technology offers. For the research community, these current market realities highlight fully printable PVSCs as a driving goal for innovation. In terms of fundamental chemical research, this implicates thermodynamic control of $CH_3NH_3PbI_3$ growth and degradation as important directions to fuel continued growth of the field. This introductory chapter offers perspective on challenges in up-scaling PVSC fabrication as well as potential solutions.

1.1.2 *Challenges inherent to PVSCs*

Each challenge inherent to $CH_3NH_3PbI_3$ is tied to a key aspect of the material's utility. Ecotoxicity, *J-V* hysteresis, and instability are impediments to the development of any hybrid perovskite based technology, and these issues take on new and more imposing character in any attempt to scale up PVSC production (summarized in **Figure 1.1**).

Pb possesses electronic properties that make it a very unique part of the periodic table. While also partly the source of its cytotoxicity,[40] the size of Pb makes the 6s electrons that stabilize the 2+ oxidation state inert. While in the 2+ oxidation state, Sn easily oxidizes to 4+ creating instability in $CH_3NH_3SnI_3$ even more troublesome than in $CH_3NH_3PbI_3$.[24] This makes Pb elimination more a matter of new material design rather than simple atomic replacement.[41] In the immediate future, the challenge thus shifts to $CH_3NH_3PbI_3$ device encapsulation,[32] end-of-life measures like recycling, and integration into other Pb based technology lifecycles.[31] Recent LCAs indicate that device encapsulation can effectively limit Pb escape during PVSC service[30] and end-of-life techniques like incineration and Pb recovery can further minimize exposure.[31] Ultimately, the degree of Pb exposure indicated by current LCAs is moderate and comparable to existing technologies, especially when PVSCs are used for Pb sequestration from already societally prevalent sources like Pb-acid batteries.[31] Specific environmental regulations controlling the implementation of photovoltaics vary throughout the world, but in terms of Pb toxicity this technology will face considerations similar to those relevant to the application of cadmium based thin film PV.

In addition to the toxicity inherent to Pb, PVSCs exhibit anomalous hysteresis.[42] In photovoltaics, hysteresis commonly manifests as a change in the shape of *J-V* characteristics. Through fierce investigation it has been unveiled that the changing electric field profile within $CH_3NH_3PbI_3$ responsible for hysteresis is largely caused by motion of ions within the $CH_3NH_3PbI_3$ lattice. [43,44]

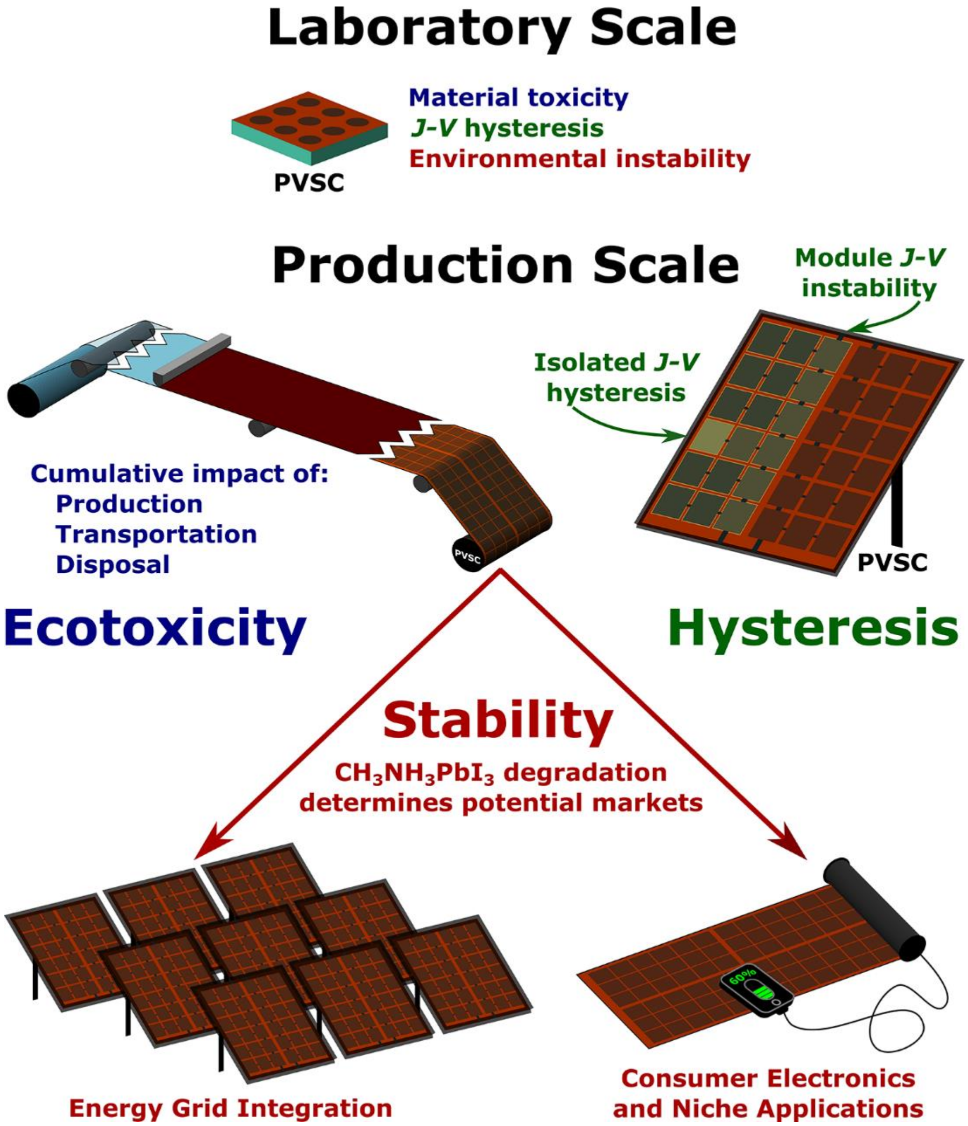

Figure 1.1. Schematic showing how each challenge intrinsic to PVSCs takes on a new weight at scale. Ecotoxicity and *J-V* hysteresis are serious issues, but environmental stability and limited service life are the sharpest determinants of potential markets for PVSCs.

In $CH_3NH_3PbI_3$, the delicate balance between Pb, iodide, and methylammonium binding enables the low temperature self-assembly responsible for this material's potentially transformative impact in the PV sector.[33] Pb can exist in many different coordination states with halogens, which is a key issue in the chemistry behind $CH_3NH_3PbI_3$ growth,[STW-2] but this flexibility also likely adds lability to the Pb-I bond in the solid state. By virtue of calculated activation energies, methylammonium, iodide, and their respective charged vacancies in $CH_3NH_3PbI_3$ are primarily implicated in ion motion behind hysteresis.[43] That said, illumination, bias, heat, and sources of degradation like water modify how hysteresis manifests in *J-V* behavior, and thus the issue may be physically quite complex.[45] On the laboratory scale, accounting for hysteresis is important to preserve accuracy of PVSC performance data.[42] On the module scale, failing to account for hysteresis may make entire blocks (individual devices in parallel) perform unstably and introduce mismatch effects along entire strings (blocks connected in series).

Beyond *J-V* hysteresis, there are a wealth of degradation mechanisms that make PVSCs vulnerable to environmental conditions, the most troublesome of which being the tendency for the material to incorporate atmospheric water into its bulk and gradually transform into hydrated analogues of the desired perovskite. Metastable monohydrate (recoverable) and stable dihydrate (unrecoverable) formation is driven by hydrogen bonding between water molecules and $CH_3NH_3^+$ in the $CH_3NH_3PbI_3$ lattice. Transformation to PbI_2 from any of these states can occur through proton transfer yielding highly volatile CH_3NH_2 or gradual CH_3NH_3I sublimation.[32] While $CsPbI_3$ perovskites eliminate this hydrogen bonding and transfer, elimination of $CH_3NH_3^+$ complicates processing and reduces performance.[24] Degradation is uniquely troublesome on the module level for the same reasons *J-V* hysteresis is problematic, but with degradation individual cells may eventually be completely removed from the circuit. Complete water exclusion can be energetically costly in many high throughput device fabrication techniques, and water interacts with $CH_3NH_3PbI_3$ growth even at small concentrations.[32] Environmental $CH_3NH_3PbI_3$ exposure can accelerate Pb liberation[30] and exacerbate *J-V* hysteresis[45] tying together all fundamental challenges in PVSC design.

Although toxicity and hysteresis affect PVSC price point, degradation establishes sharp ceilings for device lifetime and thus largely determines what markets the technology can contribute to. Although

PVSC stability over 40 days has been demonstrated,[46,47] In the short term this means that the most significant contribution from PVSCs may be to niche markets like portable electronic devices, flexible PV coatings, and BIPV. Integration of PVSCs into the energy grid may become possible, but only through opportunities in material and device design.

1.2 Prospective Research to Facilitate PVSC Scale-up

Ultimately, capitalizing on the unique strengths of PVSCs requires use of their uniquely flexible, solution processability. Specifically, this means that processing techniques like slot-die roll-to-roll coating are ideal platforms to bring PVSCs into the niche markets they are positioned to contribute to. Although roll-to-roll coating is an ideal technique to facilitate scale-up, it brings the substantial challenge of controlling perovskite growth back into the spotlight.

On the laboratory scale, spin-coating provides an expedient route for thin-film deposition from solution because at the high spin rates used, viscosity and interaction with the substrate largely determine film dimensions. This process produces a uniform film of solution, and in ideal cases optimization is geared toward controlling solvent removal. $CH_3NH_3PbI_3$ growth proceeds through many solution and solid states making even spin-coating difficult to control.[STW-4] While large area $CH_3NH_3PbI_3$ deposition techniques are already under investigation, fully printable module level PVSC production remains a significant challenge. Practically realizing this goal entails device level challenges similar to those the organic photovoltaic (OPV) field has faced[48] and material challenges unique to $CH_3NH_3PbI_3$ growth.[33,43]

The unique challenges presented by PVSC development and scale-up (ecotoxicity, J-V hysteresis, and degradation) require innovations in material, process, and device design. While device level challenges like interfacial engineering and charge transport interlayer design are important aspects of addressing these fundamental challenges, this dissertation focuses on deepening understanding of the more fundamental processing-structure-property relationships at play in the hybrid perovskite material system. The section focused specifically on device level challenges and innovations has been omitted here, but can be found in STW-1.

1.2.1 *Challenges inherent in scaling-up perovskite growth*

The primary issue that separates PVSC scale-up from other classes of solution processable photovoltaics is the complex growth behavior of $CH_3NH_3PbI_3$ and the equally complex structure-property relationships that result.[47] Hybrid perovskite colloidal and coordination chemistry creates an intimate relationship between solution chemistry and final film quality.STW-2 The nature of the just-deposited film of solution thus determines a great deal about how $CH_3NH_3PbI_3$ growth proceeds. Slot die and blade coated films initially contain much more material overall as well as a much greater fraction of solvent than comparable spin-coated films. This means that much of the work devoted to optimizing $CH_3NH_3PbI_3$ growthSTW-4 cannot be directly applied to scaled-up production without re-optimization and in some cases fundamental restructuring. The greater solvent content in films deposited with R2R coating likely shifts the growth kinetics of $CH_3NH_3PbI_3$ and its intermediates. Many relationships established between initial conditions, temperature, time, atmosphere, solution composition, growth, and resulting device performance must thus be remapped in conditions relevant to particular scalable methods. The thermodynamically limited $CH_3NH_3PbI_3$ growth in these high solvent content films makes controlling growth thermodynamics through solutionSTW-2 and interfacial chemistry[49] key to scaling-up production.

The solvent washing deposition method serves as an excellent example of the reformulation necessary to adapt lab-scale strategies to the large scale.[34] This approach produces remarkably high quality $CH_3NH_3PbI_3$ films on the laboratory scale, but it does so by capitalizing on the ability to almost instantaneously add and remove an anti-solvent through spin-coating. Since extreme substrate motion is impossible for large devices, this strategy must be fundamentally reformulated for module scale production. The physical balance responsible for the success of this technique on the lab scale is chemically intrinsic to the choice of solvent, anti-solvent, and species constituting $CH_3NH_3PbI_3$. Thus it should still be possible to use an anti-solvent to control $CH_3NH_3PbI_3$ formation in large devices. That said, for printed films a different physical means of anti-solvent exposure like vapor treatment becomes necessary, which entails another regime of exploration and optimization. Further complication stems from inevitable non-idealities intrinsic to large area processing like spatial variations in temperature, vapor composition, and solution concentration. While possible to address these issues with optimization, as has been attempted with regard to water exposure during fabrication,[50] complex interrelated processes like hydration, *J-V* hysteresis, and degradation[32] complicate optimization.

Because complexity in $CH_3NH_3PbI_3$ growth is not limited to the solid state,STW-2 regulation of solution feed stock will become a practical consideration for industrial production. Time dependent solution equilibria like aggregation[51] and complex ion formationSTW-2 will complicate consistency, an issue that illustrates the possible utility of two-step $CH_3NH_3PbI_3$ growth for scalable deposition.[52] Entirely vapor based deposition techniques avoid the complexity of $CH_3NH_3PbI_3$ growth from solution at the expense of increased cost and the difficulty inherent in controlling vapor concentration and flow across large areas. Although one-step $CH_3NH_3PbI_3$ growth from vapor circumvents $CH_3NH_3PbI_3 \cdot$ Solvent intermediates,STW-4 other intermediate phases implicit in $CH_3NH_3PbI_3$ growth like $CH_3NH_3PbCl_3$ still persist.[53] This means that the requirement to carefully control growth through processing conditions remains relevant.

$CH_3NH_3PbI_3$ growth is linked to almost every identifiable processing parameter but our understanding of the structure-property relationships defining electronic conduction, absorption, *J-V* hysteresis, and degradation in $CH_3NH_3PbI_3$ is still developing. Both $CH_3NH_3PbI_3$ carrier concentration and *J-V* hysteresis[45] are linked to halide stoichiometry, a parameter that changes throughout growth to a degree dependent on growth route and conditions. The importance of microstructure in carrier recombination has been demonstrated,[54] but the exact origins for the behavior remain unclear. The convolution of all relevant properties with illumination, bias, and temperature[55] makes $CH_3NH_3PbI_3$ a uniquely complex system to fully grasp at the design level, and thus work towards fundamental understanding still plays a role in the development of this technology. The material (A), chemical (B), and process (C) engineering necessary to achieve scaled up PVSC production is outlined in **Figure 1.2** and discussed below.

1.2.2 *Scalable solutions from material to device levels*

Fundamental thermodynamic instability,[33] susceptibility to hydration,[32] and high ionic mobility[43] are properties intrinsic to $CH_3NH_3PbI_3$. Thus, truly scalable PVSC solutions addressing these key challenges must incorporate compositional control of the perovskite lattice itself (Figure 1.2a).

Bromide and fomamidinium (FA) have been successfully incorporated into the $CH_3NH_3PbI_3$ lattice to mitigate *J-V* hysteresis[34] and eliminate fundamental thermodynamic instability.[33] The increased bond polarity of Pb-Br relative to Pb-I plays a beneficial role in crystallization. Bromine inclusion shifts the band gap[24] which allows color tuning for BIPV[39] and tandem device architectures.[24] Additionally, many have found that a small amount of Br and FA lead to a maximum in overall device PCE.[34] The precise mechanism behind these enhancements in fundamental material properties remains unclear and under illumination the otherwise complete solid solubility of Br in $CH_3NH_3PbI_3$ shifts limiting effective substitution to roughly 20 atom percent.[12] Regardless of these complexities, compositional optimization of $CH_3NH_3PbI_3$ is an inevitably necessary tool for effective scale-up.

Taking $CH_3NH_3PbI_3$ compositional engineering and the unique conditions of R2R coating into account in the optimization of $CH_3NH_3PbI_3$ growth, microstructure, and composition is an important step in realizing module scale PVSCs (Figure 1.2b). Although the sensitivity of $CH_3NH_3PbI_3$ growth toward almost all processing parameters makes production a challenge,[STW-4] it also creates unique opportunities for exerting control. The shift from spin-coating to R2R coating represents a shift from kinetically limited $CH_3NH_3PbI_3$ growth to thermodynamically limited growth. The most effective way to control growth thus becomes tuning the thermodynamics driving growth through precursor solution composition,[STW-2] the chemistry of the surface on which growth occurs,[49] annealing conditions, and atmosphere during growth.[24]

Remapping thermal annealing behavior under conditions directly relevant to large area deposition is readily done. Solution additives, solvent engineering, and spectator ions like Cl^- can be exploited to fundamentally alter $CH_3NH_3PbI_3$ growth route and control kinetics of competing processes.[STW-4] The retrograde solubility of $CH_3NH_3PbI_3$ in certain solvent systems creates unique opportunities for tuning growth thermodynamics with temperature,[56] both before deposition by controlling aggregation in solution and after deposition by controlling solubility. While an inevitable complication of large area deposition, the

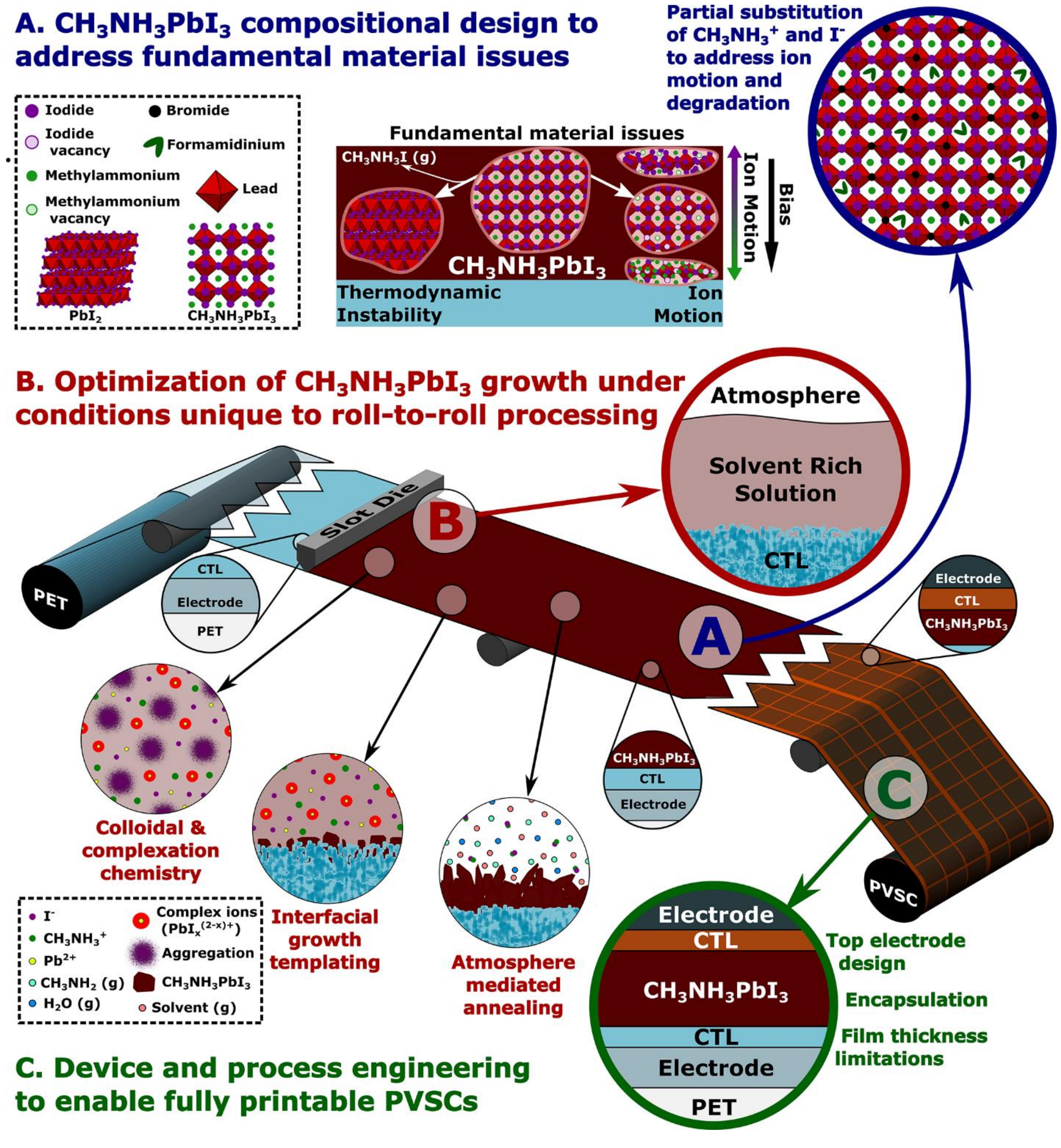

Figure 1.2. Summary of research directions necessary to fuel PVSC technology translation *via* slot die R2R coating. (A) material engineering can address intrinsic ion diffusivity and degradation of $CH_3NH_3PbI_3$, (B) optimization of perovskite growth under R2R conditions is necessary to reach performance requirements, and (C) device engineering is required to extend device life and expand the material toolbox for PVSC design (polyethylene terephthalate (PET), charge transport interlayer (CTL)).

influence of atmosphere during $CH_3NH_3PbI_3$ growth allows control of morphology and film quality through tuning the concentration of solvent, methylamine, and water vapor present.[24] Interface modification through self-assembled monolayer (SAM) deposition, solvent treatment, and a variety of other methods exploit relationships between substrate surface chemistry and $CH_3NH_3PbI_3$ growth to control crystallization without external intervention. This makes interface modification an important consideration in scale-up despite the challenge of ultra-thin film deposition with R2R coating. Vapor based post deposition modification with primary amines and moderately sterically hindered Lewis bases,[57] processes readily adaptable to R2R coating, have shown a dramatic influence on $CH_3NH_3PbI_3$ interfacial microstructure and chemistry respectively.

Because thermal and ambient instability are the sharpest limitations to PVSC market potential, the EPBT and potential price point of fully printable, flexible PVSCs are central to this technology's current capacity for commercialization. Limitations in SAM and ultra-thin film deposition through slot die R2R coating constitute an opportunity for innovation in realizing effective PVSC modules. Tuning solution feed remains the most expedient route for controlling thickness, and creative processing techniques realizing SAM modification with R2R coating[58] will enable a larger material tool box for PVSC fabrication at scale. Replacement of the often employed silver electrode is necessary to avoid expediting $CH_3NH_3PbI_3$ degradation, and electrode deposition itself is an area ripe for innovation. This is especially true for transparent electrodes to enable module scale, semi-transparent PVSCs. Inevitable contributions from J-V hysteresis must be addressed by pragmatic module design to avoid unstable performance. Device encapsulation and end-of-life techniques like recycling are practically necessary to implement PVSCs at any scale; but ultimately the color tunability, EPBT, and flexibility offered by fully printable PVSCs enable contributions to consumer electronics and other niche markets like BIPV.

1.2.3 *Concluding remarks on technology translation*

As the recent inclination within the field toward exploring new systems demonstrates, development of $CH_3NH_3PbI_3$ based PVSCs has reached the plateau appropriate to support pursuit of technological translation. Challenges facing the technology remain substantial, but through focused fundamental research addressing $CH_3NH_3PbI_3$ degradation as well as pragmatic engineering addressing Pb ecotoxicity and *J-V* hysteresis this technology may eventually become viable for energy grid integration. In the immediate future, techniques like slot die R2R processing are poised to enable the price point necessary for PVSCs to contribute to the same markets sought after by OPV. PVSC scale-up, however, requires sensitivity to the complex growth of $CH_3NH_3PbI_3$ as well as the challenges intrinsic to R2R coating. Necessary solutions to these issues range from material to device levels (Figure 1.2).

$CH_3NH_3PbI_3$ compositional engineering is necessary to address fundamental material issues like ion mobility and stability. Optimization of $CH_3NH_3PbI_3$ growth specific to the thermodynamically limited conditions inherent to R2R coating along with the exploration of post deposition treatments is necessary for ensuring quality material preparation at scale. The sensitivity that makes $CH_3NH_3PbI_3$ growth depend on virtually all processing parameters creates an equivalently wide variety of strategies for controlling growth. Intrinsic limitations of R2R coating in extremely thin film and SAM deposition along with electrode design and deposition complicate fully printable PVSC fabrication, but if addressed the resulting price point of the technology may enable PVSC market permeation via percolation through niche applications like BIPV and consumer electronics. While herein we have focused on the market potential of PVSCs alone, $CH_3NH_3PbI_3$ has great potential for application in tandem devices with silicon or CIGS based devices as well as application in light emitting and detecting technologies. Despite the challenges, $CH_3NH_3PbI_3$ has proven to have potential limited only by our ingenuity.

1.3 Research Focus

As this introduction has endeavored to show, compositional engineering plays an important role in facilitating eventual PVSC commercialization. Understanding the role each site in $CH_3NH_3PbI_3$ plays in mediating transformation is an important part of this overall effort because of the importance of material growth and eventual morphology in determining material quality and functionality. Through a series of case studies, this dissertation explores the role that each site within the perovskite lattice plays in mediating transformation and growth. In the second half of this dissertation, this insight is leveraged to explore both the role of solvent molecules in growth and the larger challenge of Pb replacement.

This introductory chapter presented a broad overview of the potential of PVSCs and the challenges inherent in realizing this potential, illustrating the key role compositional engineering plays in technology translation. Chapter 2 presents a case study of the role of Cl in perovskite growth. Chapter 3 presents a case study of post-deposition modification with CH_3NH_2 vapor. Chapter 4 presents a conceptual consolidation of this insight along with insight available in the larger field with a focus on the universal importance of nucleation kinetics in perovskite growth. Chapter 5 presents a brief survey of the periodic table with the goal of identifying potential elements to explore modification of the metal site in $CH_3NH_3PbI_3$. Chapter 6 presents a more focused and thorough study of transition metal inclusion in $CH_3NH_3PbI_3$. Finally, Chapter 7 consolidates the insight generated throughout this work. Through the relationships between composition, processing, and morphology that this work aims to understand, we ultimately offer perspective for continuing efforts toward Pb replacement and PVSC technology translation.

Chapter 2. INTERMEDIATE STATES AND KINETIC PROCESSES IN $CH_3NH_3PbI_3$ GROWTH FROM SOLUTION: Case Study of the Role of Chloride

**This entire chapter has been reproduced verbatim from STW-2 (Reproduced from Ref. STW-2 with permission from the American Chemical Society.)*

This chapter presents a mechanistic study of the impact of chloride on $CH_3NH_3PbI_3$ growth that was originally published in an article titled *Role of Chloride in the Morphological Evolution of Organo-Lead Halide Perovskite Thin-Films* (STW-2). The vast majority of the following material is reproduced verbatim from this publication with the exception that material originally published as a supporting information document has been integrated into the main text. Methods will be described in detail at the conclusion of the chapter.

2.1 Introduction

With the rapid rise in efficiencies reported in the past few years,[22] organo-lead halide perovskite photovoltaics are considered viable competitors for prevailing silicon based technologies. Many device architectures are being explored;[59–64] however, exerting better control over perovskite crystal formation remains the critical challenge in each case.[65–72] Depositing lead iodide (PbI_2) seed crystals into mesopourous TiO_2 has been demonstrated to effectively improve the quality of resulting perovskite absorber layers in dye sensitized solar cells (DSSCs), which highlights the impact of the nucleation event on the resulting crystallinity of these materials. Film growth in the planar heterojunction (PHJ) architecture has proven to be even more challenging due to the difficulty of encouraging consistent crystallization across planar interfaces, especially in the case of solution based techniques.[65,68–70,73–76] Physical vapor deposition has been demonstrated to be an effective way to grow high quality perovskite films in the PHJ architecture,[77] but in this case we lose the benefits solution processing offers. Similar to the case of DSSCs, a variety of seeded growth approaches have been investigated to modulate the crystal formation of perovskite thin-films as in the case of dip coated[66] and vapor assisted[67] film development. With regard to manufacturing, developing a simple and low temperature solution based growth process is essential to meet current commercial requirements.

Recently, Snaith *et al.* found that inclusion of chloride in the precursor solution is an immensely effective method to enhance crystal formation and morphology of perovskite thin-films. The resulting electronic properties of such films have been found to be greatly improved, most notable of which are the exciton lifetime and diffusion length which are found to increase by more than an order of magnitude.[78,79] Since this discovery, great strides in the engineering of efficient PHJ organo-lead halide perovskite solar cells have been made through the incorporation of chloride to improve perovskite morphological development and optoelectronic performance. Significant improvements have been made in systems incorporating chloride either by using the lead chloride[13,65,69,79] ($PbCl_2$) or methylammonium chloride (MACl) salt.[80] This advance has been integral to the rapid increase of device performance in a variety of architectures, but the underlying mechanism through which such dramatic enhancement is achieved still remains unclear.

There has been increasing discussion in the recent literature as to the final state of the chloride ion in these systems. Initially it was assumed that chloride preferentially occupies axial atomic coordinates in lead halide octahedra at equilibrium after annealing,[77] but the discussion has since shifted to whether or not the ion remains in the system at all rather than how it is integrated into the perovskite lattice.[71,80] Colella *et. al.* demonstrated that the development of the methylammonium (MA^+) lead iodide perovskite crystal ($MAPbI_3$) is thermodynamically preferred over the development of a predominantly lead chloride perovskite lattice ($MAPbCl_3$).[13] They found that only supplying a stoichiometrically insufficient amount of iodide to the system could ensure the existence of $MAPbCl_3$ at equilibrium. While quite informative, this result does not elucidate the mechanism through which the presence of chloride influences the system nor does it decidedly answer the question of chloride's eventual fate post-annealing.

In this study, we present a morphological investigation of the organo-lead halide perovskite system

($CH_3NH_3PbX_3$, X = I/Cl) by using scanning and transmission electron microscopy (SEM and TEM) to elucidate chloride's role in impacting crystal evolution. We find that in systems without chloride, nucleation is driven primarily by interfacial energy at the substrate's surface with continued growth occurring through self-assembly at and around already nucleated sites resulting in relatively poor coverage and crystallinity across the planar interface (PEDOT:PSS, herein). Upon the incorporation of chloride, we find that the nucleation event changes significantly owing to the preferential generation of a chloride rich phase. This phase then templates a gradual transformation to the iodide perovskite lattice through a rather complex phase evolution. The result of this templated self-assembly is dramatically increased crystallinity and considerably altered film texture. More importantly, the rapid formation of this template phase generates composition gradients throughout the evolving film, which we posit leads to the morphological diversity typically observed in perovskite films grown from solutions made with $PbCl_2$ (**Figure 2.1a**). We find that aggregation and complex ion equilibria in the precursor solution may mediate the formation of this phase and the resulting distribution of film morphologies. As far as we know, this is the first study employing TEM for direct through-plane characterization of perovskite thin films grown under conditions identical to those used for device fabrication in the PHJ architecture. This powerful analysis is capable of probing the crystallographic consequences of film growth like crystalline texture, grain structure, and elemental distribution across the breadth of a film. It both greatly increases insight into the relevant crystal chemistry and may provide direct physical evidence of how chloride inclusion leads to such significantly enhanced exciton lifetimes and diffusion lengths.

2.2 Anomalous Morphological Variety in Films Grown with Cl

When fabricating conventional PHJ devices (ITO/PEDOT:PSS/perovskite/$PC_{61}BM$/ electrode)[68] from a precursor solution made with $PbCl_2$ (solution stoichiometry of **3MAI + $PbCl_2$**), we often observe a variety of coexisting perovskite film morphologies. However, when the films are grown from a solution made with only the methylammonium iodide (MAI) salt and PbI_2 (stoichiometry of **MAI + PbI_2**), films do not show this degree of variety and are almost entirely consistent. The SEM images shown in Figure 2.1be highlight the three typically dominant morphologies observed in films grown from precursor solutions of **3MAI + PbCl$_2$**. The morphology that exhibits poor film coverage (Figure 2.1d) is highly reminiscent of that formed from a precursor solution of **MAI + PbI$_2$** (**Figure 2.2**). Figure 2.1c shows a markedly different morphology with dramatic crystal faceting, consistent 90° angles between domains, and low surface roughness. Lastly, we observe a morphology that exhibits good film coverage but a different apparent

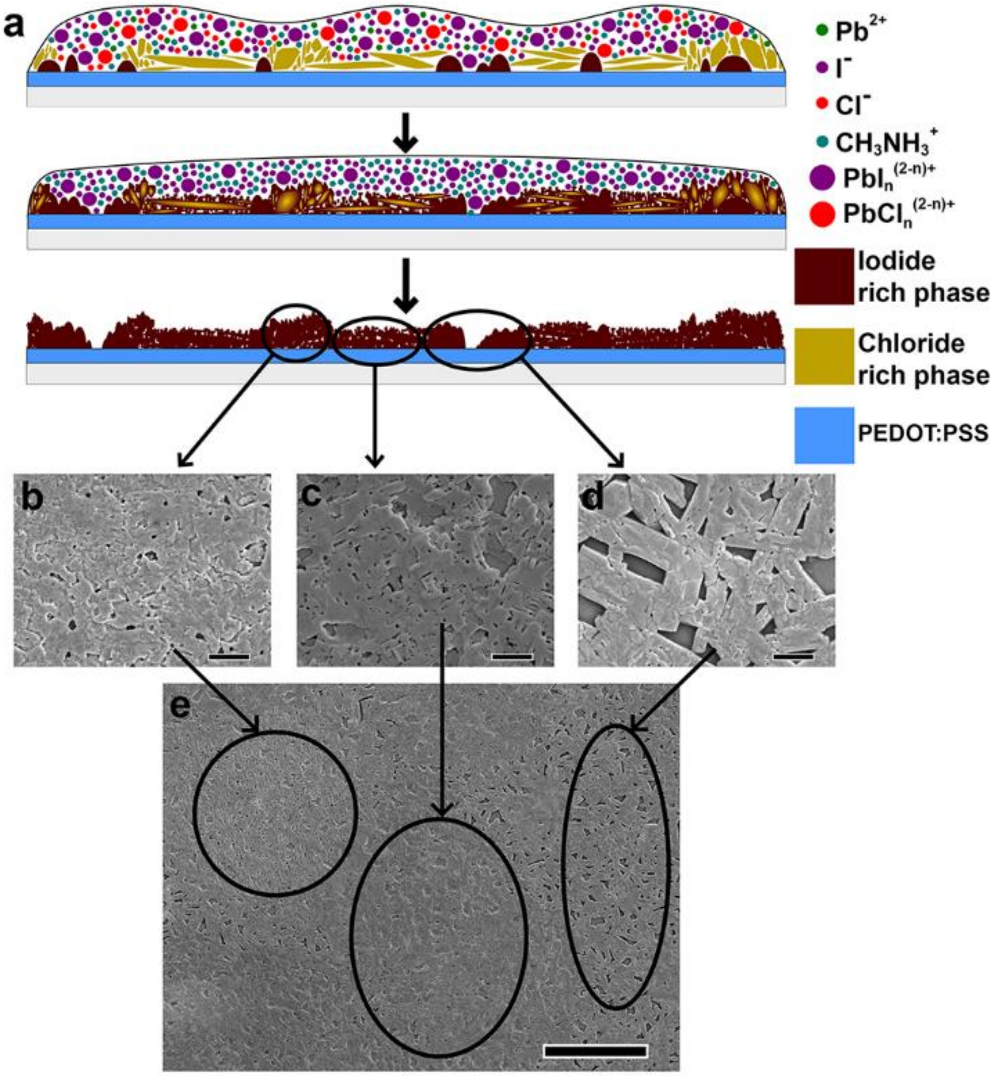

Figure 2.1: CH$_3$NH$_3$PbI$_{3-x}$Cl$_x$ thin film formation on PEDOT:PSS. (a) Schematic illustration and (b)-(d) morphologies characteristic of a perovskite film spin cast from a solution of **3MAI + PbCl$_2$**. (e) a low magnification SEM image showing all three coexisting in a typical film as regions of bright contrast (b), regions of dark contrast (c), and regions of poor coverage (d). Scale bars in (b)-(d) and (e) are 2 μm and 20 μm, respectively. The illustration in (a) represents nucleation during deposition (top), phase evolution and growth during annealing (middle), and final morphology (bottom)

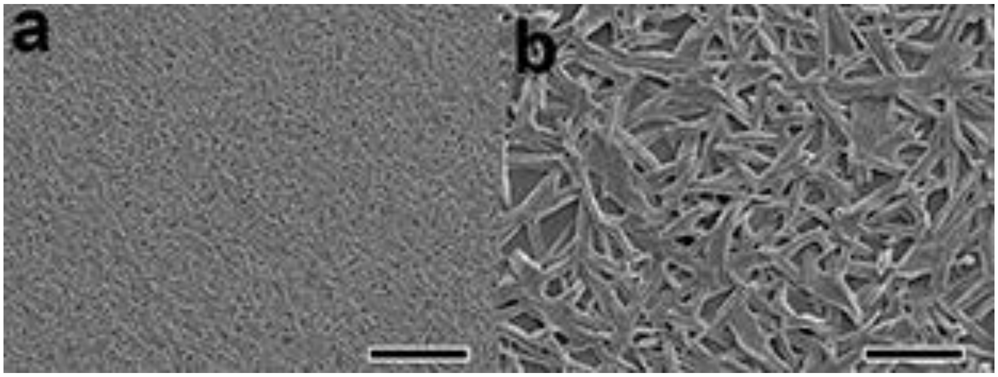

Figure 2.2: SEM images of films grown from MAI + PbI_2. Scale bars are equal to (a) 20 μm and (b) 5 μm.

collective crystal orientation, or texture, as is shown in Figure 2.1b. In low magnification images (Figure 2.1e), the regions shown in Figures 2.1b and c often appear bright and dark in contrast, respectively. Conversely, the morphology of films cast from a **MAI + PbI_2** precursor solution consistently shows a homogenous morphology with poor coverage reminiscent of Figure 2.1d (Figure 2.2). Given the unique morphological diversity in films grown from solutions prepared with $PbCl_2$, it can be speculated that the mere presence of the chloride ion does not tell the whole story regarding its impact on film evolution and crystal growth.

To determine how the presence of chloride is leading to such uniquely varied morphology, we first considered the possible impacts of coarsening, phase inhomogeneity, and compositional inhomogeneity in the final film. Coarsening is a process in which a crystal's surface is restructured through atomic diffusion to minimize surface energy. If halted before completion, this process could make the observed morphological diversity the result of a transition from a kinetically favored morphology to a thermodynamically favored structure. To see if this phenomenon is relevant in this system, the influence of extended annealing on the distribution of morphologies throughout a 24 h time frame was investigated in both films cast from **3MAI + $PbCl_2$** (**Figure 2.3 a-f**) and **MAI + PbI_2** (Figure 2.3 g-l) solutions. As annealing time increases, there is no consistent change in the prominence of the areas of poor coverage, dark contrast, and light contrast in Figure 2.3 a-f, indicating that there is no clear correlation between the prominence of any particular morphological feature and annealing time beyond the time necessary for perovskite formation. These features can be difficult to see in these images because of the low magnification, but such magnification is necessary to give an overview of the distribution of the features discussed. Although Figure 2.3 g-l is shown at a greater magnification because of the lack of morphological diversity, no significant coarsening can be observed in films cast from a **MAI + PbI_2** solution either.

Having ruled out the effect of coarsening as the cause of morphological diversity, inhomogeneity in final perovskite composition was considered as a possible culprit. If this compositional variation is to come primarily from lead, iodide, or methylammonium, we should see a destabilization of the $MAPbI_3$ phase and

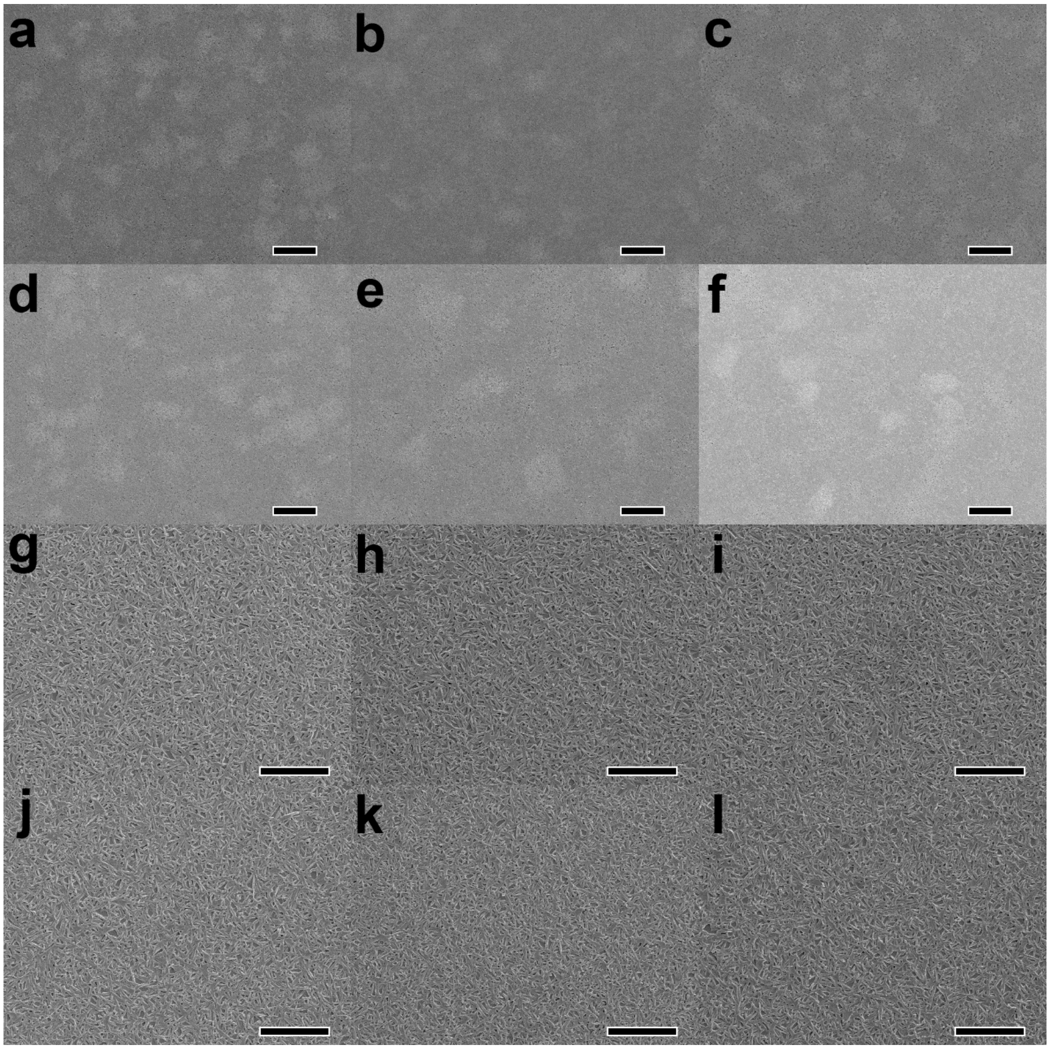

Figure 2.3: SEM images of perovskite films at extended annealing times. (a)-(f) shows films cast from solutions of 3MAI + $PbCl_2$: (a): 3h, (b): 5h, (c): 7h, (d): 12h, (e): 18h, and (f): 24h with scale bars equal to 50 µm. (g)-(l) show films cast from solutions of MAI + PbI_2: (g): 3h, (h): 5h, (i): 7h, (j): 12h, (k): 18h, and (l): 24h with scale bars equal to 20 µm. This series can be shown at a greater magnification because of the lack of morphological variety.

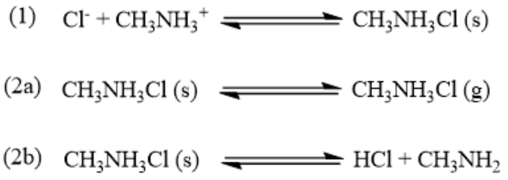

Scheme 2.1: Mechanisms for the loss of chloride. Sublimation of methylammonium chloride (2a) or decomposition into hydrochloric acid and methylamine (2b) may be responsible for the loss of chloride during film growth.

a generation of other phases. X-ray diffraction (XRD) of a selection of films from the annealing study presented in Figure 2.3 shows good phase purity with the exception of a small amount of residual PbI_2 (**Figure 2.4**), ruling out phase variation as the main cause of morphological diversity. With this in mind, the primary source of compositional variation should come primarily from changes in chloride content throughout each film, but SEM energy dispersive spectroscopy (EDS) shows no measureable chloride remaining in the bulk of any of the **3MAI + $PbCl_2$** films (**Table 2.1**).

The issue of chloride loss has been raised in recent literature.[71,80] The currently considered loss pathways center around the sublimation of MACl[71,81,82] or a degradation of MACl into the volatile hydrochloric acid (HCl) and methylamine species facilitated by residual water (**Scheme 2.1**).[83] The nature of this loss mechanism suggests that chloride must diffuse to the film's surface to ultimately escape the system, meaning that a bulk sensitive composition measurement like SEM EDS may miss residual chloride remaining at the perovskite's surface. Thus, to complement the EDS data we conducted X-ray photoelectron spectroscopy (XPS), a highly surface sensitive (~5-10 nm) composition analysis technique. As can be readily seen in **Figure 2.5**, the signal characteristic of chloride's 2p core electrons is completely absent and only the weak peak from iodide's 4s electrons can be observed. Moreover, we observe no inflection of the background with increasing annealing time. Therefore, it can be concluded that no chloride remains at the surface of these perovskite films, within the detection limits of the instrument.

Annealing Time	I:Pb ratio in MAI + PbI_2	I:Pb ratio in 3MAI + $PbCl_2$
3 hours	2.67 ± 0.02	2.65 ± 0.02
5 hours	2.71 ± 0.02	2.71 ± 0.04
7 hours	2.67 ± 0.03	2.69 ± 0.04
12 hours	2.66 ± 0.01	2.68 ± 0.01
18 hours	2.67 ± 0.11	2.68 ± 0.04
24 hours	2.68 ± 0.04	2.67 ± 0.02

Table 2.1: SEM EDS of films from the annealing time series. No chloride is detected in any sample.

Excluding the influences of coarsening, compositional inhomogeneity,

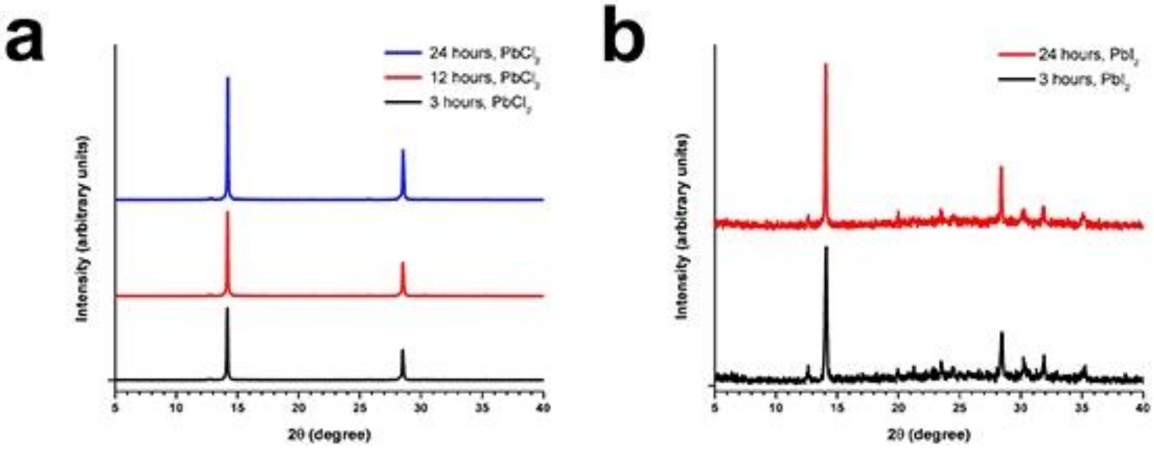

Figure 2.4: XRD patterns of a selection of films from the annealing series. (a) XRD pattern of films grown from a solution of **3MAI + $PbCl_2$** and (b) the XRD pattern of films grown from a solution of **MAI + PbI_2**.

and phase inhomogeneity as the primary sources of the observed morphological diversity suggests that final morphology is determined during deposition and initial annealing. This motivates us to evaluate the importance of the various chemical equilibria that occur within the precursor solution before deposition. Until this point, it has generally been thought in the literature that the function of the $PbCl_2$ salt is largely to introduce chloride ions into the solution, which ultimately creates competition in ligating Pb^{2+} ions upon deposition and thus modifies crystallization kinetics.[80] If this is the case, how we introduce chloride into the system should have no impact upon the final product.

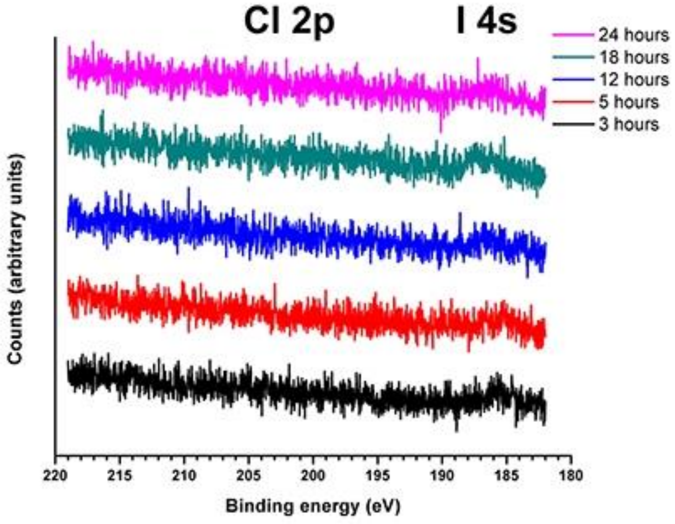

Figure 2.5: XPS of a selection of films from the annealing series. While the peak from iodide's 4s orbital is visible, no signal from chloride's 2p orbital can be observed indicating no chloride remaining at the film's surface within the technique's detection limit.

To test this, we fabricated two sets of films using solutions with identical overall compositions, but in one we introduced chloride through the

$PbCl_2$ salt and in the other we introduced chloride through the use of methylammonium chloride (MACl) (**Figure 2.6**). The solubilities of $PbCl_2$ and MACl differ in dimethylformamide (DMF), and the presence of MAI markedly increases the solubility of $PbCl_2$. The very soluble MAI quickly dissociates into its component ions which supplies a large amount of I^- driving complex ion formation with $PbCl_2$ forward in a process similar to the formation of $PbCl^+$, $PbCl_3^-$, $PbCl_4^{2-}$, PbI^+, PbI_3^-, and PbI_4^{2-} in water.[21] The aprotic nature of DMF lends to the stability of more highly coordinated lead ions.[84] Thus, it can be expected that more chloride exists as a ligand in complex lead ions in the solution prepared with $PbCl_2$ as compared to the solution

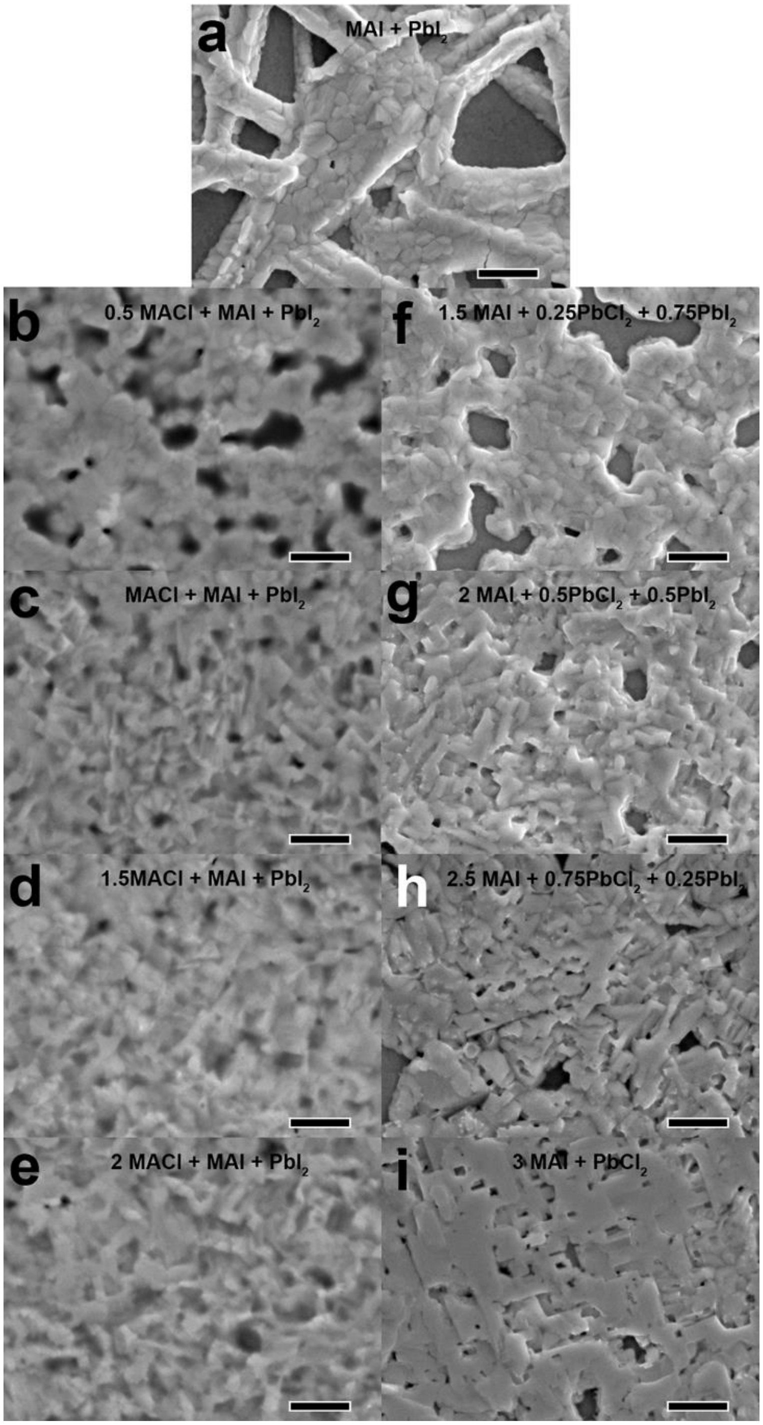

Figure 2.6: Impact of solution chemistry on $MAPbI_{3-x}Cl_x$ film growth**.** (a) is grown from a solution with the stoichiometry **MAI + PbI_2**. (b)-(e) are grown from solutions containing progressively greater quantities of MACl and–(f)-(i) are grown from solutions containing progressively greater quantities of $PbCl_2$. Adjacent images are grown from solutions with the same initial concentration of each species assuming complete solvation into discrete ions. (a) and (h) are included purely to facilitate discussion. For a more complete representation of the morphological variety unique to the case of **3MAI + $PbCl_2$** refer to Figure 2.1. All scale bars are 1 µm.

prepared with MACl. The use of MACl allows us to supply ionic chloride to the solution without the addition of any potentially problematic spectator ions which is key in isolating the influence of chloride itself.

The gradual addition of MACl (Figure 2.6b-e) seems to encourage the development of a morphology reminiscent of the regions shown in Figure 2.1b. In contrast, as we incorporate increasing amounts of $PbCl_2$ (Figure 2.6f-i), we see a gradual shift from the morphology characteristic of **MAI + PbI_2** to the morphology characteristic of Figure 2.1c. In all cases except the case of **3MAI + $PbCl_2$** (Figure 2.1), morphology throughout the film is largely homogenous beyond the micrometer scale (**Figure 2.7)**. As such, Figure 2.6i is included purely to facilitate discussion as it alone is not completely representative of the morphological variety found in systems grown from **3MAI + $PbCl_2$** (Figure 2.1).

As $PbCl_2$ content increases in Figures 2.6f-h, we can see the gradual development of the sharply faceted crystalline domains interconnected at precise right angles that are characteristic of the morphology

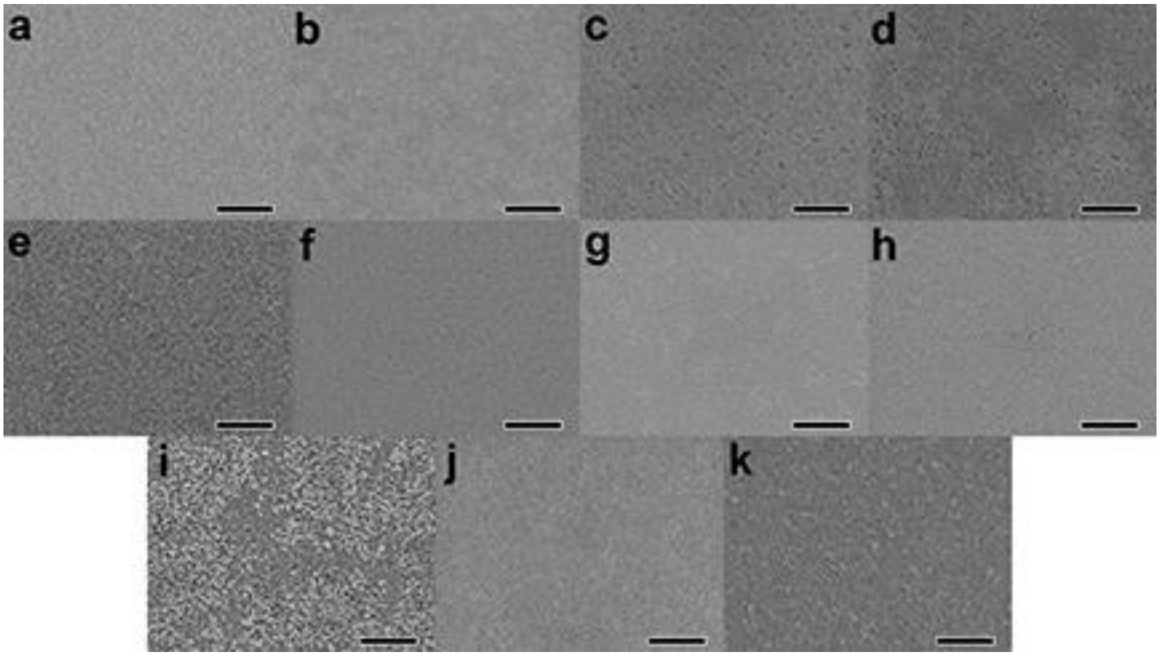

Figure 2.7: Low magnification SEM images of films cast from solutions with compositions other than 3MAI + $PbCl_2$. (a): 1.5MAI + $0.75PbI_2$ + $0.25PbCl_2$; (b): 2MAI + $0.5PbI_2$ + $0.5PbCl_2$; (c): 2.5MAI + $0.25PbI_2$ + $0.75PbCl_2$; (d): 3MAI + $PbCl_2$; (e): MAI + 0.5MACl + PbI_2; (f): MAI + MACl + PbI_2; (g): MAI + 1.5MACl + PbI_2; (h): MAI + 2MACl + PbI_2; (i): 3MAI + PbI_2; (j): 3MAI + $0.62PbI_2$ + $0.38PbCl_2$; and (k): 3MAI + $0.37PbI_2$ + $0.63PbCl_2$. All scale bars are 20 μm.

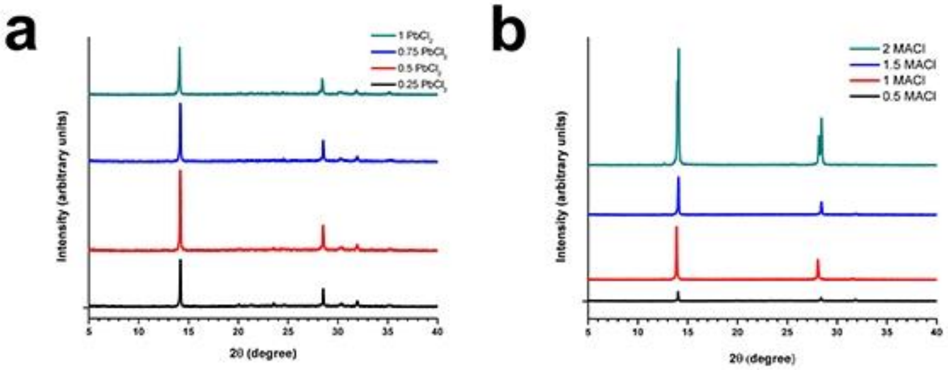

Figure 2.8: XRD patterns of films grown from a variety of compositions including the chloride ion. XRD patterns of films grown from solutions made with (a) lead chloride or (b) methylammonium chloride.

shown in Figures 2.1c and 2.6i. Furthermore, this morphological feature is only observed in systems grown from solutions made with $PbCl_2$ as opposed to those grown without chloride (Figure 2.6a) and films grown from solutions with MACl (Figure 2.6b-e). The other dominant morphologies observed in films cast from **3MAI + $PbCl_2$** solutions (Figures 2.1d and b) bear great similarity to films grown from solutions of **MAI + PbI_2** and **2MACl + MAI + PbI_2** (Figures 2.6a and e), respectively. This implicates variations in local chemistry throughout an evolving film as the cause of the unique morphological diversity observed upon chloride inclusion. This tracks well with the generation of composition gradients upon the formation of the intermediate phase. From a crystal growth perspective, this suggests that halide composition is a key factor in determining the nature of the nucleation event. It is worth noting that film coverage improves greatly upon the inclusion of chloride in the case of both MACl and $PbCl_2$. All films exhibit good phase purity (**Figure 2.8**).

2.3 Connecting Solution Chemistry to Nanoscale Crystal Development through TEM

In order to gain more insight into the influence of chemistry on film formation, we developed a sample preparation method that has allowed us to deposit and grow a perovskite film directly on a TEM grid under the same conditions used for device fabrication. More detailed information on sample preparation can be found in the experimental section. The columns in **Figure 2.9** correspond to films grown from **MAI + PbI_2** (left), **3MAI + $PbCl_2$** (center), and **MAI + 2MACl + PbI_2** (right) solutions respectively.

Figures 2.9a-f show the morphological consistency achieved between systems grown conventionally and those fabricated on TEM grids. Figures 2.9g-i are the bright field TEM images of films formed from **MAI + PbI_2**, **3MAI + $PbCl_2$**, and **MAI + 2MACl + PbI_2**. Select area electron diffractograms (SAED) of the entire visible area in the bright field TEM images are shown in Figures 2.9j-l. All SAED patterns were indexed to the tetragonal $MAPbI_3$ phase observed to be stable at room temperature[85,86] with the aid of

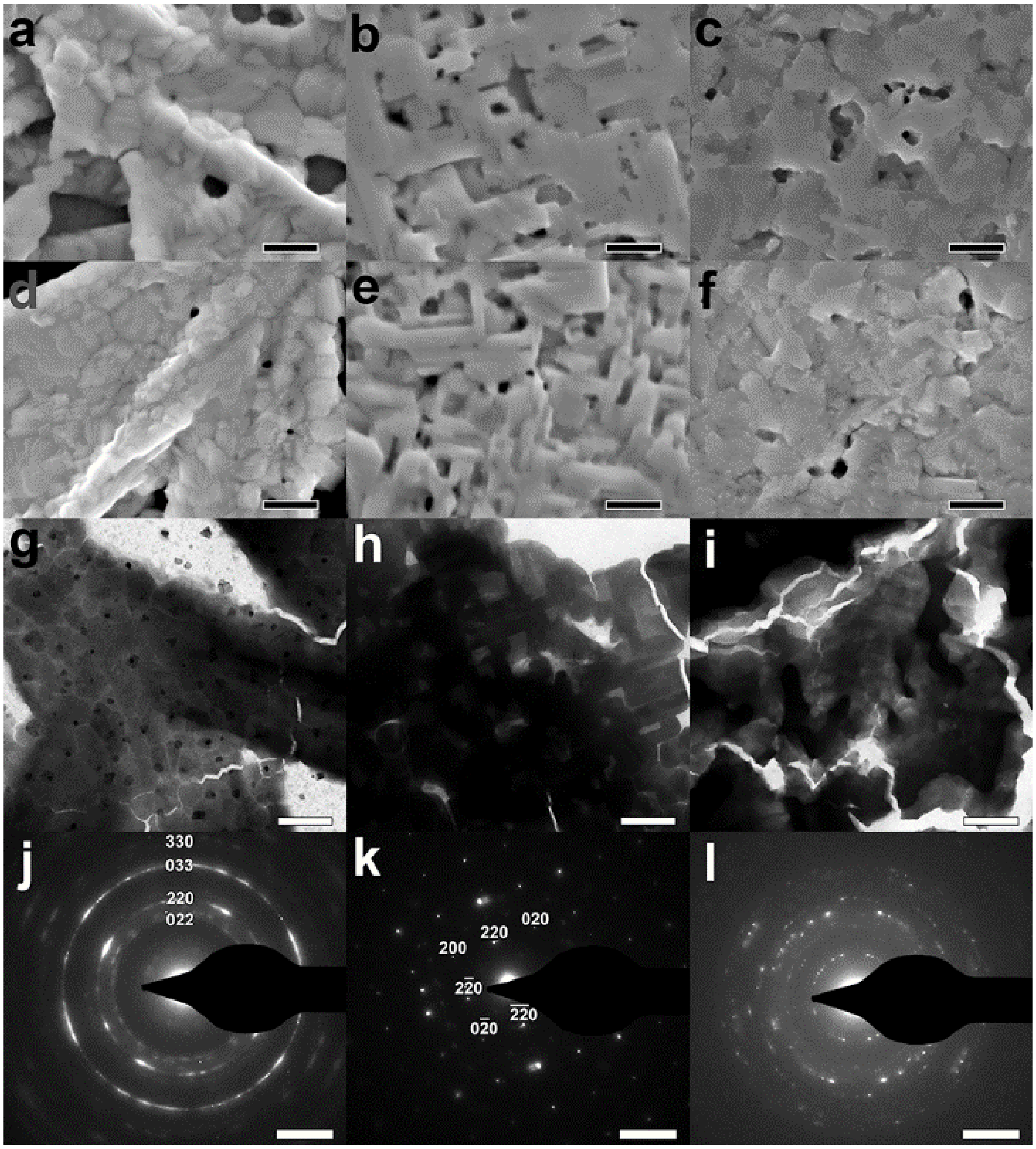

Figure 2.9: Morphology and crystallographic texture of the three compositional extremes discussed. (a-c) SEM and (d-f) TEM images of films grown from solutions of **MAI + PbI_2** (left), **3MAI + $PbCl_2$** (middle), and **2MACl + MAI + PbI_2** (right). (g)-(i) Bright field TEM images taken of the films in (d)-(f) and (j)-(l) their corresponding select area electron diffractograms. Scale bars in (a)-(i) are 500 nm and scale bars in (j)-(l) are 2 nm^{-1}.

previously reported electron diffraction studies on oxide perovskite materials.[87–89]

As is immediately apparent in the clarity of the diffraction patterns, films formed from **MAI + PbI_2** and **3MAI + $PbCl_2$** have very prominent but differing crystallographic texture. In the **MAI + PbI_2** film, grains are almost entirely oriented along the [111] zone axis. The diffraction pattern (Figure 2.9j) contains arcs rather than sharp points indicating that many orientations about this axis are represented. The **3MAI + $PbCl_2$** film's diffraction pattern (Figure 2.9k) appears like that of a single crystal. The sharp diffraction spots and the clarity of the pattern indicate long- range orientational coherence. This pattern is indexed to the [001] zone axis, which looks very distinct from the pattern belonging to the [111] zone axis (Figure 2.9j). In **3MAI + $PbCl_2$** films we observe large scale orientation along both the [001] and [100] zone axes with roughly equal frequency. The SAED pattern in Figure 2.9l shows many crystal orientations suggesting a relatively low tendency toward the generation of large scale crystallographic texture in the film grown from a solution of **MAI + 2MACl + PbI_2**. We do see some preservation of the texture about the [111] zone axis apparent in Figure 2.9j, but this is accompanied by signals from a number of different zone axes. As has been mentioned periodically, the case of **3MAI + $PbCl_2$** is more complicated. Features of the **3MAI + $PbCl_2$** film that are epitomized by the morphologies of films formed from solutions of **MAI + PbI_2** and **MAI + 2MACl + PbI_2** can be seen and they display crystallographic texture similar to their analogues.

The SAED patterns in Figures 2.9j-l reveal dramatic differences between collective crystal orientations in the three systems studied, but to get an idea of the grain structure within these systems we need to explore the information contained in the dark field. With the aid of an objective aperture, dark field imaging allows us to image the specific crystal domains responsible for creating particular diffraction signals in an SAED pattern. In **Figure 2.10** we compare bright and dark field TEM images of films grown from **MAI + PbI_2** (Figures 2.10a-c) and **3MAI + $PbCl_2$** (Figures 2.10d-e). Figure 2.10c shows eight dark field images of the entire area shown in Figure 2.10b taken around the diffraction ring characteristic of <220> reflections.

These eight dark field images taken together essentially show all the crystalline domains aligned with the [111] zone axis in the corresponding bright field image (Figure 2.10b). Each individual panel shows crystallites that are roughly oriented with each other in a particular direction about this zone axis. We choose to analyze a smaller area than that analyzed in the case of **3MAI + PbCl₂** (Figure 2.10d-e)

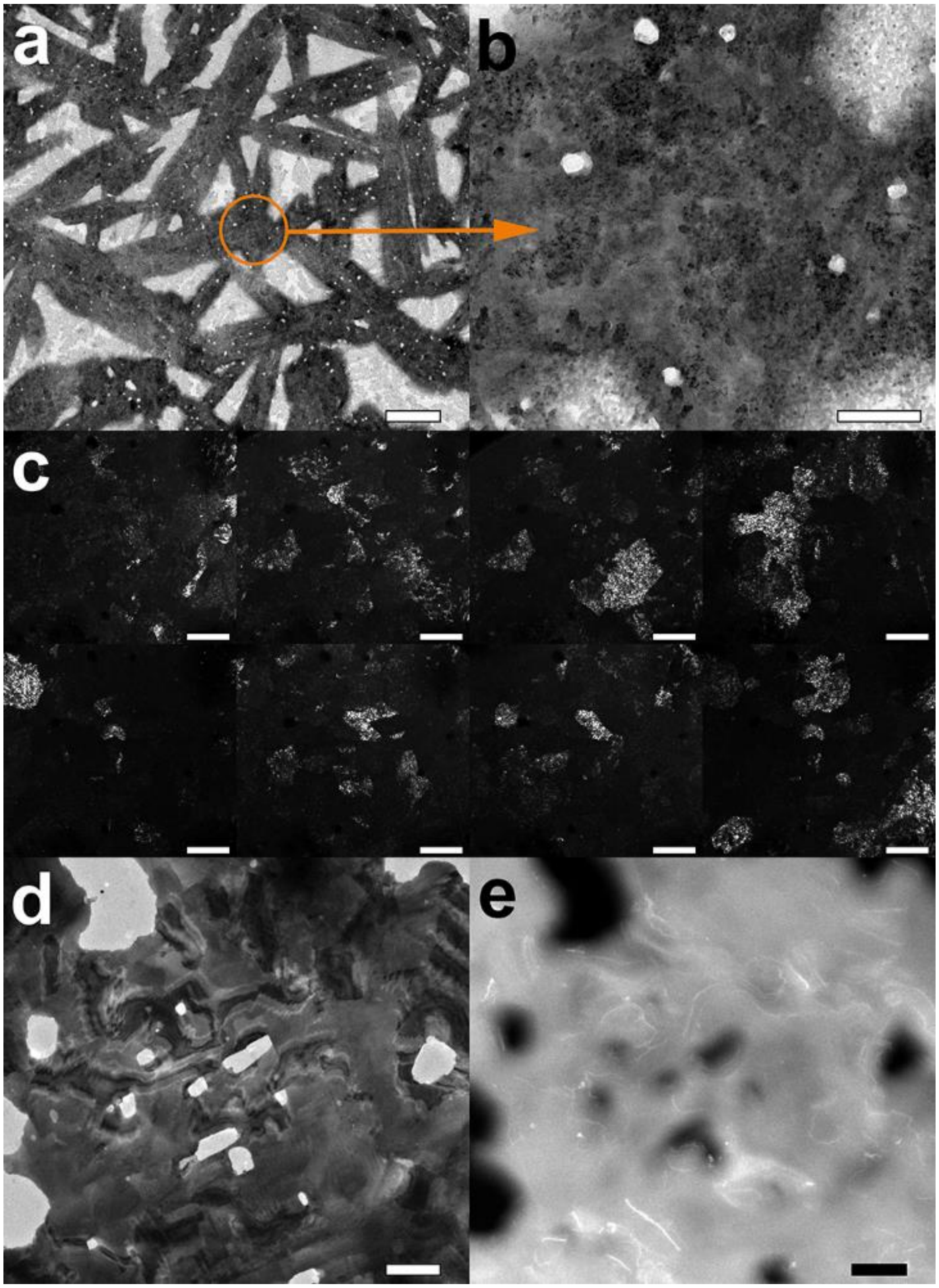

Figure 2.10: Comparison between the short range order in films grown from MAI + PbI_2 and the long range lattice coherence in films grown from 3MAI + $PbCl_2$. (a) Bright field image of a film grown from **MAI + PbI_2** (scale bar: 1 μm) and (b) an image of the area indicated in (a) (scale bar: 200 nm). (c) Eight dark field images of the region in (b) taken around the 220 and 022 diffraction rings. Scale bars are all 200 nm. (d) Bright field image of a film grown from a **3MAI + $PbCl_2$** solution, and (e) a dark field image of the same region representative of any of the region's diffraction spots which demonstrates orientational coherence at the micrometer length scale. Scale bars are both 1 μm.

because of the relatively small grain size. Figure 2.10e is a representative dark field image of the area in Figure 2.10d taken at any of its diffraction spots as there is such great orientational coherence. Structure in Figure 2.10d approaches that of a single crystal. Thus, the contrast features visible in Figures 2.9h and 2.10d may be suggestive of twin boundaries rather than randomly oriented grain boundaries. Prominent bending and mass contrast is also present, and in places it is dominant so some care should be taken when interpreting the images.

As is evident from the dark field images in Figure 2.10c, grain structure in the **MAI + PbI_2** system has an average length scale that doesn't exceed ~200 nm while films grown from a **3MAI + $PbCl_2$** solution exhibit structural coherence, if not grain size itself, at or near the micrometer length scale. This clear long range preservation of lattice coherence may provide a direct physical rational for the origin of the consistently observed but thus far poorly elucidated enhanced exciton diffusion length and lifetime in films grown from solutions with the stoichiometry **3MAI + $PbCl_2$**, and it may ground the observations of Stranks *et al.* in the crystallographic consequences of chloride inclusion.

The stark differences in texture between the three films (Figures 2.9j-l) indicate that both the presence and the chemical state of chloride species significantly affect the nature of the nucleation event, and this impact is preserved throughout film growth. The strong texture of the **MAI + PbI_2** film about the [111] zone axis combined with the lack of orientational coherence between grains indicates that nucleation is primarily driven by the interfacial energy between $MAPbI_3$ and the PEDOT:PSS substrate with continued growth occurring at already nucleated sites. In the case of the **3MAI + $PbCl_2$** film, the nucleation event is radically different as the texture observed in the **MAI + PbI_2** film is largely absent. The case of the **MAI + 2MACl + PbI_2** film seems to be intermediate between the two in which exclusive orientation about the [111] zone axis of the **MAI + PbI_2** film is lost and the long range coherence and selective orientation about the [100] and [001] zone axes of the **3MAI + $PbCl_2$** film is not achieved.

2.4 Phase Evolution During Growth

This insight is key in developing a model for the unique morphological consequences of chloride

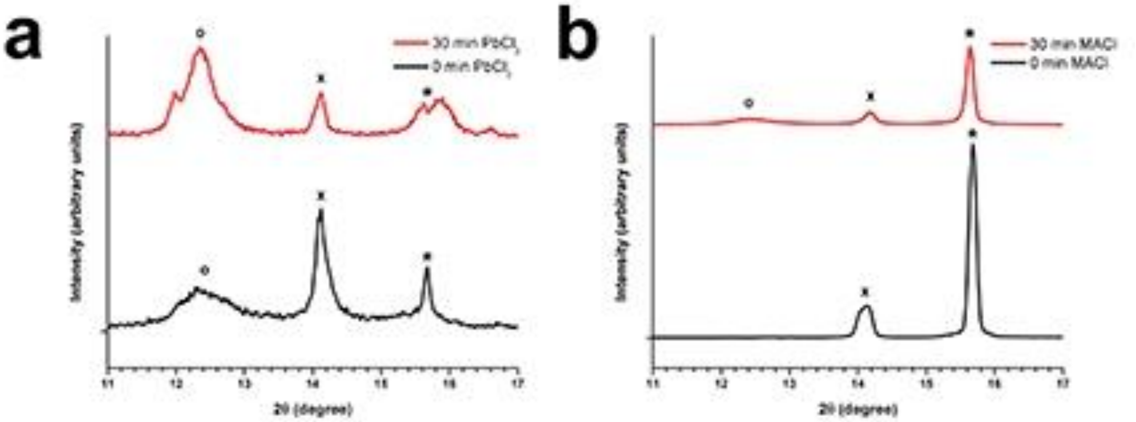

Figure 2.11: XRD patterns of films at short annealing times. XRD patterns of films grown from a solution of (a) $3MAI + PbCl_2$ and (b) $MAI + 2MACl + PbI_2$ in both the as deposited and slightly annealed states (0 and 30 minutes). o indicates reflections from PbI_2, x indicates reflections from $MAPbI_3$, and * indicates reflections from $MAPbCl_3$.These indicate both the initial formation of a chloride based perovskite phase and the gradual transition to iodide rich phases.

inclusion; however, a greater understanding of phase development upon deposition and initial annealing is still required in order to elucidate the mechanism of chloride modified crystal growth. To this end, the XRD patterns of films grown from **$3MAI + PbCl_2$** and **$MAI + 2MACl + PbI_2$** solutions were characterized, both immediately after deposition and after 30 min of annealing at 90 °C (**Figure 2.11**).

The most significant 2θ range was chosen for analysis to minimize the impact of the rapid transformation these unequilibrated films undergo upon exposure to the ambient conditions necessitated by the measurement. A wider range is shown in **Figure 2.12** for perspective. The primary phase components in both Figures 2.11 a-b are PbI_2, $MAPbI_3$, and what Colella *et al.* has characterized as a $MAPbCl_3$ phase,[13] which is unique to systems containing chloride. Tan *et al.* have also noted that this signal is unique to growth in the presence of chloride, and they have identified it as a crystalline precursor phase that plays an important role

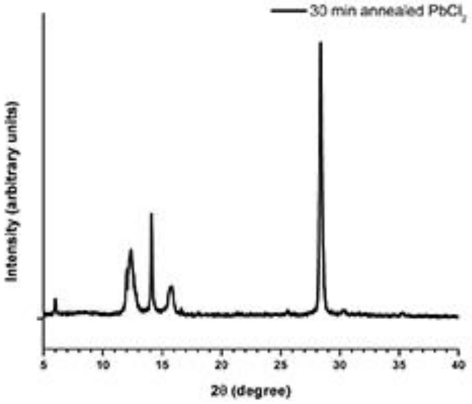

Figure 2.12: XRD pattern of a film cast from $3MAI + PbCl_2$ annealed for 30 minutes. XRD pattern showing greater 2θ range than the data in Figure 2.11 for perspective, but it is more significantly affected by ambient instability of the partially annealed film.

in film development.[72] Park *et. al.* recently observed this phase in perovskite films grown on a mesoporous TiO_2 surface and they identified it as $MAPbCl_3$ as well.[90] Since these films are admittedly unstable under the conditions necessary for characterization, we attempted to confirm this observation through slowing film evolution and stabilizing intermediate phases by supplying the system with an amount of MAI in excess of both that required to form $MAPbI_3$ and that required to react with chloride ions (**Figure 2.13**).

All of the systems presented in Figure 2.13 have been annealed for 2h at 90 °C. As can be seen both in SEM and XRD (Figures 2.13a & d), the film with the composition **3MAI + PbI_2** never evolves much past the amorphous as-cast state[68] and exhibits no strong XRD signals. This demonstrates that the overburden of MAI greatly retards transformation. As we gradually replace PbI_2 with $PbCl_2$ we see

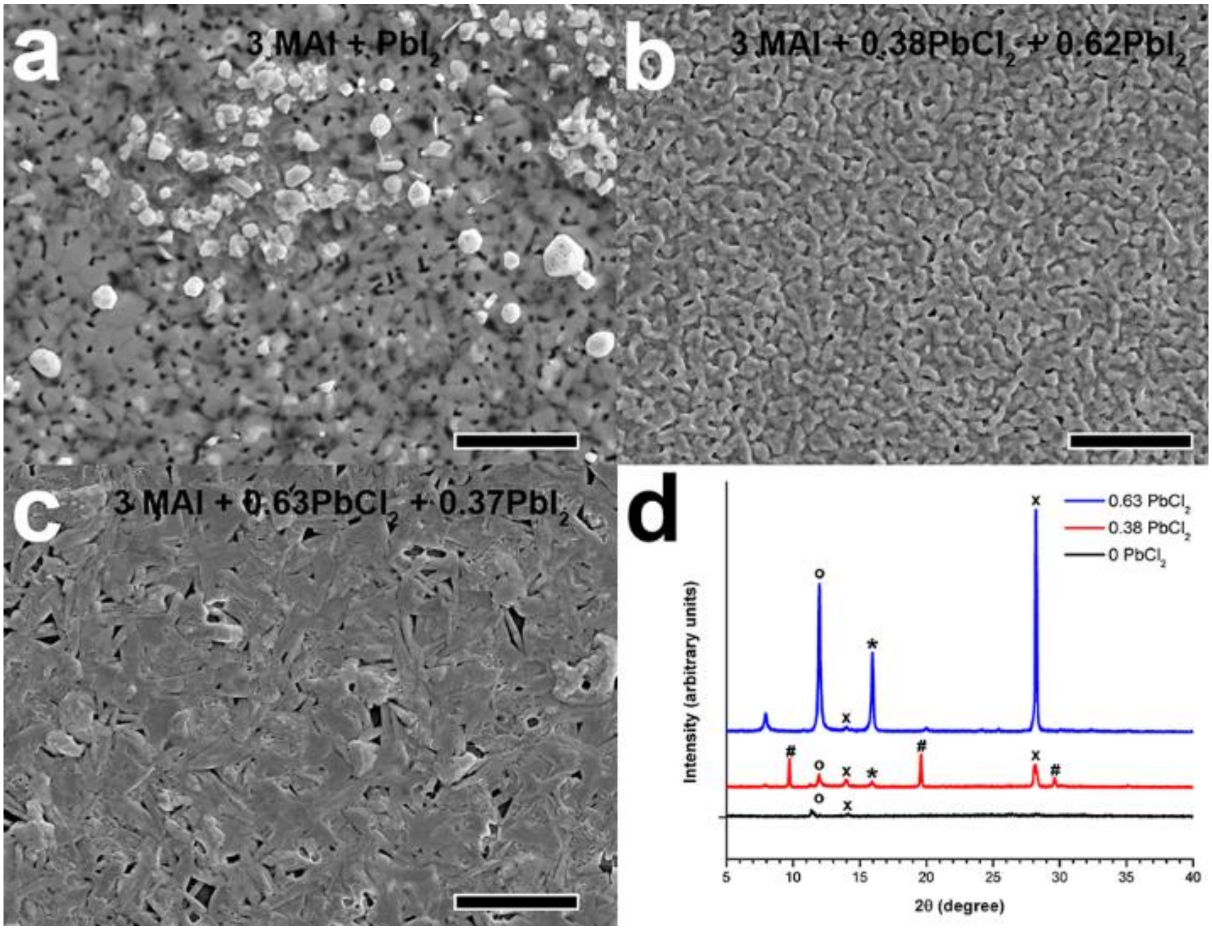

Figure 2.13: (a-c) Retarded film evolution in systems containing excess methylammonium, all scale bars are 5 μm. (d) shows XRD patterns of (a)-(c), with **o** indicating PbI_2, **x** indicating $MAPbI_3$, * indicating the template phase, and # indicating MAI.

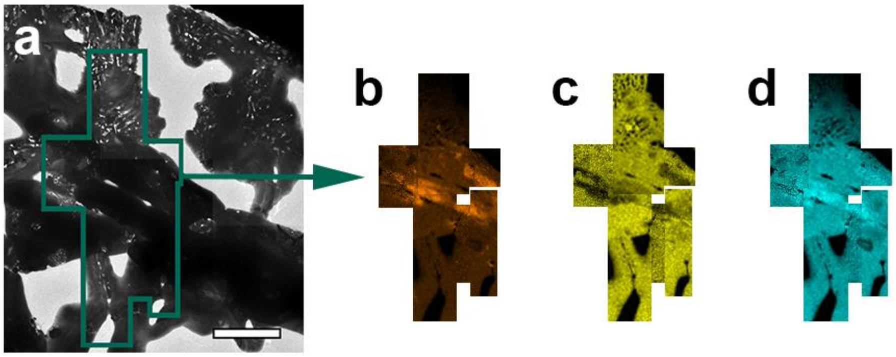

Figure 2.14: Elemental distribution in a film cast from 3MAI + $PbCl_2$ and annealed for 80 minutes. (a) Bright field TEM images arranged as a collage to show the larger area mapped by EDS in (b)-(d). The scale bar is 3 µm. (b) is the distribution of chloride, (c) is the distribution of iodide, and (d) is the distribution of lead. Maps (b)-(d) were taken in pieces and arranged afterward to mitigate the impact of software instability. At the edges of the structure imaged in (a) we can see the generation of features reminiscent of what we see in finished films.

morphological features begin to develop that are unique from what we have seen thus far (Figures 2.13b-c). If we consider the corresponding XRD patterns (Figure 2.13d) it becomes apparent that in the sample with the greatest $PbCl_2$ content (Figure 2.13c), a features indicative of the intermediate phase discussed in Figure 2.11 can be observed. Both this phase and PbI_2 become more prominent as $PbCl_2$ is added to the system. This may correlate with more rapid MA loss if we consider the reaction leading to chloride loss presented in Scheme 2.1. Regardless, it appears that the excess MAI that does remain is quenching the reaction that drives final $MAPbI_3$ formation.

To compliment this and to provide insight into the transformation from this chloride rich intermediate to the $MAPbI_3$ phase, scanning transmission electron microscopy (STEM) EDS was used to measure the spatial distribution of residual chloride in a **3MAI + $PbCl_2$** film annealed for only 80 min, 2/3 of typical annealing times (**Figure 2.14**). Residual chloride resides primarily at the center of the area indicated in the bright field TEM image in Figure 2.14a while the surrounding area is relatively iodide rich (Figures 2.14b-c); however, instrument limitations required the map to be collected in sections. Taking this observation together with the prominent formation of this chloride rich intermediate phase upon deposition and initial film evolution (Figures 2.11 & 2.13) leads us to conclude that the inclusion of chloride leads to the formation of an intermediary phase that both significantly alters the perovskite nucleation event and templates continued self-assembly.

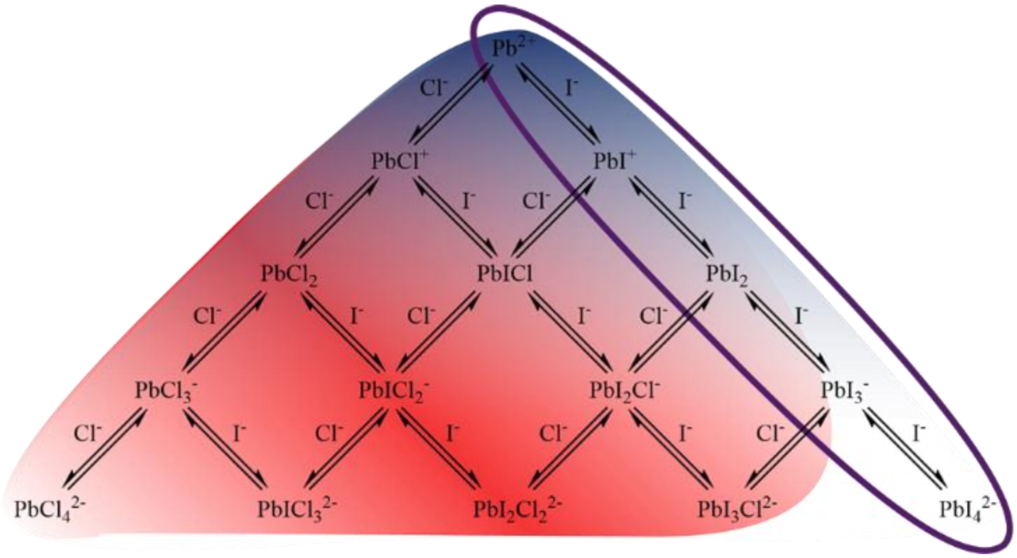

Figure 2.15: Simultaneous complex ion equilibria in solutions containing lead, chloride, and iodide. Because of the poor solubility of $PbCl_2$ and the excellent solubility of MAI in DMF, solutions with the stoichiometry **3MAI + $PbCl_2$** initially contain large concentrations of I^- and species near $PbCl_2$ in this set of equilibria (red). Due to the good solubility of PbI_2 in DMF, solutions with stoichiometries of both **2MACl + MAI + PbI_2** (blue) and **MAI + PbI_2** (circled) initially contain solvated halogen ions and species near Pb^{2+} in this set of equilibria.

2.5 Mechanism of Chloride's Impact on Crystallization

These results demonstrate that the way chloride is introduced into the solution has an impact on ultimate film growth (as revealed in Figure 2.6), and thus that the complex ion equilibria in the precursor solution displayed in **Figure 2.15** may play a non-trivial role in morphological development. Using MACl and $PbCl_2$ to differentiate how chloride is introduced into the precursor solutions (Figure 2.6) has allowed us to enter this net of chemical equilibria at different points, highlighting the kinetic subtleties associated with seeking equilibrium in each case. By virtue of its integral role in the self-assembly of the lead halide perovskite lattice, the presence of MA^+ likely also plays an important role in these solution equilibria. Possibly, this goes as far as facilitating aggregation in solution reminiscent of the self-assembly that occurs upon deposition and annealing.

Despite limited knowledge of the exact aggregation that may form in solution and its relevant optical properties, dynamic light scattering was used to characterize particle size in freshly prepared solutions with stoichiometries **3MAI + $PbCl_2$** and **MAI + 2MACl + PbI_2** (**Figure 2.16**). However, caution must be taken against a quantitative interpretation of this data as arbitrary but consistent refractive indices were chosen for aggregates in the solutions. While the more than an order of magnitude of difference in apparent aggregate size between the two systems is suggestive of the generation of solution based molecular order unique to each case, this technique is admittedly limited in interpreting what is likely to be a broad distribution of aggregate compositions and sizes. This data does motivate us to seek more sophisticated particle analysis methods to confirm aggregation and to understand its role in other solution based techniques developed.[68]

This proposed link between chemical equilibria within the precursor solution and crystal evolution in the cast film helps rationalize the rich morphological variety observed in perovskite films fabricated from chloride containing solutions (Figure 2.1). These competing chemical processes do not reach equilibrium immediately or we would not observe such great differences between the films cast with the same overall stoichiometry in Figure 2.6. A given precursor solution likely continues to change subtlety over time after it is made, impacting the nature of resulting perovskite films. To determine if such solution phase kinetics are important in controlling film development, we imaged a large area of a film cast from a freshly prepared solution of **3MAI + $PbCl_2$** and compared it with a film cast from a two week old solution of **3MAI + $PbCl_2$** (**Figures 2.17a** and **b,** respectively). As can be seen, both coverage and morphological distribution in these two films are quite disparate, with superior coverage being achieved through the use of the solution that was allowed to equilibrate for two weeks under inert atmosphere.

From the importance of solution equilibria taken together with the stark differences in crystalline texture (Figures 2.9j-l), the striking structural differences (Figures 2.10c & e), and the formation/transformation of a chloride

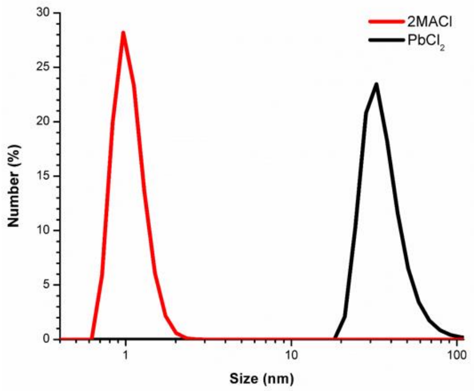

Figure 2.16: Size distribution of aggregates in freshly prepared solutions containing chloride in different forms measured with dynamic light scattering. While the difference appears stark, these statistical fits attempt to interpret systems that may contain broad distributions of aggregate states and thus we take this data as motivation to seek alternative particle analysis methods.

rich intermediate phase (Figures 2.11, 2.13, and 2.14), we propose that while a simple self-assembly process directed by substrate interfacial energy drives the formation of $MAPbI_3$ in films cast from **MAI + PbI_2**, a templated self-assembly process directed by the formation of a chloride rich intermediate phase largely guides perovskite nucleation and growth in chloride containing systems (**Figure 2.18**). As shown schematically in Figures 2.18a-b, both the position of complex ion equilibria (Figure 2.15) and differences in solution based aggregation influence the morphology, orientation, and size of the chloride rich phase formed upon deposition. As is depicted in the enlarged regions in Figure 2.18c, MA^+ and I^- then diffuse into these structural templates preceded by a reaction front where entropy gain from chloride volatilization (Scheme 2.1) and the stabilization of a newly established iodide rich phase propagates transformation onward.

The progress of this reaction front is likely accompanied by a certain degree of structural rearrangement to relieve stresses and to facilitate the continued volatilization of HCl and methylamine gas or the sublimation of MACl, but from the orientational coherence observed in the SAED pattern in Figure 2.9k and the dark field image in Figure 2.10e, it is apparent that this can proceed without inducing a significant loss of long range order. This process is likely accompanied by continued but oriented nucleation of an iodide rich phase on exposed surfaces of the template phase which becomes preferential to nucleation on the substrate. We have labeled these phases as chloride rich and iodide rich in Figure 2.18 because we

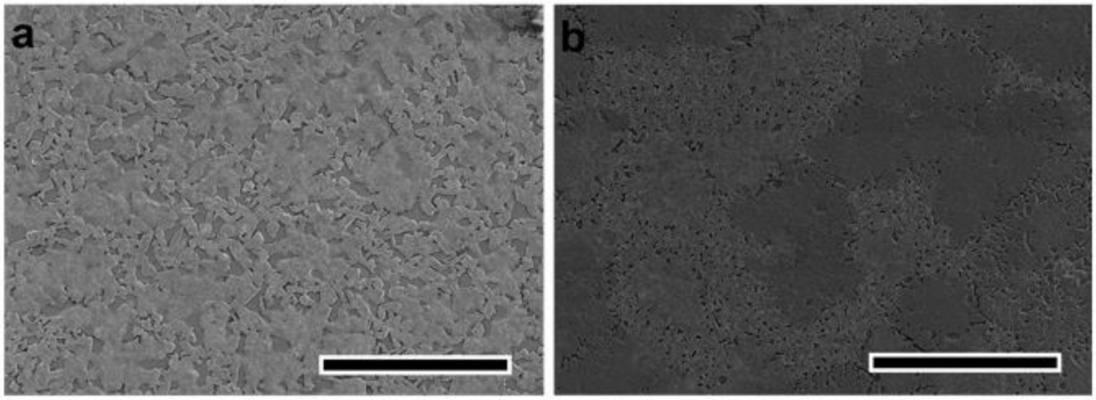

Figure 2.17: SEM images of a film cast from (a) fresh and (b) two week old solutions of $3MAI + PbCl_2$. Both scale bars are 50 µm. The differences between the morphological distributions in the two films are significant, highlighting the importance of the kinetics of solution equilibria.

anticipate that the detailed phase evolution may be complex than a simple and direct transformation, and Figures 2.11 and 2.13 indicate that PbI_2 may play a significant role as an intermediate as well. These findings are in good support of the topotactic transformation Moore *et al.* suggested may occur from a precursor salt phase to the desired lead iodide perovskite.[91] Taken together, the data presented in this study go further to suggest that it may be topotactic self-assembly of organo-lead iodide perovskite facilitated by the more structurally compatible chloride perovskite template phase that supports the generation of such unique long range order in $CH_3NH_3PbI_{3-x}Cl_x$. The final morphology of each film system shown schematically in Figure 2.18d and empirically in Figure 2.18e preserves the structural framework built into it during initial deposition and rapid chloride rich phase growth. It should be noted that the case of **3MAI + $PbCl_2$** represented in Figure 2.18 is a simplification made to highlight the formation of the morphology

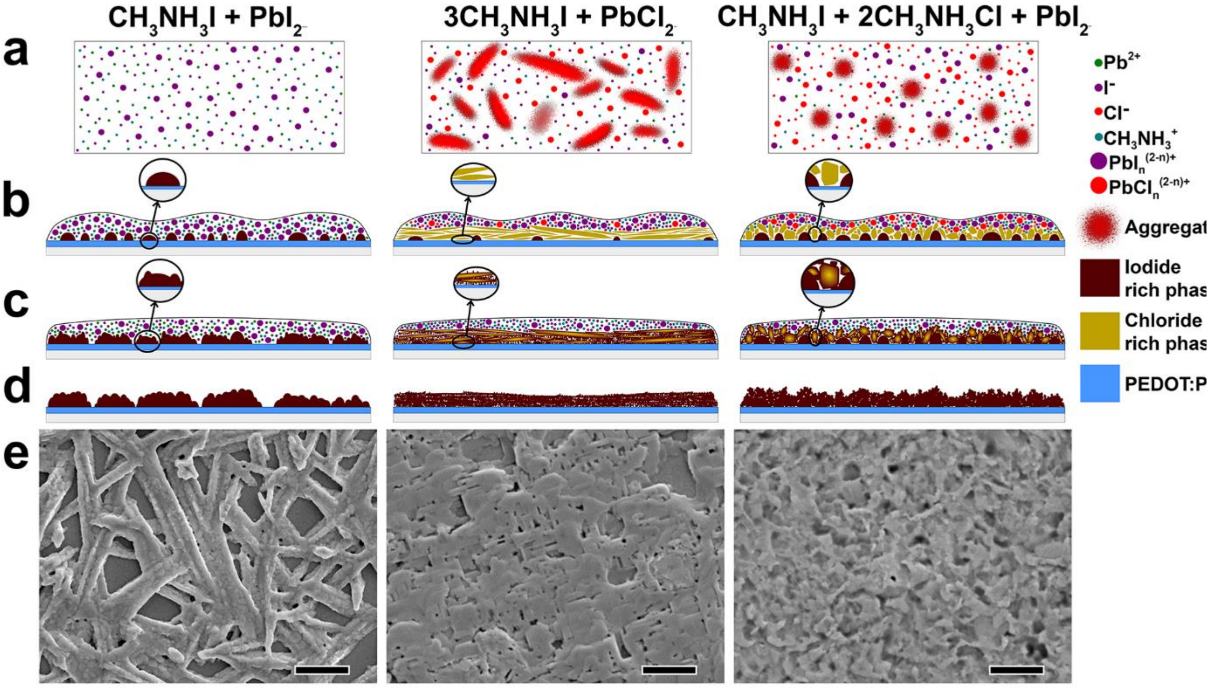

Figure 2.18: Simplified schematic representations of film formation in the three compositional extremes studied: (a) attempts to portrait the state of the solution in each case. The sizes of aggregates represented in the cases of **3MAI + $PbCl_2$** and **MAI + 2MACl + PbI_2** are intended to differ by approximately an order of magnitude. (b) illustrates nucleation during and immediately after deposition, (c) illustrates each system as it evolves during annealing, and (d) represents the film morphology after annealing is complete. (e) SEM images representative of the morphologies illustrated schematically in (d). All scale bars are 2 μm. The case of **3MAI + $PbCl_2$** is highly idealized, and as previously discussed a variety of morphologies are often observed together (Figure 2.1).

we find to be unique to the case of films grown from solutions made with $PbCl_2$. Figure 2.1 shows a more realistic representation of film growth in the case of **3MAI + $PbCl_2$** in which we endeavor to show that morphological variety we observe to be unique to this case is caused by inhomogeneities that develop as a result of compositional gradients generated during nucleation and growth. These inhomogeneities in turn lead to nucleation mediated by differing local chemistries throughout the film, with the three extremes shown schematically in Figure 2.18.

2.6 Conclusion

In summary, we have elucidated the structural role chloride plays in the evolution of organo-lead halide perovskite films on PEDOT:PSS by establishing relationships between film morphology and subtle differences in precursor chemistry. We have expanded significantly upon this level of insight by developing a sample preparation technique that enables the use of the TEM as an analytical tool to explore these systems. Because of the nature of the method, the findings are relevant to the low temperature solution processed PHJ devices currently being widely explored in the literature.[65–72,74–76] From the sum total of the trends discussed herein we offer that perovskite films grown from solutions containing chloride evolve through templated self-assembly in contrast to the conventional self-assembly. Ultimately, this is due to a change in nucleation dynamics upon chloride inclusion as well as the existence of a unique and rapidly formed chloride rich intermediate phase. The important role of chemical equilibria and aggregation in determining resulting morphology suggested by this study likely extends to most if not all other solution based perovskite preparations including those using additives[68] and mixed solvents[92] to enhance perovskite growth as well as those using other halogen anions,[93] organic cations,[66] and metal cations.[94] While these insights are of great engineering value, along the way we have established key relationships between nanoscale morphologies, textures, and grain structures unique to systems grown with and without chloride as well as a physical rationale for explaining the enhancement of exiton diffusion length in films fabricated from **3MAI + $PbCl_2$**.

This chapter introduced a number of important themes that will continue to recur throughout this dissertation. The complex ion equilibria and aggregation characteristic of the solution chemistry of lead iodide is an issue that will play a significant role in all the work to come. The importance of nucleation in determining growth route is also a theme that will recur, with Chapter 4 offering a focused conceptual account of this issue throughout the perovskite field. In addition to these themes, the disorder created by excess methylammonium iodide (Figure 2.13a and d) is an issue that is highly relevant to the work in Chapters 3 and 6 as well as the conceptual discussion offered in Chapter 4.

Finally, the morphology of films growth without Cl shown in in this chapter is representative of a very common, problematic morphology that is often encountered in the hybrid perovskite field (Figure 2.2). Many approaches have been developed to circumvent this problematic morphology, like the addition of Cl that is studied here and the post-deposition treatment discussed in the next chapter. Chapter 6 mechanistically identifies how this morphology arises and how it can be circumvented more generally.

2.7 Experimental Details

MAI and MACl Synthesis. Methylammonium iodide (MAI) and methylammonium chloride (MACl) were synthesized by reacting 24 mL of 0.20 mol methylamine (33 wt % in absolute ethanol, Aldrich), 10 mL of 0.04 mol hydroiodic (57 wt % in water with 1.5% hypophosphorous acid, Alfa Aesar) or hydrochloric acid (37% in water, Aldrich), and 100 mL ethanol in a 250 mL round-bottom flask under nitrogen at 0 °C for 2 h with stirring. After reaction, the white precipitate of MAI or MACl was recovered by rotary evaporation at 40 °C and then dissolved in ethanol followed by sedimentation in diethyl ether by stirring the solution for 30 min. This step was repeated three times, and the MAI or MACl powder was finally collected and dried at 50 °C in a vacuum oven for 24 h.

Perovskite Precursor Solution Preparation. Perovskite precursor solutions were 20 wt % for TEM, STEM EDS, and DLS characterization and 40 wt % for SEM, EDS, XPS, and XRD measurements where wt % = 100 · (total mass of solute/total mass of solution). The solutions were made in a nitrogen filled glovebox by mixing lead halide and methylammonium halide salts in anhydrous DMF in amounts appropriate to simultaneously achieve the stoichiometries noted in the text and the weight percent of solute

Solution Stoichiometry	**wt%**	**$PbCl_2$ (g)**	**PbI_2 (g)**	**MAI (g)**	**MACl (g)**
MAI + PbI_2	40	0	0.0940	0.0324	0
	20	0	0.0352	0.0122	0
3 MAI + $PbCl_2$	40	0.0466	0	0.0798	0
	20	0.0175	0	0.0299	0
2.5 MAI + 0.75 $PbCl_2$ + 0.25 PbI_2	40	0.0366	0.0202	0.0696	0
2 MAI + 0.5 $PbCl_2$ + 0.5 PbI_2	40	0.0256	0.0424	0.0585	0
1.5 MAI + 0.25 $PbCl_2$ + 0.75 PbI_2	40	0.0134	0.0669	0.0461	0
2 MACl + MAI + PbI_2	40	0	0.0772	0.0266	0.0226
	20	0	0.0289	0.0010	0.0085
1.5 MACl + 1 MAI + PbI_2	40	0	0.0808	0.0279	0.0177
1 MACl + 1 MAI + PbI_2	40	0	0.0848	0.0292	0.0124
0.5 MACl + 1 MAI + PbI_2	40	0	0.0891	0.0307	0.0065
3 MAI + 0.63 $PbCl_2$ + 0.37 PbI_2	40	0.0269	0.0262	0.0733	0
3 MAI + 0.38 $PbCl_2$ + 0.62 PbI_2	40	0.0154	0.0416	0.0694	0
3 MAI + PbI_2	40	0	0.0621	0.0643	0

Table 2.2: Exact precursor solution compositions assuming the use of 200 μl DMF.

required. Exact amounts are listed in **Table 2.2** for all solutions studied assuming a constant volume of DMF (0.2 mL). The solutions were then stirred vigorously at 80 °C for ~40 min, cooled, and subsequently filtered through 0.45 μm PTFE filters.

Fabrication of Perovskite Thin Films and TEM Samples. ITO glass substrates were cleaned sequentially with detergent and deionized water, acetone, and isopropanol under sonication for 10 min. After drying under a N_2 stream, substrates were further cleaned by a plasma treatment for 30 s. PEDOT:PSS (Baytron PVP Al 4083, filtered through a 0.45 μm nylon filter) was first spincoated onto the substrates at 5k rpm for 30 s and annealed at 150 °C for 10 min in air. To avoid oxygen and moisture, the substrates were transferred into a N_2-filled glovebox, where the thin-film perovskite layers were spin-coated from a homogeneous 40 wt % perovskite precursor solution at 6k rpm for 45 s (300-500 nm thickness) and then annealed at 90 °C for 2-3 h.

TEM samples were prepared by first mounting a TEM grid on a cleaned ITO glass substrate. It is necessary to adhere an undistorted grid to the slide in slight tension with at minimum four points of contact to ensure intimate thermal contact. Otherwise, annealing conditions cannot be faithfully replicated. This can be done with any adhesive material with adequate solvent stability, adequate thermal stability, and adequately weak adhesion such that removal does not damage or distort the delicate TEM grid. Stronger tapes are more reliable but harder to work with without causing damage. To ensure appropriate PEDOT:PSS film formation, the grid's surface is made hydrophilic through glow discharge treatment with a Solarus 950 Gatan Advanced Plasma System. The same deposition and heat treatment procedure for first the PEDOT:PSS then the perovskite are then followed as above with the exception of the use of a 20 wt % precursor solution.

Characterization. A Tecnai G2 F20 transmission electron microscope was used at 200 kV for all TEM measurements. A FEI Sirion scanning electron microscope was used for all SEM based characterization with 5 kV used for imaging and 15 kV used for EDS. A Bruker D8 Focus powder diffractometer was used for all XRD characterization with a Cu Kα source. A Versaprobe 5000 X-ray photoelectron spectrometer from Physical Electronics, Inc. was used for XPS measurements with a pass energy of 23.5 eV. A Malvern Instruments Ltd. ZEN3600 Zetasizer was used for DLS characterization.

Chapter 3. INTERMEDIATE STATES AND KINETIC PROCESSES IN POST-DEPOSITION $CH_3NH_3PbI_3$ TRANSFORMATION: Case Study of Methylamine Vapor Treatment

**This entire chapter has been adapted from STW-3 (Reproduced from Ref. STW-3 with permission from the Royal Society of Chemistry.)*

This chapter presents material that was originally published in an article titled *Design rules for the broad application of fast (<1 s) methylamine vapor based, hybrid perovskite post deposition treatments* (STW-3). This publication was co-first authored with Ting Zhao, and thus the presentation of this material here has been adapted and modified to focus on the direct contributions I made to the work. The following material is adapted from this publication. Methods will be described in detail at the conclusion of the chapter.

3.1 Introduction

The flexible processibility that makes hybrid perovskites so potentially transformative comes at the cost of complex and competing growth processes that frustrate control of film quality and coverage. Pin-hole formation, low crystallinity, and phase inhomogeneity are common morphological issues that significantly impact device function. Controlling morphology is uniquely challenging for the planar heterojunction (PHJ) structure.[95,96] Despite this difficulty, the PHJ device configuration still attracts significant interest due to the versatility of emerging low-temperature fabrication techniques and materials.

A wide variety of methods have been developed to control perovskite growth including but not limited to sequential deposition,[66,97] dual-source evaporation,[77] and vapor-assisted solution processing (VASP).[67] These strategies use a variety of phase transformations to circumvent the need for perovskite formation directly from solution. For example, two-step processing utilizes a compact lead halide template to encourage uniform growth, circumventing complexities inherent in direct perovskite growth. To kinetically control this complexity rather than avoid it, techniques have focused on thermal processing[98] and compositional tuning of precursor solutions through use of spectator ions,[65,99] additives,[68,100] and co-/anti-solvents.STW-4,[101] Despite the benefits these strategies offer, the complexity of competing processes implicit in growth hinder reproducibility and mechanistic understanding. These challenges have motivated many post deposition treatments that expand upon simple thermal annealing,[71] such as solvent annealing,[102] multi-cycled dimethylformamide (DMF) vapor treatment,[103] and hot-pressing.[104] While these treatments markedly improve film morphology, they are relatively time-consuming and complex.

This work presents a fast (<1 s) and simple post deposition chemical treatment in which crystal reconstruction induced by a methylamine (MA^0) vapor greatly improves perovskite film coverage, crystallinity, and device performance. Inspired by the discovery of a reversible phase transformation upon exposure to amine gas,[105] we speculated that this same chemistry can be utilized to establish a facile post deposition treatment to improve perovskite film quality through the recrystallization that occurs after amine vapor ingress into a perovskite film. To explore this concept, we used methylamine rather than amine vapor because of its increased similarity to species already within the $MAPbI_3$ lattice. The discussion offered here focuses on the morphological insight generated through this study rather than the design rules developed to guide implementation of this treatment in perovskite solar cell fabrication. Through detailed microscopy, we demonstrate that the nature of MA^0–perovskite coordination and its microstructural consequences are a function of MA^0 vapor pressure, interaction time, and composition of the organic sublattice.

3.2 Physical Consequences of MA^0 Vapor Treatment

To implement this post-deposition treatment, we first prepared a $MAPbI_3$ film through simple one-step spin coating from DMF on PEDOT:PSS, and then exposed this perovskite film to MA^0 vapor (**Figure 3.1a**). Immediate loss of the dark pigment inherent to $MAPbI_3$ occurred as the perovskite film was introduced to the MA^0-rich environment. This was then followed by rapid darkening upon removing the film from the vapor rich environment.

We used PEDOT:PSS as a hole- transporting layer (HTL) in our PHJ devices, and it provided the necessary interfacial energy to prevent film dewetting during this post-deposition treatment. During the preparation of this manuscript, Cui et al. implemented an analogous MA^0 vapor treatment but they used a mesoporous growth substrate rather than a PHJ architecture, and during vapor treatment the capillary action within the mesoporous scaffold played an important role in directing material diffusion and improving film quality.[106] Our use of PEDOT:PSS as a hole- transporting layer (HTL) in our PHJ devices is an important component of this treatment's success in this more challenging PHJ architecture.

Figure 3.1b shows XRD analysis of a perovskite film before and after vapor treatment. This data was collected with the exact same perovskite film, meaning that many variables that can contribute to XRD peak intensity, like the amount of material, are not causing the substantial increase in signal intensity observed in Figure 3.1b. Rather, the substantial change in XRD peak intensity can be attributed to a marked increase in overall crystallinity. While a shift in overall crystal orientation could be contributing slightly, the only peaks visible in these XRD patterns are the signals that are inherently the most intense in this material system, suggesting random crystal orientation rather than the emergence of coherent film texture.

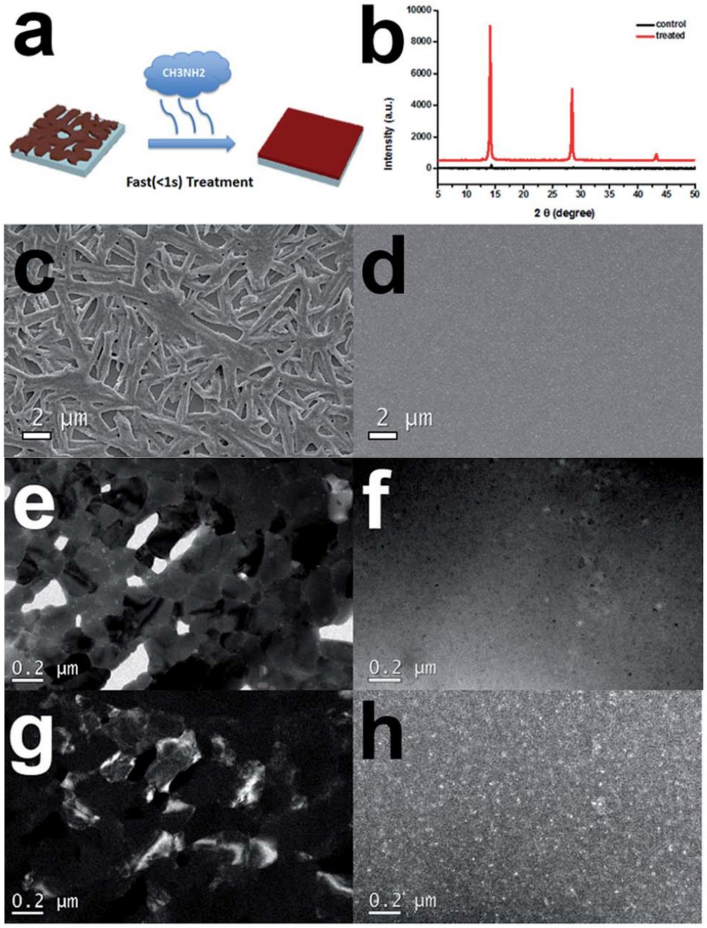

Figure 3.1: Comparison of a $MAPbI_3$ film before and after the vapor process depicted in (a): (b) XRD, (c-d) SEM, (e-f) Bright field TEM, and (g-h) dark field TEM.

XRD suggests that perovskite crystallinity markedly increases upon methylamine vapor exposure and subsequent annealing at

100 °C for 15 min (Figure 3.1b) and SEM reveals massive material diffusion (Figure 3.1c-d). As was shown in Chapter 2, the perovskite morphology that results from 1-step deposition from DMF has a rod-like morphology. This characteristic morphology is deleterious for photovoltaic device preparation because of the inadequate crystallinity and coverage shown by Figure 3.1b-c respectively. The film morphology that results after methylamine vapor treatment, however, has markedly increased crystallinity and almost complete coverage.

To more deeply examine morphology, we fabricated perovskite thin-films for transmission electron microscopy (TEM) via a methodology identical to that used for device fabrication with the exception of using a diluted perovskite solution and a PEDOT:PSS coated TEM grid substrate.

Dark field TEM is a technique that images the information contained within electrons diffracted from a sample. Bright areas correlate with a region in the image that has the crystal structure and orientation necessary to diffract some of the electron beam into the area an aperture has been used to select. That means the objects that can be seen constitute the actual grain structure of the film (**Figure 3.2**). Where bright areas are arranged in close proximity with parallel, flat boundaries we have densely packed, highly oriented grain boundaries (region 3 in Figure 3.2b). Where we see many small bright areas clustered within areas that appear from SEM and bright field TEM as a single grain, we have difficult to detect polycrystallinity (region 1 in Figure 3.2b). We are essentially seeing what satisfies the diffraction condition and thus areas within single grains that become dark are areas that violate this condition, specifically due to strain (bending) and internal defects (region 2 in Figure 3.2b). We use a circular objective aperture rather than an annular aperture for collecting this information which means that in any given dark field image we are only seeing a part of the total information contained in the sample's diffraction.

In general, most of the apparent grains do have some kind of diffracted signal but without an annular detector we can't represent the entirety of that information simultaneously. The features we see in the dark field directly show us the size, shape, and nature of crystalline regions, but we can only see what satisfies the diffraction condition so we can't see truly disordered regions or regions of a single crystal if it is highly strained or bent. This issue makes interpreting the dark field images for $CH_3NH_3PbI_3$ before vapor treatment challenging because strain and disorder are abundant. The complex microstructure buried within seemingly single crystalline grains from SEM further complicates the matter. After vapor exposure, microstructure in the dark field images becomes very simple and easy to interpret (Figure 3.1h), but Quantifying the change in grain size in this process is misleading because it would direct the reader away from the most important aspect of the process which is a fundamental change in grain structure, not just a change in size.

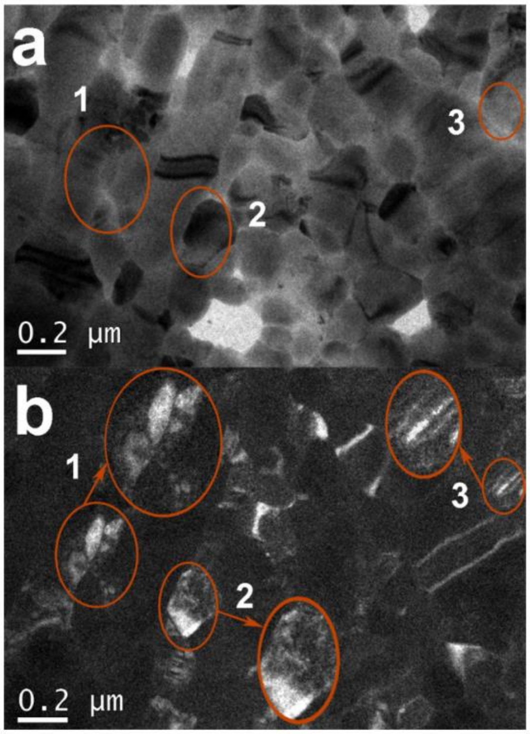

Figure 3.2: Bright- (a) and dark- (b) field TEM of a region before vapor treatment showing the microstructural complexity of $MAPbI_3$ grown by 1-step deposition. Regions that are highlighted show: (1) difficult to detect polycrystallinity, (2) highly strained and defective grains, and (3) dense and highly oriented grain boundaries. This technique cannot directly detect truly disordered domains.

Although it may be tempting to conclude from SEM that grain size doesn't change greatly upon MA^0 vapor treatment, bright and dark field TEM (Figure 3.1e-f and g-h respectively) reveal that vapor treatment induces gain size reduction rather than growth. Grain size reduction seems contradictory to the increase in crystallinity observed via XRD (Figure 3.1b), but dark field TEM analysis of perovskite grain structure before vapor exposure (Figure 3.2) reveals a variety of morphological features that are persistently unapparent in SEM. Generally, we find (1) buried polycrystallinity, (2) highly strained and defective single crystals, and (3) densely packed, highly oriented grain boundaries throughout films grown from unmodified 1-step deposition. This is in addition to the predominantly disordered regions that remain dark in dark field imaging. This level of microstructural complexity is unsurprising because of the existence of both $MAPbI_3$-DMF[107] and inherently disordered[90,108] phases prominent in spin-cast film growth, compounded with the transformation from cubic to tetragonal $MAPbI_3$ in the temperature window that typical annealing traverses.[109] Defining an exact grain size in this system before vapor treatment is challenging as there is a continuum of disorder and a variety of grain sizes and shapes.

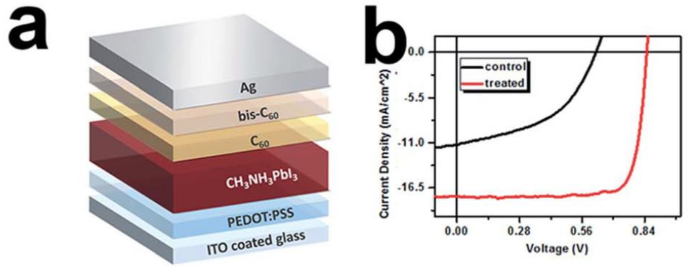

Figure 3.3: The *J*–*V* curve of the planar heterojunction photovoltaic device architecture in (a) with and without MA^0 vapor treatment is in (b).

While the microscopic morphological consequences of MA^0 vapor treatment are complex, the macroscopic benefit it serves at the device level is unambiguous. As was touched upon in Chapter 2, the perovskite morphology produced directly by 1-step deposition from a DMF solution is problematic for photovoltaic device preparation. To evaluate the efficacy of this process in improving a photovoltaic device, we fabricated PHJ devices with the structure in **Figure 3.3a**.

Control devices fabricated with unmodified 1-step perovskite growth from DMF showed a low PCE of ~3%, but after the simple vapor treatment, devices reached ~12% PCE through marked increases in all photovoltaic parameters (Figure 3.3b). More detailed device analysis including characterization of *J*-*V* hysteresis at different scan rates, stabilized power output, and EQE measurement are offered in STW-3, along with characterization of the impact of this MA^0 vapor treatment on recombination kinetics via photoluminescence spectroscopy. Although this deeper optoelectronic characterization is an important part of the design rules we ultimately offer in STW-3, this analysis is not directly relevant to the discussion here. For the purposes of this chapter, the important result of this optoelectronic investigation is the dramatic impact that improved $CH_3NH_3PbI_3$ film coverage has in improving device performance despite the morphological complication of decreased grain size. This also unambiguously demonstrates how problematic the rod-like morphology generated by 1-step deposition is for photovoltaic device function.

3.3 Chemical and Mechanistic Investigation

To broaden the application of this process to the expanding family of hybrid organic–inorganic perovskites, we explored the chemistry determining lattice reactivity toward MA^0 vapor and the physical conditions mediating transformation.

3.3.1 *Chemical factors mediating perovskite reactivity toward methylamine vapor*

The coordination chemistry between $MAPbI_3$ and neutral molecules such as DMF,[110] DMSO,[34] and H_2O[111] has garnered increasing interest due to its importance in growth and degradation. Amine gases like NH_3,[105] MA^0, and larger analogues[106] demonstrate the ability to disrupt the $MAPbI_3$ lattice with differing degrees of spontaneity and reversibility. The diverse coordination chemistry of lead halides and their hybrid analogues in both solution[51,112] and the solid state[17,105,106,111,113] makes the mechanisms that govern MA^0 vapor's interaction with the lattice somewhat difficult to pinpoint.

Lewis bases like pyridine and thiophene have been found to coordinate Pb dangling bonds[57] illustrating the metal ion's potential reactivity. The $MAPbI_3{\cdot}DMF$ crystal structure[17] suggests that DMF, also a Lewis base, preferentially hydrogen bonds with MA^+ which illustrates the potential reactivity of the organic sublattice. The halogen ion's reactivity toward the vapor should also be considered by virtue of the key role bonding between the halide and the organic cation plays in stabilizing the hybrid perovskite's 3D inorganic sublattice over the 2D lattice of PbI_2.[114]

To understand how potential sources of reactivity mediate interaction between hybrid perovskite and MA^0 vapor, we

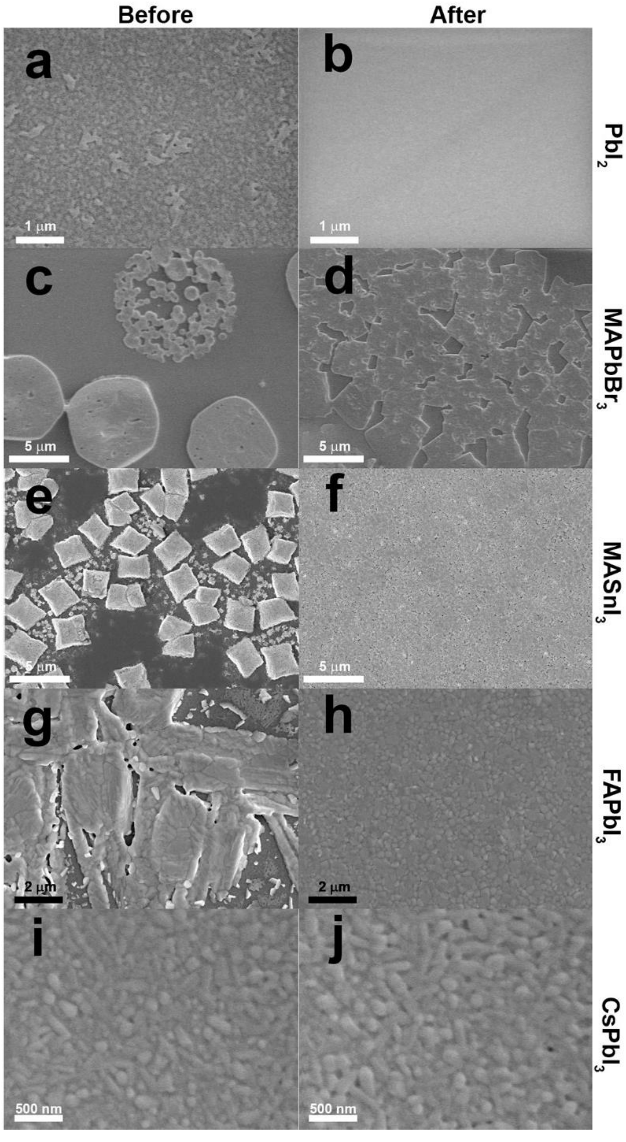

Figure 3.4: These SEM images show the effects of MA^0 vapor treatment on (a)-(b) PbI_2, (c)-(d)$MAPbBr_3$, (e)-(f) $MASnI_3$, (g)-(h) $FAPbI_3$, and (i)-(j) $CsPbI_3$ at scales necessary to see relevant microstructural detail.

systematically varied the components of the lattice and examined the microstructural response to vapor exposure with SEM. Exposure of PbI_2 to MA^0 vapor causes a transition to a transparent state followed by the brief formation of brown perovskite before most of the film reverts to yellow PbI_2, which is unsurprising as $PbI_2{\cdot}xMA^0$ is essentially analogous to $MAPbI_3{\cdot}xMA^0$ with an iodide deficiency. This process is accompanied by a drastic change in microstructure (**Figure 3.4a-b**). MA^0 vapor does not possess the formal positive charge of methylammonium but still demonstrates a capacity to drive transformation and even momentary perovskite formation, illustrating the importance of hydrogen bonding in the formation and cohesion of $MAPbI_3$ itself. This demonstrates the core importance of the nature of the inorganic halide polyhedra ($PbI_x^{(2-x)}$) in determining hybrid perovskite reactivity, and the rapid generation of the 3D perovskite lattice from the 2D PbI_2 lattice shows that interaction between MA^0 and the lead halide framework is not limited to intercalation.

Bonding within each hybrid perovskite lattice is unique, and thus the intrinsic reactivity of the metal halide framework toward MA^0 vapor is likely altered by changes in components of the crystal. Upon vapor exposure, both $MAPbBr_3$ and $MASnI_3$ films underwent the same rapid transformation to a transparent intermediate state followed by rapid reversion to the original perovskite, a process characteristic of the response of $MAPbI_3$ toward MA^0 vapor (Figure 3.4c-f). $FAPbI_3$ and $CsPbI_3$ films, on the other hand, behaved differently when exposed to MA^0.

Both the capacity to hydrogen bond and the cohesivity offered to the lattice as a whole vary as a function of the composition of the organic sublattice. $FAPbI_3$ does rapidly become transparent upon vapor exposure, but it reverts back to its initial state from this transparent intermediate state much less readily, even after annealing at 100 °C for 15 min. Despite the increased stability of this intermediate phase, there are still huge microstructural changes that occur (Figure 3.4g-h), indicating that the intermediate state is highly diffusive as in the case of $MAPbI_3$. In the more extreme case of $CsPbI_3$ however, we find no reactivity toward the vapor by virtue of no change in the film's pigment or microstructure upon vapor exposure. This indicates that the nature of bonding within the organic sublattice strongly mediates the reactivity toward MA^0 vapor that is imparted to a hybrid perovskite by the nature of its inorganic polyhedra.

3.3.2 *Mechanistic investigation of MA^0 induced transformation in $CH_3NH_3PbI_3$*

By virtue of the fact that in $MAPbI_3$ the conduction and valence band edges are composed primarily of I 5p and Pb 6s orbitals,[115] the transparency of the intermediate state likely results from a complete loss of structure within the inorganic sublattice. This loss of pigment upon vapor exposure can point both to a solvation event[106] or a dramatic but coherent change in structure via the formation of a crystalline

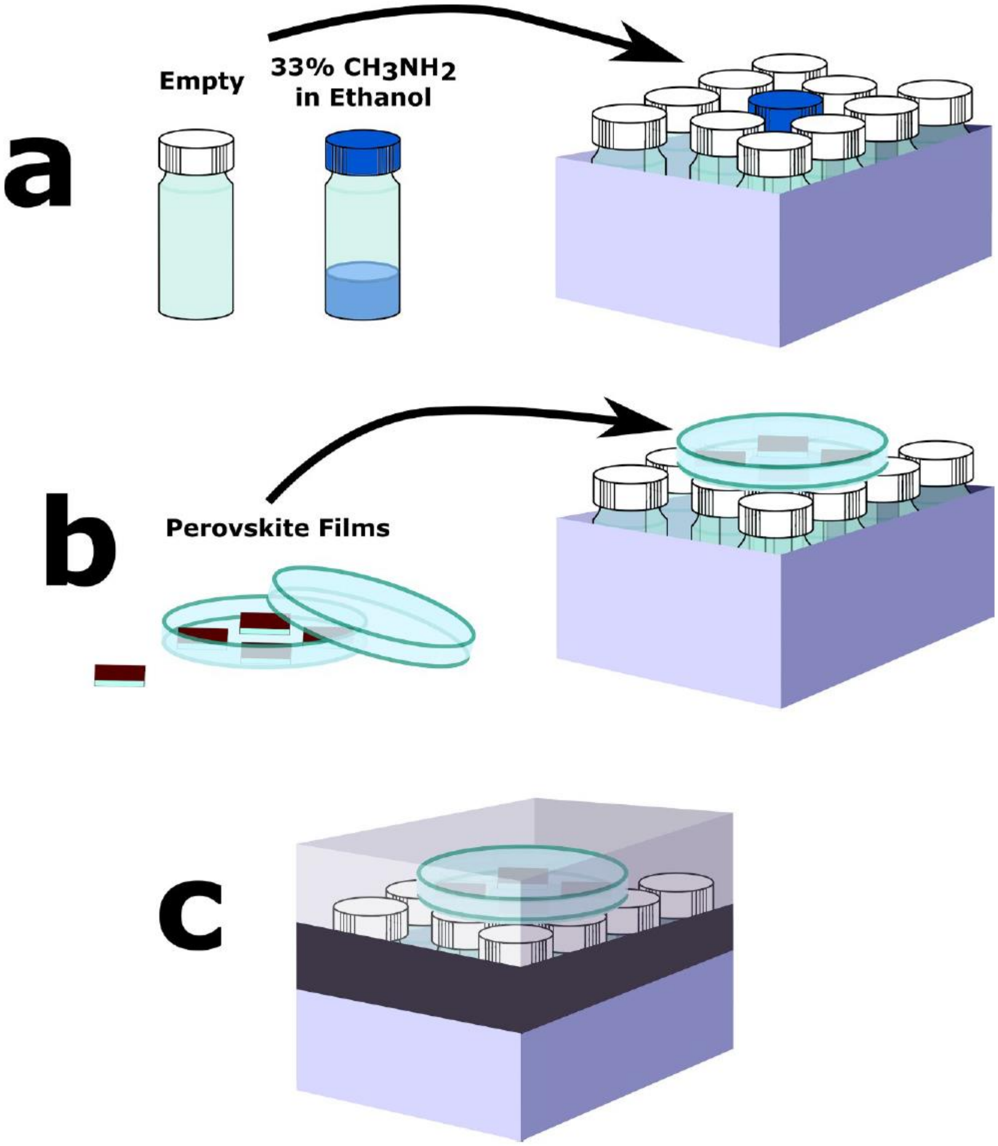

Figure 3.5: Schematic outline of the low MA^0 vapor treatment process illustrating: a) inserting capped, 20 ml vials, one with methylamine solution in the center and empty vials around it for support; b) placing perovskite films in a closed petri dish resting on the vials, centered on the vapor source; c) sealing of the chamber.

intermediate. Although Cui *et al.* do an excellent job of showing the accessibility of the solvated state and its prevalence under a high concentration of MA^0 vapor, they also demonstrated that although a transparent state can be established under NH_3 vapor,[105] complete solvation is not feasible. This illustrates the potential existence of multiple intermediate states within a single system, the nature of which likely play a role in determining the morphological consequences of the transformation.

It has been demonstrated that in solution the nature of perovskite formation depends upon methylammonium concentration.[116] Specifically, low concentrations allow topotactic transformation preserving structural elements of PbI_2, while at high concentrations dissolution occurs resulting in structure determined by the precipitation event rather than the nature of the starting material. We compared transformation under high and low methylamine vapor pressure to more completely map the impact of MA^0 vapor. Experimentally, high vapor pressure exposure followed the same protocol used for vapor treatment. This entails momentarily exposing a perovskite film to the MA^0 vapor contained in the head space of a small bottle of methylamine solution (10% in ethanol). Low vapor pressure exposure entailed placing $MAPbI_3$ films in chambers with a slow leak of MA^0 vapor for three hours (**Figure 3.5**).

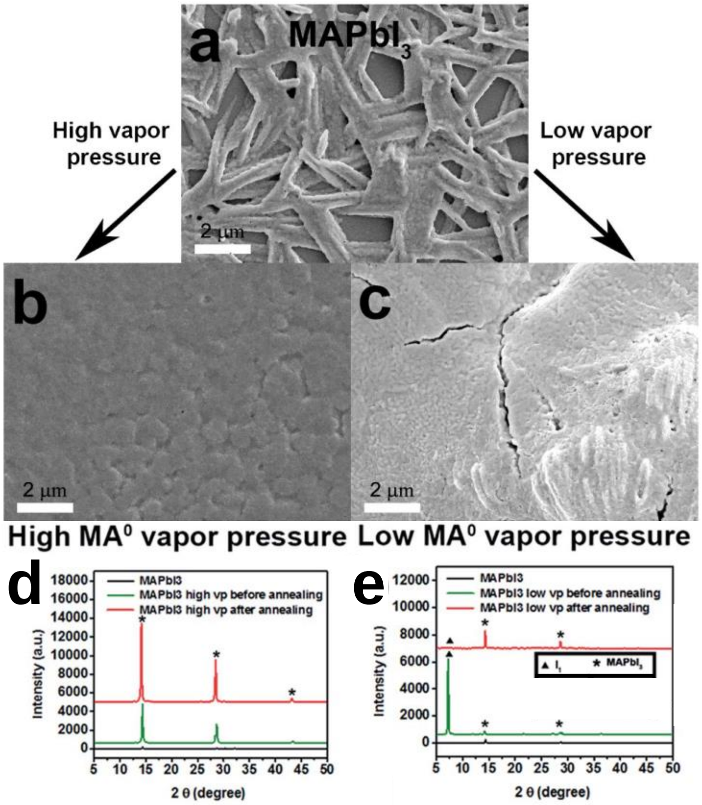

Figure 3.6: (a-c) SEM of $MAPbI_3$ before and after high and low $[MA^0]$ treatments. (d-e) Phase evolution via XRD analysis of $MAPbI_3$ under (d) high $[MA^0]$ and (b) low $[MA^0]$ treatments. The phases indicated are listed in the legend located in the center right of the figure.

Although direct analysis of intermediate states during vapor exposure is complicated by the incredible rapidity of transformation under high vapor pressure and the necessity of a closed system under low vapor pressure, we conducted XRD analysis of each perovskite film before vapor exposure, after exposure, and after annealing at 100 °C for 15 min. At high MA^0 vapor concentration (**Figure 3.6**), the intermediate state is too transient to be observed after vapor removal, but based on the work of Cui *et al.* it is clear that solvation occurs under these conditions. Perovskite crystallinity dramatically increases immediately after vapor exposure, and increases relatively little upon subsequent annealing. Exposure of $MAPbI_3$ to a low concentration of MA^0 vapor results in a relatively long lived, structurally coherent transparent state characterized by reflections marked as $\mathbf{I_1}$ in (**Figure 3.6e**). The solitary strong reflection at low 2θ (~7.2 2θ) suggests a swelling of the lattice consistent with the perturbation of the inorganic sublattice implicated by the intermediate's transparency. Annealing almost completely regenerates $MAPbI_3$, but with less crystallinity than in the case of high concentration MA^0 vapor exposure. For continued reference to the vapor treatments with high and low MA^0 vapor concentration, we will used the terms high [MA^0] treatment and low [MA^0] treatment.

While the phase evolution presented in Figure 3.6 illustrates the role of vapor concentration in mediating available transformations, we cannot directly discern whether these intermediate phases persist exclusively during vapor exposure or if they are the result of equilibration after vapor removal. That said,

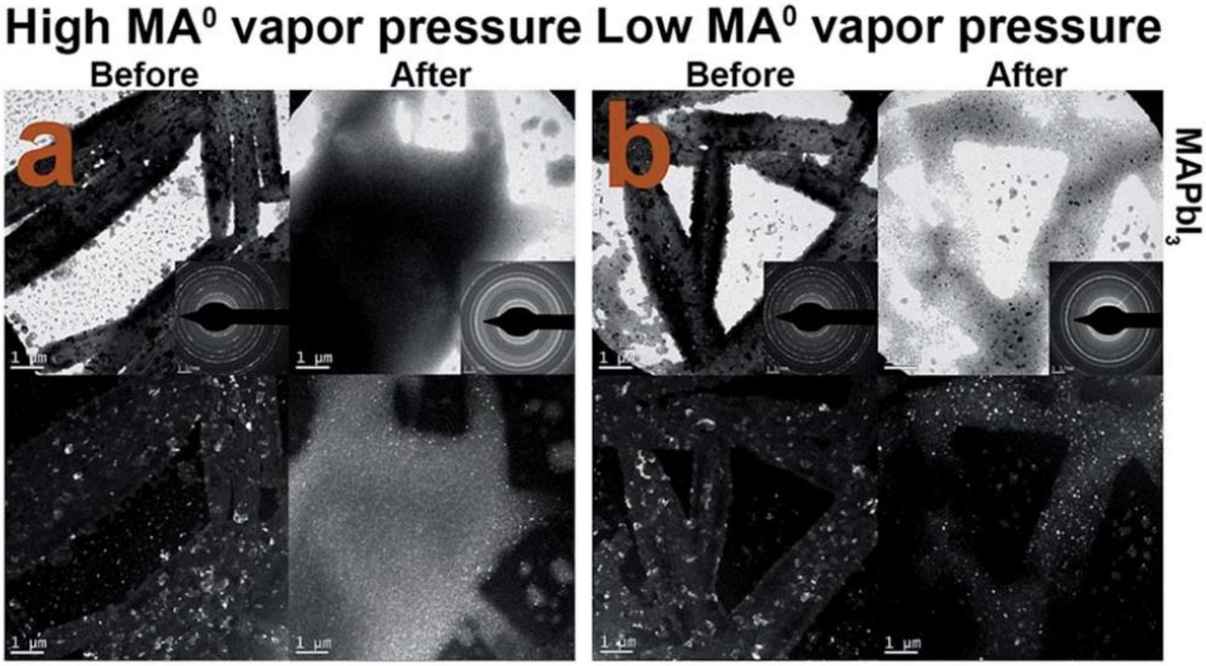

Figure 3.7: Lower magnification TEM analysis of low and high vapor pressure MA^0 post-deposition treatment. Each pane compares an identical region before and after MA^0 vapor exposure with bright field imaging (top), select area electron diffraction (inset), and dark field imaging (bottom).

through the microstructural consequences of each transformation just discussed, we can gain increased mechanistic insight. To this end we expanded the perovskite TEM analysis technique developed in Chapter 2 to enable direct correlation of specific regions of perovskite before and after vapor treatment (**Figure 3.7 and 3.8**). We correlated both bright and dark field analysis to characterize changes in grain structure.

Each pane of Figures 3.7 and 3.8 correlates bright field TEM images (top), select area electron diffraction (SAED) patterns (inset), and one representative dark filed image (bottom) of a region before and after vapor treatment. Each dark field image was taken in one quadrant of the sample's diffraction pattern. For dark field imaging, the electron beam was tilted 0.675° off the opic-axis then rotated around the optic by 90° to collect multiple exposures (not shown here). As previously discussed, because of the size of our objective aperture (~10 μm), this represents only part of the information contained within the dark field at that particular sample orientation, but the grain structure revealed is indicative of the structure in the other areas of the film.

In general, SAED patterns show little contribution from intermediate phases which is unsurprising in such a high vacuum environment. Throughout the different treatments, TEM SAED shows no clear

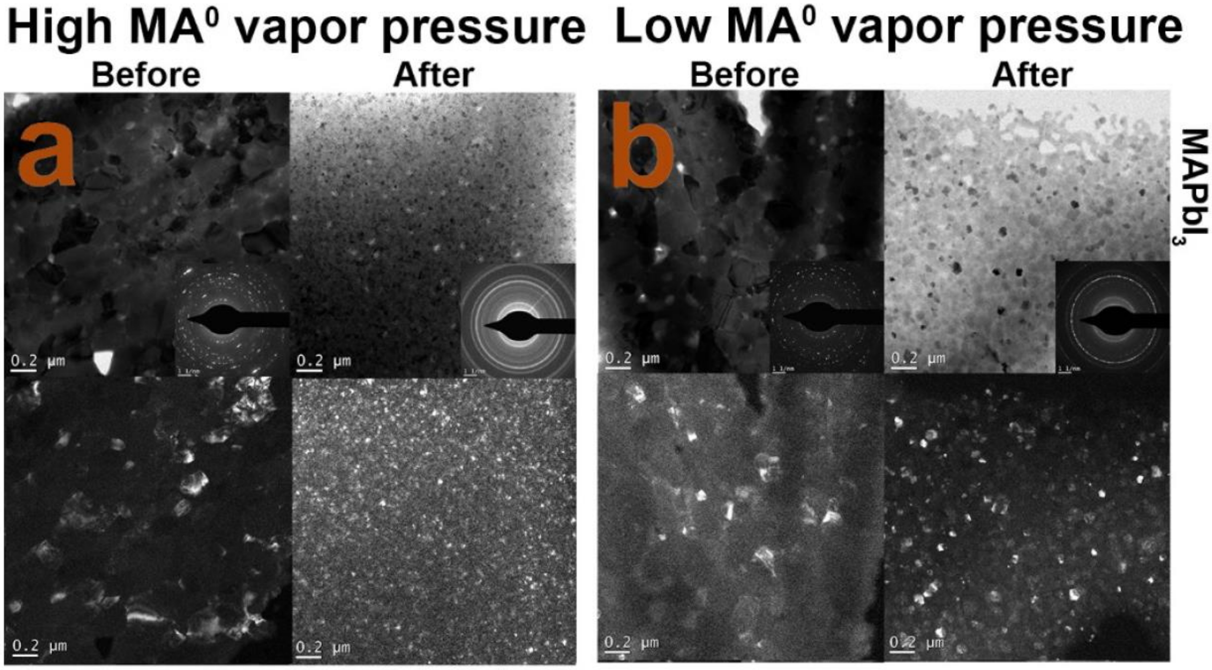

Figure 3.8: Higher magnification TEM analysis of low and high vapor pressure MA^0 post-deposition treatment (same regions as Figure 3.7). Each pane compares an identical region before and after MA^0 vapor exposure with bright field imaging (top), select area electron diffraction (inset), and dark field imaging (bottom).

change in collective crystal orientation which supports the interpretation of increased crystallinity from the XRD. In all cases the diffraction pattern becomes more ring-like and closer to a true powder after vapor treatment, a consequence of the reduction in grain size.

For $MAPbI_3$ under high [MA^0] exposure, the phase purity confirmed by SAED (Figure 3.7a inset) and the dramatic reduction in grain size apparent in the dark field images (Figure 3.7a, bottom) were already touched upon at the beginning of the manuscript. The bright field images (Figure 3.7a, top) show a great deal of diffusion unconstrained by the initial physical bounds of the material consistent with the liquid intermediate discussed by Cui et al. In contrast, diffusion in $MAPbI_3$ during low [MA^0] exposure (Figure 3.7b, top) remained constrained to the physical extent of the material before vapor exposure. Although coarsening still drives large scale diffusion which thickens some regions and depletes others, we can more clearly see the way diffusion is facilitated by the preexisting solid framework, an issue distinguishing low [MA^0] treatment from the high [MA^0] case. The dark field images (Figure 3.17b, bottom, and the higher magnification analogues in Figure 3.8) show that although grain size is still reduced compared to the initial state, final average grain size is slightly larger than in the high [MA^0] treatment. This is likely due both to grain growth within the solid intermediate and the reduction of perovskite nucleation rate caused by the more gradual change in MA^0 vapor pressure upon process completion.

The dramatic changes in morphology caused by MA^0 vapor exposure show that regardless of intermediate state, MA^0 vapor facilitates massively enhanced diffusion. The subtler distinctions apparent in Figures 3.4, 3.6, 3.7, and 3.8 suggest that $MAPbI_3$ can readily reach an essentially solvated state under high MA^0 vapor pressure, but both reducing the vapor pressure and altering composition of the organic sublattice (i.e. $CsPbI_3$) impedes the formation of this truly solvated state. Circumventing the formation of the metastable solid state intermediate (identified in Figure 3.6) during vapor based post-deposition treatment may be an important component of gaining the full value the process offers in increased film quality. The solvation event under high MA^0 concentration thus has the dual purpose of facilitating diffusion and kinetically excluding metastable, crystalline intermediates that frustrate transformation. **Figure 3.9** summarizes this insight schematically.

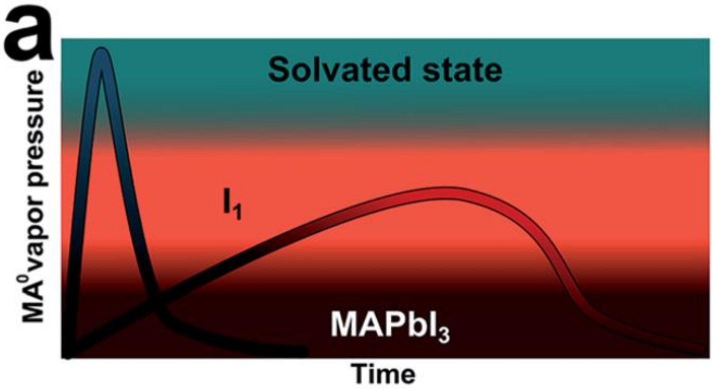

Figure 3.9: Schematic representation of the phase space available during methylamine treatment showing the impact of vapor pressure on accessing a solvated state and a solid state intermediate (I_1).

3.4 Conclusion

The methodology of this facile and high throughput post deposition treatment is potentially useful for translation to industry. Ultimately, translating this technique to larger scales requires controlling the microstructural consequences of the process and ensuring phase purity upon completion. These issues quickly become complex at scale, especially with materials with more complex phase behavior like $FAPbI_3$.

The manuscript this work first appeared in focuses on the design rules necessary to adapt this process to scale. For the purposes of this dissertation however, this work introduces a key concept that will aid effort in Chapter 6: methylamine (CH_3NH_2) can easily solvate both PbI_2 and $CH_3NH_3PbI_3$. Although we will not continue to use this processing technique specifically, the fact that an excess of methylamine effectively solvates the lattice means that an excess of methylammonium iodide (CH_3NH_3I) may have a similar kind of deleterious impact on long range order, as was shown through direct experiment in Chapter 2 (Figure 2.13a and d).

In addition to this chemical insight, this chapter illustrates how problematic the perovskite morphology generated by unmodified 1-step deposition (Figure 2.2) is for photovoltaic device function. Even though this methylamine vapor treatment actually makes grain size smaller, the fact that it physically spreads material out evenly across the substrate leads to an enhancement of device PCE from ~3% to ~12% (Figure 3.3). This simple study illustrates how problematic the morphology obtained by one step spin coating is. In Chapter 4, we present a conceptual review of the literature to broaden this thinking to $CH_3NH_3PbI_3$ growth in general, but in Chapter 6 we experimentally identify the mechanism through which this problematic morphology arises and thus also the routes necessary to circumvent it.

3.5 Experimental Details

Materials. All materials were purchased from Sigma-Aldrich without further purification unless stated specifically. CH_3NH_3I was synthesized by reacting 33 wt% CH_3NH_2 in ethanol with 57% HI in water solution at a 2 : 1 molar ratio of CH_3NH_2 to HI and 0 °C for 2 h. The product was collected by removing solvent through rotary evaporation, followed by diethyl ether washing until colorless and recrystallized twice in methanol. The crystalline white powder was finally dried in a vacuum oven at 60 °C for 24 h.

Substrate cleaning, $CH_3NH_3PbI_3$ film fabrication, and vapor treatment process. ITO (15 ohm sq^{-1}) glass substrates were cleaned sequentially with detergent, deionized water, acetone, and isopropanol under sonication for 10 min each. After drying under a N_2 stream, substrates were further cleaned by a UV ozone treatment for 10 min. PEDOT:PSS (Baytron P VP Al 4083, filtered through a 0.45 mm nylon filter) was first spin-coated onto the substrates at 5k rpm for 30 s and annealed at 150 °C for 10 min in air. To avoid any possible influence from oxygen and moisture, the substrates were transferred into a N_2-filled glovebox. The perovskite precursor solution was made by dissolving an equimolar ratio of PbI_2 (1 M) and CH_3NH_3I (1 M) in DMF at 60 °C and filtering through 0.45 mm PTFE filter. Perovskite layers were formed by spin-coating the precursor solution at 6k rpm for 45 s and then annealing at 100 °C for 15 min. After annealing, MA^0 vapor treatment was conducted by holding the perovskite film upside down right above a 20 mL open vial (28 mm outer diameter, 61 mm height, and 22 mm aperture diameter) with 6 mL of 33 wt% CH_3NH_2 solution in ethanol at room temperature. Upon turning clear (less than 1 s), the film was immediately removed vertically. Rapid vertical removal of the film from the MA^0 vapor source is important to prevent inhomogeneities that develop when the film is moved laterally through a MA^0 concentration gradient. The film was annealed again at 100 °C for 15 min to further increase thin-film crystallinity.

Chemical sources of reactivity toward MA^0 vapor: sample preparation. The perovskite films of differing compositions fabricated for comparison of reactivity were fabricated using an analogous method as that just described.

$MAPbBr_3$: a 1 M $CH_3NH_3PbBr_3$ precursor solution in DMF obtained by dissolving equimolar $PbBr_2$ (1M) and CH_3NH_3Br (1 M) in DMF at 60 °C and filtering through 0.45 µm PTFE filter was spin casted on top of PEDOT:PSS coated glass substrate at 6k rpm for 45 s and then annealed at 100 ºC for 15 min. Vapor treatment was implemented as described under the section discussing vapor treatment procedure.

$MASnI_3$: a 1 M $CH_3NH_3SnI_3$ precursor solution in DMF obtained by dissolving equimolar SnI_2 (1 M) and CH_3NH_3I (1 M) in DMF at 60 °C and filtering through 0.45 µm PTFE filter was spin casted on top of PEDOT:PSS coated glass substrate at 6k rpm for 45 s and then annealed at 100 ºC for 15 min. Vapor treatment was implemented as described under the section discussing vapor treatment procedure.

$FAPbI_3$: a 1 M $CH_3(NH_2)_2PbI_3$ precursor solution in DMF obtained by dissolving equimolar PbI_2 (1M) and $CH_3(NH_2)_2I$ (1 M) in DMF at 60 °C and filtering through 0.45 µm PTFE filter was spin casted on top of PEDOT:PSS coated glass substrate at 6k rpm for 45 s and then annealed at 170 ºC for 15 min. Vapor treatment was implemented as described under the section discussing vapor treatment procedure.

$CsPbI_3$: a 0.6 M $CsPbI_3$ precursor solution in DMF obtained by dissolving equimolar PbI_2 (0.6 M) and CsI (0.6 M) in DMF at 60 °C and filtering through 0.45 µm PTFE filter was spin casted on top of PEDOT:PSS coated glass substrate at 6k rpm for 45 s and then annealed at 100 ºC for 15 min. Vapor treatment was implemented as described under the section discussing vapor treatment procedure.

Low [MA^0] vapor treatment process. The low [MA^0] vapor treatment was conducted by sealing perovskite films in a container with a source of MA^0 vapor for 3 hours. The detailed experimental set up is presented in Figure 3.5. To avoid moisture, all processes were conducted in an N_2 filled glove box. Pure $CH_3NH_3PbI_3$ films were obtained through the procedure described above. Perovskite films were put into a plastic petri dish (35mm x 10mm) and capped. A BT Barrier Pipette Tips box (15cm x 10cm x 10cm) was used to hold capped, 20mL vials, one of which contained 6 mL of 33wt% MA^0 in ethanol without any internal or external gasket in the cap to allow a slow leak of vapor. The petri dish with perovskite films was placed atop this vapor source. The lower density of amine vapor compared to N_2 facilitated exposure with this chamber geometry. The box was sealed by three layers 3M 88 Electrical Tape to slow vapor leakage.

Device fabrication and characterization. ITO glass cleaning, PEDOT:PSS deposition, and $CH_3NH_3PbI_3$ film growth are discussed above. Atop the $CH_3NH_3PbI_3$ film, C_{60} (15 mg mL^{-1} in ortho-dichlorobenzene (DCB)) and bis-C_{60} surfactant (2 mg mL^{-1} in isopropyl alcohol) were sequentially deposited by spin coating at 1k rpm for 60 s and 3k rpm for 60 s, respectively. Silver electrodes with a thickness of 120 nm were finally evaporated under vacuum ($<2 \cdot 10^{-6}$ Torr) through a shadow mask. The device area was defined as 3.14 mm^2. All *J–V* curves were recorded using a Keithley 2400 source meter unit. The device photocurrent was measured upon illumination from a 450 W thermal Oriel solar simulator (AM 1.5G) calibrated with a standard Si photodiode detector equipped with a KG-5 filter, which can be traced back to the standard cell of the National Renewable Energy Laboratory (NREL).

Characterization. X-ray diffraction (XRD) experiments were performed using a Bruker F8 Focus Powder XRD operating at 40 kV and 40 mA with a Cu Kα (1.54 Å) X-ray source. Secondary electron images were taken with a FEI Sirion scanning electron microscope at 5 kV. TEM samples were prepared by first adhering a finder TEM grid with a Carbon B coating to a cleaned ITO glass substrate (specifically EF400-Ni from Electron Microscopy Services). Before mounting, grids were glow discharge treated for 30 s with an oxygen/hydrogen plasma with a Solarus 950 Gatan Advanced Plasma System. The grid is mounted in slight tension on a glass slide with scotch tape to ensure intimate thermal contact. The same deposition and heat treatment procedure for first PEDOT:PSS then the desired perovskite are followed as above with the exception of the use of a 0.4 M perovskite precursor solution. Vapor exposure was also identical except for the use of a MA^0 vapor source with a smaller aperture (4 mL vial with a 10 mm diameter neck rather than 20 mL with a 22 mm diameter neck) for high vapor pressure exposure. When the grid is removed from the glass slide for characterization, the points of contact between the tape and the grid are carefully cleaned with isopropanol (IPA) to prevent contamination of the high vacuum environment of the TEM. A Tecnai G2 F20 transmission electron microscope was used at 200 kV for all TEM measurements.

Chapter 4. CONCEPTUAL REVIEW OF THE LITERATURE TO BROADEN THIS UNDERSTANDING TO GENERAL HYBRID PEROVSKITE GROWTH

**This entire chapter has been reproduced verbatim from STW-4 (Reproduced from Ref. STW-4 with permission from the John Wiley and Sons, Inc.)*

This chapter presents material that was published in a concept article titled *Navigating Organo-Lead Halide Perovskite Phase Space via Nucleation Kinetics toward a Deeper Understanding of Perovskite Phase Transformations and Structure–Property Relationships* (STW-4). To preserve the content in the form it was peer-reviewed, this chapter has been reproduced verbatim from STW-4 with the exception of blending material that was originally published as supporting information into the main text. This material expands the discussion in Chapters 2 and 3 and it provides conceptual context for the work presented in Chapters 5 and 6.

4.1 Introduction

The rapid development of organo-metal halide perovskite photovoltaics can largely be attributed to diverse innovations in processing.[65,67,101,117] Ultimately, the majority of works devoted to perovskite fabrication since the material's introduction to the field[1,118] have a common aim: control over the phase transformation that governs film evolution. This has proven to be an uniquely rich area for development because of the remarkably idiosyncratic transformation behavior intrinsic to this relatively new class of materials.STW-2,[65,67,101,117,119–121] Low temperature deposition strategies[122] have enabled devices with performance nearing that of prevailing silicon technologies,[123] demonstrating the material's union of the facile processing and superior photo-physical performance inherent to organic and inorganic materials, respectively.

1- and 2-step perovskite depositions have been developed in the context of vapor- and solution-based approaches, with variants designed to control kinetic and thermodynamic landscapes. As we learn more about this material's growth, it becomes clear that intermediates play a key role. [67,90,101,108,117,120,121] In any solid, internal microstructure is determined by how the final product is reached. The route the material takes through phase transformations standing between its initial state and the desired end determines the nature of the overall product. When structure matters, this becomes an important consideration, as is the case with modern steels.[124] Internal microstructure determined by transformation pathway separates hard, brittle martensitic steel from soft, ductile pearlitic steel.

The field of perovskite photovoltaics has evolved enough to provide perspective on navigating the complex array of intermediates relevant to organo-lead iodide perovskite growth. Even though this material serves a very different purpose than steel, structure matters in perovskite photovoltaics.[125–133] In either meso-superstructured or thin-film architectures, crystal size, crystallinity, grain structure, and crystal orientation contribute to the effectiveness of a perovskite absorber.[130–133] That said, as of yet the exact influence on ultimate device performance is difficult to ascertain clearly, partially because controlling these parameters is a challenge due to the competing intermediates relevant in perovskite growth.

As with steel, understanding what intermediates exist and how to navigate them kinetically may help to realize this material's full potential. To this end, this concept paper endeavors to summarize current understanding on this material's various growth pathways with the aim of equipping the reader with new perspective for creatively designing perovskite processing routes. Our focus on interrelating deposition strategies through growth pathways in a usable model makes the graphical information we present very dense; but Zhao *et al.* recently published a more general summary of solution-based perovskite depositions that serves as an excellent companion to this discussion.[80]

4.2 Transformation Pathways and Intermediates

The hybrid nature of this class of perovskite imparts to it a rich phase space. Here, phase space refers to all phases accessible in the composition, temperature, and time windows relevant during perovskite formation. With careful examination of the recent literature surrounding perovskite processing, it can be concluded that direct $CH_3NH_3PbI_3$ ($MAPbI_3$) nucleation is rarely encountered. Choi *et al.* demonstrated that 1-step deposition from a γ-butyrolactone (GBL) solution of equal parts methylammonium iodide and lead iodide (MAI + PbI_2) produces a 70 atom percent disordered perovskite film.[108] This is unsurprising as it is often noted that unoptimized 1-step solution deposition produces poorly crystalline films, an issue that motivates much of the work aimed at improving material deposition.[80] Park *et al.* showed that gradual crystallization persists well after film fabrication both with and without chloride.[90] We observed that excess MAI stabilizes this amorphous state, so to simplify reference to this phase we will use the formula a-$(CH_3NH_3)_{1+x}PbI_{3+x}$ (a-$(MA)_{1+x}PbI_{3+x}$).STW-2

With dark field transmission electron microscopy (TEM) and electron diffraction, we have seen that perovskite nucleation within the bulk of a-$(MA)_{1+x}PbI_{3+x}$ domains results in isolated, randomly oriented nanoscale crystallites.STW-2 Tuning kinetics with solvent gradation during deposition creates an intermediate composed of perovskite precursor species and solvent molecules (dimethyl sulfoxide, DMSO),[101] which ultimately produces a much more highly crystalline $MAPbI_3$ film. Shen *et al.* demonstrated similar solvent co-crystalline intermediates in 1-step growth from N,N-dimethylformamide (DMF) and dimethylacetamide (DMAc).[134] **Scheme 4.1a** summarizes intermediates relevant to pure iodide 1-step perovskite depositions.

Lee *et al.*[1a] developed a 1-step deposition that vastly improves carrier lifetime by incorporating

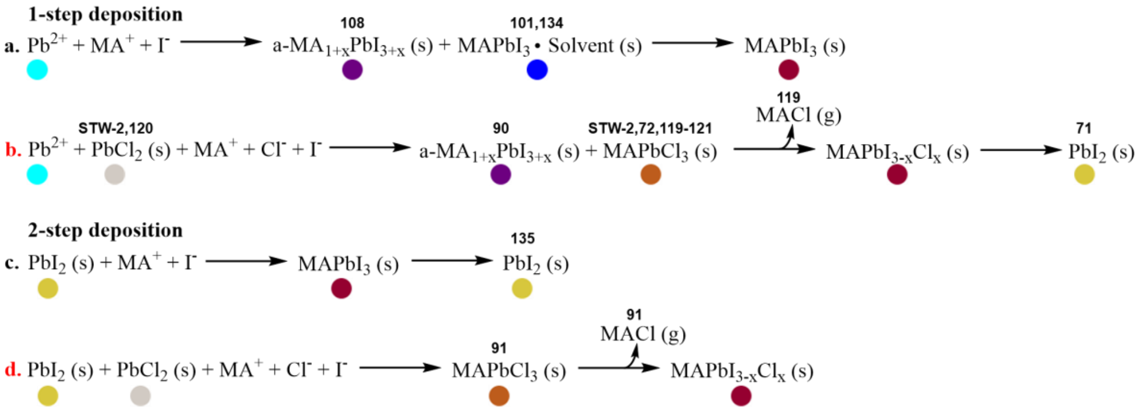

Scheme 4.1: Reactions showing all intermediates relevant for perovskite transformation during 1-step deposition without and with Cl [(a) and (b)], and 2-step deposition without and with Cl [(c) and (d)]. No distinction is made at this point between solution and vapor deposition, and this scheme does not attempt stoichiometric accuracy as balance between competing phases depends sensitively on kinetics. The bright red highlights (b and d) are to make comparing this with Figure 4.1c expedient.

$$Cl^- + CH_3NH_3^+ \rightleftharpoons CH_3NH_3Cl\ (s)$$

$$CH_3NH_3Cl\ (s) \rightleftharpoons CH_3NH_3Cl\ (g)$$

Scheme 4.2: Sublimation of MACl, a primary contributor to chloride loss.

chloride into the precursor solution based on the supposition that the addition of chloride generates an alloy perovskite ($MAPbI_2Cl$).[79] However, more recent studies have elucidated that although chloride results in increased crystallographic orientation, crystal size, and overall crystallinity,STW-2,[65,80] little (~ 4 at%) remains in the system after annealing provided a stoichiometrically sufficient amount of iodide is supplied.[13] Upon closer investigation, an intermediate phase seemingly unique to the case of growth in the presence chloride appears during transformation with a single consistently visible XRD signal matching a plane in $MAPbCl_3$.[13] As the vast majority of chloride and excess methyl ammonium volatilize (**Scheme 4.2**),[119] the dramatic increase in carrier diffusion length[79] must be partly attributed to structural rather than purely compositional changes.STW-2,[119–121]

The question of exactly how this intermediate alters film formation has compelled a number of studies,STW-2,[119–121] which have revealed that alterations in nucleation dynamics lie at the core of this intermediate's structural impact. These changes extend as far back as the solution state pre-deposition. Tidhar *et al.* found that nanocrystalline $PbCl_2$ nuclei exist in a precursor solution derived from $PbCl_2$ and MAI,[120] and we demonstrated that the influence of this solid phase is mediated by kinetically limited complex ion and solvation equilibria in solution.STW-2 Extended annealing is found to generate PbI_2 with or without chloride because of its irreversible loss.[71,119,135] Scheme 4.1b summarizes intermediates relevant to 1-step deposition with chloride. The exact structure of the $MAPbCl_3$ intermediate is unclear, and although it seems to only be observed in the presence of chloride,[72] chloride may simply encourage its formation rather than be a primary constituent. For simplicity we will refer to it as $MAPbCl_3$.

Shortly after the use of chloride in 1-step deposition,[65] Burschka *et al.* popularized a 2-step approach previously developed by Liang *et al.*[117] in which PbI_2 is first deposited from DMF followed by immersion in an isopropanol (IPA) solution containing MAI.[66] Perovskite nucleation then occurs at and within preexisting PbI_2 crystallites improving overall crystallinity as well as material infiltration into mesoporous structures. This procedure has been widely adopted and modified to include chloride in the

1-Step Deposition

Vapor

$$\mathrm{PbI_2\ (v) + MAI\ (v) \longrightarrow MAPbI_3\ (s)}$$

$$\mathrm{Pb^{2+} + MA^+ + 3Br^- \xrightarrow{\text{nebulization @ 250 }^{o}\text{C}} MAPbBr_3\ (s)}$$

$$\mathrm{PbCl_2\ (v) + 4MAI\ (v) \longrightarrow ??? \longrightarrow MAPbI_{3\text{-}x}Cl_x\ (s)}$$

$$\mathrm{Pb^{2+} + X^- \rightleftharpoons PbX^+}$$

$$\mathrm{PbX^+ + X^- \rightleftharpoons PbX_2}$$

$$\mathrm{PbX_2 + X^- \rightleftharpoons PbX_3^-}$$

$$\mathrm{PbX_3^- + X^- \rightleftharpoons PbX_4^{2-}}$$

X = I, Br, or Cl

Solution

$$\mathrm{Pb^{2+} + MA^+ + 3I^- \longrightarrow MAPbI_3\ (s)}$$

$$\mathrm{Pb^{2+} + MA^+ + 3Br^- \longrightarrow MAPbBr_3\ (s)}$$

$$\mathrm{Pb^{2+} + MA^+ + (3\text{-}x)I^- + xBr^- \longrightarrow MAPbI_{3\text{-}x}Br_x\ (s)}$$

$$\mathrm{Pb^{2+} + MA^+ + 3I^- \longrightarrow MAPbI_3\ (s) + a\text{-}MAPbI_3\ (s)}$$

$$\mathrm{Pb^{2+} + MA^+ + 3I^- \xrightarrow{\text{toluene wash}} MAPbI_3 \bullet DMSO\ (s) + MAPbI_3\ (s) \longrightarrow MAPbI_3\ (s)}$$

$$\mathrm{Pb^{2+} + MA^+ + 3I^- \xrightarrow{\text{CB wash}} MAPbI_3}$$

$$\mathrm{Pb^{2+} + 2NO_3^- + 3MA^+ + 3I^- \longrightarrow MAPbI_3\ (s)}$$

$$\mathrm{Pb^{2+} + 3MA^+ + 2Cl^- + 3I^- \longrightarrow MAPbI_{3\text{-}x}Cl_x\ (s)}$$

$$\mathrm{Pb^{2+} + 3MA^+ + 2Cl^- + 3Br^- \longrightarrow MAPbBr_{3\text{-}x}Cl_x\ (s)}$$

$$\mathrm{Pb^{2+} + 3MA^+ + 2Cl^- + 3I^- \longrightarrow MAPbI_{3\text{-}x}Cl_x\ (s) + a\text{-}MAPbI_{3\text{-}x}Cl_x\ (s)}$$

$$\mathrm{Pb^{2+} + 3MA^+ + 2Cl^- + 3I^- \longrightarrow MAPbI_3\ (s) + MAPbCl_3\ (s) \longrightarrow MAPbI_3\ (s) \longrightarrow MAPbI_3\ (s) + PbI_2\ (s)}$$

$$\mathrm{Pb^{2+} + 3MA^+ + 2Cl^- + 3I^- + PbCl_2\ (s) \longrightarrow MAPbI_3\ (s) + PbCl_2\ (s) \longrightarrow MAPbI_3\ (s)}$$

$$\mathrm{Pb^{2+} + 3MA^+ + 2Cl^- + 3Br^- + PbCl_2\ (s) \longrightarrow MAPbBr_3\ (s) + PbCl_2\ (s) \longrightarrow MAPbBr_3\ (s)}$$

2-Step Deposition

Vapor

$$\mathrm{PbI_2\ (s) + MAI\ (v) \longrightarrow MAPbI_3\ (s) + PbI_2\ (s) + MAI\ (s) \longrightarrow MAPbI_3\ (s)}$$

$$\mathrm{PbCl_2\ (s) + MAI\ (v) \longrightarrow MAPbI_3\ (s) + PbI_2 + MAPbCl_3\ (s) \longrightarrow MAPbI_3\ (s)}$$

$$\mathrm{PbI_2\ (s) + MAI\ (v) \longrightarrow MAPbI_3\ (s) + PbI_2\ (s) + MAI\ (s) \longrightarrow MAPbI_3\ (s) + a\text{-}MAPbI_3\ (s) \longrightarrow MAPbI_3\ (s)}$$

$$\mathrm{PbI_2\ (s) + MAI\ (v) \longrightarrow MAPbI_3\ (s) + PbI_2\ (s) + MAI\ (s) \longrightarrow MAPbI_3\ (s) \longrightarrow MAPbI_3\ (s) + PbI_2\ (s)}$$

Solution

$$\mathrm{PbI_2\ (s) + MA^+ + I^- \longrightarrow MAPbI_3\ (s) + PbI_2\ (s)}$$

$$\mathrm{PbI_2\ (s) + MA^+ + I^- \longrightarrow MAPbI_3\ (s)}$$

$$\mathrm{PbI_2\ (s) + MA^+ + Cl^- \longrightarrow MAPbI_{3\text{-}x}Cl_x\ (s)}$$

$$\mathrm{PbI_2\ (s) + MA^+ + I^- + Cl^- \longrightarrow MAPbI_{3\text{-}x}Cl_x\ (s)}$$

$$\mathrm{PbI_2\ (s) + MA^+ + I^- + Br^- \longrightarrow MAPbI_{3\text{-}x}Br_x\ (s)}$$

$$\mathrm{PbX_2\ (v) \longrightarrow PbX_2\ (s)}$$

$$\mathrm{Pb^{2+} + 2X^- \longrightarrow PbX_2\ (s)}$$

$$\mathrm{Pb^{2+} + I^- + Cl^- \longrightarrow 0.5PbI_2\ (s) + 0.5PbCl_2\ (s)}$$

X = I, Br, or Cl

$$\mathrm{PbI_2\ (s) + PbCl_2\ (s) + MA^+ + I^- \longrightarrow MAPbI_{3\text{-}x}Cl_x\ (s)}$$

$$\mathrm{PbCl_2\ (s) + MA^+ + I^- \longrightarrow MAPbI_{3\text{-}x}Cl_x\ (s)}$$

$$\mathrm{PbI_2\ (s) \xrightarrow{\text{DMF}} PbI_2 \bullet DMF\ (s) \longrightarrow MAPbI_3\ (s) + MA_4PbI_6 \bullet 2H_2O\ (s)}$$

$$\mathrm{PbI_2\ (s) + MA^+ + I^- + Cl^- \longrightarrow MAPbI_{3\text{-}x}Cl_x\ (s) + MAPbCl_{3\text{-}y}I_y\ (s)}$$

$$\mathrm{PbCl_2\ (s) + MA^+ + I^- + Cl^- \longrightarrow MAPbI_{3\text{-}x}Cl_x\ (s) + MAPbCl_{3\text{-}y}I_y\ (s)}$$

Scheme 4.3: Listed are the transformation pathways discussed throughout the literature that were consolidated in creating Scheme 4.1 in the main text. Although the vast majority of the reaction pathways are only partially complete, each contributes to the understanding of the overall process. Scheme 4.1 presents only information relevant to $MAPbI_{3\text{-}x}Cl_x$ and disregards information concerning $MAPbI_{3\text{-}x}Br_x$ for brevity. Although a number of references correlate to each pathway listed, the majority of the most significant contributions are discussed throughout the manuscript. We include this list here to contextualize the meaning in Scheme 4.1, but we avoid the lengthy endeavor of listing each reference relevant here because of limited value the list would have without context.

sseed phase[136] and immersion solution[137] as well as alterations of the means of MAX (MA = methylammonium and X = Cl and/or I) exposure including spin-coating[97] and vapor treatment[67,138]. The intermediate $MAPbCl_3$ phase is observed in the case of 2-step growth with chloride,[91] suggesting that the considerations discussed above are also relevant. Intermediates relevant for 2-step deposition without and with chloride are represented in Scheme 4.1 c-d, respectively.

1-Step vapor deposition is more rarely encountered in the current literature,[53,77,139,140] and as such phase evolution during growth is sparsely elucidated. The technique has been successfully adapted to the growth of pure iodide,[139] pure bromide,[140] and mixed iodide/chloride[77] perovskites. Malinkiewicz *et al.* found that the preferential crystal orientation about the [100] and [001] directions characteristic of growth with chloride can be achieved from a pure iodide deposition.[139] This may indicate that direct perovskite nucleation is possible from vapor.

To generate Scheme 4.1, we scoured the current perovskite literature looking for each transformation pathway considered. A consolidated list of this summary is offered in **Scheme 4.3** at the conclusion of the supporting information. Although each pathway in Scheme 4.3 is incomplete in some way, each provides important perspective on the relevant overall process.

4.2.1 *Representing perovskite phase space*

Using Scheme 4.1 we can assemble a schematic representation of perovskite phase space to relate these many different processing techniques (**Figure 4.1**). Because of the complex nature of this class of perovskite, we resort to a kinetic rather than purely thermodynamic model. The most convenient axes are time (radial, r) and starting conditions (theta, θ) (Figure 4.1a). Moving forward in time for 1-step deposition (red arrows in Figure 4.1a) entails the loss of volatile components (solvent, MACl, MAI, etc.). 2-Step deposition is the reverse of this so moving forward in time (blue arrows in Figure 4.1a) entails an increase in volatile components.

Although the sophistication of Figure 4.1a is all that is required to use this diagram for the purpose of summarizing information, the detailed physical relationships imbedded in this model are presented in

Figure 4.1b. In the following section (3.2.2) we provide more thorough elucidation of the meaning in Figure 4.1b and 4.1c. In short, this diagram is a synthesis of time-temperature-transformation diagrams developed to map kinetic relationships in steel processing[141] and 2D representations of material band structure developed to map electronic states in reciprocal space.[142]

The most significant variable buried within the broadly defined θ-axis (circular axis) is

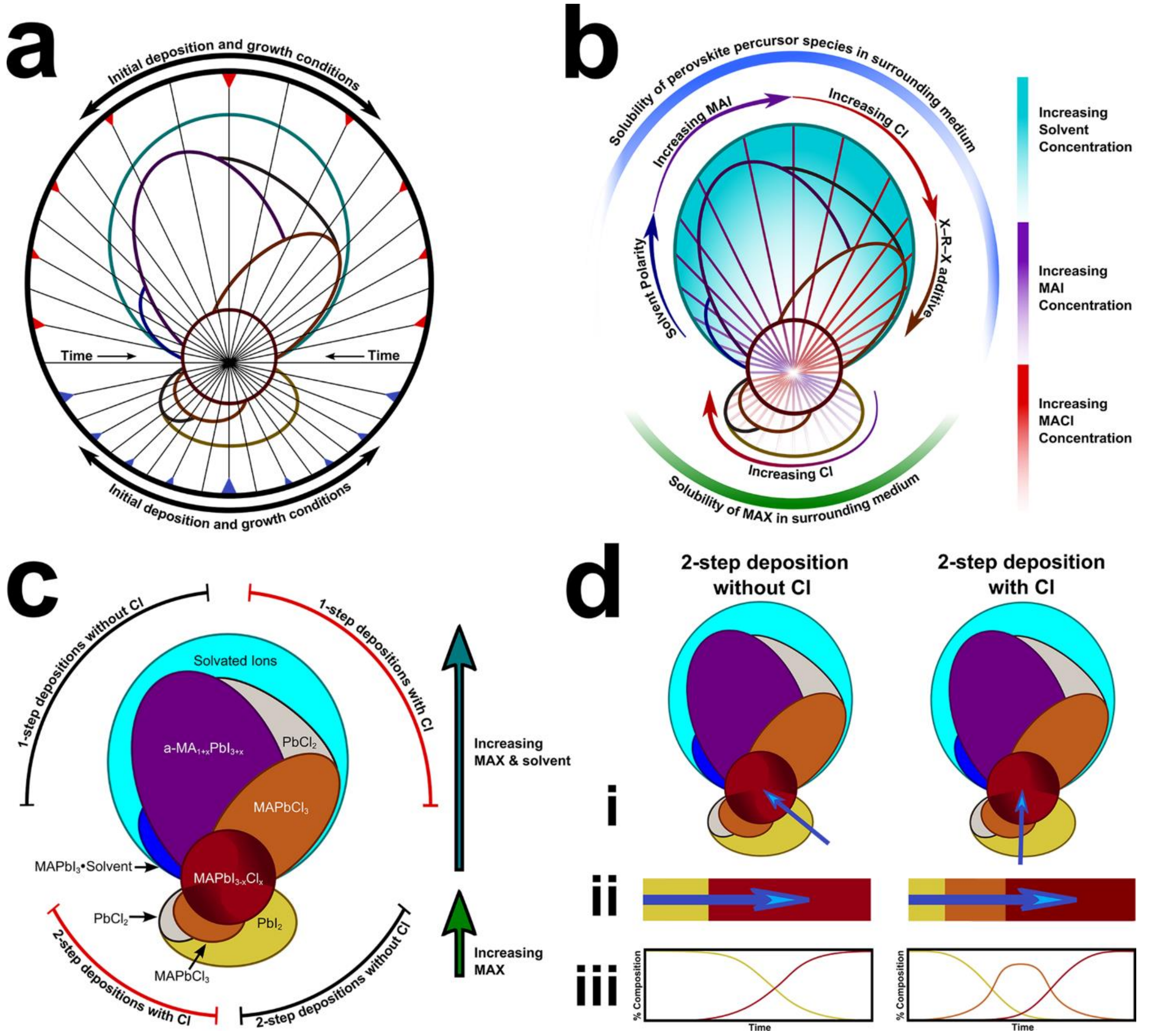

Figure 4.1: Schematic representation of $MAPbI_{3-x}Cl_x$ phase space. (a) shows what phase each region correlates to, as well as the general logic with which the space is assembled. In a, red arrows show the forward time direction during 1-step deposition and the blue arrows show the forward time direction during 2-step deposition. (b) and (c) provide a more systematic and thorough representation of the axes that the space is defined in. (c) shows that each region is correlated to a phase relevant during growth under a given set of conditions which is set by choosing a point around the figure. The dark red gradient in the center of (c) signifies increasing chloride content in $MAPbI_{3-x}Cl_x$. (d) briefly illustrates how the diagram is used.

composition. In the case of 1-step deposition, variations in initial solvent, halide, methylammonium, and halogenated additive concentration change the pathways available. For 2-step deposition, available pathways are controlled by variations in lead halide salt and halide intercalant. The other key variable embedded in the θ-axis is solubility in the surrounding medium. For 1-step depositions, this is the solubility of all perovskite precursor species while for 2-step depositions this is the solubility of the methylammonium halide salt. Because time correlates with the gain or loss of volatile species, the radial axis also defines solvent, MAI, and MACl concentration. Regions outlined in Figure 4.1a-b and defined in Figure 4.1c represent phase fields corresponding to the phases highlighted in Scheme 4.1. The central region represents the equilibrium $MAPbI_{3-x}Cl_x$ phase obtained through the surrounding processes, which means the region can be used to broadly relate transformation pathway to changes in equilibrium composition, microstructure, and properties. Currently, the shading in this region indicates gradually increasing chloride content in $MAPbI_{3-x}Cl_x$, up to ~ 4 at%.[13]

To use this diagram, we first choose starting conditions and draw a line towards the middle of the central organo-lead iodide perovskite phase field (Figure 4.1d *i*). Phase fields this line passes through before reaching the desired end are intermediates that determine microstructure in the final film (Figure 4.1d *ii*). As the line passes into a new field, that phase begins to nucleate (Figure 4.1d *iii*). In the qualitative sense presented here, the relative size of each field traversed represents that phase‘s dominance in determining final microstructure. The size disparity between regions corresponding to 1- and 2-step depositions (top and bottom) is due to the greater change in overall composition necessary to achieve the final perovskite film in 1-step solution deposition (top), a consequence of the presence of solvent and often excess methylammonium. As is, regions are carefully designed to summarize trends in phase evolution between all current perovskite deposition techniques with the use of the growing consensus in the literature rather than physical data, and thus this realization of the PTT curve is purely conceptual. To extend this model to represent quantitative, physical data, these phase fields are replaced by percent composition curves for each intermediate measured during growth through analytical *in situ* diffractometry or spectroscopy.[53] An example of using this graphical methodology to quantitatively represent physical parameters is discussed in the end of the following section to clarify the meaning and illustrate the flexibility of the PTT curve.

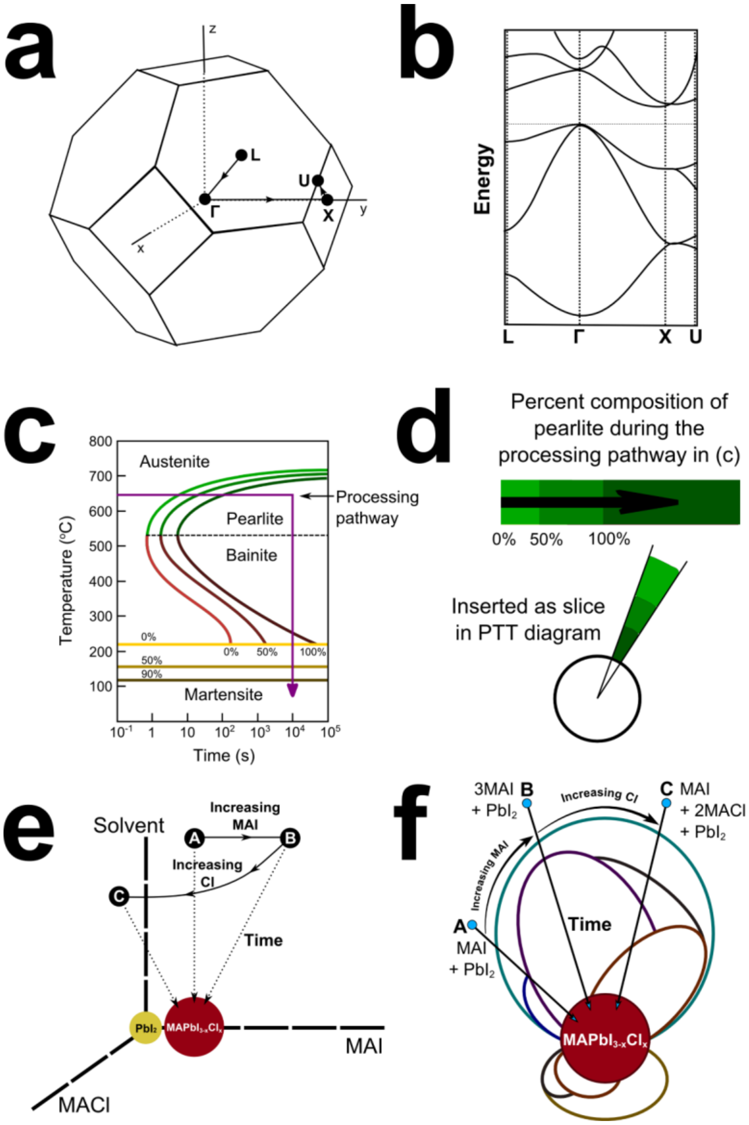

Figure 4.2: Brief graphical depiction of the logic behind the process-time-transformation (PTT or pin-cushion) diagram. (a) depicts the first Brillouin zone in Si, and (b) is a representation of the electronic band structure plotted about the path depicted in (a). The way of representing complex information used to depict a material's band structure is the same logic used to construct the PTT curve. (c) shows a a time-temperature-transformation (TTT) diagram for the eutectic composition in an unalloyed steel. (d) shows how, after setting a particular processing route, the percent composition curves in the TTT diagram are then inserted as a slice of the PTT diagram. (e) depicts a small portion of the parameter space of interest for perovskite deposition and (f) is a representation of perovskite transformation behavior plotted about the path depicted in (e). The entire space that the PTT diagram in (f) represents contains ~8 axes, instead of just those in (e). (a) and (b) are original vector graphics based on the open source representation by Mohamed Mohamed [CC0], via Wikimedia Commons (http://commons.wikimedia.org/wiki/File%3AWiki_mc_fig45_new.PNG). (c) is an original vector graphic based off of the information in W. D. Calister, D. G. Rethwisch, *Materials Science and Engineering: An introduction*, 8th Ed., Wiley and Sons Inc., Hoboken, USA **2010**, pp. 343-381.

4.2.2 *Technical aspects behind constructing this representation*

The challenge of making sense out of the large number of processes and conditions used for organo-lead halide perovskite growth is a familiar one in contemporary science. Many systems depend on such a large number of interrelated parameters that creating a useful model is daunting. One of the most elegant strategies for dealing with such a task is what we use to represent a material's electronic band structure.[141,142] **Figure 4.2** shows a cartoon representation of silicon's first Brillouin zone. The band structure itself is a complex surface that extends along what would be a fourth axis in this figure: energy. Instead of trying to represent the band structure's entirety, it is more useful to choose points of interest and map contours along simple paths connecting them. This allows an informative 2D model of what would otherwise be a prohibitively complex 4D surface. The points labeled **L**, **Γ**, **X**, and **U**, in Figure 4.2a and the paths connecting them are mapped in Figure 4.2b, essentially constituting an unfolding of the complicated 4D space in Figure 4.2a into two dimensions. Even though this diagram maps out a very small amount of the existent information, we can already get most of what we would need because of our careful choice of key points and paths.

This establishes the logic used to move through the complex ~10 dimensional parameter space relevant to perovskite processing, but we borrow some of the physical rationale behind time-temperature-transformation (TTT) curves to establish what physical parameters we actually plot.[141,142] Figure 4.2c shows a schematic example of a (TTT) curve representing the eutectic composition in an unalloyed steel. Fields in the image represent microstructures that can be reached through certain heating curves (if a microstructure curve is contacted by the heating profile, it begins to form). This kind of graph allows one to kinetically visualize the microstructural consequences of many different heat treatments, but its limitation is that it is only valid at an exact set of conditions (composition, pressure, etc.). When composition shifts entirely new curves become relevant, making this exact graphical methodology cumbersome for hybrid perovskites. Figure 4.2d endeavors to show that each radial slice of the PTT curve is essentially an individual TTT curve with a temperature profile set by the process in question (with time equal to zero along the outside edge). In fact, the process in question sets a great number of parameters, hence generalizing from “temperature” to “process,” so it becomes important to only plot processes that differ in a small number of variables, ideally one, adjacent to each other. Otherwise, the wild variation between points would convolute visible relationships. Since the relationship between kinetics and competing phases is well established in the field of steel design, microstructure curves can be generated. In the case of hybrid perovskites, we are only beginning to understand the array of intermediates relevant in growth let alone the range of microstructures they can create so we have replaced the microstructure curves of TTT diagrams with percent phase composition curves for each relevant intermediate in the PTT diagram.

In adapting these strategies to kinetically representing phase transformations in the organo-lead halide perovskite system, one must visualize a space like that in Figure 4.2e. In this space we’ve replaced x, y, and z coordinates with axes representing the concentration of MAI, MACl, and solvent. These are the same axes that can be seen at the center of Figure 4.1b, although in this representation they are much easier to understand. The points **A**, **B**, and **C** indicate starting conditions for unoptimized 1-step deposition, deposition with excess MAI, and deposition from a solution made with MACl. These correspond to the points in Figure 4.2f, in which the solution stoichiometry of each is shown as well as their positions in the PTT, or pin-cushion, diagram. After we turn time on, so to speak, these systems progress toward the equilibrium state at the center of Figure 4.2e and f: $MAPbI_{3-x}Cl_x$.

The PTT curve presented in this manuscript is completely conceptual because it is populated with trends from the literature rather than quantitative information, but this need not be the case. **Figure 4.3** shows a schematic example of applying this graphical methodology quantitatively. Although Figure 4.3 is not filled with actual data, it is meant to emulate the results of Moore et al.[91] and Dharani et al.[143] in their studies on 2-step deposition with and without chloride. In Figure 4.3a, the colored phase fields of the PTT diagram in the main text are replaced by more specific percent phase composition contours. As the fraction of $PbCl_2$ composing the initial system increases, the prevalence of the $MAPbCl_3$ intermediate increases as well. Concomitant with this is a change in overall growth kinetics because each process entails both differing composition and temperature-time profiles. Since time varies between processes, we have a couple of choices of how to represent the radial axes. We chose to normalize elapsed time to the overall process time to allow the axes to be compact, but one could plot un-normalized time as long as the distortion this would create in the coordinate system is acceptable. The center of the diagram in Figure 4.3b plots resulting perovskite grain size. This and trends in amounts of competing intermediates are emulated from the two cited works. At the conclusion of this chapter, we will adopt a similar methodology to represent currently observed trends in properties and connections to processing more generally in the $MAPbI_3$ system.

To actually fill the example in Figure 4.3 with quantitative data it would be necessary to analytically characterize percent composition of each intermediate in situ during growth using either spectrometry or

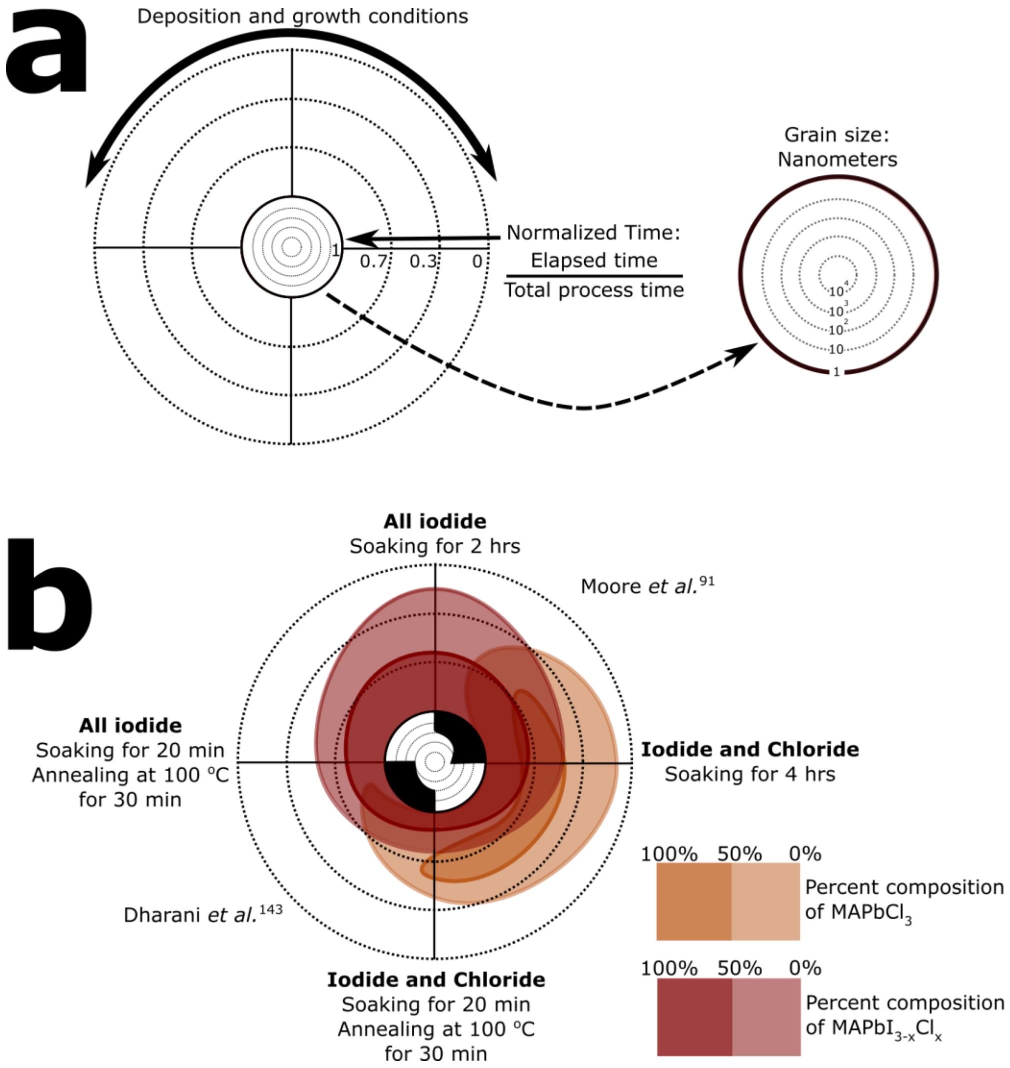

Figure 4.3: Example of a quantitative extension of the PTT curve. (a) shows what each axis entails in more detail, and (b) uses the diagram to plot information corresponding to Moore et al.[91] and Dharani et al.[143]

diffractometry, as well as measure the range of properties of interest in the material resulting from the processes. This is no small task experimentally, and it would only be worthwhile if there are strong correlations between the prevalence of different intermediates, microstructure, and resulting properties. Although making a qualitative in situ measurement analytically quantitative is not trivial, Pistor et al. among others have demonstrated that such in situ monitoring of intermediate growth and transformation is definitely experimentally tractable.[53] While we do want to illustrate the quantitative extension of this methodology, we also believe the attempt to quantitatively render the PTT diagram may give the reader greater insight into the diagram itself.

One could make similar representations in a Cartesian coordinate system rather than a polar coordinate system, but we choose a polar system to make it easy to add in processes of interest, or remove them. One could plot as few as two processes instead of the four in Figure 4.3b, and in principle as many processes can be plotted simultaneously as is useful. The simultaneous changes in growth time, temperature profile, and composition between processes in Figure 4.3b does make its representation a bit awkward, and ideally processes should only be separated by one or two variables. That said, we think these related processes provide a reasonable example of a context in which the quantitative use of the PTT curve might aid in identifying correlations between growth pathway and resulting properties.

4.3 Controlling Transformation Pathway *via* Kinetics

While composition and conditions determine phases accessible during perovskite formation (Scheme 4.1), kinetic controls unique to each system allow navigation of this space once established. The path that the system traverses toward the desired perovskite determines film microstructure and thus properties. In the case of unoptimized 1-step solution deposition, the amorphous $(MA)_{1+x}PbI_{3+x}$ phase discussed by Choi *et al.*[108] and Park *et al.*[90] seems to kinetically dominate initial nucleation resulting in poor crystallinity and long range order. The formation of this phase is greatly enhanced by the presence of excess MAI,[STW-2] and its gradual loss and diffusion leads to slow and long-lasting structural change.[90] Jeon *et al.* demonstrated that this can be circumvented by gradating solvent composition during 1-step deposition. Specifically, they found that when washing a $MAPbI_3$ film with toluene during spin-coating right after perovskite deposition from a γ-butyl lactone (GBL)-DMSO solution, an intermediate forms between DMSO and perovskite precursor species.[101] $MAPbI_3$ gradually nucleates from this phase, producing a much more highly crystalline film. A similar solvent intermediate recently reported by Shen *et al.* in the case of deposition from DMF and DMAc demonstrates that this process may be generally relevant to 1-step solution deposition.[134] This is why the arrow indicating unoptimized 1-step deposition lies at the boundary of the a-$(MA)_{1+x}PbI_{3+x}$ and $MAPbI_3{\cdot}$Solvent regions in **Figure 4.4**. This placement is to suggest that slight changes may encourage one over the other. Jung *et al.* note that tuning the dipole moment of the wash solvent can largely circumvent even this solvent co-crystal, allowing direct perovskite formation and lower annealing temperatures.[144]

Chloride addition opens up another route to circumvent perovskite nucleation from an amorphous phase through creating the kinetically accessible and structurally coherent $PbCl_2$ and $MAPbCl_3$

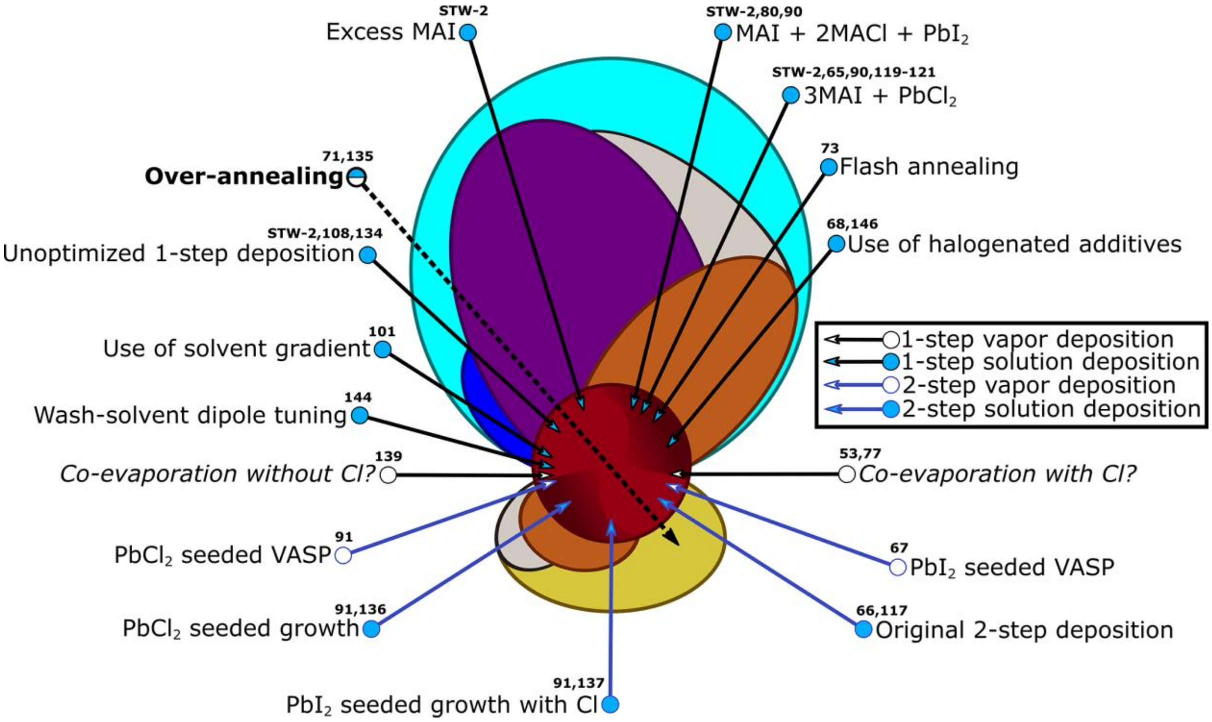

Figure 4.4: Summary of currently prevailing perovskite deposition techniques along with the paths they travel through perovskite phase space. Film growth proceeds from the outside in, and as an arrow passes into a new region, that phase begins to nucleate. Thus, the nucleation of the following phases will be mediated by what has already formed. Because chloride loss is irreversible, all paths will tend toward the dotted line after perovskite formation is complete.

intermediates. We recently showed that kinetically limited complex ion, solvation, and aggregation equilibria in chloride containing solutions control the templating influence of intermediate phases through choice of chloride source (specifically $PbCl_2$ or MACl).STW-2 Stamplecoskie *et al.* demonstrated spectroscopically that solvated complex ions are the primary species from which perovskite films grow even without chloride.[145] These equilibria are impacted by the presence of alkyl halide additives (X–R–X) both in the solution phase and during crystal growth. In effect, their presence slows film development through competition with ionic halogen ligands at growing crystal surfaces.[68,146] Upon deposition, Saliba *et al.* demonstrated that a high-temperature nucleation event in the presence of chloride encourages large-scale orientation (referred to as flash annealing in Figure 4.4).[73] This observation combined with the link between $MAPbCl_3$ and long-range orderSTW-2,[119–121] suggests that kinetic dominance of chloride rich intermediates is temperature dependent. This and other 1-step depositions with chloride are plotted in the upper right of Figure 4.4.

Direct $MAPbI_{3-x}Cl_x$ nucleation may be possible from the vapor phase in the case of co-evaporation both with and without chloride.[77,139] This possibility is plotted along the horizontal axis in Figure 4.4, but as this paper was under preparation Pistor *et al.* found that during 1-step vapor deposition of $MAPbI_{3-x}Cl_x$ two distinct intermediates of the approximate form $MAPbCl_{3-y}I_y$ are observable demonstrating that co-deposition from vapor may be mediated by transformation pathways comparable to what has been discussed.[53] Vapor assisted 2-step depositions (VASP) offer a method to allow MAX exposure of lead seed phases during an annealing process which likely facilitates efficient perovskite nucleation.[67,91] This is plotted below the center line of Figure 4.4. 2-Step depositions based on immersion generally require annealing after exposure to allow diffusion of MAI into remaining PbI_2 and any other intermediates present. These depositions are plotted at the bottom of Figure 4.4, but the presence of the solid MAI phase is omitted for clarity. Because it has been demonstrated that over-annealing in both films grown with[135] and without[71,90] chloride leads to PbI_2 formation the two sides of this phase space are connected through the dotted line plotted in Figure 4.4 indicating over-annealing (**Figure 4.5**).

Through a comprehensive study of 2-step deposition, Moore *et al.* demonstrated that overall transformation kinetics depend on the composition of both seed phase ($PbCl_2$, PbI_2, & $Pb(NO_3)_2$) and intercalant phase (MAI in IPA, MACl in IPA, & MAI vapor).[91] Competing but thermally activated MAX

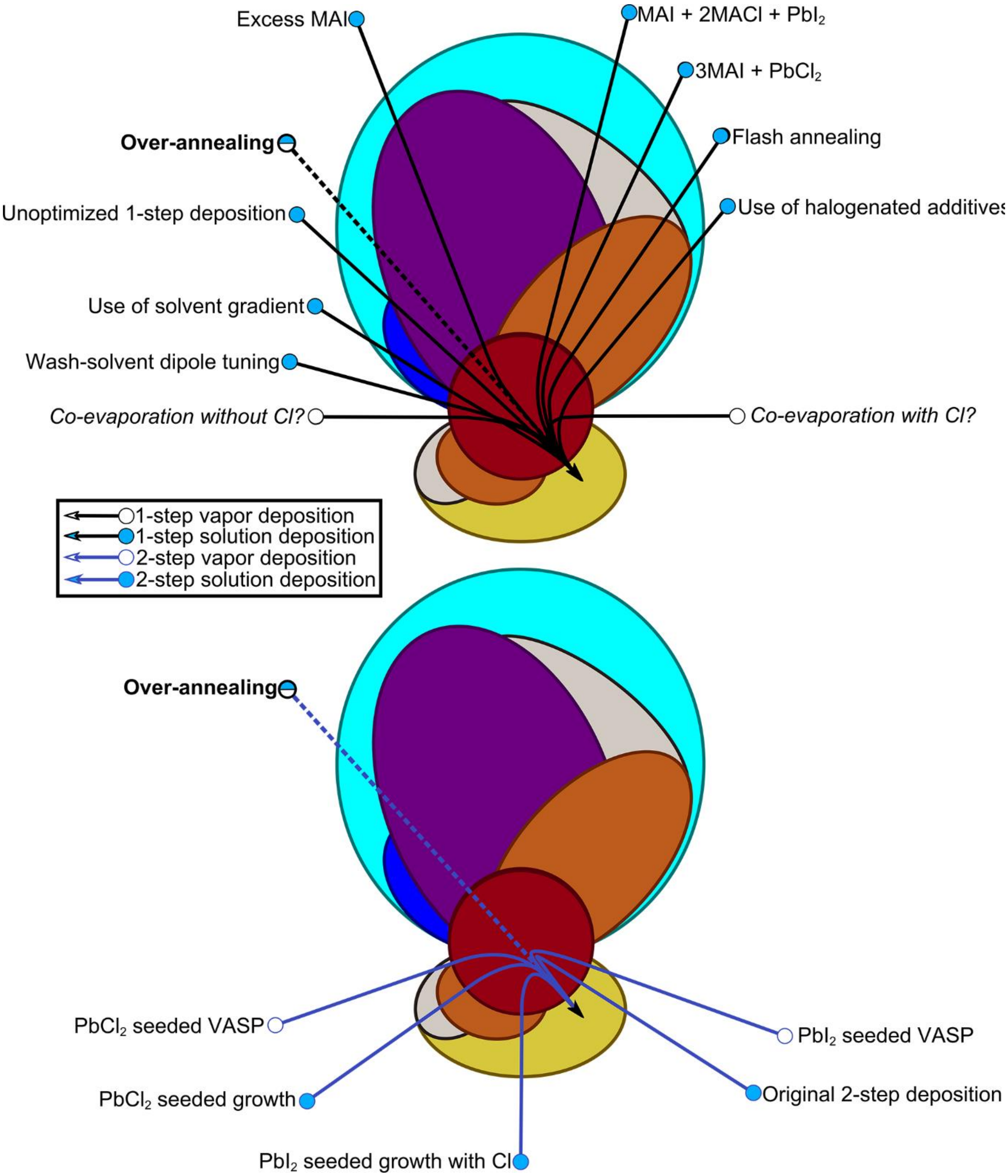

Figure 4.5: Representations of the paths each deposition method will take after perovskite formation has completed. These serve to demonstrate how the two sides of this phase space are connected.

sublimation (Scheme 4.2) is coupled with the various transformations that ultimately produce the desired perovskite phase in both 1- and 2-step depositions.STW-2,[82,91,119] Temperature thus mediates the balance of processes that govern transformation and determines which kinetics are relevant along with the magnitude of rates themselves. Similarly, in 2-step deposition MAX concentration provides additional kinetic control,[147] as does annealing atmosphere.[67,102] Xiao *et al.* demonstrated that mimicking the conditions of solution deposition by annealing a PbI_2 film in the presence of solvent vapor after dipping in an MAI solution produces much larger grains.[102] Atmosphere is an important consideration in general as work is increasingly being done under ambient conditions.[122]

We touched briefly on the interpretation of Figure 4.4 in the discussion of Figure 4.1d, but **Figure 4.6** more completely presents the physical meaning imbedded in this kind of representation. Four 1-step, solution processing routes are plotted in the PTT diagram from Figure 4.1 and Figure 4.4, and a more detailed schematic representation of each transformation pathway is plotted below. Cartoonized electron images of actual films are inset at important stages along each path illustrating both morphology and phase content. Larger magnifications of the final films produced by each pathway are displayed around the PTT diagram. While these cartoons are fabricated from actual data at identical magnifications, the images are simplified during rendering and scale bars are omitted to reinforce the fact that these images are only approximate representations of what is a complex reality. All viable, competing phases are in general always present making the colorization approximate as well. Our goal is not to define exact morphology and feature size in each of the cases in Figure 4.6, it is rather to illustrate the dramatic link between transformation pathway and structure.

Relationships between routes shown in Figure 4.6 are interpretable by using Figure 4.1 to see how individual points are connected. As mentioned earlier, in this conceptual representation, the relative size of regions the arrows pass through essentially indicates that region's dominance in governing film development. If replaced by quantitative percent composition curves, this meaning is preserved by virtue of the logic that if the system consists of a greater fraction of a given intermediate, that intermediate will have an increased influence on structural evolution. Unoptimized 1-step deposition proceeds largely through an amorphous intermediate (solvent co-crystal intermediate omitted for clarity) but produces a reasonable amount of crystalline perovskite after annealing (Figure 4.6a). As more MAI is included, the amorphous phase plays an increasingly significant role kinetically, eventually to the extent of preventing any significant perovskite nucleation during even 2 h of annealing at 90 °C (Figure 4.6b). [STW-2] Gradating solvent polarity with a 1:1 MAX:Pb ratio during deposition kinetically excludes the amorphous phase but locks in a different intermediate in its place (Figure 4.6c). Substituting chloride for iodide with a 3:1 MAX:Pb ratio creates intermediates that kinetically compete with the amorphous phase, as well as provides a thermodynamically more expedient route for the system to reach the appropriate stoichiometry for

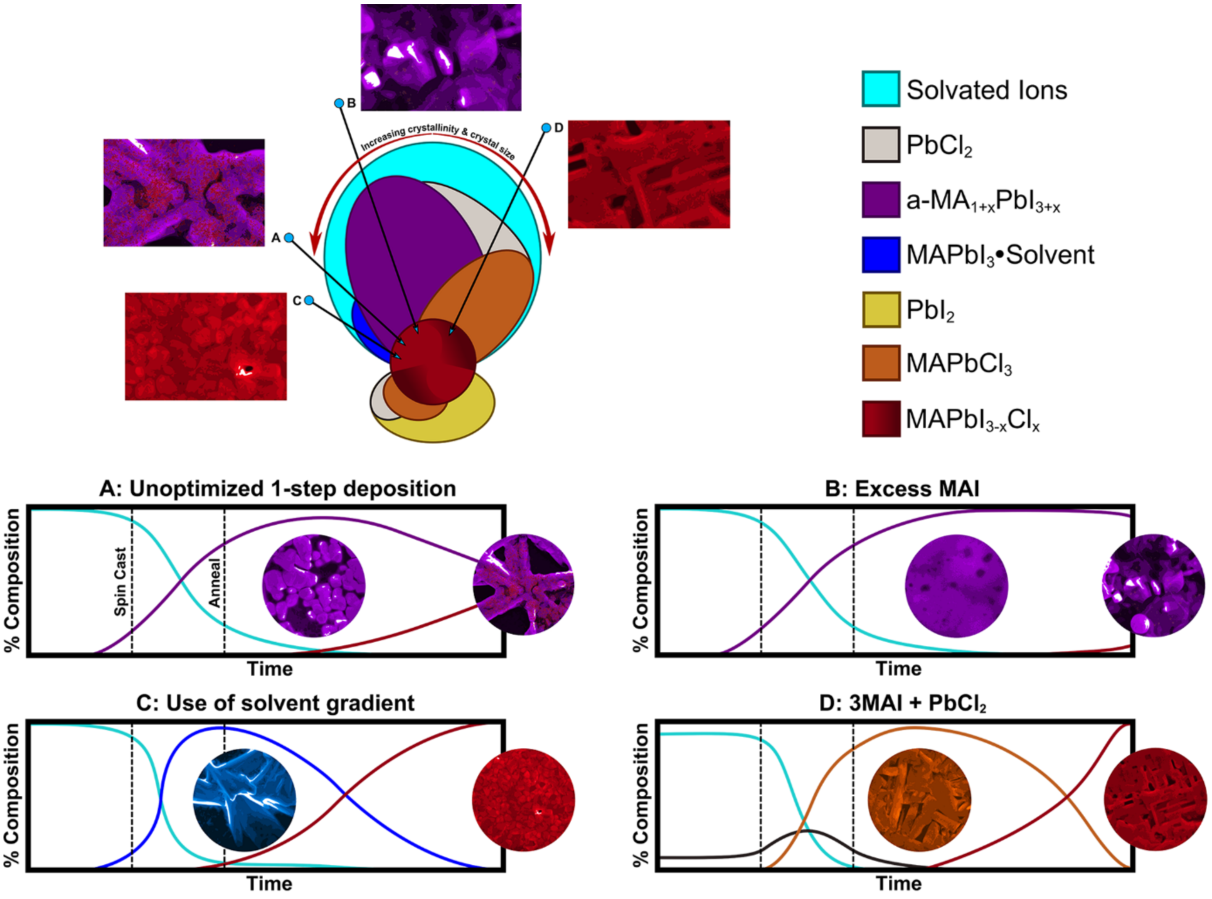

Figure 4.6: Detailed representation of select 1-step solution deposition routes. Transformation during (a) unoptimized 1-step deposition, (b) deposition with excess MAI, (c) deposition with a solvent gradient, and (d) deposition with chloride provided by a $PbCl_2$ salt are schematically represented in terms of % composition of each phase as a function of time. Relationships are exaggerated to more clearly represent differences between processes, but competing phases are likely always present even if only at small concentrations, which includes PbI_2 and $MAPbI_3$·Solvent intermediates. The insets in the graphs are cartoonized SEM images color coded to show phase content representative of the growth stage indicated by the placement of the inset. The images surrounding the PTT diagram are larger magnification views of the final product, showing the striking differences between the perovskite film microstructure obtained *via* these different but related processes.

$MAPbI_{3-x}Cl_x$ through MACl sublimation (Figure 4.6d). This produces a crystallinity similar to the case of solvent gradation, but different microstructure, crystal size, and crystal orientation. While this diagram can be reformatted in a variety of ways to accommodate quantitative or qualitative information, conditions altering transformation rate that are not represented (atmosphere during growth,[67,102,122] and growth substrate[74,148–151]) can compress or expand regions associated with different phases, changing the extent to which they contribute to the overall process.

4.3.1 *Importance of morphological control*

It has been proposed theoretically[128] and empirically[152] that ferroelectricity plays a role in the unique transport behavior of $MAPbI_{3-x}Cl_x$.[125,127,128,153] Inherent anisotropy then likely links lattice orientation and ferroelectric structure[154] meaning crystal orientation[130,131] and crystal size[132,133] may be key in design. Currently, links between photophysical properties and crystallographic characteristics are still developing in this dynamic field, but recent work has begun to correlate transformation pathways, composition, microstructure, and resulting properties. Just as the central $MAPbI_{3-x}Cl_x$ region shows variations in equilibrium chloride content in Figure 4.1, 4.4, and 4.6, the enlarged central regions in the PTT curves of **Figure 4.7** schematically map developing understanding of trends in equilibrium $MAPbI_{3-x}Cl_x$ film properties.

As $MAPbI_{3-x}Cl_x$ growth conditions change, many aspects of its final structure and defect composition change with it. While the PTT curve is a convenient context for the summary of perovskite transformation, its real value is succinctly correlating structure, composition, and properties to the transformation pathways that generate them. The width (**θ**) of each region defined at the center of PTT curves in **Figure 4.7** is determined by the growth conditions the information correlates to. To determine the process correlated with a given point in a property curve (i.e. grain size) draw a line radially out from the center of the white circle and through a given point of interest. The thickness (**r**) of the central property curves correlates to the magnitude of the property being represented. We illustrate these trends to facilitate discussion of growing consensus and disagreement in the field rather than to define precise relationships.

Plotted in Figure 4.7a is grain size, which is the same trend illustrated in Figure 4.6. In addition to trends already discussed in the context of Figure 4.6, the increase in crystal size upon flash annealing a film obtained by spin-coating a solution of 3MAI + $PbCl_2$[73] and the progression to smaller crystal size reported by Dharani *et al.* upon gradually replacing PbI_2 with $PbCl_2$ in 2-step growth[143] appear in Figure 4.7a. Oga *et al.* found a correlation between $MAPbI_3$ grain size and carrier mobility[155] which is extrapolated in Figure 4.7b. Growth conditions used to observe this correlation were limited, and variation of growth substrate

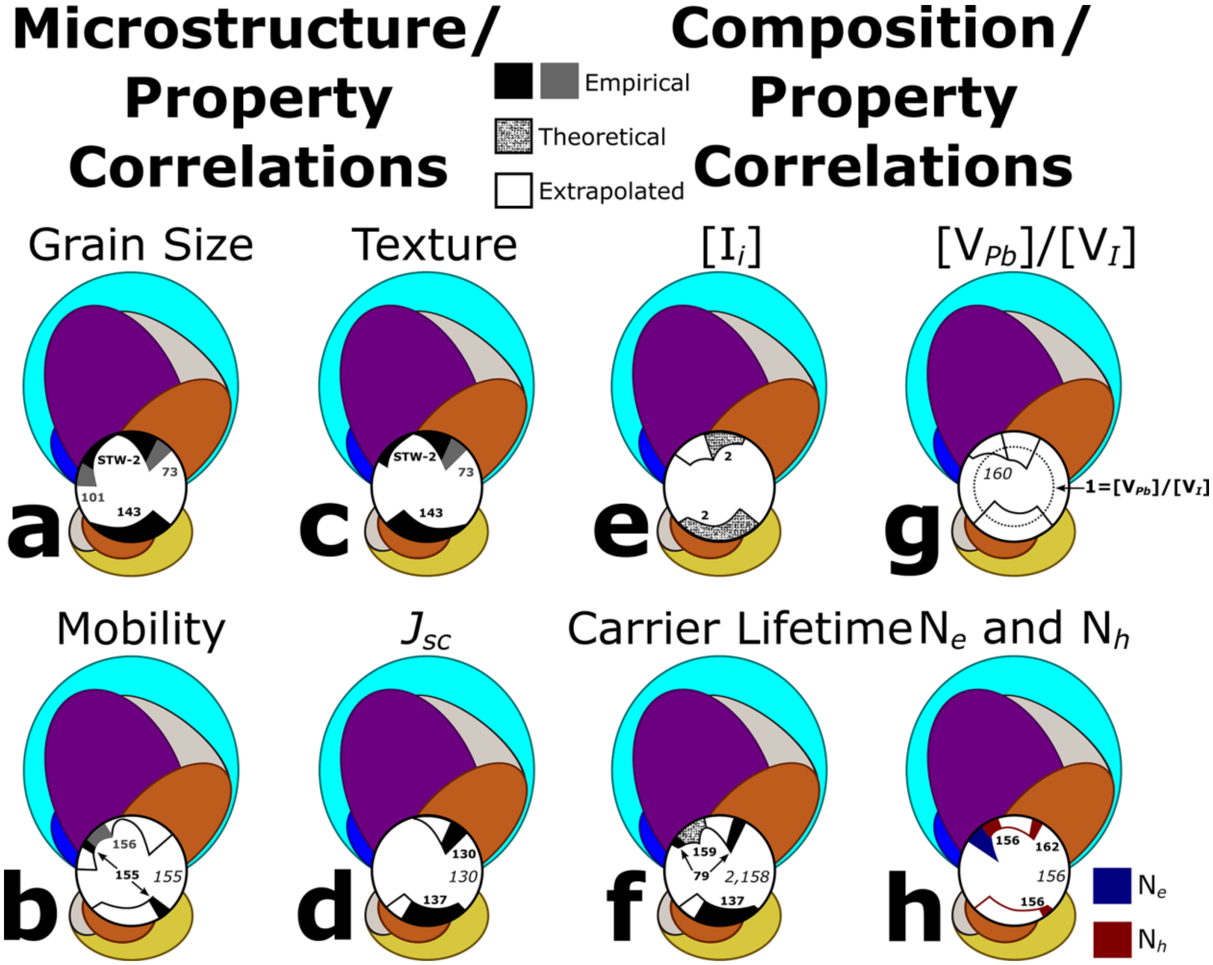

Figure 4.7: PTT diagrams schematically plotting variations in structure, composition, and properties as a function of processing route. Each curve in the top row correlates with the curve directly below (a/b; c/d; e/f; g/h). The legend in the center shows how each trend correlates to current literature and next to each region is a reference relevant to the discussion in the main text. Solid black and grey colors represent empirical data, with the only reason for variation being visual clarity. Checkered regions represent modeled data. Empty regions are trends largely extrapolated from current literature. The primary reference being used to extrapolate trends in a given PTT curve is italicized and placed to the side of each central region. The correlated trends being represented are: grain size and carrier mobility (a and b); film texture and short circuit current (c and d); concentration of iodide interstitials and carrier lifetime (e and f); and lead/iodide vacancy ratio and majority carrier concentration (g and h).

played a key role so it is unsurprising that this monotonic extrapolation is violated when populations of defects become non-negligible. Wang *et al.* demonstrated that Hall mobility increases with increasing MAI excess during 1-step deposition,[156] despite the possible reduction in grain size. Wehrenfennig *et al.* find no change in mobility between films grown from solutions of MAI + PbI_2 and 3MAI + PbI_2,[157] which also suggests that the relationship between crystal size and mobility may be more convoluted in $MAPbI_3$ than is typical.

Trends in crystalline texture (orientation) are plotted in Figure 4.7c. In addition to the correlation between increasing chloride content and overall texture along [110], [100] and [001] directions[STW-2,[65,71,105]] are the influence of flash annealing[73] and the slight tendency toward texture along the [111] direction in the absence of chloride.[STW-2] Dharani *et al.* reported an increase in overall orientation upon gradually replacing PbI_2 with $PbCl_2$ in 2-step growth[143] which is also included in Figure 4.7c. Both this and the decrease in grain size Dharani *et al.* reported in the same study contradicts the findings of Moore *et al.*,[91] but, while composition was comparable, the two studies used very different growth times and thermal conditions. While we consider this issue in the example we provide of quantitatively extending of the PTT curve (Figure 4.3), it is more interesting to consider the correlation Docampo *et al.* draws between crystal orientation and resulting device short circuit current (J_{sc})[130] which is extrapolated monotonically in Figure 4.7d. This result is loosely echoed in the case of two step deposition by Docampo *et al.*,[137] but there is clearly a diminishing return in J_{sc} with increasing chloride making the exact reason behind its increase difficult to pinpoint.

While still difficult to measure faithfully, microstructural properties are easier to directly probe than defect chemistry so a great deal of modeling has been done to predict how composition relates to defects in $MAPbI_{3-x}Cl_x$. Interstitial defects, specifically iodide interstitials (I_i), have been linked to deep trap states and thus a reduction in the lifetime of photogenerated carriers.[2,158] Through modeling Du *et al.* note that chloride increases I_i formation energy thus reducing its concentration ($[I_i]$),[2] a finding plotted in Figure 4.7e. We also extrapolate from Le Chatelier's principle that excess MAI increases $[I_i]$ to at least some extent. Comparing $[I_i]$ to carrier lifetime (Figure 4.7f), the inverse correlation Duan *et al.* predicts[158] is largely apparent by virtue of the findings of Stranks *et al.*[79] (1-step deposition) and Docampo *et al.*[137] (2-step deposition). That said, theoretical lifetimes plotted in the upper left quadrant contradict a monotonically inverse relationship between [I_i] and carrier lifetime. Agiorgousis *et al.* theoretically predict that between iodide rich and iodide poor conditions there is a maximum in carrier lifetime because of a minimization of iodide vacancies (V_I) and iodide ions in MA^+ sites (I_{MA}).[159] We have placed the maximum predicted by these results near the solution stoichiometry Wang *et al.* suggests leads to stoichiometric $MAPbI_3$ (2MAI + PbI_2).[160] Along the same lines, but not in Figure 4.7f, Bai *et al.* showed empirically that with heating after initial annealing at increasing temperatures carrier lifetime decreases.[161] By virtue of the tendency of $MAPbI_{3-x}Cl_x$ to PbI_2,[135] increased post annealing temperatures should lead to lower [I_i] demonstrating that a wider variety of properties are relevant in determining overall carrier lifetime than [I_i] alone.

Defects associated with deep trap states are the primary concern in preserving long carrier lifetimes, but shallow defects are most relevant in controlling carrier concentration. Wang *et al.* implicate lead and iodide vacancies (V_{Pb} & V_I) as primarily responsible for changes in carrier concentration.[156] Near the condition they identify as leading to stoichiometric $MAPbI_3$,[160] conduction changes from n (lead rich) to p (iodide rich) type. The correlation between N and the relative concentration of V_{Pb} and V_I ([V_{Pb}]/[V_I]) Wang *et al.* implicate is extrapolated in the upper left of Figure 4.7g, with the dotted line representing [V_{Pb}] = [V_I]. They take the case of 2-step deposition to be the system exposed to the greatest excess of MAI. We have also extrapolated from Le Chatelier's principle that upon chloride addition V_I generation may be suppressed through competition with Cl_I while [V_{Pb}] may remain largely unchanged because growth still occurs under methylammonium halide rich conditions. Thus chloride might lead to a slight increase in [V_{Pb}]/[V_I]. Majority carrier concentration (N_h or N_e) is plotted in Figure 4.7h. In addition to the findings of Wang *et al.* just discussed[156] is the hole concentration in $MAPbI_{3-x}Cl_x$ measured by Guerro *et al.*[162] Although comparable to $MAPbI_3$ grown with excess MAI, this N_h is notably higher than what Wang *et al.* found in 2-step grown $MAPbI_3$, suggesting chloride may still encourage a certain amount of p-doping.

4.4 Conclusion

Navigating intermediates *via* kinetic control has defined the development of modern materials like steels, solders, and ceramics. As Chapters 2 and 3 experimentally show, this issue is key in organo-lead halide perovskites, and accounting for it allows one to approach the literature regarding perovskite processing systematically. Although our understanding of the connections between intermediate structure, final microstructure, and photophysical properties is limited, insight into the roles these issues play in hybrid perovskite design is developing rapidly. While most of the trends discussed have remained robust in the developing literature, there are two notable issues which must be mentioned.

Firstly, with regard to perovskite growth *via* the solvent washing procedure, we replicated the original argument made by those who introduced this technique in Figure 4.6c, but this representation is not correct. As we show experimentally in Chapter 6, the solvent-perovskite co-crystalline phase is actually the source of the problematic morphology that the original authors of the solvent washing method were trying to avoid. While these authors originally thought that this intermediate state was tied to the success of the method, it is rather tied to the process that makes the method necessary in the first place. Although it may seem like a trivial point of clarification at the moment, Chapter 6 shows that growth through this solvent-perovskite co-crystal is the mechanistic origin of the problematic morphology that both Chapters 2 and 3 worked to circumvent. In Chapter 6, we circumvent this morphology by forcing direct perovskite nucleation, demonstrating conclusively that the problematic, rod-like morphology is tied to solvent-perovskite co-crystal growth rather than $CH_3NH_3PbI_3$ growth itself.

In addition this expanded understanding of the role of solvent-perovskite co-crystalline states, the field has also developed a deeper understanding of the complex phase space created by introducing methylammonium iodide to PbI_2. Throughout this chapter, we have referred to an amorphous state that plays a significant role in perovskite growth and final structure, but this is a somewhat imprecise way to view the issue. As recent work has shown,[163] there are a large number of intermediate states that exist with differing amounts of methylammonium, iodide, and solvent molecules. This means that many intermediate states will frustrate structural evolution of $CH_3NH_3PbI_3$ during growth unless conditions are carefully controlled. Thus, the amorphous state discussed in this conceptual review should be thought of as a consequence of both partial solvation caused by excess methylammonium (Chapters 2 and 3) and structural frustration caused by uncontrolled transformation through a multitude of intermediate states.

Chapter 5. RATIONALLY SELECTING ELEMENTAL CANDIDATES TO EXPLORE Pb-SITE MODIFICATION IN $CH_3NH_3PbI_3$

Chapter 1 discussed the limitations inherent to hybrid organic-inorganic perovskites (AMX_3) and their application in photovoltaics. The fundamental challenges of reducing material toxicity, eliminating J-V hysteresis, and increasing stability are connected to the processing-structure-property relationships unique to this relatively new class of material. This ties composition, growth, and morphology together in complex ways that are still being explored. Chapters 2 and 3 presented experimental accounts of the manipulation of the X^- and A^+ sites, respectively; and Chapter 4 presented a broader conceptual account of processing-structure-property relationships and their dependence on composition.

This chapter presents a brief overview of the periodic table to contextualize an exploration of elements to modify the Pb-site in $CH_3NH_3PbI_3$. From eight classes of potential metals that are identified, three are selected to experimentally survey. To efficiently survey these potential perovskite alloys, this survey is directed toward the specific question of whether the elements of interest thermodynamically tend to precipitate into secondary phases during growth or readily become integrated into the hybrid perovskite lattice. A simple technique to characterize this thermodynamic tendency is developed to facilitate this survey, and it is implemented to identify a single set of potential elements that are then explored more deeply in Chapter 6.

The conceptual overview of the periodic table (Section 5.1) and the rationale behind the growth technique developed (Section 5.2) have been composed for this dissertation. The experimental survey in Section 5.3 partially contains results originally published in an article entitled *Realizing a new class of hybrid organic-inorganic multifunctional perovskite* (Section 5.3.3, STW-5). Notes have been added in Section 5.3 to indicate the source of the presented material.

5.1 Navigating the Complexity of Pb-Site Modification

The challenge associated with understanding the fate of a new element added to a material system is substantial because of the difficulty inherent in identifying if the new element resides within the material or only at the boundaries. The flexible lattice of $CH_3NH_3PbI_3$ and its peculiar behaviour under a variety of conditions makes the challenge of understanding the eventual fate of new species even more daunting than it would otherwise be. To expand understanding about how this lattice responds to foreign species, we select a model set of elements to explore.

5.1.1 *Design parameters to guide modification of the metal site in* $CH_3NH_3PbI_3$

Elemental properties that determine how an element will impact the perovskite lattice include, but are not limited to:

- Preferred oxidation state
- Ionic size
- Electronegativity
- Valence structure
- Prevalence of relativistic effects (spin-orbit coupling)
- Preferred coordination geometry
- Nature of bonding (cohesive forces the element is capable of supporting)

The first four criteria are easily considered, but the last three are difficult to define except in extreme cases.

Preferred Oxidation State

To occupy the Pb site in $CH_3NH_3PbI_3$ without generating a charged defect, the 2+ oxidation state must be the preferred oxidation state for the new metal ion. That being said, hybrid perovskites possess a very dynamic internal defect equilibrium of iodide and methylammonium vacancies that largely determine functional properties like and carrier concentration and ionic mobility.[43] Additionally, direct substitution of the Pb site is only one of a multitude of possible mechanisms for incorporating a new metal, most of which do not present a clear best choice in terms of oxidation state. Thus, elements that prefer an ionic charge of 2+ are good candidates for integration, but we should approach the issue of charge as a design parameter to be understood rather than a ridged design rule. If multiple oxidation states are possible, the nature of the metal's ligands will play a role in determining which state is preferred. Even elements that possess an oxidation state of 2+ may not remain in that state upon integration into $CH_3NH_3PbI_3$.

Ionic Size

Ionic size is determined by charge, elemental size, surrounding ligands, and coordination geometry. It is difficult to precisely predict the size of a given ion upon incorporation into perovskite. Ionic radii of species in the same coordination geometry and oxidation state should be compared if possible.

Electronegativity

The Pb-I bond has a significant covalent component despite its ionicity. The use of most other metals will increase the polarity of the metal halide bond. Instead of thinking about how to exactly replicate the polarity of the Pb-I bond, it is better to be mindful of how much polarity we are introducing through a new species. It is useful to view ionic size and electronegativity together as chemical hardness. Pb and I are soft elements because of their large size and low electronegativity. Species further up in the periodic table quickly become much harder.

Valence Structure

The charge of the Pb^{2+} ion is important in making Pb based hybrid perovskites possible, but this is partly due to the fact that this charge results in a filled valence s-orbital on Pb and empty p-orbitals available for bonding. Directly emulating this in a new element is near impossible because the property that stabilizes the pair of s-electrons on Pb stable is spin-orbit coupling. This property is a consequence of the fact that because of the size of Pb, electrons around it move at relativistic speeds which alters the energies of their states. Because valence structure at this level of detail is not readily emulated, it is important to remain mindful of which vacant valence orbitals the metal ion will use for bonding to its surrounding environment.

Prevalence of Relativistic Effects

The inert pair effect mentioned above exists in similar heavy metals like Hg and Bi. Although most elements display enough spin-orbit coupling to characterize with techniques like X-ray photoelectron spectroscopy, these relativistic effects do not become a significant part of the element's behavior until approximately the last two rows of the periodic table.

Preferred Coordination Geometry

To substitute Pb directly, candidate metal ions must support an octahedral coordination geometry with iodide. Preferred coordination geometry is a manifestation of the relationship between a metal ion and its ligands rather than a ridged property of a metal ion. Although qualitative, accounts of comparable systems in the literature allows an impression of preferred coordination geometry.

Nature of Bonding

$CH_3NH_3PbI_3$ is ionic in the sense that it is composed of ions, but it behaves very differently than conventional ionic crystals like sodium chloride. While sodium chloride is itself a metal halide, it is in almost every way different from lead iodide, another simple metal halide. If one looks more broadly at metal halides, it becomes clear that there are three basic groupings of materials based on their behavior: ionic metal halides, molecular metal halides, and polymeric metal halides. The differences between these systems lie most strongly in the nature of the stable subunit from which the lattice is constructed.

In the case of ionic metal halides like sodium chloride, bonding is almost exclusively electrostatic which allows polar water molecules to completely disrupt the lattice, reducing the system to non-interacting, isolated, and discrete ions (Na^+ and Cl^-). Molecular metal halides operate very differently, with titanium tetrachloride being a molecular gas at room temperature ($TiCl_4$). Polymeric metal halides lie between these extremes to an extent. Bonding is far more complex than the simple electrostatic cohesion in NaCl, but bonding conditions are not so rigid that only one molecular species can exist as in the case of $TiCl_4$. Lead iodide (PbI_2) is a perfect example of a polymeric metal halide. Water does not readily solvate PbI_2, but upon the addition of I^- solvation proceeds aggressively. Without addition of this extra iodide, the Pb ions in the PbI_2 lattice cannot easily pull away from their halide ligands. Adding excess iodide allows the gradual liberation of $PbI_x^{(2-x)}$ complex ions, species that serve as dynamically changing stable subunits. This was identified experimentally in Chapter 2, and further discussed in Chapter 4.

5.1.2 *Potential classes of metals*

Our selection of elements to attempt to alloy perovskite is motivated by the goal to most efficiently expand understanding of how the hybrid perovskite lattice operates. This material centric focus makes eventual exploration of photovoltaic properties more effective. To this end, we have broken the periodic table up into groups of elements with regard to the criteria discussed in Section 5.1.1 (**Figure 5.1**).

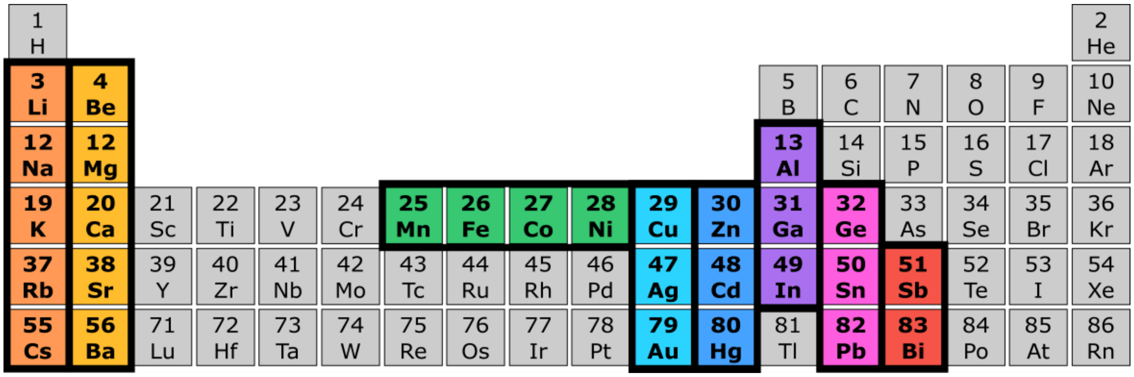

Figure 5.1: Eight classes of potential alloying elements for $CH_3NH_3PbI_3$.

Strongly Ionic Metals (s-block elements)

Although iconicity varies throughout the periodic table and is a property of a bond rather than an isolated element, the first and second column in general contain the metals with the most strongly ionic bonding.

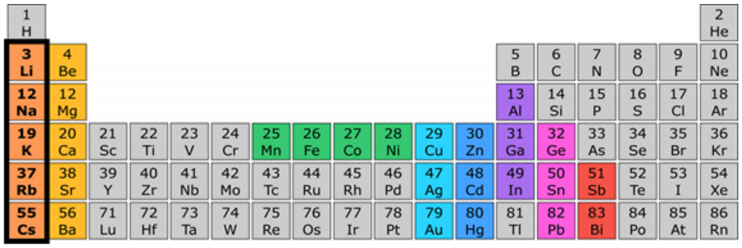

Figure 5.2: Alkali metals.

Alkali Metals: While potentially interesting, the monovalent alkali metals in general share too much in common with the monovalent organic cation that exists in $CH_3NH_3PbI_3$ to be expected to directly modify the metal halide framework. Cesium is well known to serve the same purpose as methylammonium in $CsPbI_3$. Preferred coordination geometry for these species in their metal halide forms, like NaCl, is often octahedral, but as mentioned earlier, NaCl and related materials are ionic metal halides, and thus do not possess the appropriate bonding to readily modify the metal halide framework. Valence structure is very different from Pb^{2+} because of the empty valence s-orbital.

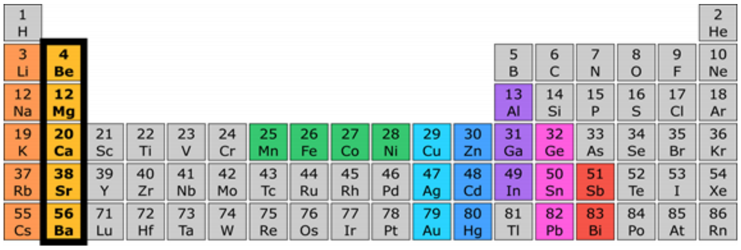

Figure 5.3: Alkaline earth metals.

Alkaline Earth Metals: Compared to the alkali metals, this divalent class of element has more potential to modify the metal halide framework in $CH_3NH_3PbI_3$. Still, the dominant ionic nature of their bonding puts these elements at a similar disadvantage as alkali metals. The range of size possible in this series may enable some species to prefer substitution of the metal site, but similarities with Cs^+ may drive these elements to prefer substitution on the organic cation site.

Transition Metals (d-block elements)

Making useful classifications among the transition metals is more challenging than in the other areas of the periodic table because vertical and horizontal trends are much less simple, especially in the heavier transition metals. Thus, we isolate ourselves to the upper right portion of the transition metal block.

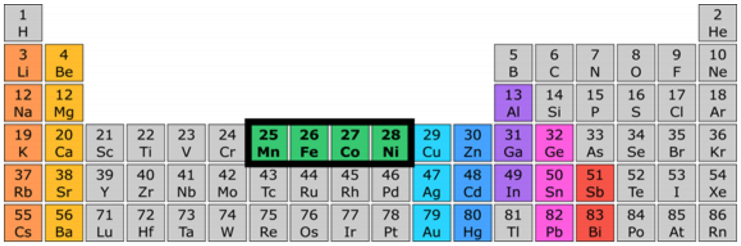

Figure 5.4: First row transition metals.

First Row Transition Metals: The elements Mn through Ni are all first row transition metals that can adopt a 2+ oxidation state. Although other oxidation states are accessible, intrinsic reduction-oxidation chemistry with iodide tends to force these elements into their lowest non-zero oxidation state (2+). Although these elements form metal halides with partially molecular character, these materials also tend to exhibit solvation behavior similar to PbI_2 in certain solvents[164] as well as tending to form 2D hybrid perovskites with halogens smaller than iodide.[165] This tendency toward 2D perovskite formation indicates a preference for octahedral coordination by halogens. While preferred oxidation state, bonding type, and coordination geometry are close to ideal, these elements are much smaller than Pb. On top of this, frontier electronic structure is very different from Pb^{2+}. While these elements do have a filled 4s orbital and empty 4p orbitals, the unfilled 3d orbitals may create a significant perturbation to local electronic structure in $CH_3NH_3PbI_3$. The consistencies between ionic size, electronegativity, and bonding in the series of elements from Mn to Ni makes them ideal for probing the effect of changing electronic structure on the surrounding perovskite without complications from differences in basic elemental properties like ionic size. This series of elements provides a case study of how subtle differences in the electronic structure affect perovskite functionality.

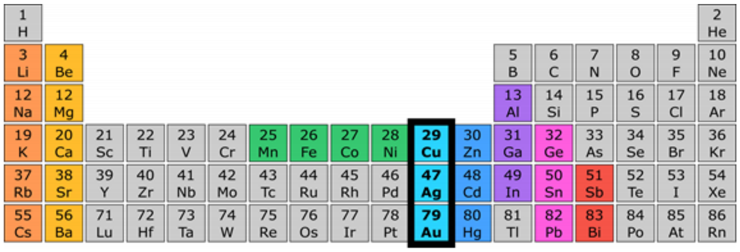

Figure 5.5: Noble transition metals.

Noble Transition Metals: This category of elements contains Cu, Ag, and Au. Cu is the only element in this series that can adopt a 2+ oxidation state but it also has a stable 1+ oxidation state. This proves to be troublesome as in the presence of iodide, Cu^{2+} transforms to Cu^{+} and rapidly forms CuI. For both Cu and Ag, pure metal halide formation (i.e. CuI and AgI) is an aggressive process that can be difficult to prevent in both solution and solid states. Au is in general more inert, but also does not possess a stable 2+ oxidation state. Cu has been observed to form bromide based 2D hybrid perovskites in the early literature[166] which does make it potentially valuable to study.

Heavy Metals and Metalloids (p-block elements)

The p-block elements bear the greatest similarity to Pb^{2+} in electronic structure. Many species in this region have filled s- and d-orbitals as well as empty p-orbitals, but many don't have a 2+ charge.

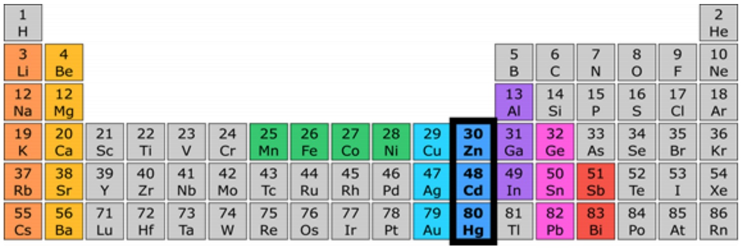

Figure 5.6: Zn group metals.

Zn Group Metals: Although all these elements possess 2+ oxidation states, they also exhibit a somewhat stronger preference for tetrahedral coordination by halides than the nearby transition metals. Although Cd and Hg are problematic due to their toxicity, trends in this series of elements may prove useful to explore due to the wide range of size.

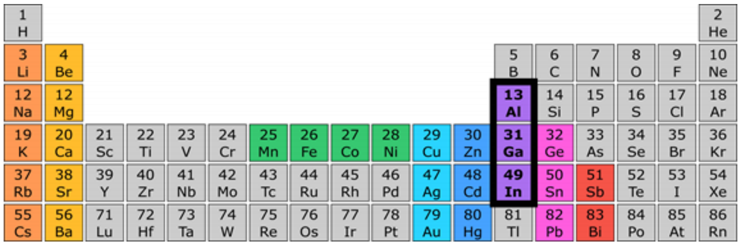

Figure 5.7: Boron group metals.

Boron Group Metals: The lighter members of this column only have 3+ oxidation states which entail both empty s- and p-orbitals, but In does possess a 1+ state which has a very similar electronic configuration to Pb^{2+}. Electronegativity and size make B and Al different from Pb^{2+}, but bonding inherent to In allows it to form a wide variety metal halides. Coordination geometry for B and Al is ridged, but the coordination of indium is flexible. Octahedral coordination with halogens is possible, but not exclusively.

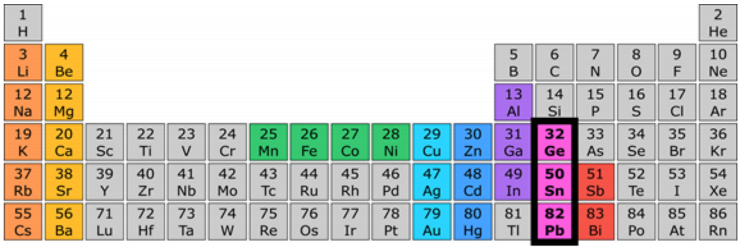

Figure 5.8: Carbon group metals.

Carbon Group Metals: This is the family of elements that contains Pb, and thus nearby elements like Sn and Ge are in theory excellent candidates for integration into the lead halide framework of $CH_3NH_3PbI_3$. In Pb, the 2+ oxidation state is stabilized by the relativistic effects caused by its size. In Sn this effect is significantly diminished, and the 2+ state is very fragile. For Ge, this 2+ state is even more fragile. Sn is the only metal cation that is well understood in the hybrid perovskite material system as there is a well-studied class of materials based on tin halide frameworks (i.e. $CH_3NH_3SnI_3$). Sn^{2+} directly replaces Pb in $CH_3NH_3PbI_3$, and the challenge associated with its use is preventing its oxidation by atmospheric oxygen.

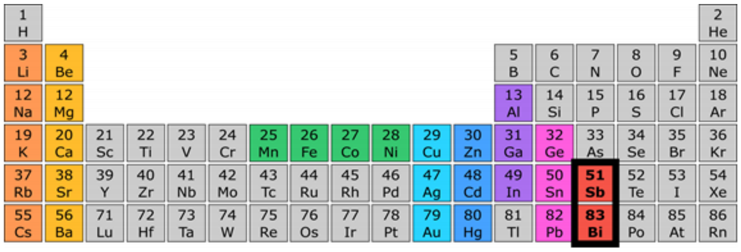

Figure 5.9: Heavy pnictogens.

Heavy Pnictogens: This family contains the element in the periodic table that has the greatest electronic similarity to Pb other than Sn: Bi. Bi is large enough to possess the same inert pair of s-electrons that makes the 2+ oxidation state of Pb stable, but this leads to Bi^{3+} rather than a 2+ oxidation state. The preferred coordination geometry with halogens for both Bi and Sb is approximately octahedral.[167]

Rare Earth Metals (f-block elements)

The challenge with selecting useful rare earth metal candidates is similar to the difficulty in selecting useful heavy transition metal candidates. Fundamental properties like electronic structure, bonding, coordination geometry, and chemical reactivity vary more dramatically both vertically and horizontally. As with the deeper transition metals, the exploration of these species should be motivated by a more complete model of how foreign metal species impact the hybrid perovskite lattice.

5.1.3 *Selecting model sets of elements for experimental exploration*

The vast majority of possible elements for integration into the lead halide framework of $CH_3NH_3PbI_3$ are smaller and less electronegative than Pb. Similarly, alterations in atomic electronic structure are inevitable because of how unique the electronic structure of Pb^{2+} is compared to most other elements in the periodic table. Because of the dominance of intrinsic defect equilibria in determining the functional properties of $CH_3NH_3PbI_3$, species with ionic charges other than 2+ should not automatically be excluded from consideration by virtue of their possible utility in electrostatically controlling equilibria between competing charged defects. Based on the classes of elements discussed in Section 5.1.2, we identified **first row transition metals** (Mn, Fe, Co, & Ni), **Zn group metals** (Zn, Cd, & Hg), and **heavy p-block metals** (Sb, Bi, & In) as classes of elements well suited to facilitate a broad survey (**Figure 5.10**).

Neglected Classes of Elements

We neglect **s-block elements** because of their strongly ionic bonding and possible preference for the organic cation site in $CH_3NH_3PbI_3$. We neglect the **noble transition metals** because of the intrinsic redox processes that pushes these species to the 1+ oxidation state and encourages precipitation. We neglect **carbon group metals** because Sn is the only element in the periodic table for which the ability to modify $CH_3NH_3PbI_3$ is already well investigated. Sn is also the only candidate in this family with a meaningful chance of stably modifying the metal halide framework in $CH_3NH_3PbI_3$. We neglect the **lighter members of the boron group** because of practical considerations related to their reactivity in candidate solvent systems used for processing. Both **f-block elements** and heavy transition metals are neglected because the convoluted trends in these areas of the periodic table require a more complete model to explore.

Selected Classes of Elements

The three selected classes of elements were chosen in part because of the relationships between them.

Heavy p-block metals are compelling for two key reasons. (1) They bear the greatest similarity to Pb in size, electronic structure, bonding, and relevance of relativistic effects. (2) The difference in valence (3+ rather than 2+) is an important issue to investigate because other than Sn, most elements capable of supporting electronic structure comparable to Pb^{2+} do not have the same charge. The heavy pnictogens, Bi^{3+} and Sb^{3+}, are trivalent ions with analogous electronic structure to Pb^{2+}. Between them, size, electronegativity, and hardness vary. In^{3+} has similar size to Sb and similar charge to both Bi and Sb but has an empty valence s-orbital while Sb and Bi have a full valence s-orbital.

Zn group metals, while largely not useful for technologically relevant perovskites due to toxicity, allow a number of key relationships to be probed because of their varied electronegativities and sizes. Hg^{2+} represents a metal that bears a great deal of similarity to Pb^{2+} in all things except electronic structure and preferred coordination geometry.

First row transition metals allow a great number of relationships to be mapped, and they are one of the most ideal candidates for direct Pb replacement. This is because of their tendency toward molecular/polymeric bonding rather than ionic bonding, preferred 2+ oxidation states in the presence of iodide, and tendency toward octahedral coordination by halogens. While the sizes and electronegativities of this set of elements are internally very consistent, they are collectively very different from Pb. This series of elements allows us to probe how important size and electronegativity are in determining how new species are incorporated into $CH_3NH_3PbI_3$. Internally, this set of elements contains a very important trend to understand in perovskite alloy design: gradually varying electronic structure. Because size, electronegativity, oxidation state, coordination geometry, and bonding are consistent throughout the series, we can study the influence of slight changes in the electronic structure of foreign metal species.

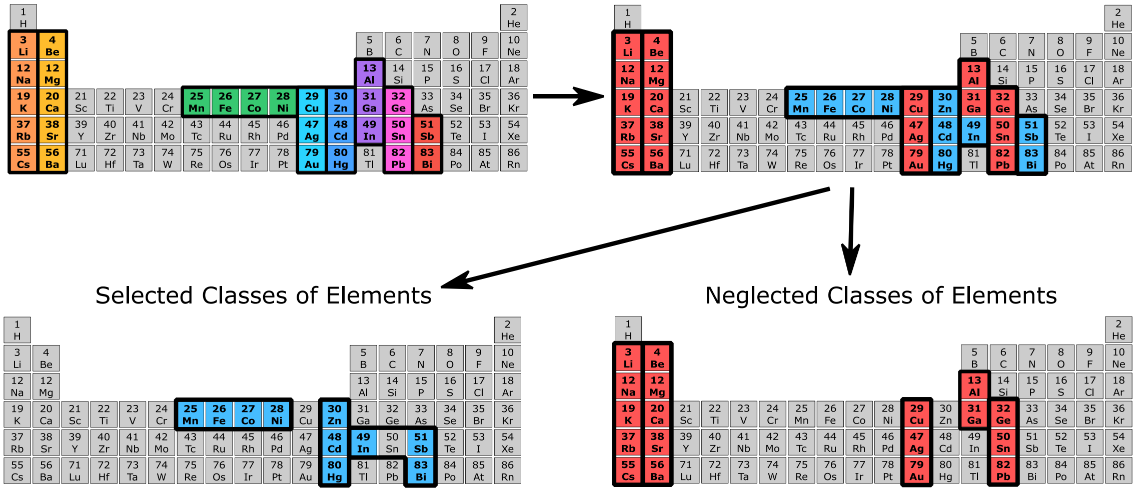
Selected Classes of Elements

Neglected Classes of Elements

Figure 5.10: Selected and neglected classes of elements.

5.2 Designing an Approach to Analyze the Thermodynamic Tendencies of Potential Hybrid Perovskite Alloys

As in many complex systems, trends demonstrated internally within a set of meaningfully related systems are often more useful than the information that can be interpreted from outright quantification of properties in a single system. Understanding the impact of these new metal species on the hybrid perovskite material inevitably requires addressing their impact on growth. Because of the complexities inherent to this material system and the lack of current understanding surrounding how the lattice responds to foreign metal species, approaching this question requires a new approach to material characterization tailored to hybrid perovskites. It is useful to build processing conditions around the nature of the information that is necessary.

To understand how $CH_3NH_3PbI_3$ responds to these foreign metal species, the most basic and important information is identifying a thermodynamic tendency toward either the formation of a solid solution or phase separation. If these systems are forced to their thermodynamic end through the processing route used, then observations of phase separation and morphological evolution become directly representative of the intrinsic chemistry underlying the material's growth.

Identifying a Universal Solvent System

Understanding of how solvent molecules mediate perovskite growth is still growing, but it is clear that the process is one of the most significant factors in growth. All the elements being considered form metal halide salts with greater iconicity than PbI_2, but the solvation and precipitation of PbI_2 and these progressively more polar metal halides must be coordinated by a single solvent system to maintain consistency throughout the study. In perovskite precursor solutions, a range of complex ions ($PbI_x^{(2-x)}$) dominate so it would be ideal for solvated foreign metal species to emulate this molecular subunit. With even fairly polar salts like FeI_2 and CoI_2, polar a-protic solvents tend to encourage solvation of molecular metal halide subunits rather than the isolated ions encouraged by polar protic solvents like water.

To compare these potential perovskite alloys on equal footing, we chose the very polar solvent dimethyl sulfoxide (DMSO) as a universal solvent system for perovskite alloy growth. For simplicity, we used pure DMSO. Although solvent engineering is a key part of tuning hybrid perovskite growth from solution, that level of complexity may convolute trends important to this study.

Encouraging Thermodynamically Limited Growth

To ensure a system reaches its thermodynamic limit during growth, growth must be adiabatic. This means that it must be slow enough so that at every moment the system is essentially at equilibrium. Since we are growing the material from solution, this means that the processes of crystal formation, diffusion in solution, and solvent evaporation must at all times be allowed to reestablish equilibrium. The typically employed spin coating procedure cannot be used for perovskite growth in this survey because it forces crystal formation to far out-pace solvent removal and diffusion.

A drop casting procedure, which is simply the heated drying of a drop of solution on a clean substrate, easily allows all three processes just discussed to maintain equilibrium throughout growth. In a typical spin coated perovskite film crystal formation begins during spin-coating and, provided no ligands compete with iodide other than solvent molecules, growth takes only ~15 minutes complete at 90 °C. Comparatively, a ~5 µL drop of 0.2 molar perovskite solution takes ~2 hours to complete solvent removal and crystal formation at 90 °C. In this case, no crystal formation occurs until the slow solvent evaporation induces gradual precipitation. Drop casting allows thermodynamically limited growth to dominate, and the dilute concentrations required for this process make it ideal for exploring these potential perovskite alloys.

A final but vital consideration is whether or not to employ ligands other than iodide to facilitate perovskite growth. Spectator ions like chloride (Chapter 2) and acetate have commonly been used to ligate metal ions during growth to tune kinetics. The problem with the use of these species in this study, and in the growth of perovskite alloys generally, is that the kinetic control they offer very quickly becomes a liability. The phase that forms first during growth is a seed phase containing the spectator ion which then transforms to the desired perovskite through gradual volatilization of the spectator ion. This process is in reality a number of coupled and often competing processes with their own kinetics. Competing ligands like Cl and acetate also complicate the natural complex ion equilibria that direct perovskite growth (Chapter 2). To prioritize the identification of thermodynamic tendencies underlying how these foreign species interact with $CH_3NH_3PbI_3$, we employ pure metal iodide salts rather than salts that introduce spectator ions.

Prioritizing Identification of Phase Separation

Using XRD combined with scanning electron microscopy (SEM) and energy dispersive spectroscopy (EDS) to characterize the thick films produced *via* drop-casting creates an ideal setting to reliably identify phase separation. The thermodynamically limited growth conditions used make these drop cast films directly representative of the thermodynamic tendencies of each material system. Of course, high quality thin films must be made to analyze functional properties like absorption and electronic transport (Chapter 6), but this more demanding synthetic challenge can be streamlined by the fundamental material understanding generated through this larger survey.

In the next section, XRD and elemental maps are presented for each system. The compositions examined for each element were 0% (pure Pb perovskite reference), 5%, 10%, and 25% foreign species.

Percentage is defined as atom % of foreign metal compared to total metal present in the precursor solution.

5.3 Experimental Survey of Potential Elements

**Data in Section 5.3.3 has been reproduced from STW-5 and is further analyzed in Chapter 6.*

The material and results presented in Section 5.3.3 were originally published in STW-5, but the material in Sections 5.3.1 and 5.3.2 has been composed for this dissertation. Methods are discussed in detail at the conclusion of the chapter.

5.3.1 *Heavy p-block metals*

In the case of these trivalent species, the use of pure iodide salts causes an excess of iodide, but complications from spectator ions make this excess preferable compared to the alternative in this survey. Phase separation is clearly apparent in these systems *via* XRD and SEM-EDS elemental mapping (**Figure 5.11** and **5.12**). Phases other than $CH_3NH_3PbI_3$ are marked with symbols indicated in the legend of Figure 5.11 (top). Perovskite peaks are indexed by hand because of the complexity of the diffraction data. One of the utilities of using a drop cast film for analysis is that there are many (>15) clearly analyzable peaks for $CH_3NH_3PbI_3$, but another key utility of this method is the significantly increased signal that minor components of the system contribute.

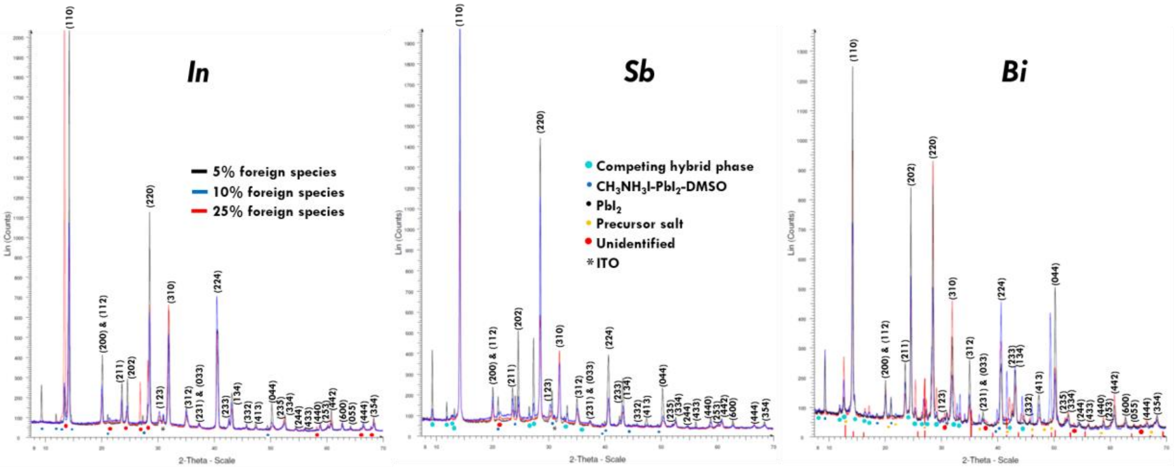

Figure 5.11: XRD of heavy p-block metals showing universal phase separation.

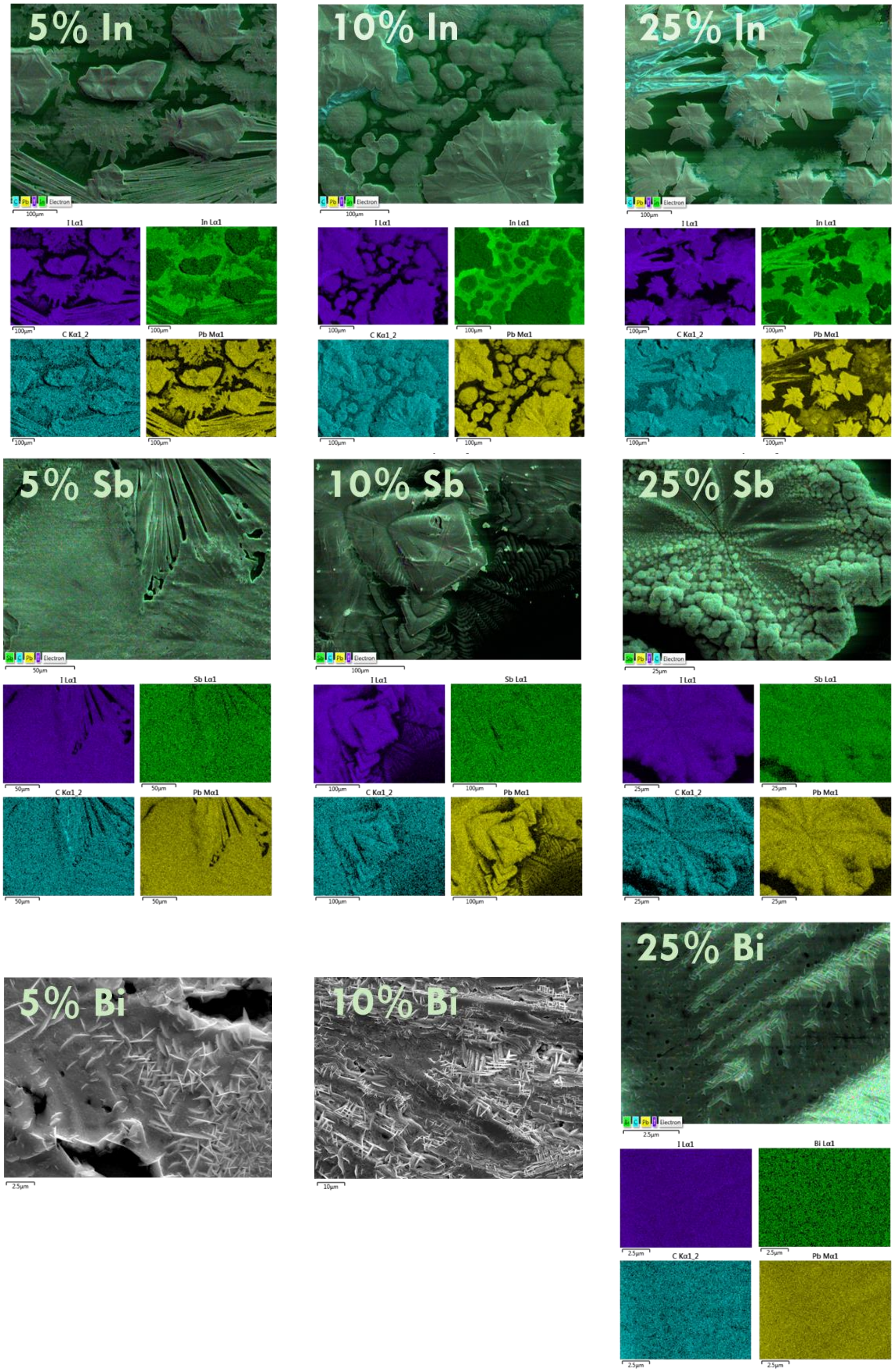

Figure 5.12: SEM-EDS elemental mapping of heavy p-block metals showing universal phase separation.

In the case of SbI_3 and BiI_3, the vast majority of the impurity peaks arise from a unique hybrid phase[167] rather than the pure metal halide salts (SbI_3 and BiI_3). In the case of InI_3, phase separation is coming from the aggressive formation of a solvent-perovskite co-crystal.[168] This phase separation makes these elements non-ideal for integration into $CH_3NH_3PbI_3$. Limited EDS mapping was done with Bi because convolution in the EDS spectrum rendered this mapping ineffective at low Bi concentrations.

5.3.2 *Zn group metals*

This entire family of elements exhibits aggressive phase separation at even low concentrations of foreign metal species (**Figure 5.13** and **5.14**). Among these elements, Zn is the least compatible with $CH_3NH_3PbI_3$, but this incompatibility is lessened with the larger elements in the series (Cd and Hg). In all three cases, aggressive phase separation makes these elements non-ideal for integration into $CH_3NH_3PbI_3$. Limited EDS mapping was conducted with Hg based systems because convolution of signals in the EDS spectrum rendered mapping ineffective at low Hg concentrations. In both this class of element and in the case of the p-block elements surveyed, close structural analysis of the XRD data presented is of limited value because of changes in composition created by phase separation. Thus, structural data from these systems serve only to identify phase separation.

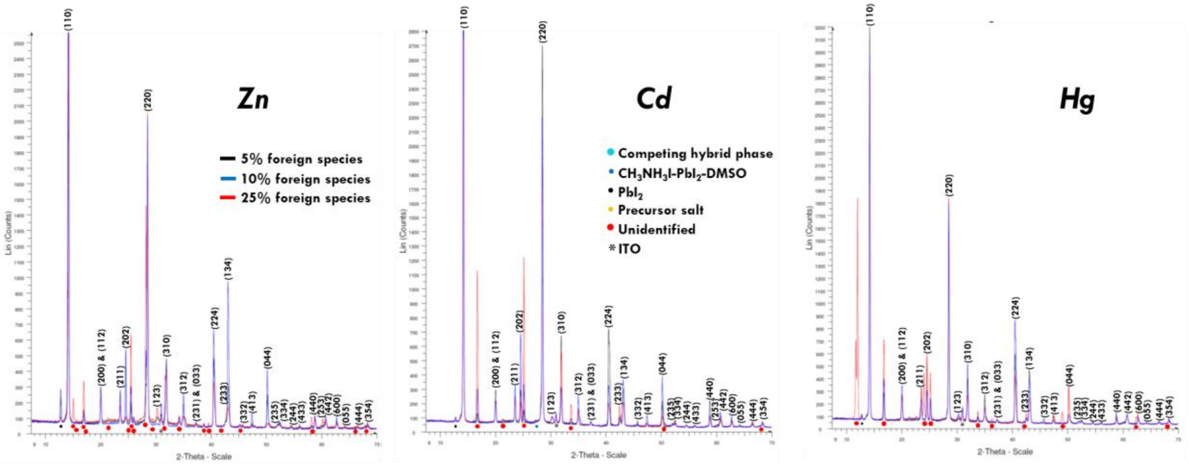

Figure 5.13: XRD of Zn group metals showing phase universal phase separation.

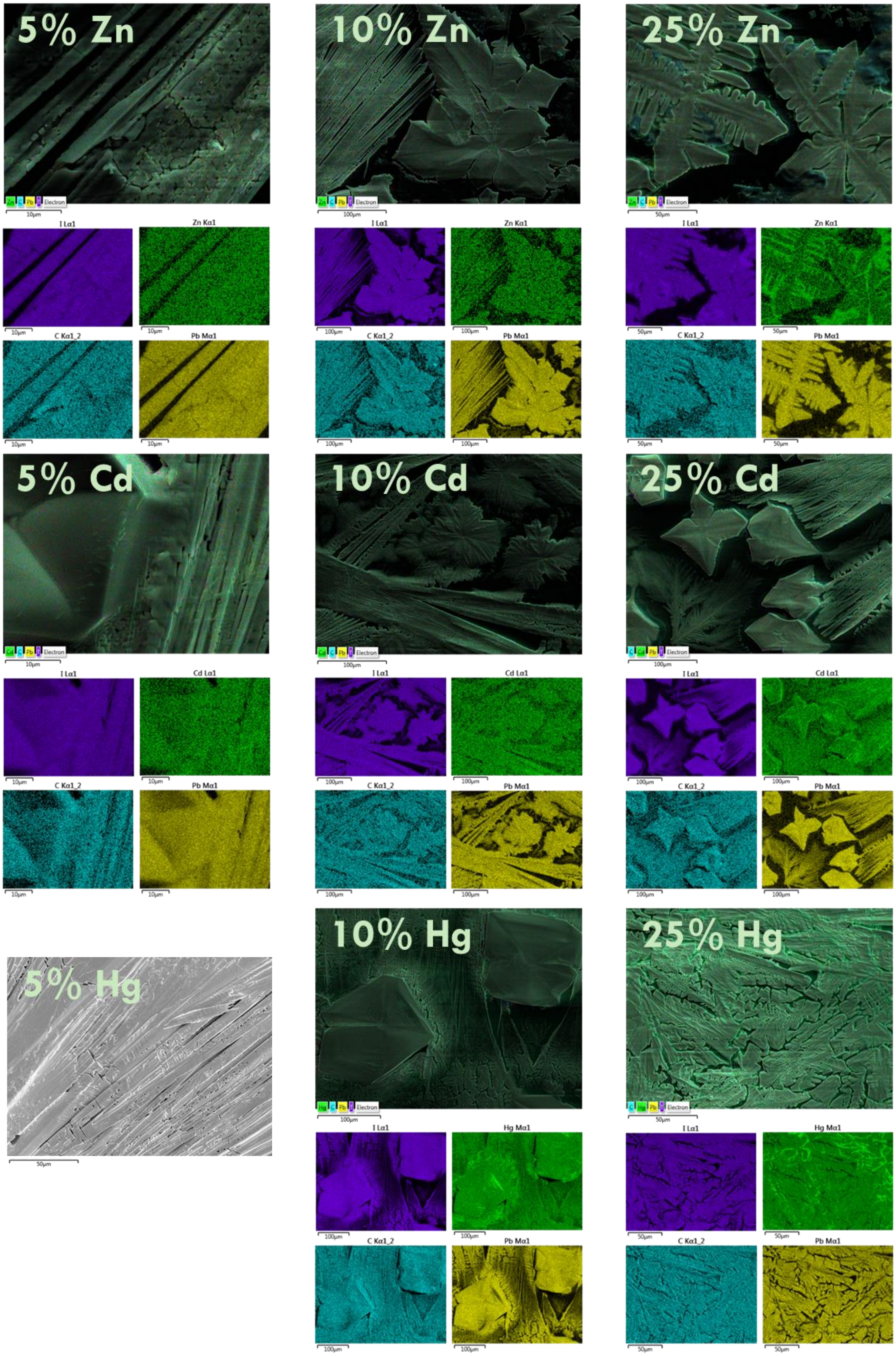

Figure 5.14: SEM-EDS elemental mapping of Zn group metals showing phase universal phase separation.

5.3.3 *First row transition metals*

**Data in this section has been reproduced from STW-5 and is further analyzed in Chapter 6. (Reproduced from Ref. STW-5 with permission from the Royal Society of Chemistry.)*

In sharp contrast to both the p-block and transition metals explored above, these species exhibit no detectable phase separation until a slight degree of precipitation at 25 at% foreign metal (**Figure 5.15** and **5.16**). Alone, this suggests that these species are reasonably compatible with the $CH_3NH_3PbI_3$ lattice, but in light of the results in Figures 5.11, 5.12, 5.13, and 5.14, this lack of phase separation sharply distinguishes this class of perovskite alloy from the other systems surveyed. The high compatibility that Mn, Fe, Co, and Ni display makes this class of element ideal for studying the impact of metal cation manipulation on the growth, structure, and properties of $CH_3NH_3PbI_3$. This is the focus of Chapter 6.

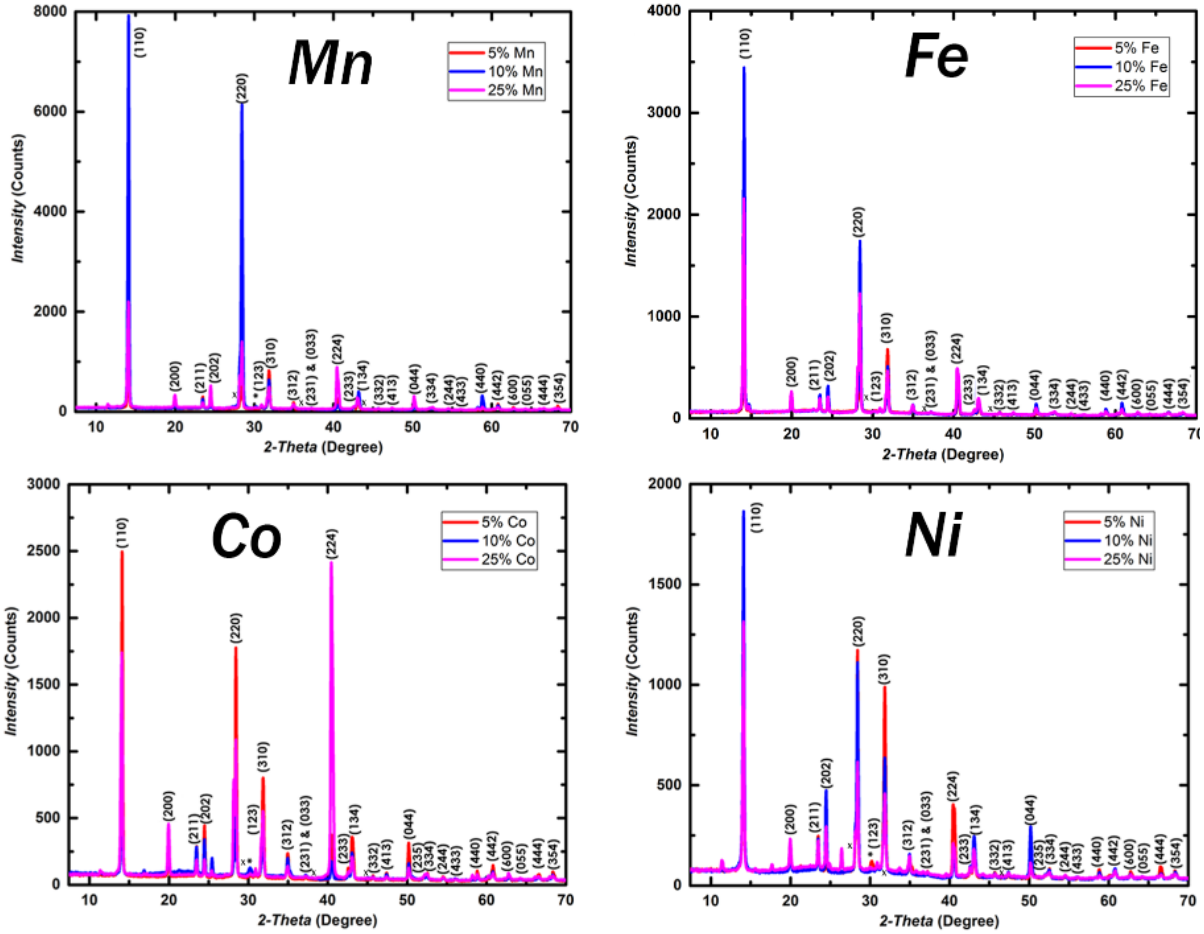

Figure 5.15: XRD showing phase purity of drop cast films of first row transition metal inclusion in $CH_3NH_3PbI_3$. Positions of the three strongest peaks of the pure transition metal halide salts (i.e. MnI_2, FeI_2, CoI_2, and NiI_2) are indicated with an **x** to show the lack of phase separation. Peaks from ITO are marked with an asterisk (*****).

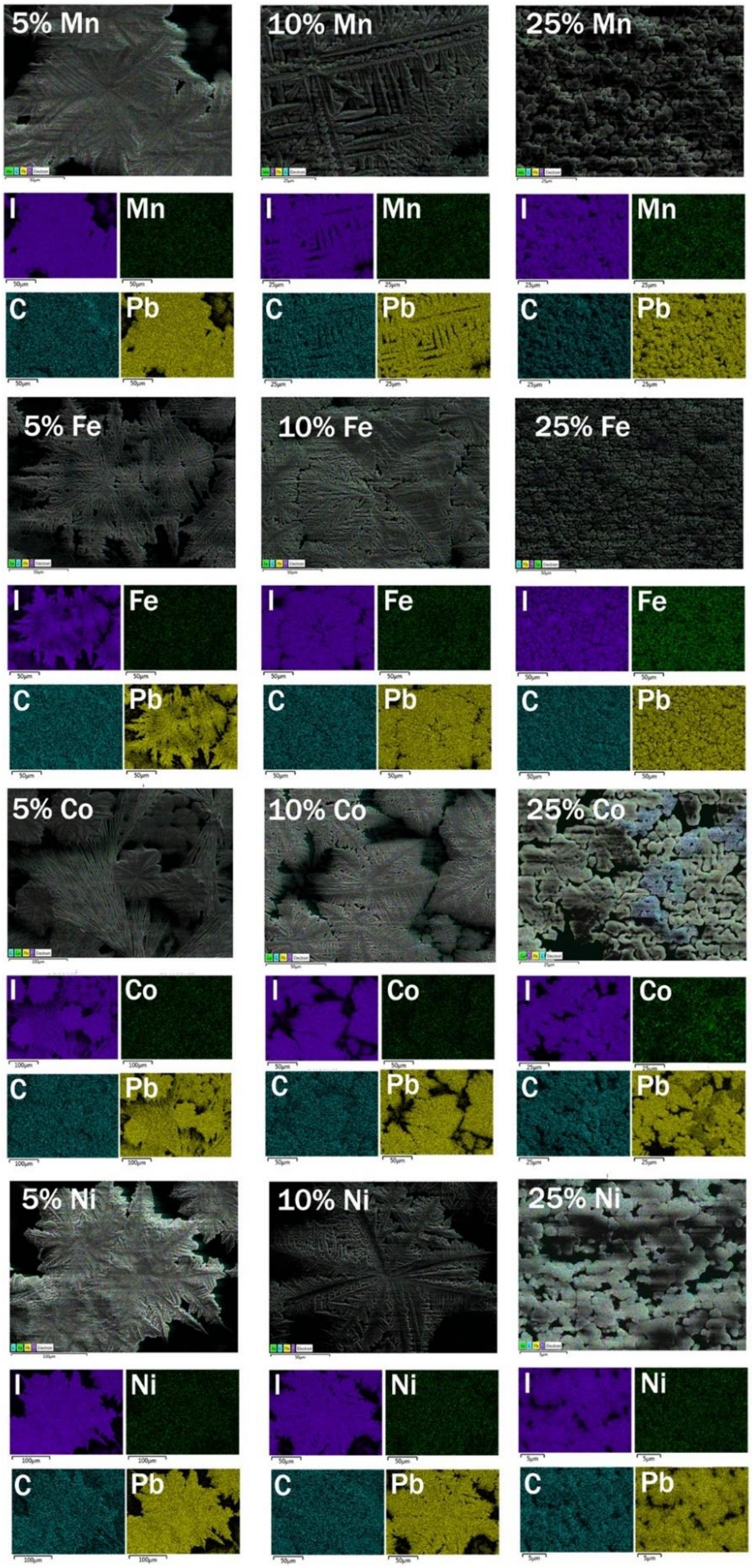

Figure 5.16: Elemental mapping *via* SEM EDS of $CH_3NH_3PbI_3$ grown with increasing amounts of first row transition metals (expressed in at%) showing high degree of solid solubility.

5.4 Conclusion

This brief survey of the periodic table is intended to provide the reader with enough context to broaden the insight that will be generated in Chapter 6 to the larger challenge of Pb replacement. As Chapter 6 will show, this issue is far more challenging than simply identifying elements with a 2+ charge and an appropriate size. Chapter 6 mounts a focused study of the impact of transition metal inclusion on $CH_3NH_3PbI_3$ growth, morphology, and functionality. There are a finite number of possible choices for Pb replacement in the periodic table (summarized in Chapter 7), and thus, with the conceptual and experimental context provided in this chapter, even a focused study like that offered in Chapter 6 enables broader perspective on the challenge of Pb replacement.

5.5 Experimental Details

**Reproduced from STW-5.*

Materials. All precursors and solvents were purchased from Sigma-Aldrich and used without further purification. Methylammonium iodide (CH_3NH_3I) was synthesized as discussed in Chapters 2 & 3.

Drop cast film fabrication: ~5 μL of 0.2 M perovskite solution in DMSO was deposited on ITO substrates at 90 °C in a glovebox. This was annealed for 2 hours at this temperature with a 10 minute nitrogen purge at the conclusion of annealing to ensure solvent removal. 7 films were prepared at a time.

Solution Preparation. All perovskite precursor materials were stored and weighed in a nitrogen filled glove box. Molarity of perovskite precursor solutions was defined as the total molarity of metal ions in solution, percent foreign metal was defined as atom percent foreign metal relative to total metal ions (foreign metal/ (foreign metal + Pb)). A 1 : 1 ratio was used for total metal : methylammonium in solution. After weighing out the appropriate amount of starting material, DMSO was added and the solution and was stirred at 60 °C for 1 h. Solutions were then aged for a minimum of two days before filtration and use.

Microscopy, and X-ray diffraction. An FEI Sirion scanning electron microscope was used for SEM characterization with 5 kV for imaging and 20 kV for EDS. A Bruker D8 Discover 2-D XRD with a Cu Kα source was used for all X-ray diffraction measurements. All XRD peaks were indexed by hand.

Chapter 6. DECONVOLUTING THE COMPOSITIONAL AND MORPHOLOGICAL IMPACT OF FOREIGN METALS ON $CH_3NH_3PbI_3$: Case Study of Transition Metal Inclusion

**This entire chapter has been adapted from STW-5, with portions reproduced verbatim. (Reproduced from Ref. STW-5 with permission from the Royal Society of Chemistry.)*

The material presented in this chapter was originally published in an article titled *Realizing a new class of hybrid organic-inorganic multifunctional perovskite* (STW-5). This work was co-first authored by Adharsh Rajagopal and myself. The device expertise and deep intuition for electronic processes in perovskite solar cells that Rajagopal brought to the study was seamlessly integrated into the expertise in material design and intuition for perovskite growth developed throughout this dissertation. Rajagopal and I worked hand-in-hand conceptually and experimentally to understand growth processes at play and their impact on material performance. This intimate experimental interplay prohibits simple division between the contributions of Rajagopal and myself, but this work plays very different roles in our overall contributions to the field.

6.1 Introduction

Developing strategies to modify the hybrid perovskite lattice has become a dominant theme in the perovskite field because of the need to modify material properties like ion diffusivity,[43] carrier concentration,[169] band gap,[10,11] and thermodynamic stability.[33] This effort has been directed at different sites in the perovskite lattice with varying degrees of success.[4,10,12,16,17,65,119,170–172] Initial attempts to realize $CH_3NH_3PbI_{3-x}Br_x$[10] and $CH_3NH_3PbI_{3-x}Cl_x$[65] solid solutions gave way to realizations of photoinstability in $CH_3NH_3PbI_{3-x}Br_x$[12] and large scale loss of Cl in $CH_3NH_3PbI_{3-x}Cl_x$.[65,119] Exploration of $CH_3NH_3SnI_3$[16] has led to identification of anomalous band-gap behaviour in $CH_3NH_3Pb_{1-x}Sn_xI_3$[107] and the utility of Sn in addressing intrinsic material issues like the photoinstability of $CH_3NH_3PbI_{3-x}Br_x$.[170] The organic cation has received significant attention as well, with work on materials employing variants of $CH_3NH_3^+$ like formamidinium,[4] Cs,[171] and Rb[172] giving way to realization of new routes to increase material stability.[173–175] Efforts in compositional modification are already reaching into more exotic areas of the periodic table.[176–180]

Despite the aggressive effort that has led to the rapid growth of this area of research, challenges in understanding relationships between material growth, morphology, and resulting properties have complicated progress. In the early progression of research directed toward compositional engineering, this issue manifested in the initial attempts to understand how Cl modifies $CH_3NH_3PbI_3$ (Chapter 2). Initially it was thought that a substitutional alloy was readily realized with significant amounts of Cl,[65] but over time it became clear that instead of remaining in the perovskite film, the vast majority of Cl leaves the system.[119] Rather than a simple change in composition, this revealed that the impact of Cl on perovskite was partially due to a dramatic impact on morphology caused by a modification of growth route.[STW-2]

As has been shown experimentally in Chapters 2 and 3 as well as conceptually in Chapter 4, hybrid perovskite morphology is controlled by a great many synthetic parameters, making it a challenge to identify how growth route specifically impacts resulting structre. When it comes to understanding how a new element modifies a material, especially one as complex as $CH_3NH_3PbI_3$, understanding material growth is paramount. It has been shown in many ways that morphology of pure hybrid perovskite is a strong determinant of resulting properties. Adding another level of complexity like the use of Cl, or various other less well studied species, creates the possibility for new kinds of chemical processes,[STW-2,][119] phase separation events,[12] complex secondary phases,[177] and compositional gradients,[181] making morphology and growth even more important considerations for the compositional engineering of hybrid perovskites.

As was touched on in Chapters 2 and 5, the coordination structure inherent to the metal cation plays a very important role in the growth and function of $CH_3NH_3PbI_3$. Chapter 5 explored three classes of potential elements to modify the metal site in $CH_3NH_3PbI_3$, and in Section 5.3.3 we identified that a set of closely related transition metals (Mn, Fe, Co, and Ni) do not exhibit the aggressive phase separation exhibited by the other systems studied (Zn, Cd, Hg, In, Sb, and Bi). Our analysis also indicated that these four species have strong but strikingly similar impacts on material growth. To fully understand the impact of these elements on $CH_3NH_3PbI_3$, it is necessary to first identify what primary controlling variables shape material growth and morphological evolution.

6.2 Elucidating Primary Variables Controlling Growth and Morphology

In Section 5.3.3 we presented XRD and SEM-EDS characterization of drop-cast films of transition

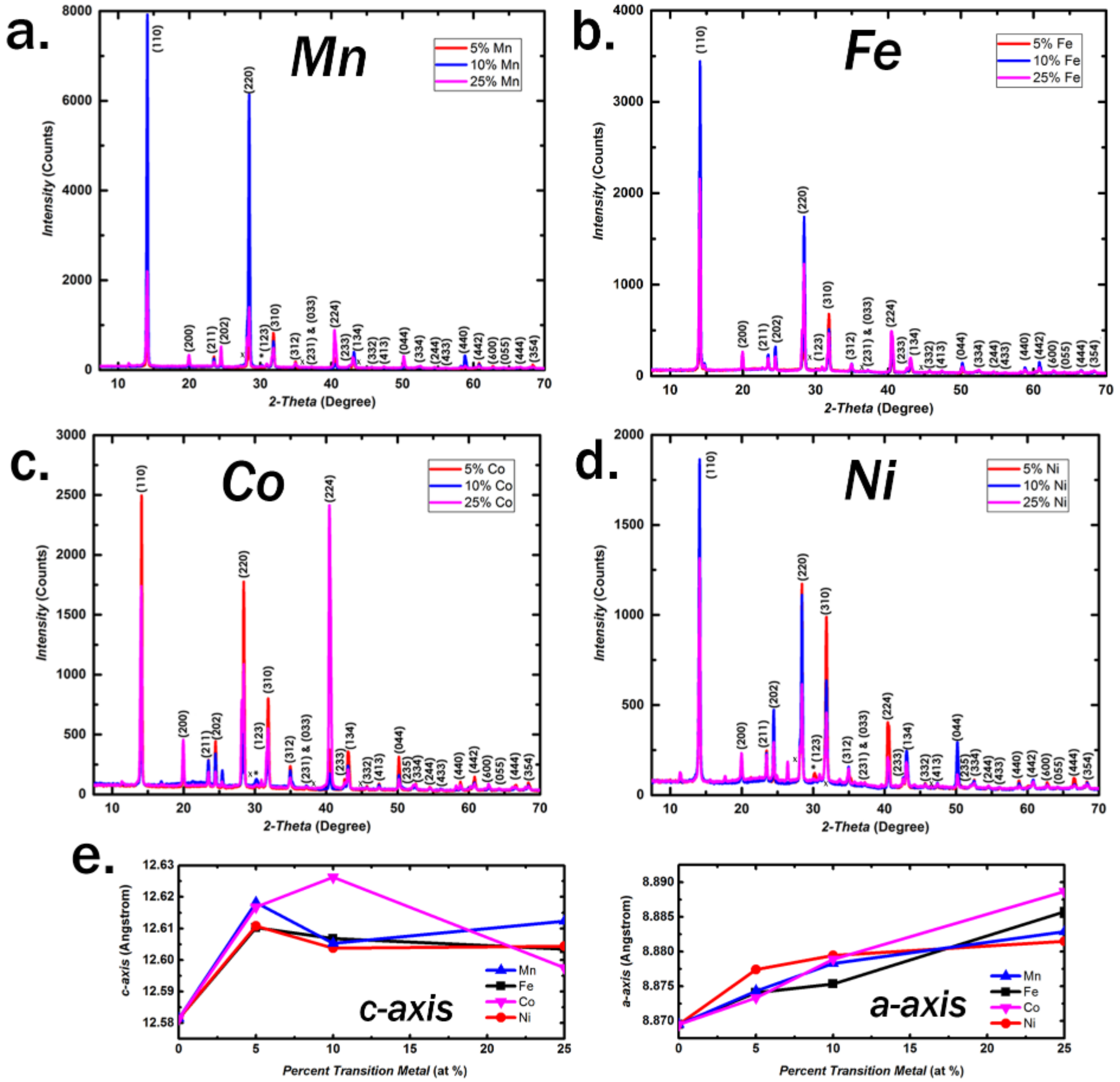

Figure 6.1: (**a**)-(**d**) XRD showing phase purity of drop cast films of Mn, Fe, Co, and Ni based transition metal perovskite alloys respectively; amount of transition metal is expressed in at%. Positions of the three strongest peaks of the pure transition metal halide salts (i.e. MnI_2, FeI_2, CoI_2, and NiI_2) are indicated with an **x** to show the lack of phase separation, and peaks from ITO are marked with an asterisk (*****). (**e**) Lattice parameters calculated from diffraction patterns in (**a**)-(**d**) showing slight but consistent lattice expansion.

metal perovskite alloys containing 5, 10, and 25 at% foreign metal. This data showed that phase separation does not become apparent until the relatively extreme composition of 25 at% foreign metal, but this was as far as the analysis was taken in Chapter 5. Because of the lack of phase separation in $CH_3NH_3PbI_3$ grown with Mn, Fe, Co, and Ni, more insight can be drawn from both the morphological and structural trends that were only briefly explored in Section 5.3.3.

6.2.1 *Structural trends in drop-cast films*

Although the vast majority of work in the hybrid perovskite field has focused exclusively on the fabrication and analysis of thin films *via* spin-casting, the unique information available in the drop-casting based analysis developed in Chapter 5 allows more direct characterization of the thermodynamic tendencies of the material systems of interest. **Figure 6.1** reproduces the XRD data presented in Figure 5.13 with the addition of trends in lattice parameters. These metals are smaller than Pb^{2+}, however we see slight but consistent lattice expansion rather than the lattice contraction previously observed[178,179] (Figure 6.1e). Although there is only very slight expansion, there is an absence of the contraction that would be expected if these elements directly replaced Pb^{2+} without any other inclusion mechanisms at play. This suggests that these elements may not occupy substitutional sites within the perovskite lattice.

Because the shifts in lattice parameter are quite small, we used Rietveld refinement to more thoroughly explore the possible ways in which these transition metals become integrated into perovskite. We used three structural models to fit the XRD data in Figure 6.1: direct Pb substitution by transition metal, interstitial transition metal inclusion along the c-a plane, and interstitial transition metal inclusion along the a-b plane (fitting details are offered at the conclusion of this chapter). To gauge the relative efficacy of these different models, we used each model to evaluate the fractional site occupancy of Pb, I, and transition metal sites (**Table 6.1**). The strong and simultaneous crystal orientation along both [110] and [200] directions in these drop cast films along with the assumption of constant FWHM and the ambiguity inherent in the mechanism of transition metal inclusion limit the insight that can be taken from this analysis. However, differentiating the potentially physically meaningful values from physically unmeaningful values produced by fitting with these three models suggests that a simple model based on direct Pb substitution by transition metals does not adequately describe the behavior of this class of hybrid perovskite alloy. With the flexibility and defect tolerance of $CH_3NH_3PbI_3$ in mind, this slight expansion may suggest partial inclusion *via* the solid solvation of molecular transition metal halide species (e.g. FeI_2).

Because of ambiguity in how these transition metals become integrated into $CH_3NH_3PbI_3$, we will adopt a new way of writing a formula for these perovskite alloys. We will refer to this class of transition

	Interstitial model (c-a)				Interstitial model (a-b)				Substitutional model			
	Pb 4a	I 4a	I 8c	TM 8c	Pb 4a	I 4a	I 8c	TM 4b	Pb 4a	I 4a	I 8c	TM 4a
5% Fe	0.99	0.56	0.78	0.12	0.9	0.27	0.89	0.086	0.5	0.6	0.64	0.86
10% Fe	0.98	1.07	0.68	0.39	1	0.98	0.99	0.97	0.0046	0.4	0.27	1.17
25% Fe	1.15	0.69	1.02	0.59	0.91	0.92	0.86	1.01	0.016	0.52	1.04	1.96
5% Mn	0.98	0.91	0.96	0.048	0.89	0.64	1.06	0.098	0.45	0.7	0.87	0.9
10% Mn	1.17	0.92	1.02	0.4	0.72	0.53	0.74	0.013	0.2	0.53	0.73	1.95
25% Mn	1	0.89	1.09	0.49	0.9	1.03	0.99	0.84	0.027	0.18	0.31	0.61
5% Co	0.92	0.78	0.8	0.12	1.47	1.31	1.5	0.093	0.45	0.82	0.85	0.98
10% Co	1.08	0.77	0.99	0.0024	0.98	0.83	1.05	0.006	0.58	0.77	0.99	0.79
25% Co	1.09	0.96	1.02	1.27	0.96	1.05	0.8	1.52	0.56	0.95	1.11	0.87
5% Ni	0.77	0.65	0.61	0.36	1	0.63	0.93	0.6	0.54	0.79	1.25	2
10% Ni	0.92	0.84	0.94	0.25	0.64	0.55	1.29	0.056	0.19	0.66	0.72	1.88
25% Ni	1.49	1.49	1.29	0.064	0.72	0.24	1.16	0.04	0.14	0.62	0.46	1.26

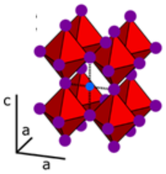

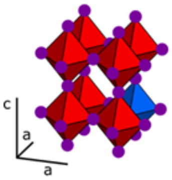

Table 6.1: Results of Rietveld refinement of the data in Figure 6.1 showing fractional occupancy of Pb, I, and various candidate transition metal sites (shown below in cartoon unit cells). Details concerning the parameters and the process of the model and fitting are presented in Section 6.6. Despite the abundant signal in these drop cast films, simultaneous strong orientation around [110] and [200] axes along with slight precipitation in films with high Co and Ni content limit the quantitative precision of the fitting. It is rather the qualitative trends in the results obtained through different structural models that are important to note. In unaltered $CH_3NH_3PbI_3$, the nominal occupancy for each of the Pb 4a, I 4a, and I 8c sites is 1 (space group I4cm). Cells that deviate from this value by more than 25% are highlighted in the table above, with transition metal sites (TM 8c, TM 4b, or TM 4a depending on the model) given more leeway because of the uncertainty in the mechanism of inclusion. The highlighted cells indicate non-physical values for site occupancies, indicating possible inadequacy in the structural model. Taken together, this shows that a simple model based on direct substitution of Pb by transition metals does not adequately explain the behavior of this class of hybrid perovskite alloy.

at% T **at% = [mol TI_2 / (mol PbI_2 + mol TI_2)]**	**Formula** **$CH_3NH_3Pb(T)_yI_3$**	**y =** **$(T)_y$**
0%	$CH_3NH_3PbI_3$	y = 0
5%	$CH_3NH_3Pb(T)_{0.053}I_3$	y = 0.053
10%	$CH_3NH_3Pb(T)_{0.1}I_3$	y = 0.1
15%	$CH_3NH_3Pb(T)_{0.18}I_3$	y = 0.18
20%	$CH_3NH_3Pb(T)_{0.25}I_3$	y = 0.25
25%	$CH_3NH_3Pb(T)_{0.33}I_3$	y = 0.33

Table 6.2: The corresponding formula for each at% discussed, where T is transition metal (Mn, Fe, Co, and Ni). Stoichiometry of the transition metal (**y**) is rounded to two significant figures.

metal perovskite alloy with the formula $AM(T)_yX_3$ where (T) is transition metal and y is its stoichiometry relative to Pb. **Table 6.2** shows how each composition discussed thus far (at%) translates to expression *via* the formula $AM(T)_yX_3$. We continue to use an amount of CH_3NH_3I directly proportional to total moles of metal (i.e. PbI_2 + FeI_2) until we optimize methylammonium iodide stoichiometry directly in Section 6.3.1.

6.2.2 *Microstructural trends in drop-cast films*

Despite the homogenous composition demonstrated by SEM-EDS and XRD in Section 5.3.3 (Figures 5.15 and 5.16), two distinct morphologies compete in each of these transition metal perovskite alloys (**Figure 6.2**). Morphology in the absence of transition metal is rod-like, and as transition metal content is increased, this becomes strongly out-competed by a leaf-like morphology.

To understand what competing growth routes are generating these two starkly different morphologies, we first address the origin of the rod-like morphology that occurs in the absence of transition metal. **Figure 6.3** shows the morphology (SEM) and phase content (XRD) of a partially transformed, pure Pb, drop-cast perovskite film (~50 °C for 2 hrs). The morphology in Figure 6.3a is identical to the morphology of fully transformed pure Pb films (Figure 6.2, 90°C for 2 hrs), but as Figure 6.3b shows, phase content is very different. While the fully transformed film is $CH_3NH_3PbI_3$, the partially transformed film with similar morphology is primarily DMSO-PbI_2-CH_3NH_3I,[101] which implicates DMSO-PbI_2-CH_3NH_3I

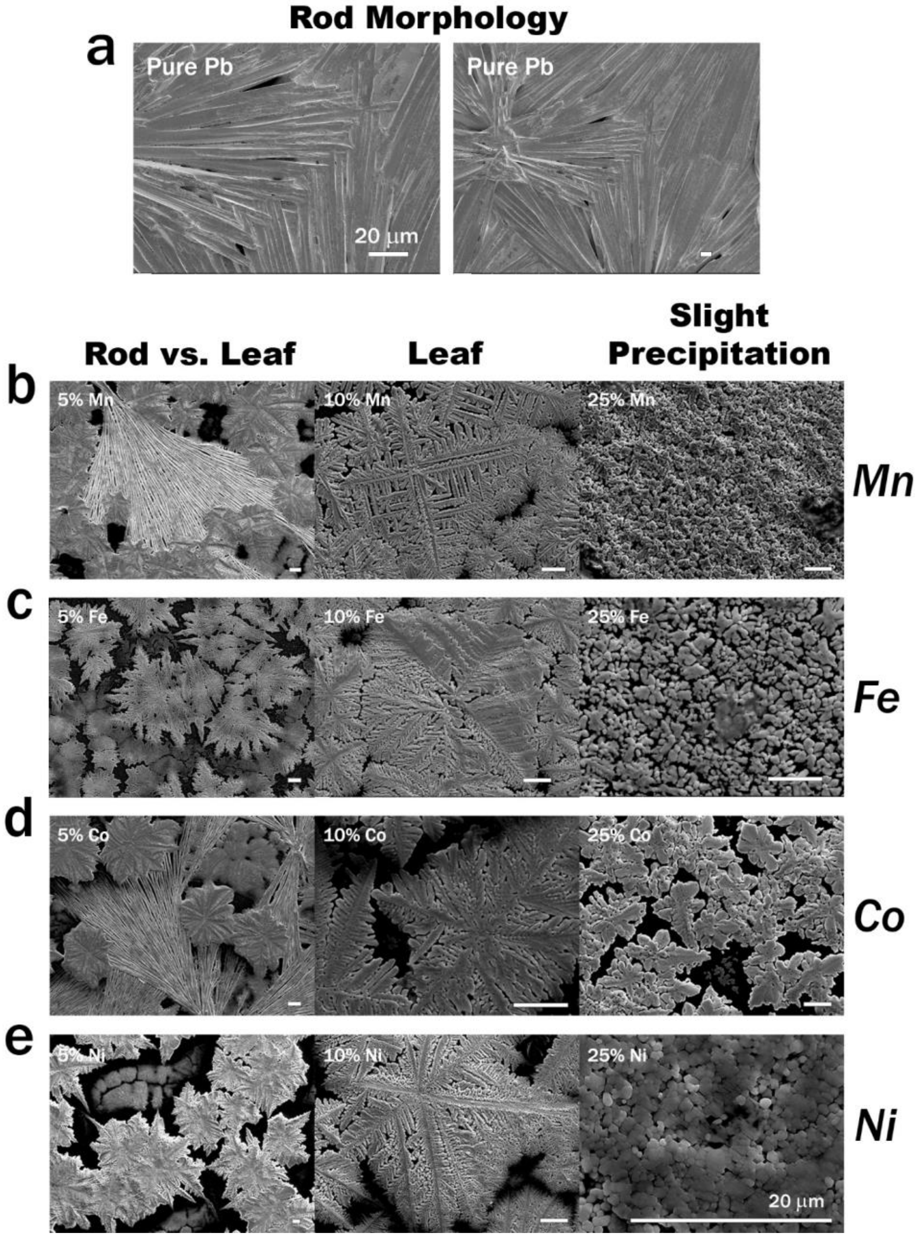

Figure 6.2: (**a**) SEM micrographs of the rod-like morphology produced by $CH_3NH_3PbI_3$ growth from DMSO (drop-cast). (**b**)-(**e**) Drop cast perovskite films grown with increasing amounts of Mn, Fe, Co, and Ni (expressed in at%). The two competing transformation pathways and their microstructural consequences (rods vs. leaves) are highlighted, as well as eventual slight precipitation.

formation as a likely cause of the rod-like morphology in Figure 6.2. This suggests that growth route may be the most significant controlling variable determining morphology.

6.2.3 *Extending investigation to thin film fabrication: Case study of Fe*

To translate insights from our drop-casting based analysis to solar cell preparation, we carried out

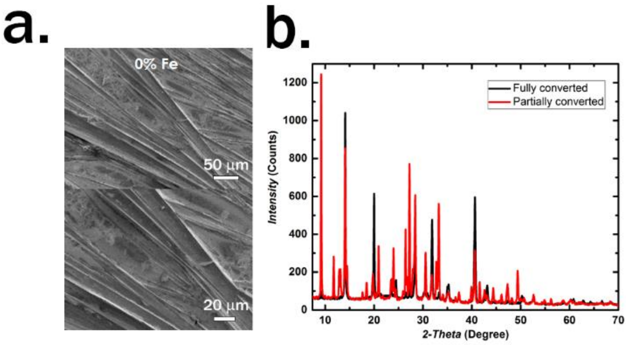

Figure 6.3: (**a**) SEM images showing the morphology of the CH_3NH_3I-PbI_2-DMSO phase in a partially transformed drop cast film. (**b**) XRD showing the presence of the CH_3NH_3I-PbI_2-DMSO phase compared with a fully transformed drop cast film. The red curve is the full range of the XRD data presented above in Figure 6.6. The black curve is the full range of the XRD data for pure Pb perovskite presented in Figure 6.1.

a closer investigation of growth route in thin films. Because of the consistent morphological, compositional, and structural impacts of Fe, Mn, Co, and Ni, we use a single representative species (Fe).

Figure 6.4 shows SEM images of perovskite thin films fabricated with a range of compositions. In the kinetic extreme of spin-coating, competition between growth routes is fiercer. Below $y = 0.1$, morphology is exclusively rod-like, but past $y = 0.1$ a high quality thin film forms with full substrate coverage and reasonable grain size. Past $y = 0.1$, films begin to require annealing to grow, but near $y = 0.1$, films grow readily without annealing. However, if films with less than $y = 0.1$ are left at room temperature a white film forms rather than perovskite, a phenomenon that will soon be addressed directly.

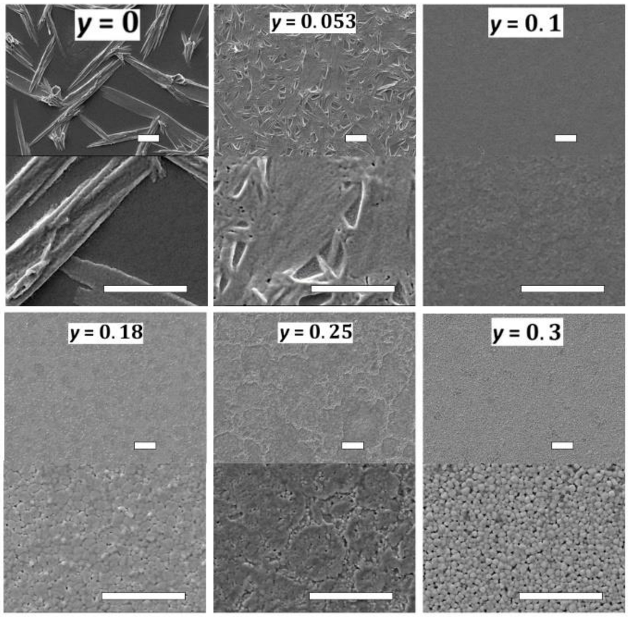

Figure 6.4: SEM images of films fabricated from 0.6 M solutions with progressively greater percentages of iron.

Figure 6.5a shows XRD patterns of these $CH_3NH_3(Fe)_yPbI_3$ films. These films show excellent phase purity, but the uniqueness of $CH_3NH_3Pb(Fe)_{0.1}I_3$ is more important to note. Not only is crystallinity quite high in $CH_3NH_3Pb(Fe)_{0.1}I_3$, crystal orientation is unique. Analysis of the 2D

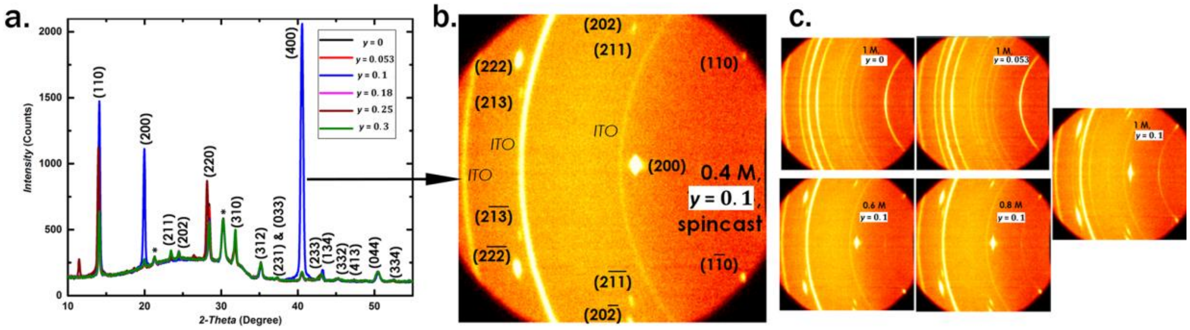

Figure 6.5: (**a**) XRD of thin films grown from 0.6 M perovskite solutions with differing amounts of Fe illustrating the intense crystallinity and unique crystal orientation of $CH_3NH_3Pb(Fe)_{0.1}I_3$ films. Peaks marked with an asterisk (*) are from ITO. (**b**) A 2D diffraction pattern of a film grown from a more dilute solution (0.4 M) is indexed to illustrate almost complete crystal orientation along the [100] direction in thin films of this composition. (**c**) shows how orientation and the direct perovskite nucleation that enables it depend weakly on solution concentration and strongly on amount of transition metal.

XRD patterns reveals that in these $CH_3NH_3Pb(Fe)_{0.1}I_3$ films there is nearly complete orientation along the (100) axis (Figure 6.5b). With less Fe, orientation rapidly becomes random (Figure 6.5c), a phenomenon also linked to solution concentration (Figure 6.5c).

Morphological trends in these films (Figure 6.4) show that growth route is having an impact in thin films that is similar to the impact it had on the corresponding drop-cast films of the same systems (Figure 6.2). The structural trends in these thin films (Figure 6.5) show that whatever is leading to the rod-like morphology is also leading to random crystal orientation and thus more limited long-range order, while the growth route enabled by transition metal addition is leading to almost complete collective crystal orientation and thus greater long-range order. While this is informative, we still need direct insight into the nature of the growth route created by DMSO, its morphological consequences, and how the process is being altered by transition metal inclusion.

We investigated the impact of DMSO exposure on thin perovskite films containing different amounts of Fe by fabricating perovskite thin films via spin-casting, annealing in a glovebox, and then allowing the films to sit while exposed to the DMSO vapor generated during deposition. This simple experiment revealed that DMSO vapor readily invades perovskite films even at low concentrations, with CH_3NH_3I-PbI_2-DMSO formation eventually leading to film bleaching (**Figure 6.6**).

Figure 6.6 shows perovskite films fabricated *via* the commonly used solvent washing technique after fabrication, after sitting in the resulting DMSO rich glovebox environment for 15 min, and then again after another round of thermal annealing for 15 min (Figure 6.6a). This reversible bleaching is due to formation of CH_3NH_3I-PbI_2-DMSO (identified in Figure 6.6b via XRD[101,182]). This same phase is evident in drop cast $CH_3NH_3PbI_3$ films annealed at a temperature too low to ensure complete conversion to perovskite (Figure 6.3 and 6.6c). This bleaching has also been shown by Guo et al.[183] Film bleaching is impeded in films grown with 10 at% FeI_2 (Figure 6.6b and d), but it is not forbidden.

Although Figure 6.6 shows that transition metal inclusion increases resistance toward bleaching, it also shows that CH_3NH_3I-PbI_2-DMSO formation proceeds in even completely formed $CH_3NH_3PbI_3$ films at low DMSO vapor pressures. To understand more closely how CH_3NH_3I-PbI_2-

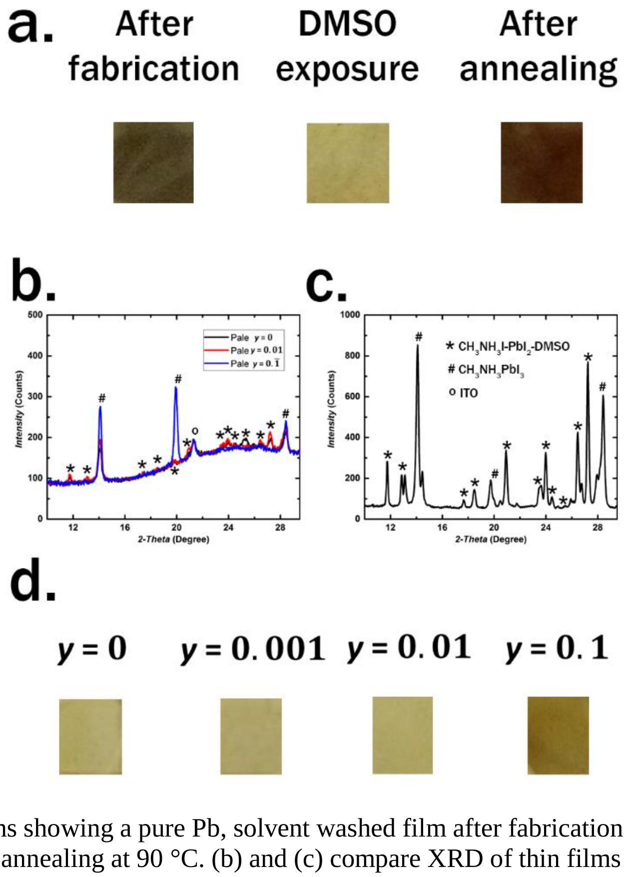

Figure 6.6: (a) Photographs showing a pure Pb, solvent washed film after fabrication, after bleaching by DMSO, and after another round of annealing at 90 °C. (b) and (c) compare XRD of thin films of varying iron content that have been exposed to DMSO. (c) shows the XRD of a partially transformed drop-cast film. (d) shows photographs of films in the bleached state with differing amounts of iron showing that 10 at% Fe films are uniquely robust.

DMSO formation impacts morphology in the transition metal modified perovskite films this work aims to understand, we directly investigated the structural and microstructural consequences of CH_3NH_3I-PbI_2-DMSO formation by simply fabricating three 10% Fe perovskite films in sequence with 35 µl of 0.6 M solution each. In **Figure 6.7**, we show the macroscopic impact of CH_3NH_3I-PbI_2-DMSO formation with photographs, the microscopic impact with SEM, and the impact on atomic order within the film with XRD. The photographs show that CH_3NH_3I-PbI_2-DMSO formation leads to a less reflective film, SEM shows that this is a result of a reduction in film quality at the microstructural level, and XRD shows (200) reflections disappearing upon DMSO ingress.

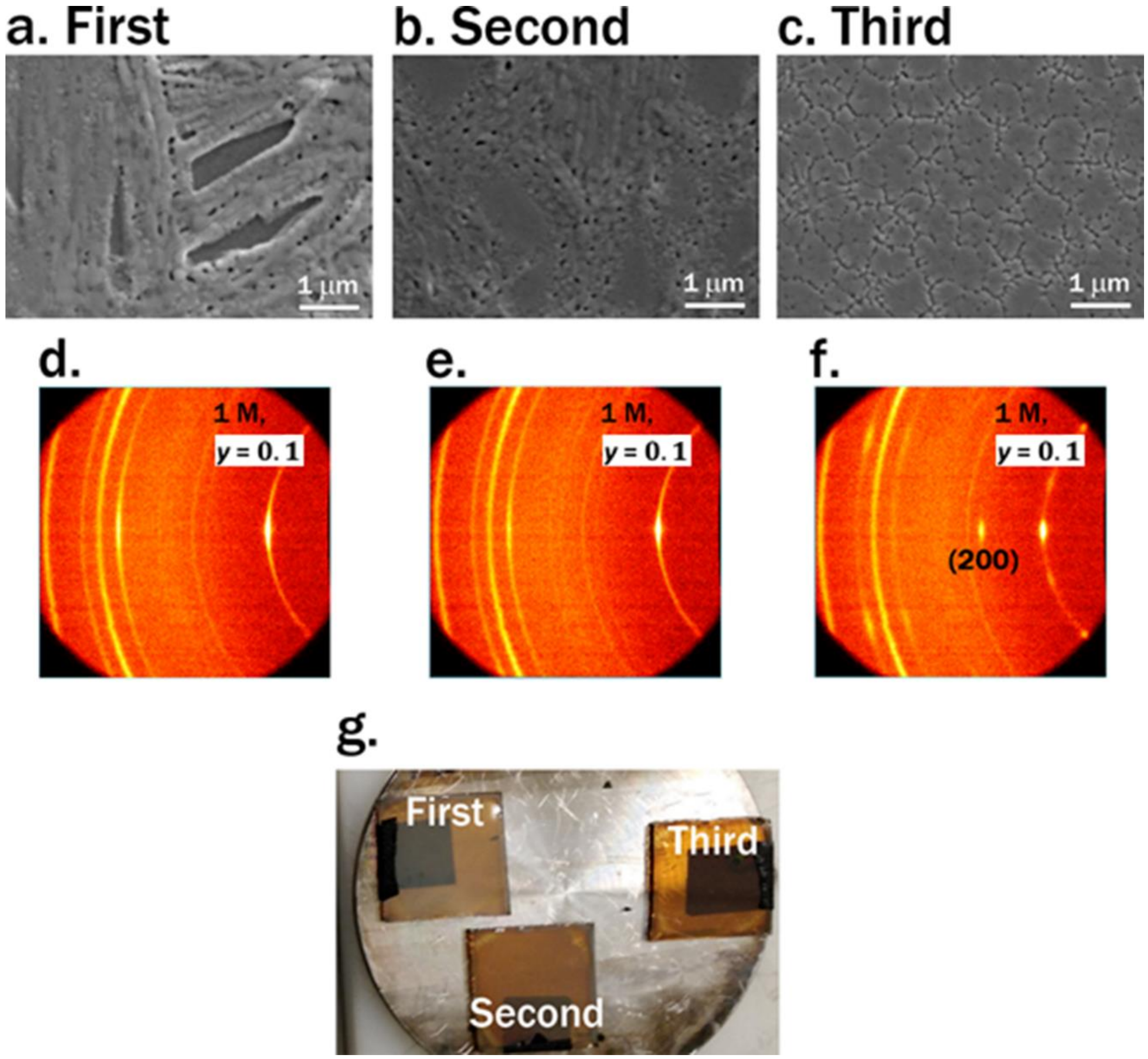

Figure 6.7: Morphological influence of DMSO vapor via (a-c) SEM micrographs, (d-f) 2D XRD showing crystal orientation and (g) photographs; First, Second and Third correspond to the order of spin coating. Magnitude of DMSO exposure decreases from First to Second to Third.

This demonstrates clearly that the ingress of even small quantities of DMSO into the highly-ordered perovskite lattice formed in the presence of transition metal (Figure 6.7f) leads to a rapid degradation of short range (Figure 6.7d-e) and long range (Figure 6.7a-b) order.

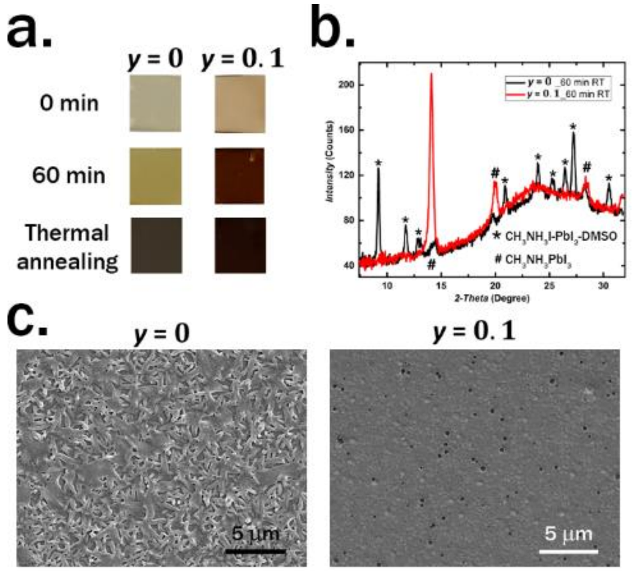

Figure 6.8: Characterization of the two competing transformation pathways *via* (**a**) photographs, (**b**) XRD of films mid transformation (60 min of room temperature annealing), and (**c**) SEM images of final film morphologies. Films were made from 1 M solutions.

Although this clarifies the intrinsic role of DMSO and CH_3NH_3I-PbI_2-DMSO in morphological development, it does not show what process is enabled by transition metal inclusion that circumvents these issues. To directly analyze growth route, we grew spin-cast $CH_3NH_3Pb(Fe)_yI_3$ films with $y = 0$ & 0.1 (**Figure 6.8**). XRD of $CH_3NH_3PbI_3$ after room temperature annealing for 60 min (Figure 6.8b) shows that the white phase that spontaneously forms is CH_3NH_3I-PbI_2-DMSO. Conversely, XRD of the brown phase that forms directly after spin-coating $CH_3NH_3Pb(Fe)_{0.1}I_3$ shows pure perovskite, demonstrating that direct perovskite nucleation is responsible for the high quality film formation inherent to $CH_3NH_3Pb(Fe)_{0.1}I_3$. Direct perovskite nucleation is thus also responsible for the leaf-like morphology in Figure 6.2.

Figure 6.8 shows that the problematic rod-like morphology and film dewetting common to perovskite fabrication is an issue inherent to solvent-perovskite co-crystal formation. This is consistent with perovskite growth from DMF (**Figure 6.9**), a solvent enabling an analogous solvent-perovskite co-crystal.[184] This understanding is important for the field as a whole. For the sake of this work specifically, this shows that growth route is the most significant variable controlling morphology in these transition metal modified perovskite films.

Atmospheric composition, solution concentration, and annealing profile control the

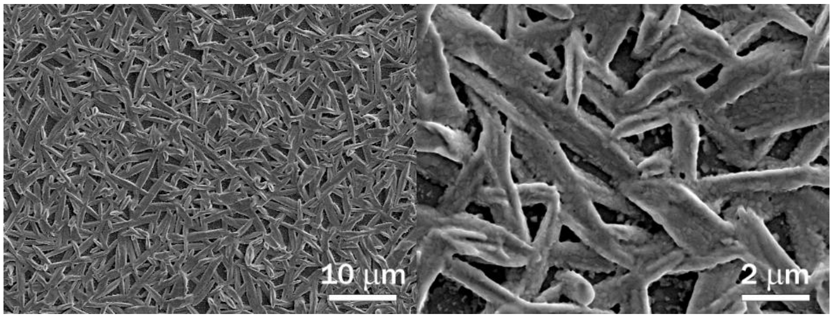

Figure 6.9: SEM images of a pure lead perovskite film fabricated via 1-step deposition from DMF to show the morphological similarities to films generated from DMSO solutions.

dynamic balance between these competing growth routes (Figure 6.5, 6.6, 6.7, and 6.8). Transformation through direct perovskite nucleation in the presence of transition metal is encouraged through low solution concentrations and room temperature annealing (Figure 6.5c and 6.8), while DMSO in the atmosphere aggressively encourages CH_3NH_3I-PbI_2-DMSO formation (Figure 6.7). In our continued study of these transition metals, we thus used relatively low solution concentrations, room temperature annealing before brief thermal annealing, and control of atmosphere (experimental details at the conclusion of the chapter). Before transitioning to an analysis the impact of transition metals on properties, two other secondary variables must be noted that significantly impact morphology and resulting optoelectronic quality.

6.3 Elucidating Secondary Variables Controlling Growth and Morphology

The exact amount of transition metal in a growing perovskite film is key in determining growth route, but two other variables that have a significant impact on growth and resulting morphology must be discussed: (1) CH_3NH_3I stoichiometry and (2) magnetic field.

6.3.1 *Morphological and functional impact of CH_3NH_3I stoichiometry*

CH_3NH_3I stoichiometry impacts material quality more dramatically in these alloyed systems than it does in pure Pb perovskites.[163,185,186] While our growth optimization enabled $CH_3NH_3Pb(Fe)_{0.1}I_3$ films on PEDOT:PSS for photovoltaic study, these films exhibited unstable, poorly defined diode *I*-*V* curves

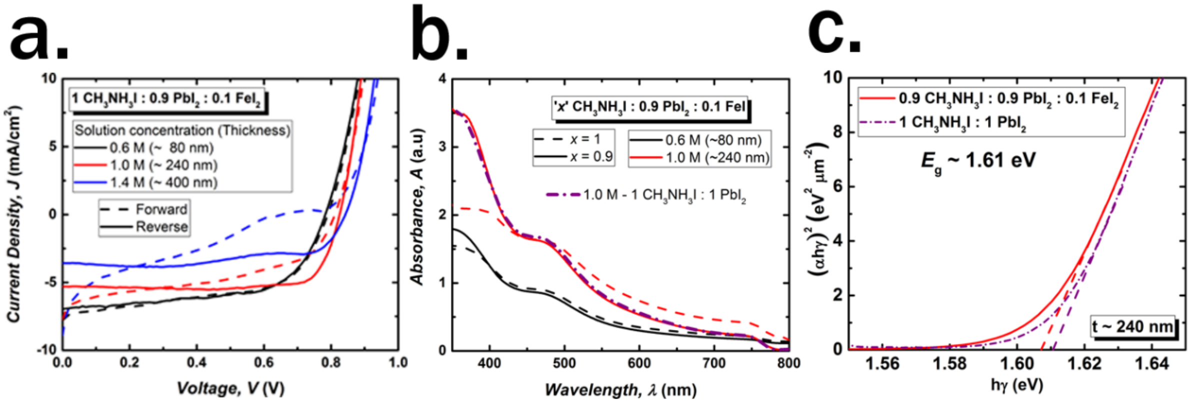

Figure 6.10: (**a**) Unstable and poorly defined *I-V* characteristics for devices made with a stoichiometric precursor composition (1:1 ratio between CH_3NH_3I and metal halides). (**b**) Absorbance of $CH_3NH_3Pb(Fe)_{0.1}I_3$ films with varied CH_3NH_3I stoichiometry vs. pure $CH_3NH_3PbI_3$ fabricated by standard solvent washing with toluene. (**c**) Tauc plot showing the band gap of optimized $CH_3NH_3Pb(Fe)_{0.1}I_3$ films.

before stoichiometric optimization of CH_3NH_3I (**Figure 6.10a**). While otherwise dark and reflective, under the solar simulator these films appeared bright white **(Figure 6.11a)**. If these transition metals do not simpy replace Pb, there is likely an excess of CH_3NH_3I. In the kinetic extreme of spin coating, this excess may create disorder at a scale that is difficult to structurally detect.[163,186]

We tuned $CH_3NH_3^+$ and I^- stoichiometry by reducing CH_3NH_3I in precursor solutions which resulted in elimination of internal scattering under solar simulator light (Figure 6.11a) and more defined absorption features (Figure 6.10b) (x CH_3NH_3I:0.9 PbI_2:0.1 FeI_2, where x = relative moles of CH_3NH_3I).[186–188] In contrast to most compositional modifications of $CH_3NH_3PbI_3$, band-gap is unchanged by Fe inclusion (Figure 6.10c) and absorption features are identical to pure $CH_3NH_3PbI_3$, solvent washed films. PV devices made with varied CH_3NH_3I stoichiometry (x = 0.8, 0.9, 1) show that x = 0.8 and 0.9 devices

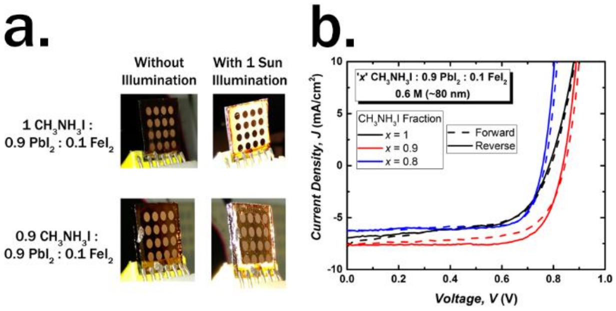

Figure 6.11: (**a**) Photographs showing the otherwise hidden difference between films made from solutions with differing CH_3NH_3I stoichiometry revealed by the intense light of the solar simulator. (**b**) *I-V* characteristics of $CH_3NH_3Pb(Fe)_{0.1}I_3$ solar cell devices with varying fractions of CH_3NH_3I. All devices show significant hysteresis between forward (short circuit (SC)→open circuit (OC)) and reverse (OC→SC) scans.

have more well-defined diode curves (Figure 6.11b). While, disorder caused by excess CH_3NH_3I (Figure 6.11a) leads to poor material performance (Figure 6.10a and 6.11b), matching CH_3NH_3I stoichiometry (x = 0.9) with PbI_2 minimizes the issue and its functional consequences (Figure 6.10b-c and 6.11b). The overall stoichiometry represented by $x = 0.9$ equates to an exact stoichiometry of $CH_3NH_3Pb(Fe)_{0.1}I_3$. This formula is now exact with regard to the stoichiometry of all species in the precursor solution.

6.3.2 *Morphological and functional impact of magnetic field*

We began to suspect that the magnetic stir-bar in our hot plate was affecting film formation. $CH_3NH_3Pb(Fe)_{0.1}I_3$ films were grown under magnetic fields of different strengths to explore this possibility (**Figure 6.12**). Magnetic field encourages high quality film growth with larger grains and better coverage (**Figure 6.13a**), but linear and highly oriented features also appear. These features are indicative of a response to strain that resolves in a manner dependant on the underlying lattice, possibly indicative of a process like magnetostriction induced twinning, a tendency common in oxide perovskites.[154,189] Despite the apparent enhanced film quality induced by magnetic field, there is a negative impact on optoelectronic quality (**Figure 6.14**).

In $CH_3NH_3PbI_3$ grown with chloride, indications of ferroelasticity have been previously identified.[190] Recently, twinning has been observed as an important intrinsic part of $CH_3NH_3PbI_3$ functionality regardless of compositional modification.[191] This is a very common property of oxide

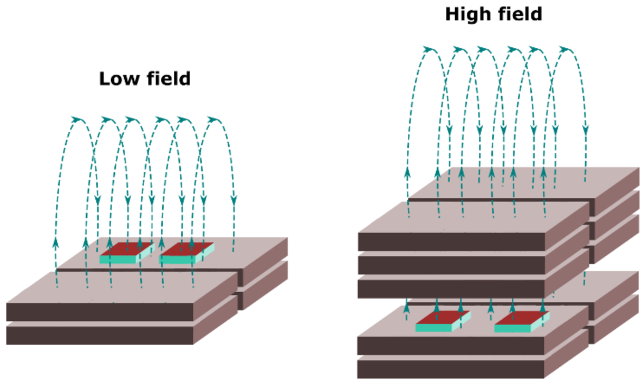

Figure 6.12: Schematic illustrations of how perovskite growth under external magnetic field was accomplished. Grey boxes represent individual ferrite block magnets. Red films represent how substrates are arranged in the field. Blue lines illustrate the orientation of the magnetic field with arrows signifying the direction. The space between magnet stacks in the high field case was created with stacked glass spacers that are not shown.

perovskites,[154,189] and often occurs in material systems with a high to low symmetry phase transformation. Previously, highly oriented, periodic grain boundaries have been identified in pure $CH_3NH_3PbI_3$[STW-3] as a component of overall grain structure. The similarities in size and hardness between Fe and Cl ions makes the identification of ferroelastic fingerprints in $CH_3NH_3PbI_{3-x}Cl_x$[190] a very important consideration for these transition metal perovskite alloys and other systems like them, but the direct identification of twinning in $CH_3NH_3PbI_3$[8] demonstrates the broad importance of this consideration.

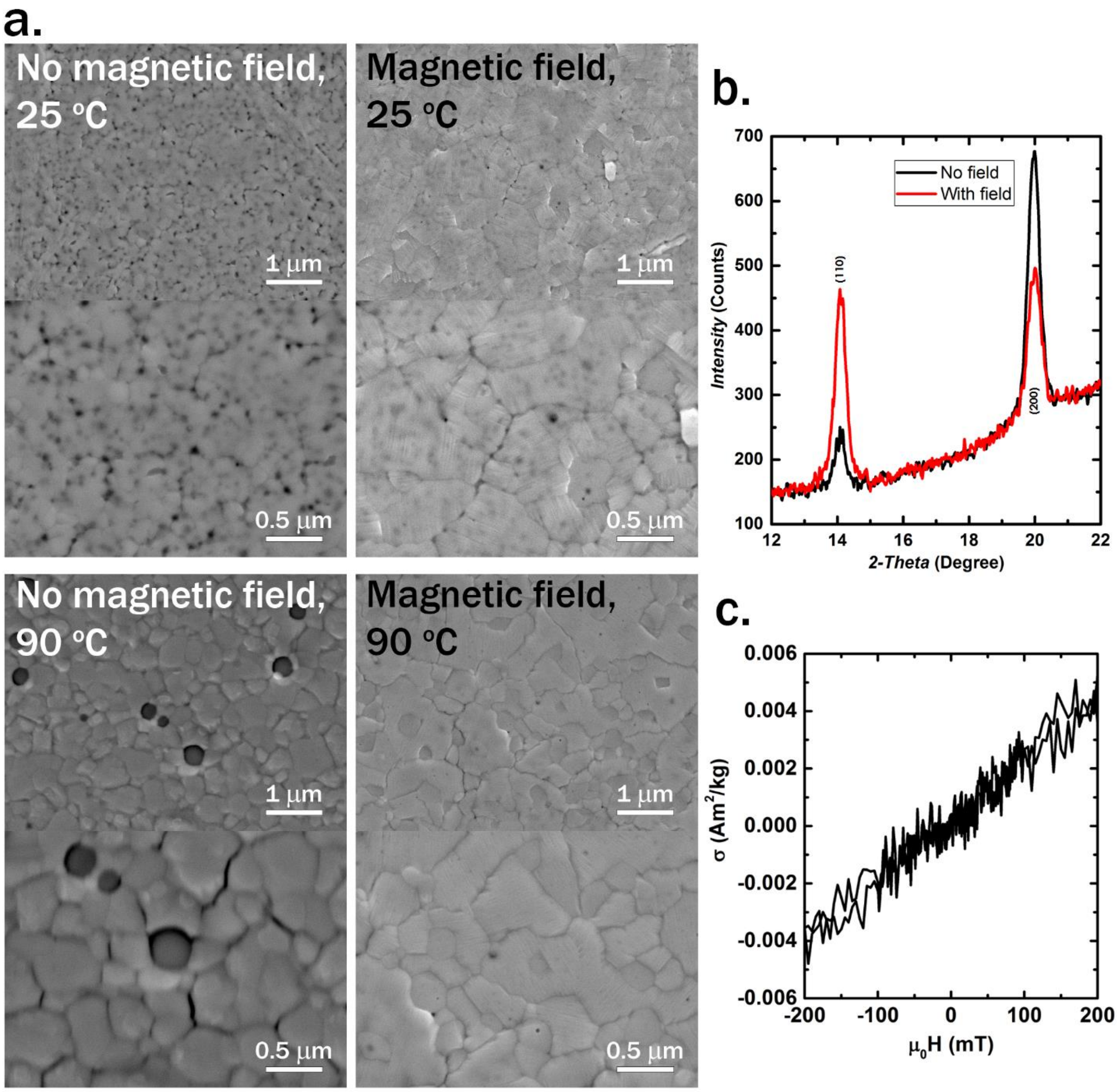

Figure 6.13: Characterization of the morphological impact of applying a magnetic field during growth of $CH_3NH_3Pb(Fe)_{0.1}I_3$ films and characterization of magnetic properties. (**a**) SEM images comparing growth both with and without a magnetic field as well as with and without thermal annealing. (**b**) Shift in film texture caused by annealing a thin film in an upwards magnetic field. (**c**) Mass magnetization versus external flux for a $CH_3NH_3Pb(Fe)_{0.1}I_3$ drop cast perovskite film characterized with VSM showing a paramagnetic response.

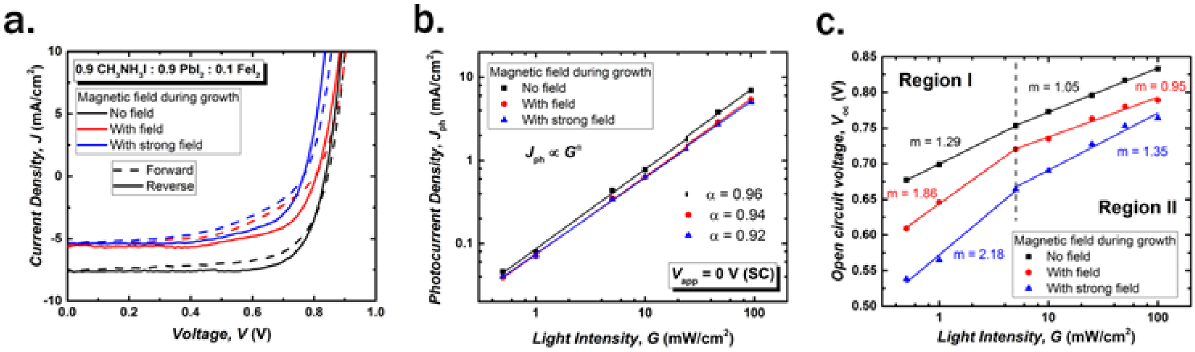

Figure 6.14: Influence of magnetic field during growth of $CH_3NH_3Pb(Fe)_{0.1}I_3$ films shown via (a) *I-V* characteristics of solar cell devices; light intensity dependence of (b) photocurrent density at short circuit condition (V_{app} = 0 V) and (c) open circuit voltage. The light intensity dependence of J_{ph} and V_{oc} illustrates increased trap-assisted recombination with increased field strength during growth.

When grown above the tetragonal to cubic transition, the linear features created by growth in a magnetic field soften (Figure 6.13a). This combined with absence of this microstructure in films grown without magnetic field at 90 °C shows that spontaneous strain generated by cooling is not alone enough to generate these linear features. To substantiate this link between magnetic field and growth, Figure 6.13b shows the impact of magnetic field on crystal orientation via XRD. A field traveling through the plane of the film encourages a shift toward [110] orientation. This relationship between growth and magnetic field implies the existence of new magnetic properties. Vibrating sample magnetometry (VSM) was used to directly characterize magnetic properties of drop-cast $CH_3NH_3Pb(Fe)_{0.1}I_3$ films. After subtracting the diamagnetic signal of the silicon substrate, a clear paramagnetic response was apparent (Figure 6.13c). This paramagnetism is likely part of what leads to such dramatic and unique crystal orientation in $CH_3NH_3Pb(Fe)_{0.1}I_3$ films.

Mn, Fe, Co, and Ni atoms all have magnetic properties, but to impart magnetic properties to $CH_3NH_3PbI_3$ these species must become a part of the material. Magnetic properties have been found in $CH_3NH_3Pb(Mn)_{0.1}I_3$,[192] so the impact of magnetism likely extends well past $CH_3NH_3Pb(Fe)_{0.1}I_3$. Although a strong magnetic field encourages larger grains and better coverage (Figure 6.13a), it also leads to new and subtle morphological features indicative of twinning[191] and an accompanying decrease in optoelectronic quality (Figure 6.14). The impact of magnetic field on morphology, crystal orientation, and material performance taken together with the paramagnetic response of the material indicate new magnetic functionality.[192] While these magnetic properties are potentially interesting, herein we minimize their impact on growth by keeping magnetic stirring off.

6.4 Impact of Transition Metal Inclusion on Optoelectronic Properties

Identifying growth route as the most significant controlling variable in morphological evolution allows us to realize systems that primarily bear the compositional impact of added transition metal rather than a convolution of morphological and compositional impacts. Although this effort by no means completely eliminates the impact that the environment has on morphology, rational control over solution preparation, annealing profile, and atmospheric composition puts us in the best possible position to analyze the impact of these transition metals themselves on perovskite optoelectronic properties. The work in Sections 6.2 and 6.3 allows us to systematically eliminate the impact of nonidealities on material performance like poor film quality caused by CH_3NH_3I-PbI_2-DMSO formation (Figure 6.7), disorder induced by excess methylammonium iodide (Figure 6.10 and 6.11), and the morphological impacts of magnetic fields (Figure 6.14). Before expanding our investigation to all species in this study (Fe, Mn, Co, and Ni), we first more closely analyze optoelectronic quality in Fe perovskite alloys as a model system.

6.4.1 *Impact of transition metal inclusion on J-V hysteresis and photovoltaic performance: Case study of Fe*

$CH_3NH_3Pb(Fe)_{0.1}I_3$ films preserve optical properties of $CH_3NH_3PbI_3$ (Figure 6.10b-c), but even though band-gap remains unchanged, these transition metals invariably introduce valence d-orbitals that may alter recombination kinetics despite the preservation of optical properties.[193,194] The absorption of $CH_3NH_3Pb(Fe)_{0.1}I_3$ films scale with perovskite thickness as expected (**Figure 6.15a**), but performance does not (Figure 6.15b). Specifically, J_{sc} does not proportionately scale with absorption (**Figure 6.16a**) and V_{oc} decreases with increasing thickness, paralleling *FF* trends. The ideality factor (η) of 1.6 – 1.8, calculated with dark *I-V* characteristics (Figure 6.16b), indicates dominant monomolecular recombination.[195] Comparable series and shunt resistances among these devices (Figure 6.15b) implicates this recombination as the cause of *FF* trends with thickness.

Light intensity (*G*) dependent *I-V* measurements (Figure 6.15c-d) were performed to identify the nature, extent, and origin of this monomolecular recombination. Slight variation in photocurrent (J_{ph}) with voltage can be linked to ineffective charge transport resulting from trap-assisted recombination as low exciton binding energies[196] eliminate geminate recombination as a possibility. At SC, $J_{\mathrm{ph}} \propto G^{\alpha}$ where α is related to extent of recombination. This metric (α) decreases

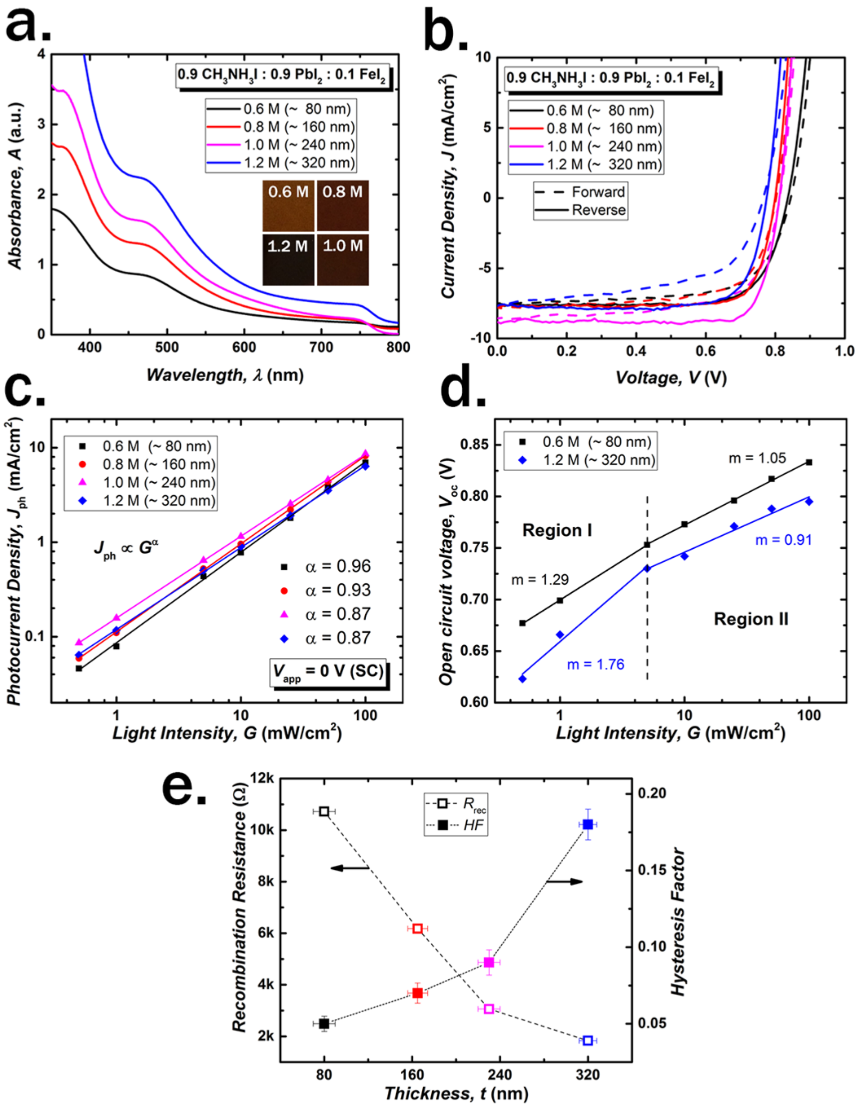

Figure 6.15: Optoelectronic characterization of $CH_3NH_3Pb(Fe)_{0.1}I_3$ films with varying thickness *via* (**a**) UV-vis absorption spectra (photographs inset) and (**b**) *I-V* characteristics of solar cell devices. (**c**)-(**e**) Recombination analysis for different thicknesses of $CH_3NH_3Pb(Fe)_{0.1}I_3$ films *via* light intensity dependence of **(c)** photocurrent density at short circuit condition (V_{app} = 0 V) and (**d**) open circuit voltage. (**e**) Variation of recombination resistance and hysteresis factor with thickness.

with increasing thickness (Figure 6.15c) pointing towards recombination centers within the perovskite bulk as the cause of the anomalous trend in J_{sc} with thickness (Figure 6.16a).

To verify this, we investigated V_{oc} dependence on G to determine light ideality factor (m)[197] using $\partial V\mathrm{oc}/\partial \log G = (mk_{\mathrm{B}}T)/(2.303q)$. V_{oc} vs. G (Figure 6.15d) exhibited different slopes at low and high light intensities, a trend characteristic of intensity dependent recombination.[198] A transition region around 5 mW/cm^2 (0.05 Sun) defines a boundary between trap-dominated recombination at low G (higher slopes) and bimolecular recombination at high G (lower slopes). At low light intensities, thinner films have low slopes (m = 1.29) compared to thicker films (m = 1.76), and at higher intensity slopes become comparable (m ~ 1). This trend is consistent with trap-assisted recombination within the perovskite bulk and likely results from trap filling at increased light intensities. These findings were further confirmed by impedance spectroscopy,[STW-5] but this analysis is not directly relevant here.

Hysteresis in perovskite solar cells is a combined effect of the influence of trap sites and ion motion.[43,102,199,200] The J-V hysteresis observed in these systems (Figure 6.15b) is intimately related to transition metal inclusion as hysteresis is not normally observed in perovskite solar cells with PEDOT:PSS and $\mathrm{PC_{61}BM}$ interlayers regardless of processing routes used.[STW-3,[98,102,201–204]] To quantify and compare hysteresis among devices,[205] we define *Hysteresis Factor (HF)* as $HF =$

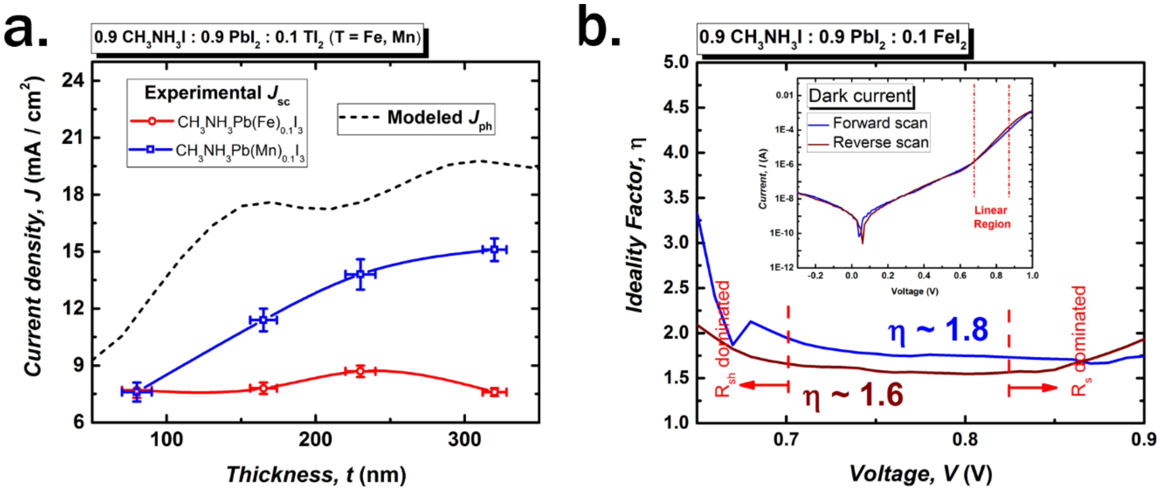

Figure 6.16: (a) Comparison of experimental short circuit current density for different film thickness to the theoretical maximum predicted from absorption profile obtained by transfer matrix modeling. We show both the Jsc exhibited by Fe and the Mn devices discussed later. (b) Dark ideality factor for solar cell devices with $\mathrm{CH_3NH_3Pb(Fe)_{0.1}I_3}$ films.

$\left|1-\frac{A_{\text{Forward}}}{A_{\text{Reverse}}}\right|$ where A_{Forward} and A_{Reverse} are areas under $SC \rightarrow OC$ and $OC \rightarrow SC$ scans respectively. Larger *HF* was observed for thicker active layers (Figure 6.15e), correlating with trends in trap assisted recombination (Figure 6.15c-d) and recombination resistance (Figure 6.15e).

While helpful in understanding the functional impact of transition metals on $CH_3NH_3PbI_3$, this does not fully probe the potential of this class of hybrid perovskite alloy. If defect states induced by the d-orbital of the transition metal are indeed leading to troublesome recombination behavior, it is possible that differing energetics and occupancy of d-orbitals on the other transition metals studied[178] may alter these limitations.

6.4.2 *Compositional impact of transition metal inclusion: Mn, Fe, Co, and Ni*

In previous sections, we identified that growth route is the most significant controlling variable in the morphological evolution of these transition metal modified perovskites (Figure 6.8). Through the drop-casting analysis mounted in this chapter and Chapter 5, we also identified that each of the four transition metals studied (Fe, Mn, Co, and Ni) modify growth route in essentially the same manner (Figure 6.2). The consistent high solid solubility of these species (Figure 5.16 and 6.1), our insight into the importance of stoichiometry (Figure 6.4, 6.5, 6.9, and 6.10), and the impact of environmental conditions in directing transformation (Figure 6.5c, 6.7, and 6.8) allow us to compare the compositional impacts of Fe, Mn, Co, and Ni with minimal convolution from

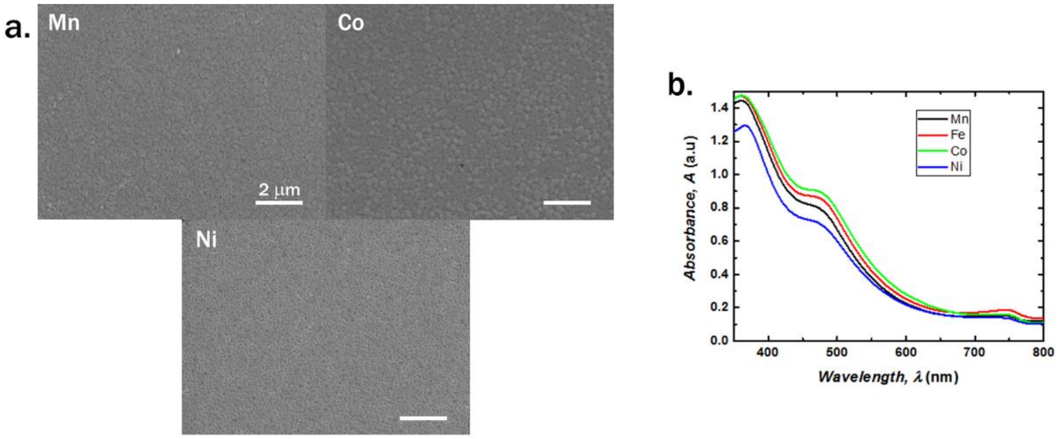

Figure 6.17: (a) SEM of $CH_3NH_3Pb(T)_{0.1}I_3$ films made with 0.6 M solutions, where T = Mn, Co, and Ni. (b) UV-Vis absorption of $CH_3NH_3Pb(T)_{0.1}I_3$ films.

morphological differences. Morphology and absorption profiles of $CH_3NH_3Pb(Mn)_{0.1}I_3$, $CH_3NH_3Pb(Fe)_{0.1}I_3$, $CH_3NH_3Pb(Co)_{0.1}I_3$, and $CH_3NH_3Pb(Ni)_{0.1}I_3$ thin films are consistent (**Figure 6.17**). Band gaps are comparable to $CH_3NH_3PbI_3$ (Figure 6.10b-c and 6.17b).[178,179]

Solar cells based on each different perovskite alloy display distinct characteristics in terms of device performance and *I-V* hysteresis (**Table 6.3** and **Figure 6.18a**). $CH_3NH_3Pb(Ni)_{0.1}I_3$ devices show worst performance and highest *HF*, with steadily increasing performance and decreasing *HF* moving backwards through the periodic table from Ni → Co → Fe → Mn (Table 6.3). Difference in performance between Fe and Mn based devices is slight, but the hysteresis ubiquitously present

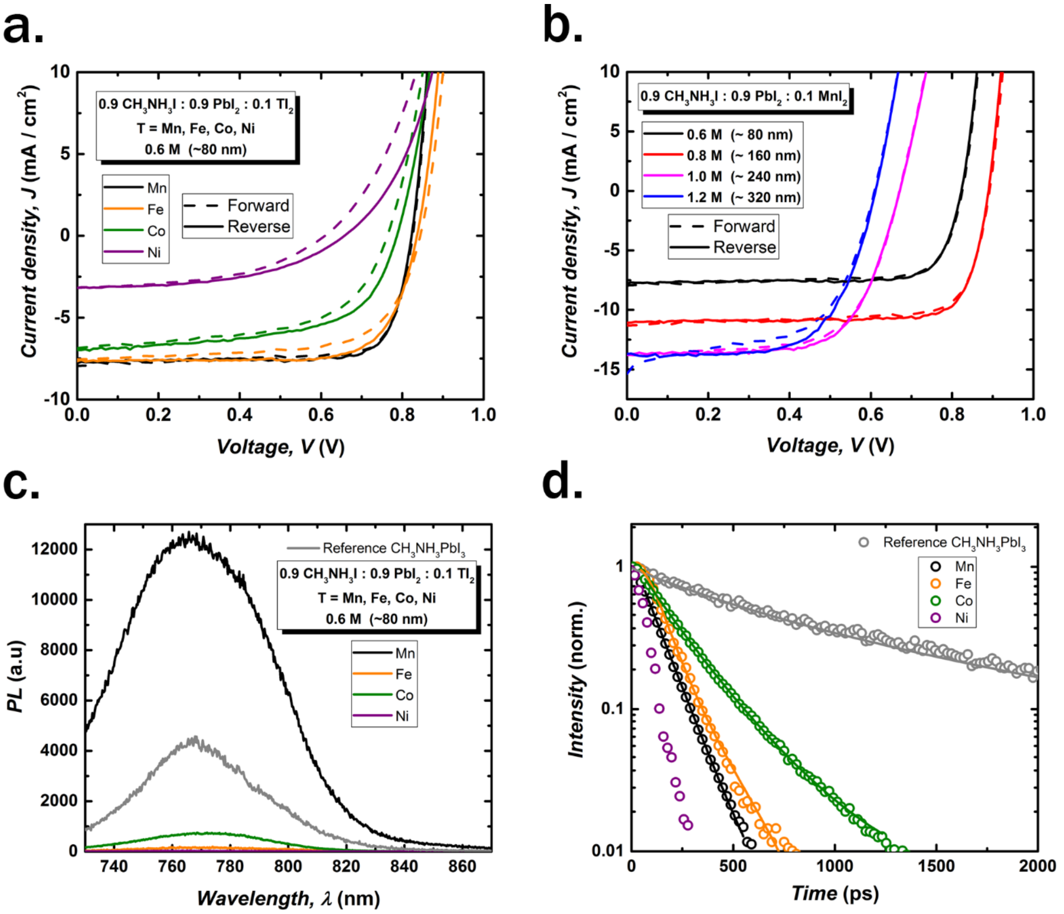

Figure 6.18: (**a**) *I–V* characteristics of $CH_3NH_3Pb(T)_{0.1}I_3$ solar cell devices demonstrating the influence of different transition metal inclusion (T = Mn, Fe, Co, Ni) on photovoltaic performance and hysteresis. (**b**) *I-V* characteristics of solar cell devices with varying $CH_3NH_3Pb(Mn)_{0.1}I_3$ film thickness; a less dramatic increase in hysteresis with thickness is observed in sharp contrast to the $CH_3NH_3Pb(Fe)_{0.1}I_3$ case discussed earlier. (**c**) Emission spectra of $CH_3NH_3Pb(T)_{0.1}I_3$ alloys under 1μJ/cm^2 365 nm excitation; all spectra were corrected with respect to excitation pulse to accommodate the luminescent quantum yield. (**d**) Transient photoluminescence dynamics of $CH_3NH_3Pb(T)_{0.1}I_3$ alloys; the data for a ~200 nm thick $CH_3NH_3PbI_3$ film prepared by solvent washing was included for reference.

T	Scan Direction	V_{oc} (V)	J_{sc} (mA/cm^2)	FF (%)	PCE (%)		Hysteresis Factor
					Average	Highest	
Mn	**Forward**	**0.83 ± 0.01**	**7.8 ± 0.5**	**76 ± 2**	**4.95 ± 0.32**	**5.30**	**0.01**
	Reverse	**0.83 ± 0.01**	**7.4 ± 0.5**	**80 ± 2**	**5.08 ± 0.34**	**5.50**	
Fe	Forward	0.84 ± 0.01	7.7 ± 0.4	66 ± 1	4.28 ± 0.22	4.69	0.05
	Reverse	0.83 ± 0.01	7.7 ± 0.4	77 ± 1	4.88 ± 0.24	5.30	
Co	Forward	0.77 ± 0.04	6.3 ± 0.4	57 ± 4	2.74 ± 0.34	3.02	0.07
	Reverse	0.78 ± 0.04	6.4 ± 0.4	58 ± 4	2.91 ± 0.42	3.28	
Ni	Forward	0.62 ± 0.01	2.9 ± 0.3	49 ± 1	0.89 ± 0.05	0.94	0.10
	Reverse	0.66 ± 0.01	2.9 ± 0.2	50 ± 1	0.98 ± 0.07	1.04	

Table 6.3: Performance metrics for $CH_3NH_3Pb(T)_{0.1}I_3$ based solar cell devices, where T = Mn, Fe, Co, Ni corresponds to the transition metal incorporated.

in $CH_3NH_3Pb(Fe)_{0.1}I_3$ devices (Figure 6.15) is negligible in $CH_3NH_3Pb(Mn)_{0.1}I_3$ devices (Figure 6.18a and Table 6.3). We fabricated a series of devices with increasing perovskite thickness in the same fashion as in Figure 6.15b to establish if $CH_3NH_3Pb(Mn)_{0.1}I_3$ minimizes the severity of recombination caused by transition metal inclusion. In contrast to the case of $CH_3NH_3Pb(Fe)_{0.1}I_3$ (Figure 6.15b), the $CH_3NH_3Pb(Mn)_{0.1}I_3$ devices showed minimal increase in hysteresis with increasing thickness (Figure 6.18b).

As has been noted, synthetic variables like solution concentration (Figure 6.5c) have an influence on which route perovskite growth proceeds through. When considering the data in Figure 6.18b, it is important to note that Mn slightly less aggressively alters perovskite transformation compared to Fe (Figure 6.2). The increased tendency to transform through CH_3NH_3I-PbI_2-DMSO with increasing solution concentration noted in the case of Fe (Figure 6.5c) becomes uniquely problematic in $CH_3NH_3Pb(Mn)_{0.1}I_3$ films deposited from solutions above 0.8 M (**Figure 6.19**). Morphological problems are

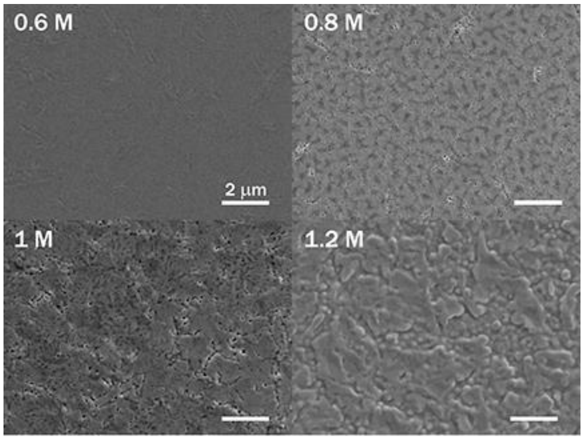

Figure 6.19: SEM of $CH_3NH_3Pb(Mn)_{0.1}I_3$ films made using 0.6, 0.8, 1, and 1.2 M perovskite solutions.

the likely cause of suppressed performance for devices with $CH_3NH_3Pb(Mn)_{0.1}I_3$ films made from 1 and 1.2 M solutions. However this series of Mn based devices shows that J_{sc} is not sharply limited as in the case of $CH_3NH_3Pb(Fe)_{0.1}I_3$ (Figure 6.16a). V_{oc} also increases with thickness for $CH_3NH_3Pb(Mn)_{0.1}I_3$ devices until problems with growth set in at 1 M. The $CH_3NH_3Pb(Mn)_{0.1}I_3$ device made with a ~160 nm perovskite film (0.8 M solution) yielded the highest power conversion efficiency (PCE) in this study (**Figure 6.20a**) and it exhibited largely hysteresis free function (Figure 6.20b)**.**

Dramatic reduction of hysteresis and elimination of the strict limit on J_{sc} and V_{oc} with thickness suggest that Mn minimizes the impact of deleterious trap-assisted recombination inherent to transition metal inclusion in $CH_3NH_3PbI_3$, but we used time resolved photoluminescence (trPL) spectroscopy to further compare $CH_3NH_3Pb(T)_{0.1}I_3$ films (experimental and fitting details at the conclusion of the chapter). Figure 6.18c and Figure 6.18d compare emission spectra and radiative decay kinetics for each alloy under 365 nm excitation with 1 μJ/cm^2 fluence. This excitation corresponds to a charge carrier density in the range of 10^{17} cm^{-3}, which is near the onset of amplified spontaneous emission. Although Mn minimizes the negative impact of transition metal inclusion on device performance, emission did not persist the longest in this system. Rather, the dominance of fast radiative decay over non-radiative loss in this system led to a relatively short lifetime but a

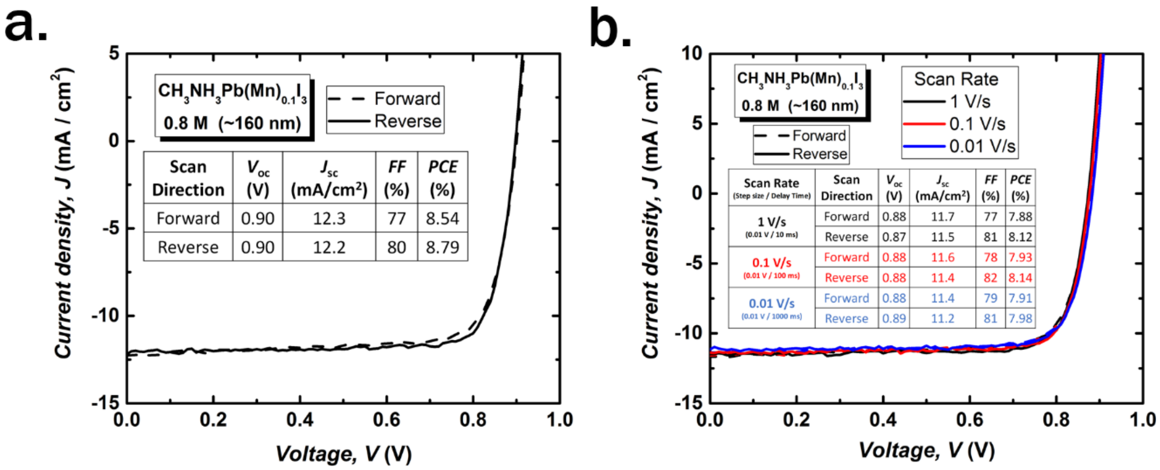

Scan Direction	V_{oc} (V)	J_{sc} (mA/cm^2)	*FF* (%)	*PCE* (%)
Forward	0.90	12.3	77	8.54
Reverse	0.90	12.2	80	8.79

Scan Rate (Step size / Delay Time)	Scan Direction	V_{oc} (V)	J_{sc} (mA/cm^2)	*FF* (%)	*PCE* (%)
1 V/s (0.01 V / 10 ms)	Forward	0.88	11.7	77	7.88
	Reverse	0.87	11.5	81	8.12
0.1 V/s (0.01 V / 100 ms)	Forward	0.88	11.6	78	7.93
	Reverse	0.88	11.4	82	8.14
0.01 V/s (0.01 V / 1000 ms)	Forward	0.88	11.4	79	7.91
	Reverse	0.89	11.2	81	7.98

Figure 6.20: (a) *I-V* characteristics of the best device in this study utilizing a ~160 nm $CH_3NH_3Pb(Mn)_{0.1}I_3$ as photoactive layer and (b) scan rate (0.01 – 1 V/s) dependent *I-V* characteristics for a typical ~160 nm $CH_3NH_3Pb(Mn)_{0.1}I_3$ based solar cell device. Devices show consistently negligible hysteresis and the corresponding solar cell performance metrics are provided in figure insets.

significant increase in quantum yield compared to all other alloyed systems and pure $CH_3NH_3PbI_3$. On the other hand, despite showing lower performance and larger *HF* than both Mn and Fe based alloys, $CH_3NH_3Pb(Co)_{0.1}I_3$ showed the longest carrier lifetime (**Table 6.4**).

Two primary things distinguish the optoelectronic behaviour of $CH_3NH_3Pb(Mn)_{0.1}I_3$. Firstly, $CH_3NH_3Pb(Mn)_{0.1}I_3$ is much more emissive than all other materials in this class of perovskite alloy. Secondly, together with its peculiar luminescence efficiency, the relatively short lifetime of $CH_3NH_3Pb(Mn)_{0.1}I_3$ implies an abnormally high radiative bimolecular recombination rate rather than a fast loss of carrier density caused by defective traps. Overall, transition metal inclusion leads to alterations in recombination processes originating from modification of band structure, creation of trap sites, and/or modification of trap site populations and distributions.[206,207]

Klug et al.[178] have found that transition metals can alter band positions despite invariance of band gap. Their modelling indicated that the energy of states generated by transition metals are dependent on what metal is used,[178] possibly to the extent of moving trap states near or within bands. Counterintuitive distinctions between $CH_3NH_3Pb(Mn)_{0.1}I_3$ and $CH_3NH_3Pb(Co)_{0.1}I_3$ identified here may point to complex modifications to band structure. Regardless, minimization of the deleterious impact of trap-assisted recombination and markedly improved quantum yield

Formula $CH_3NH_3Pb(T)_{0.1}I_3$	**n_0 (10^{17} cm^3)**	**k_1 (10^9 s^{-1})**	**k_2/n_0 (10^{-9} cm^3 s^{-1})**	**τ (ps)**	***%QY (calc.)***	***%QY (meas.)***
$CH_3NH_3PbI_3$ (Ref)	3.0	0.942	0.038	314.7	1.195	< 0.50
$CH_3NH_3Pb(Co)_{0.1}I_3$	2.1	2.477	0.030	84.8	0.302	*0.062*2)
$CH_3NH_3Pb(Fe)_{0.1}I_3$	2.1	3.160	0.020	66.5	0.132	*0.015*2)
$CH_3NH_3Pb(Mn)_{0.1}I_3$	3.0	3.783	0.620	75.6	4.686	1.8
$CH_3NH_3Pb(Ni)_{0.1}I_3$1)	3.2	*N.A.*	*N.A.*	*N.A.*	*N.A.*	*0.004*2)

1) Decay was close to instrumental response (~20 ps)

2) Values were below the resolution limit of the instrument and estimated by scaling PL spectra with measurable samples.

Table 6.4: PL metrics extracted from parametric optimization. Initial values for the fitting were given in ratio according to the measured QY values.

offered by $CH_3NH_3Pb(Mn)_{0.1}I_3$ make this system ideal for tuning material growth and properties for optoelectronic applications.

6.5 Conclusion

Study of a new class of hybrid organic-inorganic perovskite alloy was enabled through a deep morphological investigation revealing growth route to be the most significant variable controlling morphological evolution. We developed a drop-casting based technique to analyze material consequences of alloying with new species, and through this showed that Fe, Mn, Co, and Ni have comparably high solubility in $CH_3NH_3PbI_3$, comparable impacts on the lattice, and a comparably dramatic impact on growth route. Although DMSO is ideal in the solution state, we found that it causes CH_3NH_3I-PbI_2-DMSO formation which leads to the rod-like thin film morphology that a great deal of work in the perovskite field endeavours to circumvent *via* creative processing techniques like 2-step deposition and solvent washing. We found that transition metal inclusion allows direct perovskite nucleation to strongly compete with CH_3NH_3I-PbI_2-DMSO formation. Although we found that solution concentration, atmospheric composition, and annealing profile all impact the route through which transformation proceeds, CH_3NH_3I stoichiometry and magnetic field have unique optoelectronic consequences that should be considered when studying this class of perovskite alloy.

CH_3NH_3I stoichiometry and magnetic field were found to be secondary variables that have unique impacts on material quality in these systems, but as has been shown, synthetic variables like solution concentration and atmospheric conditions alter the balance between competing growth routes. Ultimately, growth route is the most significant controlling variable determining morphological development in these systems. The deleterious role that DMSO can play in perovskite growth identified by this work contradicts some opinions about simple benefits of solvent molecules and intermediates they create,[101] but as the work of Guo et al. demonstrates,[183] with careful kinetic control these intermediates can become navigable and possibly even beneficial.

That said, the transition metals studied here (Fe, Mn, Co, and Ni) allow direct perovskite nucleation to compete with CH_3NH_3I-PbI_2-DMSO formation (Figure 6.2 and 6.8), enabling high quality films without kinetically limited processes like solvent washing.

This extensive analysis of growth allowed us to minimize convolution from morphological issues and directly analyze the compositional impact of transition metal inclusion on optoelectronic properties of $CH_3NH_3PbI_3$. With Fe based alloys as a model system, we closely studied recombination behavior and its impact on photovoltaic performance and J-V hysteresis. Although this revealed that trap-assisted recombination induced by transition metal inclusion is problematic, extending this functional analysis to the other transition metals discussed revealed that Mn mitigates the impact of trap-assisted recombination inherent to this class of transition metal perovskite alloy and significantly enhances photoluminescence quantum yield. In addition to this functional analysis, this study also gives insight into other currently relevant aspects of perovskite design including the magnetic properties these transition metals impart,[192] the origin of complex J-V hysteresis,[185,208] the impact of morphological phenomena like CH_3NH_3I induced disorder[163,185,186] and field induced twinning,[191] and the roles of transformation route[STW-2,4] and solvent induced intermediates[183] in determining morphology. Methodology and insights developed herein provide a general approach for navigating the complexity of perovskite compositional modification.

This chapter definitively identifies the cause of the problematic perovskite morphology discussed at length in Chapters 2, 3, and 4. In addition to identifying the impact of solvent-perovskite co-crystal formation, this work also shows the functional impact of disorder induced by excess methylammonium iodide, an issue relevant to the work presented in Chapters 2, 3, and 4. Through the context provided by the conceptual and experimental survey of the periodic table offered in Chapter 5, we will expand the insight generated in this chapter to provide perspective on the larger challenge of Pb-replacement at the conclusion of Chapter 7.

6.6 Experimental Details

Materials. All precursors and solvents were purchased from Sigma-Aldrich and used without further purification, unless specified. Methylammonium iodide (CH_3NH_3I) and surfactant Bis-C_{60} were synthesized using our previously reported procedures.[STW-2,[209]]

Solution Preparation. All perovskite precursor materials were stored and weighed in a nitrogen filled glove box. Molarity of perovskite precursor solutions was defined as the total molarity of metal ions in solution, percent Fe was defined as atom percent Fe relative to total metal ions (Fe / (Fe + Pb)), and stoichiometry of methylammonium was varied as noted in the main text (x = 1, 0.9, & 0.8). After weighing out the appropriate amount of starting material, DMSO was added and the solution was stirred at 60 °C for 1 h. Solutions were then aged for a minimum of two days before filtration and use.

Notably, we used a 1 to 1 ratio between total metal ions in solution and methylammonium iodide to fabricate perovskite solutions for the work that precedes the stoichiometric optimization in Figures 6.1, 6.2, 6.3, 6.4, 6.5, 6.6, 6.8, and 6.9. For the remainder of the work, an optimized stoichiometry of 0.1 TI_2 : 0.9 PbI_2 : 0.9 CH_3NH_3I was used. All solutions were at room temperature and filtered with 0.45 µm PVDF filters before spin-coating.

Drop cast film fabrication: ~5 µL of 0.2 M perovskite solution in DMSO was deposited on ITO substrates at 90 °C in a glovebox. This was annealed for 2 hours at this temperature with a 10 minute nitrogen purge at the conclusion of annealing to ensure solvent removal.

1-step deposition for transition metal-incorporated perovskite films: The precursor solutions (~30 µl per substrate) were spin coated (5000 rpm, 60 s). For the data discussed in Figures 6.4, 6.5, and 6.8, films were immediately annealed at 90 °C for 15 min. For the majority of the other data discussed, films were first annealed at room temperature for 60 min followed by 90 ºC for 10 min. The one exception to this is for the final data presented (Figure 617, 6.18, 6.19, and 6.20), where a shorter room temperature annealing time of 20 minutes was used to allow the more efficient fabrication of a larger number of films. Films of different thicknesses were achieved by varying solution concentration from 0.6 M to 1.2M. Glovebox atmosphere was periodically purged to avoid CH_3NH_3I-PbI_2-DMSO formation. Also to limit the deleterious impact of DMSO, we used only ~30 uL per sample and only 1 to 2 samples per batch.

Solvent wash deposition for standard $CH_3NH_3PbI_3$ films: Precursor solutions were prepared by dissolving a 1:1 molar ratio of CH_3NH_3I and PbI_2 in mixed solvent (40 wt% / 1M) of dimethyl sulfoxide and γ-butrylactone (3:7 by volume); the mixture was then stirred at 60 °C for 12 h. Subsequently, they were spin coated (1000 rpm for 15 s, then 4000 rpm for 45 s) with 700 μL of toluene dropped in the last 15−20 s and annealed at 100 °C for 15 min.

*Perovskite growth under magnetic fields***.** Ceramic (ferrite) block magnets were purchased from Master Magnets, Inc. (item no. 07044, ~0.2 T). Two conditions were used for perovskite growth: low field and high field (Figure 6.12). Magnets of opposite orientations were placed side by side to increase field strength without increasing the height of the stack. For growth under both low and high fields, perovskite films were exposed to the appropriate field for the entire duration of growth which includes room temperature annealing, thermal annealing, and cooling to room temperature. Because ferrite is a thermal insulator, we preheated magnet stacks for at least an hour at a temperature above 100 °C to accommodate any thermal gradient. Exact annealing conditions vary as discussed in the main text (room temperature annealing vs. thermal annealing). Thermal annealing for all samples in this work was accomplished with an Isotemp heated magnetic stir plate (model number 11-100-16sh).

Vibrating Sample Magnetometry. A silicon wafer for perovskite deposition was cut and then wrapped in the amount of Scotch tape necessary to eventually encapsulate a perovskite film for measurement. The weight of the tape was recorded to be replicated for actual encapsulation later on. This substrate was then characterized with a Lakeshore vibrating sample magnetometer (VSM) with a Lakeshore 735 controller by varying applied field from 200 mT to -200 mT and then back to 200 mT to characterize a full hysteresis loop. The measurement began with brief soaking at 220 mT to make all measurements consistent. Tape was then removed from the silicon wafer and the wafer was scrubbed with hexane, acetone, and isopropanol. This was then plasma cleaned for a full 10 minutes immediately before perovskite deposition.

10 μL of 1 M perovskite solution was deposited (drop-cast) on this silicon wafer at 90 °C in a glovebox and annealed for 3 h. Annealing was concluded with a 10 min purge with nitrogen to ensure

solvent removal. Then, still in the glovebox, an amount of Scotch tape identical to that used initially was used to wrap and encapsulate the perovskite film. This was then once again characterized with the VSM via the same procedure discussed above. Signal from the substrate was then subtracted from the signal of the perovskite sample. By using the exact same piece of silicon wafer and same weight of tape, this subtraction allows all signals including the sample rod to be removed leaving only the signal from the perovskite film.

Photovoltaic Device Fabrication. Solar cells used here employed a device structure of Glass / ITO / PEDOT:PSS / "*Perovskite*" / $PC_{61}BM$ / Bis-C_{60} / Ag and were fabricated using procedures similar to those in our previous publications.[201,210] After cleaning the ITO-coated glass substrates, PEDOT:PSS (Baytron PVP Al 4083) films were spin coated (5000 rpm, 30 s) and annealed (150 ^{o}C, 15 min) in ambient atmosphere. All the subsequent layers were processed in a N_2-filled glovebox with relatively low O_2 levels (<10 ppm). Appropriate perovskite layers (choice of precursor solution and processing condition) were fabricated using the corresponding procedure mentioned above. $PC_{61}BM$ (15 mg/mL in chloroform) films were spin coated (4000 rpm, 60 s) and annealed (100 °C, 5 min) on top of perovskite. Subsequently, surfactant Bis-C_{60} (2 mg/mL in IPA) were spin coated at 3000 rpm for 30 s. Silver (Ag) electrodes (150 nm) were deposited by thermal evaporation under a vacuum pressure of 9×10^{-7} Torr with an evaporation rate of 2.0 Å/s; shadow masks were used to define the device area (3.14 mm^2).

Thin film characterization, microscopy, and X-ray diffraction. Thin film absorption measurements were performed using a UV-Vis spectrophotometer (Agilent Cary 5000). Film thicknesses were measured using a stylus profiler (Bruker DektakXT). The thickness of films deposited from 0.6 M, 0.8 M, 1 M and 1.2 M solutions were 80 ± 10 nm, 165 ± 9 nm, 230 ± 10 nm and 320 ± 8 nm respectively. An FEI Sirion scanning electron microscope was used for all SEM based characterization with 5 kV used for imaging and 20 kV used for EDS. A Bruker D8 Discover 2-D XRD with a Cu Kα source was used for all X-ray diffraction measurements. All XRD data that is directly compared in any given figure is integrated from 2D scans with identical integration parameters to allow quantitative comparison of peak heights and peak height ratios.

All XRD peaks were indexed by hand. Lattice parameters were characterized with a minimum of 15 clearly analyzable peaks. The evolutionary algorithm in the Solver package of Excel was used to minimize the sum of residuals squared produced between measured and calculated plane spacings to arrive at lattice parameters providing the best fit for the data assuming a tetragonal Bravais lattice. Rietveld analysis was done with MDI Jade and the reference PDF #01-083-7584. The space group is I4cm, with nominal fractional occupancies of Pb 4a, I 4a, and I 8c sites all equal to 1. To emulate three different possibilities for the location of transition metal inclusion, the appropriate transition metal atom was added to the structural model provided by PDF #01-083-7584 (Mn, Fe, Co, or Ni) in different locations. To emulate interstitial inclusion along the c-a plane, a transition metal (TM) was placed in the 8c Wyckoff site with shifts in the x and z directions of 0.25 and 0.24 respectively. To emulate interstitial inclusion along the a-b plane, a TM was placed in the 4b site with no shift. To emulate direct Pb substitution by TM atoms, a TM was placed directly on the 4a site with no shift, and fractional occupancy of Pb and TM sites was set to .5 as a starting value. The background was fit with a refinable polynomial and constant FWHM was assumed. Fitting was done systematically, in the order of background, specimen displacement, scale factor, preferred orientation (110), lattice parameter, and finally fractional site occupancy.

I-V Characterization. Standard *I-V* measurements were performed using a SMU (Keithley 2400) with a fixed scan rate (0.01 V step size, 100 ms delay time). For varying scan rate, the step size was unchanged (0.01 V) and the delay time was changed from 10 ms to 1000 ms. Every measurement ensued an uninterrupted sequence of forward and reverse scans (reverse bias (RB) → forward bias (FB) → RB) and the scan range was fixed as -0.2 V to 1 V, unless specifically mentioned. The devices were stored and measured inside a N_2-filled glovebox to avoid any complications from potential degradation issues. For light I-V characteristics, AM 1.5 solar illumination was obtained using a Class A solar simulator (Solar light 16S-300). A NIST-certified Si-photodiode with KG5 filter was used for 1 Sun (100 mW/cm^2) calibration. Stabilized power output was obtained by applying a constant voltage corresponding to the maximum power point and measuring the current response as a function of time. A minimum of 8 devices were used to calculate statistics for solar cell parameters. For consistency, the best device in a given condition was used to determine *Hysteresis Factor (HF)* using a previously reported procedure.[205]

Illumination intensity (*G*) dependent measurements were performed using a set of neutral density filters. *I*-*V* characteristics were measured under seven different intensities ranging between 0.5 mW/cm^2 to 100 mW/cm^2. A slight difference in V_{OC} and J_{SC} dependence on *G* was observed between forward and reverse because of the persistent hysteresis in *I*-*V* curves. However, the reported trends (Figures 6.14 and 6.15) are consistent regardless of scan direction. For consistency and clear interpretation, reverse scan data were used for all the analysis reported in this work, unless specifically mentioned. The linear fits of data had high degree of accuracy, with the R^2 values generally being in the range of 0.96 – 1. The analysis and interpretation of illumination intensity dependent I-V data are in accordance with previously reported solar cell device physics related literature.[195–197,211–217]

Transfer Matrix Optical Modeling. The real (*n*) and imaginary (*k*) part of the refractive index for different layers in the device stack were obtained using Spectroscopic Ellipsometry (Woollam-M-2000). A custom-made Matlab program was used to perform transfer matrix optical simulations for obtaining the active layer absorption as a function of thickness. Theoretical J_{SC} corresponding to different active layer thicknesses were calculated using the modelled absorption, assuming 100% internal quantum efficiency.

Photoluminescence Spectroscopy and Modeling. TrPL was taken by using the Libra laser system (50 fs FWHM at 1kHz repetition rate, 1mJ/cm^2, 800 nm fundamental wavelength) combined with collection optics, spectrometer and streak camera (Hamamatsu model C-10627). Streak camera and laser source were synchronized through synchronous delay generator (C-10647) and jitters were regulated by delay unit (C1097-05). The minimum time resolution is around 20 ps. The excitation fluence was modulated by 2 consecutive neutral density filters. The diameter of spot size is 1 mm. The samples for trPL were all encapsulated with glass slides and epoxy.

We assumed band structure were dominated by the invariant metal halide framework in perovskite alloys, in which direct bandgap facilitates radiative bimolecular recombination.

$$\frac{dn}{dt} = -k_1 n - k_2 n^2$$

$$\frac{I(t)}{I_0} = k_2 nN + k_2 n^2$$

Where k_1 is total monomolecular decay rate through both non-radiative (k_1^{nr}) and radiative decay (k_1^r) pathway; $k_1 = k_1^{nr} + k_1^r N$. k_2, *n* and *N* correspond to the product of initial photocarrier density (n_0) and bimolecular recombination rate ($\overline{k_2}$), normalized carrier density of electron and holes with respect to n_0 and the relative density of the emissive monomolecular recombination center, respectively. n_0 was calculated by Beer-Lambert's law, $n_0 = (I_{ex}\lambda/hc)(1 - e^{-\alpha L})/L \sim I_{ex}\lambda/Lhc)$, where I_{ex} is fluence at wavelength λ, α is absorption coefficient at λ and L is thickness. The differential equation was numerically solved with parametric optimizations to fit the decay data. Assuming the dominance of bimolecular recombination in emission at the excitation fluence near the onset of amplified spontaneous emission, the characteristic lifetime (τ) and PL quantum yield (QY) can be acquired as follows,

$$\tau = \frac{1}{k_1 + \overline{k_2} n_0}$$

$$QY = \frac{\overline{k_2} n_0}{k_1 + k_2^0 n_0}$$

Provided that initial carrier densities n_0 are almost identical for all films (complete absorbance) and the non-radiative relaxations are the major decay pathway, relative change of decay rate and QY indicate intrinsic difference of bimolecular recombination, possibly originating from carrier mobility, dielectric environment as well as the change of density of state and band structure.

Chapter 7. CONCLUSION: Perspective for Continued Perovskite Design

**Figures in this chapter have been reproduced from STW-1, STW-2, STW-3, STW-4, and STW-5 with permission from the respective publishers.*

The fundamental studies of connections between $CH_3NH_3PbI_3$ composition, growth, and morphology offered in Chapters 2, 3, and 6 were complimented by the conceptual exploration of perovskite growth in Chapter 4 and the survey of the periodic table offered in Chapter 5. During the course of this more fundamental work, the diversity of the Jen group at the University of Washington afforded the opportunity to contribute to a wide variety of research connected to the larger scale development of hybrid perovskite photovoltaics, organic photovoltaics, and functional electronic materials in general. This included efforts toward rational perovskite solar cell design through functional investigations of abnormal *J*-*V* hysteresis,[201] interaction at perovskite/fullerene interfaces,[210] and interaction at perovskite/oxide interfaces[218] along with works aimed at developing organic[219] and inorganic[220] charge transporting interlayers for realizing high-performance perovskite photovoltaics. Efforts to adapt perovskite[221] and organic[222] solar cell fabrication to a scalable production technique were complimented by investigations of microscopic processing-structure-property relationships in organic bulk heterojunction absorbers,[223] small molecule based absorbers,[224] and functional fullerene assemblies.[225]

In addition to the examinations of relationships between $CH_3NH_3PbI_3$ growth, morphology, and function presented here,[STW2-5] studies of the impact of alkyl halide additives[68,146] and anti-solvent composition[144] on perovskite growth and performance informed continued material design. Work aimed at tuning halogen composition to increase perovskite band-gap[226] was complimented by efforts to stabilize large-band gap perovskite absorbers under illumination.[170] The compositional studies presented here were shaped in part by contributions to studies aimed at integrating Sr[227] and Sn[173,228] into $CH_3NH_3PbI_3$ to reduce material toxicity while maintaining performance and stability. This is in addition to unpublished, failed attempts to integrate Cu into $CH_3NH_3PbI_3$.

The hybrid perovskite photovoltaic research community has grown rapidly, as has our understanding of this still relatively new material system. As was discussed in Chapter 1,[STW-1] fundamental material challenges still impede commercialization. Efforts to control material properties through compositional design simultaneously impact material growth, structure, and resulting functionality. This complexity has complicated rational material development.

This chapter consolidates the understanding developed over the course of this dissertation with a focus on the relationships established between $CH_3NH_3PbI_3$ composition, growth, and structure. We then leverage this to provide perspective on the larger challenge of Pb-replacement. Each section that follows reproduces select figures from the material being summarized to facilitate brief discussion about how the understanding of perovskite processing-structure-property relationships has evolved through this work.

7.1 Role of Halogen in Mediating $CH_3NH_3PbI_3$ Transformation

The first experimental study presented was focused on the impact of the chloride ion on $CH_3NH_3PbI_3$ growth (Chapter 2). We found that the presence of Cl^- enables and encourages the formation of a chloride rich intermediate phase that then directs continued transformation. Because of the dynamic, time dependent complexation and aggregation occurring in perovskite precursor solutions with chloride and iodide, morphological evolution depends on how this spectator ion (Cl^-) is introduced to the system. The presence of Cl^- fundamentally shifts growth route, but ultimately this halogen ion is replaced by iodide and almost completely volatilizes out of the growing film.

The rod-like perovskite morphology depicted in Figure 7.1 for the case of $CH_3NH_3PbI_3$ 1-step growth from solution (left) is an excellent example of the persistently troublesome morphology that much of the perovskite field has endeavored to circumvent through creative innovations in processing. As was demonstrated in Chapter 3, this troublesome morphology is inadequate for photovoltaic device preparation. Chapter 3 further showed that simply spreading material out flat on a substrate through rapid solvation with methylamine vapor increases overall solar cell performance significantly (~3-12% PCE) **(**Figure 3.3) despite the significant decreases in grain size caused by this kind of post-deposition treatment (Figure 3.1).

The work presented in Chapter 6 revealed why the troublesome rod-like morphology depicted at the left in **Figure 7.1** has proven to be such a common problem in perovskite solar cell development. This morphology is generated by the formation of a solvent-perovskite co-crystal. Both solvents commonly used for perovskite growth (DMF and DMSO) are particularly prone to this tendency, thus it is unsurprising that this morphology is a commonly encountered limitation of direct perovskite growth from solution. As Figure 7.1 depicts, the change in growth route provided by chloride addition circumvents growth through these solvent intermediates, resulting in a higher quality film. That said, this introduces complex kinetics that must be carefully navigated to ensure a product with the desired quality and properties.

Chapter 2 showed that Pb-Cl bond formation leads to a self-assembly event that circumvents transformation through solvent-perovskite intermediate phases, but this aggressive control over transformation route does not extend to growth in the presence of Br. While the increased hardness of the

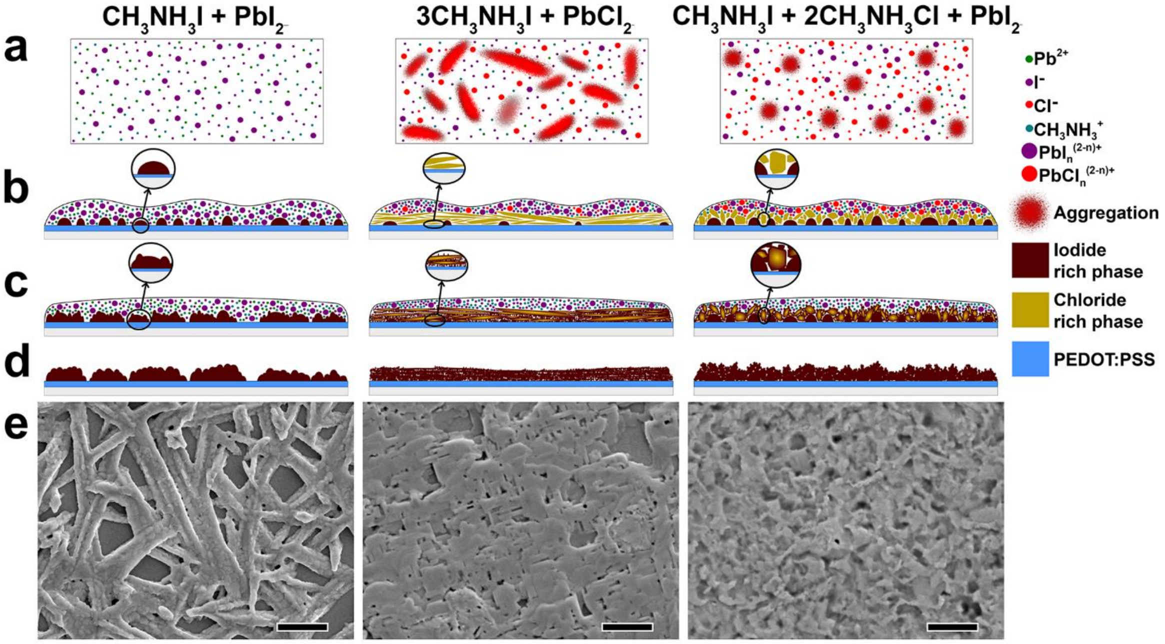

Figure 7.1: ***Reproduced from Chapter 2, Figure 2.18 (STW-2)*** Simplified schematic representations of film formation in the three compositional extremes studied: (a) attempts to portrait the state of the solution in each case. The sizes of aggregates represented in the cases of **3MAI + $PbCl_2$** and **MAI + 2MACl + PbI_2** are intended to differ by approximately an order of magnitude. (b) illustrates nucleation during and immediately after deposition, (c) illustrates each system as it evolves during annealing, and (d) represents the film morphology after annealing is complete. (e) SEM images representative of the morphologies illustrated schematically in (d). All scale bars are 2 μm. The case of **3MAI + $PbCl_2$** is highly idealized, and as previously discussed a variety of morphologies are often observed together (Figure 2.1).

Pb-Cl bond is enough to circumvent the impact of these solvent-perovskite intermediates, the work we have done surrounding bromine inclusion in $CH_3NH_3PbI_3$[170,226] shows that Pb-Br bond formation does not control growth as aggressively.[226] That said, it is clear that halide composition impacts $CH_3NH_3PbI_3$ transformation in solution, during deposition, and even during annealing in the solid state (Figure 7.1).

7.2 Role of CH_3CH_2 and CH_3CH_3I in Mediating $CH_3NH_3PbI_3$ Transformation

Chapter 3 presented a study of a post-deposition methylamine (CH_3NH_2) vapor treatment and its impact on perovskite morphology. Once again, the troublesome morphology generated by 1-step perovskite deposition from solution was circumvented, but in this case not until after formation of this rod-like morphology had already occurred (**Figure 7.2)**. Chapter 3 shows that CH_3CH_2 has the ability to fully solvate $CH_3NH_3PbI_3$ at high concentrations, and it is this solvation and subsequent recrystallization that is the source of the utility of the post-deposition treatment discussed in Chapter 3. That said, the ability of CH_3NH_2 vapor to solvate $CH_3NH_3PbI_3$ extends to excess CH_3NH_3I[51,116] which leads to morphological problems in the solid state that must be accounted for in the analysis and optimization of $CH_3NH_3PbI_3$ films (Chapter 6).

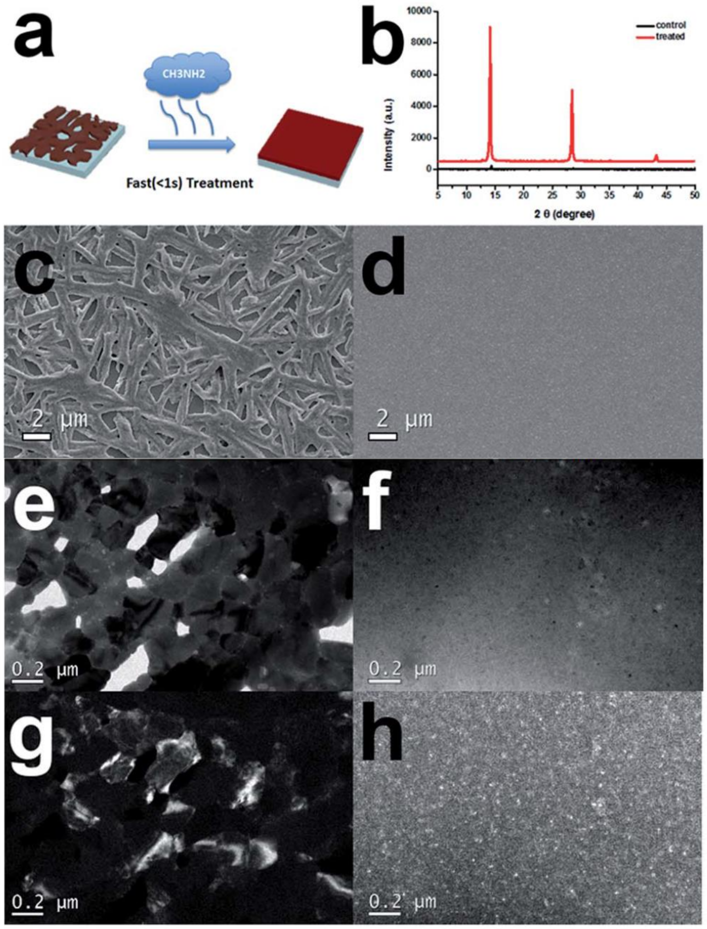

Figure 7.2: ***<u>Reproduced from Chapter 3, Figure 3.1 (STW-3).</u>*** Comparison of a $MAPbI_3$ film before and after exposure to CH_3NH_2 vapor (a): (b) XRD, (c-d) SEM, (e-f) Bright field TEM, and (g-h) dark field TEM.

Chapter 2 briefly investigated the impact of excess methylammonium on perovskite structure, and it was found that excess CH_3NH_3I does prevent the formation of short and long range crystalline order resulting in what appears to be an amorphous film (**Figure 7.3a** and **d**). Chapter 6 showed the functional consequences of this kind of disorder through solar cell device analysis (Figure 6.10 and 6.11), and Chapter 4 developed the concept of the role of an amorphous state during growth and its dependence on CH_3NH_3I concentration. While useful, it should be said that this assumption of an amorphous state is an approximation of a more complex reality.

It has been shown that the phase space of $CH_3NH_3PbI_3$ becomes complex when methylammonium iodide concentration is considered a variable rather than a constant.[163] There are a variety of complex but discrete phases that complicate structural evolution when methylammonium iodide concentration changes during growth, and this complexity is magnified by the prominence of solvent-perovskite co-crystalline phases discussed in Chapters 4 and 6. A common result of perovskite transformation through these complex

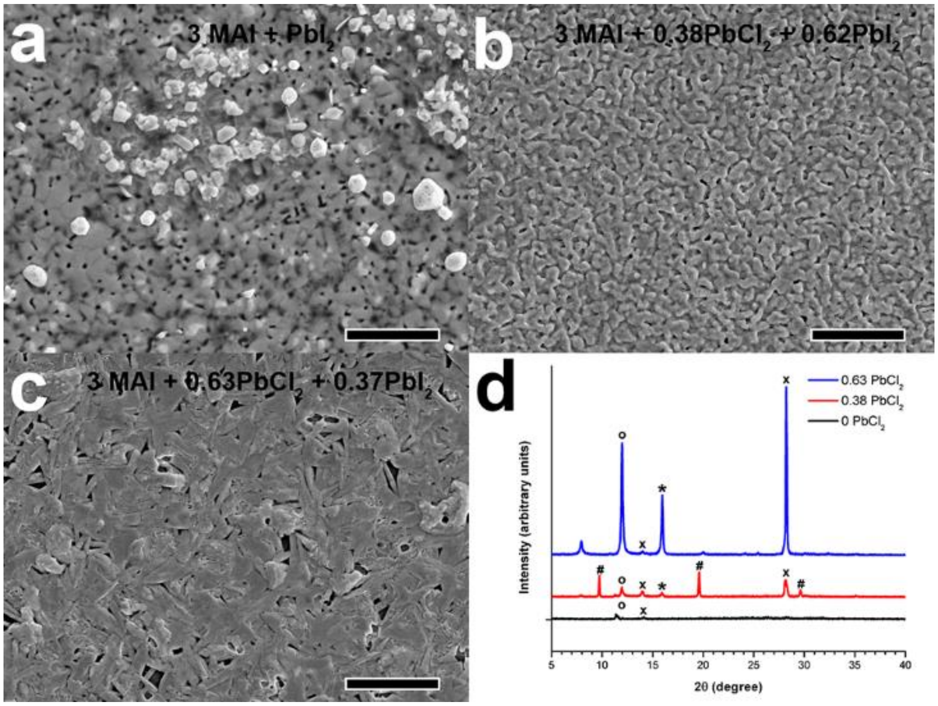

Figure 7.3: **Reproduced from Chapter 2, Figure 2.13 (STW-2).** (a-c) Retarded film evolution in systems containing excess methylammonium, all scale bars are 5 µm. (d) shows XRD patterns of (a)-(c), with **o** indicating PbI_2, **x** indicating $MAPbI_3$, ***** indicating the template phase, and # indicating MAI. *Although this figure is built around showing the impact of MAI on growth with chloride, (a) and (d) both show an example of the morphology that results from a large excess of methylammonium iodide (3 : 1 MAI : PbI_2) without the presence of chloride. Both SEM and XRD indicate a material with very little crystalline structure and long range order.*

pathways is a material with low crystallinity that lacks robust long range order and thus appears partially amorphous.

Approaching the challenge of perovskite growth with a full picture of perovskite phase space allows rational tuning of processing and resulting structure. In Chapter 2 we touched on the structural consequences of excess CH_3NH_3I, and in Chapter 6 we discussed functional consequences of the disorder induced by excess CH_3NH_3I. In Chapter 3, we showed how interaction with CH_3NH_2 is mediated by the composition of the organic sublattice, and we showed how the morphological impact of CH_3NH_2 vapor treatment is a function of vapor pressure during exposure. Despite the reduction in grain size apparent in Figure 7.2, the methylamine treatment explored in Chapter 3 was ultimately beneficial for solar cell function because of its ability to eliminate the troublesome rod-like perovskite morphology generated by growth through solvent-perovskite intermediate states (Figure 7.2c, e, and g).

7.3 Role of Metal Cation in Mediating $CH_3NH_3PbI_3$ Transformation

Chapter 2 showed that the coordination structure determined by the metal cation is key in growth and Chapter 3 showed that the metal cation imparts the intrinsic reactivity toward methylamine and methylammonium necessary to build the perovskite lattice. Chapters 5 and 6 leveraged this insight toward the more challenging goal of modifying the metal cation site in $CH_3NH_3PbI_3$. While this effort was motivated in part by the need to replace Pb and reduce $CH_3NH_3PbI_3$ toxicity, one of the most important products of this effort

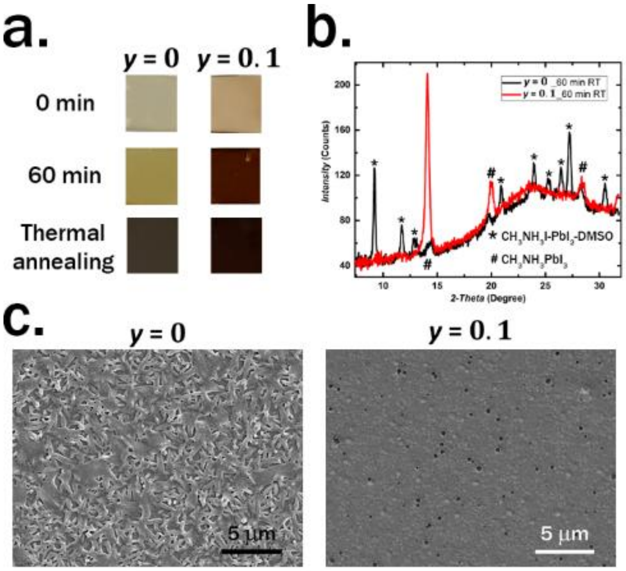

Figure 7.4: ***<u>Reproduced from Chapter 6, Figure 6.8 (STW-5).</u>*** Characterization of competition between CH_3NH_3I-PbI_2-DMSO formation and direct $CH_3NH_3PbI_3$ transformation pathways *via* (**a**) photographs, (**b**) XRD of films mid transformation (60 min of room temperature annealing), and (**c**) SEM. *This shows how 10 at% transition metal inclusion enables direct perovskite nucleation and high-quality film formation.*

was the insight generated into the fundamental nature of hybrid perovskite growth processes.

Chapter 4 showed that achieving direct $CH_3NH_3PbI_3$ nucleation is a significant challenge regardless of which processing method is employed, but Chapter 6 showed that direct $CH_3NH_3PbI_3$ nucleation becomes possible with the addition of certain top row transition metals (Me, Fe, Co, and Ni). Chapter 6 also showed that direct perovskite nucleation is capable of generating high quality films with high coverage, high crystallinity, and almost completely coherent crystal orientation (**Figure 7.4**) while growth through solvent-perovksite co-crystalline states leads to significant degradation of long range order (**Figure 7.5a-c**), short range order (Figure 7.5d-f), and macroscopic film quality (Figure 7.5g). Through this effort, we showed that CH_3NH_3I-PbI_2-DMSO and/or CH_3NH_3I-PbI_2-DMF formation is the mechanistic origin of the troublesome rod-like morphology encountered ubiquitously throughout the field.

Figure 7.6 is an adaptation of Figure 4.6 that consolidates the understanding this dissertation generates into perovskite growth routes and their dependence on composition. This figure has been modified from Chapter 4 to reflect the improved understanding generated in the course of this dissertation. Figure 7.6 illustrates four commonly employed perovskite growth routes and their structural consequences, as well as the intermediate states that mediate structural evolution in each case. Chapter 4 discusses the meaning of

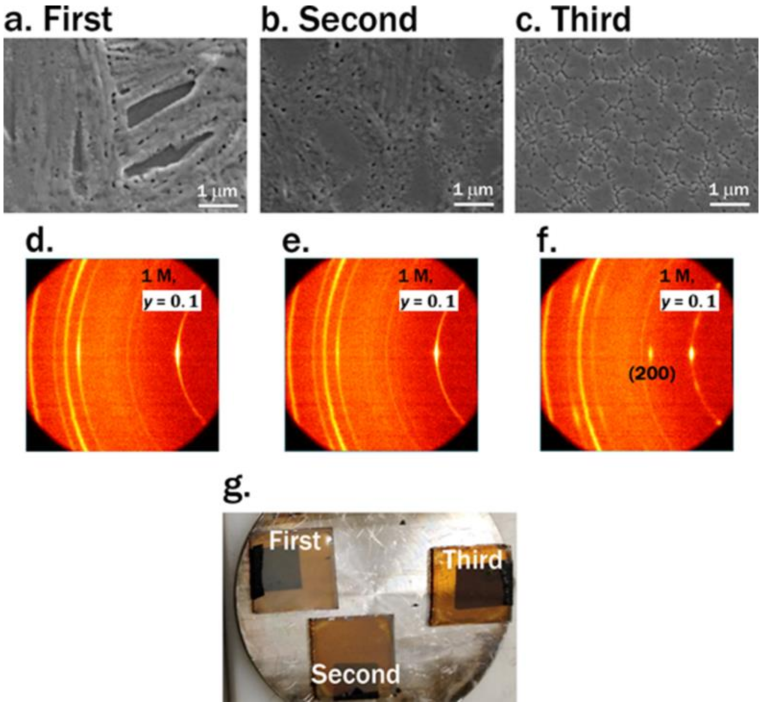

Figure 7.5: ***Reproduced from Chapter 6, Figure 6.7 (STW-5).*** Morphological influence due to back conversion under a DMSO atmosphere shown via (a-c) SEM micrographs, (d-f) 2D XRD showing crystal orientation and (g) photographs; First, Second and Third correspond to the order of spin coating with samples being exposed to varying DMSO amounts resulting from subsequent film fabrication. *The impact of the solvent molecule is most severe in the first film fabricated which was exposed to two subsequent depositions nearby. The impact of the solvent molecule is least severe in the third film fabricated which was not exposed to any further depositions.*

this representation in much more detail, but here this figure serves to highlight the differences between (**A**) growth through unoptimized 1-step deposition, (**B**) growth in the presence of a large excess of CH_3NH_3I, (**C**) growth using solvent engineering / transition metal inclusion, and (**D**) growth in the presence of chloride. The modifications made to parts (**A**) and (**C**) of this figure reflect the improved understanding developed in Chapter 6.

(**A**) has been altered to more accurately show the role that solvent-perovskite co-crystalline phases play in generating the troublesome rod-like morphology encountered during 1-step deposition from solution. (**C**) has been altered to more accurately reflect the remarkable ability of both solvent engineering

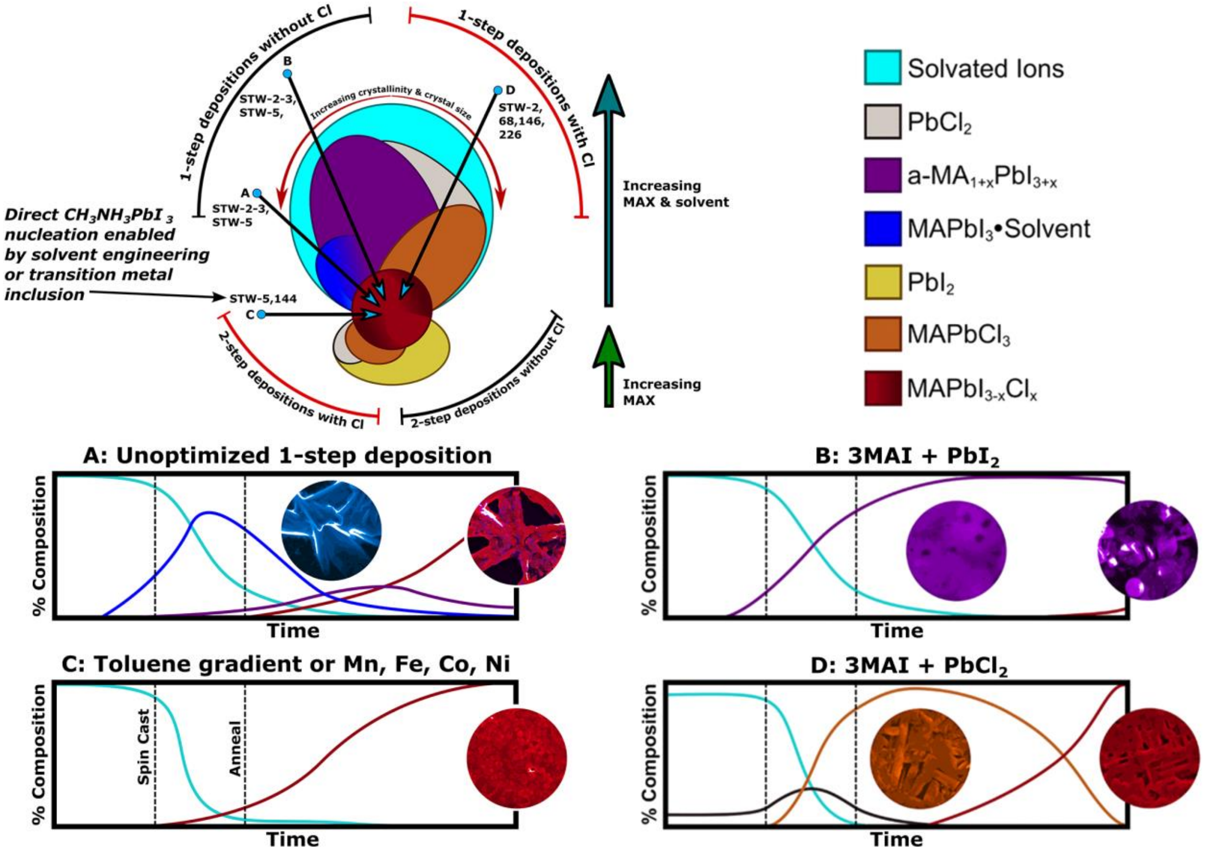

Figure 7.6: ***Adapted from Chapter 4, Figure 4.6 (STW-4)*****:** Detailed representation of select 1-step solution deposition routes using the process-time-transformation (PTT) curve developed in Chapter 4. This figure schematically shows growth routes inherent to (**A**) unoptimized 1-step deposition, (**B**) deposition with a large excess of MAI, (**C**) deposition with solvent engineering / transition metal inclusion, and (**D**) deposition with chloride provided by a $PbCl_2$ salt. Intermediate phases relevant during growth and final film morphology are shown as a function of time. *Parts (**A**) and (**C**) of this figure have been modified from their original, published form to more accurately represent the improved understanding generated through the work in this dissertation. (**A**) has been modified to show the role that $MAPbI_3$·Solvent phases play in generating the troublesome rod-like thin film morphology encountered throughout the field. (**C**) has been modified to more accurately represent the remarkable ability of solvent engineering and transition metal inclusion to enable direct perovskite nucleation.*

and transition metal inclusion to facilitate growth through direct perovskite nucleation. Chapter 6 showed that transition metal inclusion enables direct perovskite nucleation, and extending this insight to our previous work with solvent engineering[144] shows that the use of toluene during perovskite deposition similarly discourages CH_3NH_3I-PbI_2-DMSO formation and encourages direct perovskite nucleation.

7.4 Perspective for Continued Effort Toward Pb-Replacement and Commercialization

The systematic approach to element selection presented in Chapter 5 established that a class of closely related transition metals (Mn, Fe, Co, and Ni) readily becomes integrated into $CH_3NH_3PbI_3$. Chapter 6 presented extensive effort toward deconvoluting the compositional and morphological impact of these transition metals on $CH_3NH_3PbI_3$ functionality, and through this effort it became possible to characterize the impact of specific elemental choice on material performance (Figure 6.18). Although we found that trap-assisted monomolecular recombination within the perovskite bulk is an impact of transition metal inclusion (Figure 6.15), we also found that Mn both circumvents this limitation and significantly increases emissivity.

Despite this insight, we found that the simple assumption that first row transition metals (Fe, Mn, Co, and Ni) directly replace Pb does not adequately explain the behavior of these systems. While Pb replacement may still be a possibility, it cannot be the only mechanism responsible for transition metal inclusion in $CH_3NH_3PbI_3$. This issue combined with the problematic trap-assisted recombination in these systems (Figure 6.15) significantly impacts the broader effort toward Pb-replacement.

While the work in Chapters 5 and 6 contributes significant understanding to the impact of composition on perovskite growth and resulting structure, it also paints a somewhat grim picture for efforts toward Pb-replacement. The transition metals studied in Chapter 6 do not unambiguously replace Pb, and this class of metal was the only set of elements that did not exhibit aggressive phase separation in Chapter 5. While Mn, Fe, Co, and Ni do not effectively address the challenge of Pb-replacement themselves, the work in Chapters 5 and 6 along with other work done in the course of this dissertation[173,,227,228] provides perspective on continued efforts to replace Pb.

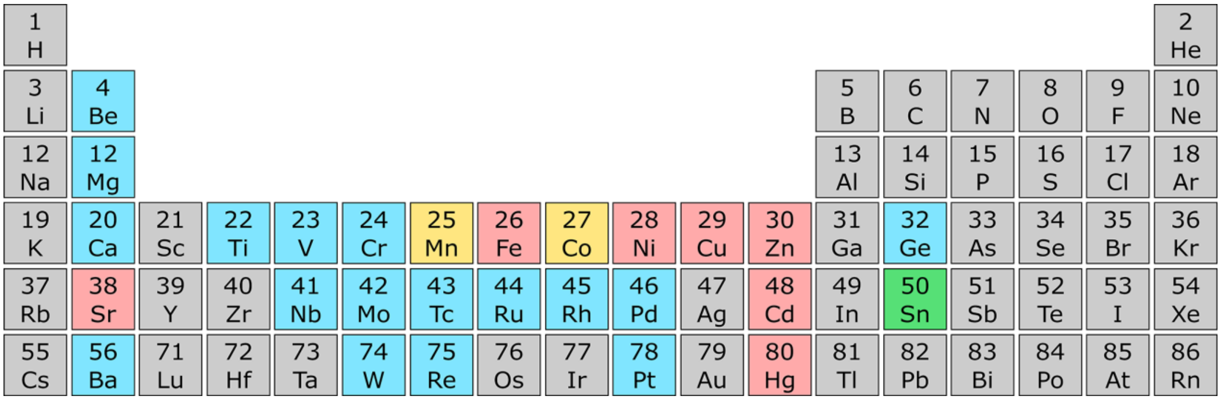

1 H																	2 He
3 Li	🟦 4 Be											5 B	6 C	7 N	8 O	9 F	10 Ne
12 Na	🟦 12 Mg											13 Al	14 Si	15 P	16 S	17 Cl	18 Ar
19 K	🟦 20 Ca	21 Sc	🟦 22 Ti	🟦 23 V	🟦 24 Cr	🟨 25 Mn	🟥 26 Fe	🟨 27 Co	🟥 28 Ni	🟥 29 Cu	🟥 30 Zn	31 Ga	🟦 32 Ge	33 As	34 Se	35 Br	36 Kr
37 Rb	🟥 38 Sr	39 Y	40 Zr	🟦 41 Nb	🟦 42 Mo	🟦 43 Tc	🟦 44 Ru	🟦 45 Rh	🟦 46 Pd	47 Ag	🟥 48 Cd	49 In	🟩 50 Sn	51 Sb	52 Te	53 I	54 Xe
55 Cs	🟦 56 Ba	71 Lu	72 Hf	73 Ta	🟦 74 W	🟦 75 Re	76 Os	77 Ir	🟦 78 Pt	79 Au	🟥 80 Hg	81 Tl	82 Pb	83 Bi	84 Po	85 At	86 Rn

Figure 7.7: Periodic table summarizing all metals that possess a 2+ oxidation state (actinides and lanthanides are omitted). **Blue** fields indicate elements that have not been directly studied through the research that led to this dissertation. **Red** fields indicate elements that have limited potential to successfully replace Pb in $CH_3NH_3PbI_3$. **Yellow** fields indicate elements that may be problematic in attempts to replace Pb. **Green** fields indicate elements that readily replace Pb.

Figure 7.7 summarizes all metals in the periodic table that support a 2+ oxidation state. In Figure 7.7, we have indicated which elements have not been studied directly in the course of this dissertation. Among the elements that have been explored directly, we qualitatively indicate the degree to which the element has the potential to replace Pb in $CH_3NH_3PbI_3$ without complication.

As was discussed in Chapter 5, the alkaline earth metals in column 2 of the periodic table are not ideally suited to replace Pb because of their highly ionic bonding. We had the opportunity to see how this issue complicates efforts to replace Pb in our attempt to integrate Sr into $CH_3NH_3PbI_3$.[227] Although we have not studied the majority of these elements directly, we suggest that Pb-replacement cannot be simply achieved with this family of metals.

Also as discussed in Chapter 5, the nature of bonding in strongly molecular metal halides like $TiCl_4$ makes the use of elements like Ti potentially prohibitive. Nearby candidates V, Cr, Nb, Mo, and W are potentially interesting, but their 2+ oxidation states are very fragile relative to the other transition metals discussed. Although we haven't studied these species directly, they likely don't have the ability to replace Pb in $CH_3NH_3PbI_3$ without significant complication.

As we continue to move across the transition metals, we come to the four elements studied in Chapter 6 (Mn, Fe, Co, and Ni). Although we did find that these species do readily become integrated into $CH_3NH_3PbI_3$ up to relatively high concentrations, we also found that it is difficult to pinpoint what site within the perovskite lattice that they preferentially occupy. Although a certain extent of Pb-replacement is possible in these systems, these small transition metals do not prefer substitution on the Pb-site strongly enough to make them simple solutions for the challenge of Pb-replacement. That said, while Fe and Ni have strongly negative optoelectronic impacts on $CH_3NH_3PbI_3$ functionality, Co and Mn lessen the magnitude of these problems making them more attractive avenues for future work.

The Cu and Zn families of elements are each potentially interesting species for exerting control over perovskite functionality, but in terms of the specific goal of Pb-replacement, both these classes of elements are problematic. As discussed in Chapter 5, the Cu family of elements does not have a stable 2+ oxidation state which results in the aggressive formation of CuI in both solution and solid states, a phenomenon we studied in unpublished work that in part led to the results presented here. Additionally, Chapter 5 shows that the entire Zn family of transition metals aggressively phase separates rather than becoming readily integrated into $CH_3NH_3PbI_3$.

Although elements like Tc, Pd, and Pt support the formation of extended coordination polymers with halide ions and organic species, the chemical behavior of these heavier transition metals quickly becomes complex. While Tc and Re have been found to support 2+ oxidation states in the presence of halogens, these states involve metal-metal bonding and are rarely stable with heavier halogens like iodide. By virtue of the impact of transition metal electronic structure on $CH_3NH_3PbI_3$ functionality explored in Chapter 6 (Figure 6.15 and 6.18), caution should be used when exploring Ru, Rh, Pd, and Pt even though their 2+ oxidation states are far more robust than those supported by Tc and Re.

Both through our own work[173,228] and the larger efforts of the field, it is clear that Sn is a viable candidate for Pb-replacement while its neighbor Ge is too unstable in the 2+ oxidation state to have the same potential. Although Pb replacement with Sn is complicated by a strong tendency toward oxidation into the 4+ state, the work presented here suggests that Sn is the only metal in the periodic table with a reasonable chance of leading to stable, high-performance, Pb-free hybrid perovskite solar cells (PVSCs).

To reiterate the importance of compositional design in the field's overall effort toward PVSC commercialization, a figure from STW-1 is reproduced below (**Figure 7.8**). The increased understanding this dissertation offers with regard to the impact of compositional engineering on perovskite growth, morphology, and functionality is intended to make compositional engineering a more powerful tool for rationally designing technologically relevant hybrid organic-inorganic perovskites at the atomic scale. This level of rational design is becoming increasingly necessary as we continue to address fundamental material challenges like Pb-toxicity, *J*-*V* hysteresis, and stability in pursuit of eventual PVSC technology translation.

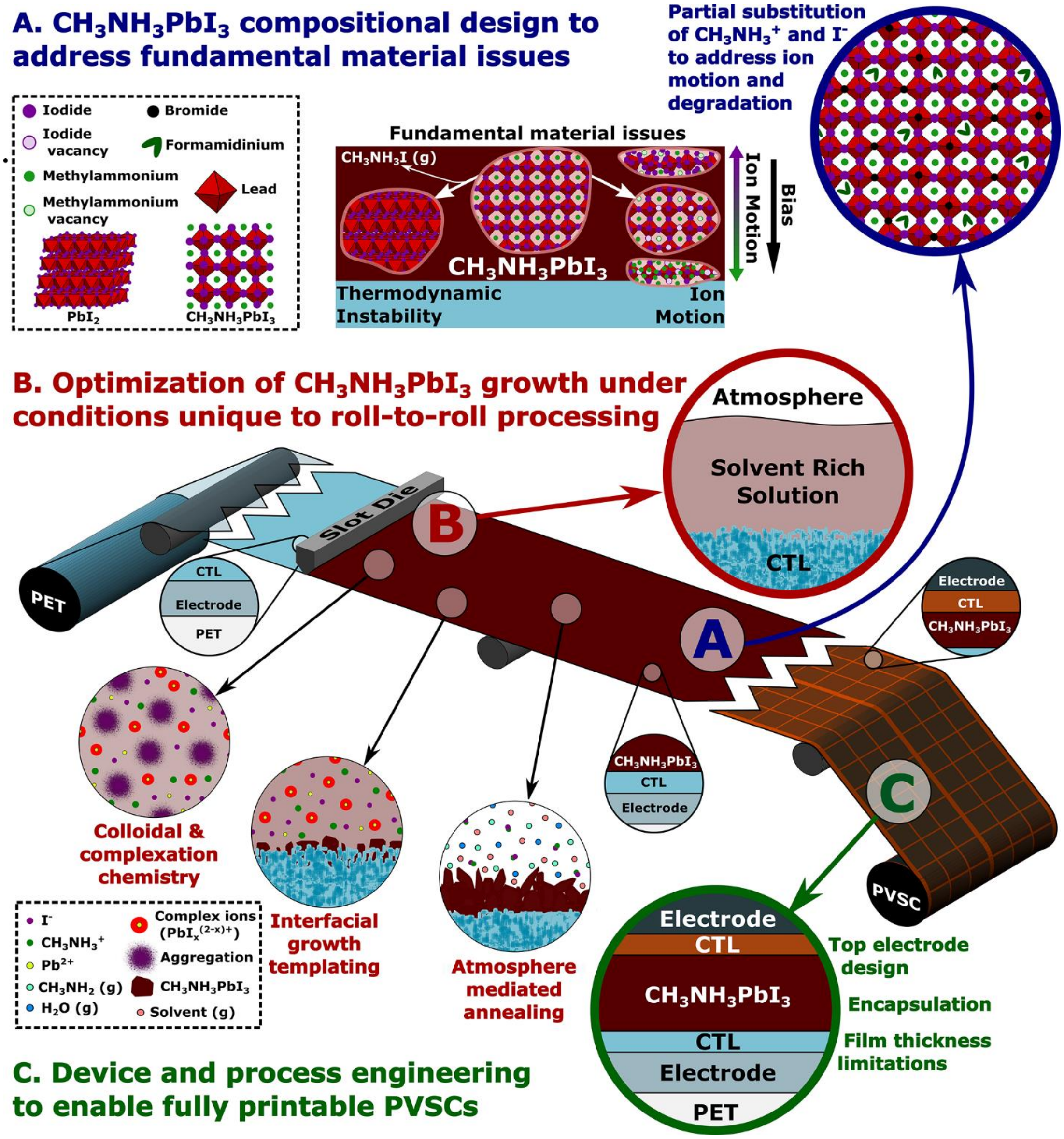

Figure 7.8. ***<u>Reproduced from Chapter 1, Figure 1.2 (STW-1).</u>*** Summary of research directions necessary to fuel PVSC technological translation *via* slot die R2R coating. (A) material engineering can address intrinsic ion diffusivity and degradation of $CH_3NH_3PbI_3$, (B) optimization of perovskite growth under R2R conditions is necessary to reach performance requirements, and (C) device engineering is required to extend device life and expand the material toolbox for PVSC design.

BIBLIOGRAPHY

First and co-first author works comprising this dissertation:

STW-1: S. T. Williams, A. Rajagopal, C.-C. Chueh, A. K.-Y. Jen, *J. Phys. Chem. Lett.* **2016**, *7*, 811.

STW-2: S. T. Williams, F. Zuo, C.-C. Chueh, C.-Y. Liao, P.-W. Liang, A. K.-Y. Jen, *ACS Nano* **2014**, *10*, 10640.

STW-3: T. Zhao, S. T. Williams, C.-C. Chueh, D. W. deQuilettes, P.-W. Liang, D. S. Ginger, A. K.-Y. Jen, *RSC Adv.* **2016**, *6*, 27475.

STW-4: S. T. Williams, C.-C. Chueh, A. K.-Y. Jen, *Small* **2015**, *11*, 3088.

STW-5: S. T. Williams, A. Rajagopal, S. B. Jo, C.-C. Chueh, T. F. L. Tang, A. Kraeger, A. K.-Y. Jen, *J. Mater. Chem. A* **2017**, *5*, 10640.

Other references:

[1] A. Kojima, K. Teshima, Y. Shirai, T. Miyasaka, *J. Am. Chem. Soc.* **2009**, *131*, 6050.

[2] M. H. Du, *J. Mater. Chem. A* **2014**, *2*, 9091.

[3] G. Giorgi, J.-I. Fujisawa, H. Segawa, K. Yamashita, *J. Phys. Chem. C* **2014**, *118*, 12176.

[4] J.-W. Lee, D.-J. Seol, A.-N. Cho, N.-G. Park, *Adv. Mater.* **2014**, *6*, 4991.

[5] A. Amat, E. Mosconi, E. Ronca, C. Quarti, P. Umari, M. K. Nazeeruddin, M. Grätzel, F. De Angelis, *Nano Lett.* **2014**, *14*, 3608.

[6] O. Knop, R. E. Wasylishen, M. A. White, T. S. Cameron, M. J. M. V. Oort, *Can. J. Chem.* **1990**, *68*, 412.

[7] E. J. Juarez-Perez, R. S. Sanchez, L. Badia, G. Garcia-Belmonte, Y. S. Kang, I. Mora-Sero, J. Bisquert, *J. Phys. Chem. Lett.* **2014**, *5*, 2390.

[8] S. González-Carrero, R. E. Galian, J. Pérez-Prieto, *Part. Part. Syst. Charact.* **2015**, *32*, 709.

[9] J. Feng, B. Xiao, *J. Phys. Chem. Lett.* **2014**, *5*, 1278.

[10] A. Sadhanala, F. Deschler, T. H. Thomas, E. Dutton, K. C. Goedel, F. C. Hanusch, M. L. Lai, U. Steiner, T. Bein, P. Docampo, D. Cahen, R. H. Friend, *J. Phys. Chem. Lett.* **2014**, *5*, 2501.

[11] N. Kitazawa, Y. Watanabe, Y. Nakamura, *J. Mater. Sci.* **2002**, *37*, 3585.

[12] E. T. Hoke, D. J. Slotcavage, E. R. Dohner, A. R. Bowring, H. I. Karunadasa, M. D. McGehee, *Chem. Sci.* **2015**, *6*, 613.

[13] S. Colella, E. Mosconi, P. Fedeli, A. Listorti, F. Gazza, F. Orlandi, P. Ferro, T. Besagni, A. Rizzo, G. Calestani, G. Gigli, F. De Angelis, R. Mosca, *Chem. Mater.* **2013**, *25*, 4613.

[14] B. Suarez, V. Gonzalez-Pedro, T. S. Ripolles, R. S. Sanchez, L. Otero, I. Mora-sero, *J. Phys. Chem. Lett.* **2014**, *5*, 1628.

[15] S. Mishra, E. Jeanneau, O. Iasco, G. Ledoux, D. Luneau, S. Daniele, *Eur. J. Inorg. Chem.* **2012**, *16*, 2749.

[16] N. K. Noel, S. D. Stranks, A. Abate, C. Wehrenfennig, S. Guarnera, A. Haghighirad, A. Sadhanala, G. E. Eperon, S. K. Pathak, M. B. Johnston, A. Petrozza, M. Herz, H. J. Snaith, *Energy Environ. Sci.* **2014**, *7*, 3061.

[17] F. Hao, C. C. Stoumpos, R. P. H. Chang, M. G. Kanatzidis, *J. Am. Chem. Soc.* **2014**, *136*, 8094.

[18] J. Han, S. Nishihara, K. Inoue, M. Kurmoo, *Inorg. Chem.* **2015**, *54*, 2866.

[19] G. Srinivasan, E. T. Rasmussen, B. J. Levin, R. Hayes, *Phys. Rev. B* **2002**, *66*, 29901.

[20] R. E. Cohen, *Nature* **1992**, *358*, 136.

[21] H. L. Clever, F. J. Johnston, *J. Phys. Chem. Ref. Data* **1980**, *9*, 751.

[22] NREL, "Best Research-Cell Efficiencies," can be found under http://www.nrel.gov/ncpv/images/efficiency_chart.jpg, **2015**.

[23] A. A. Asif, R. Singh, G. F. Alapatt, *J. Renew. Sustain. Energy* **2015**, *7*, 43120.

[24] Q. Chen, N. De Marco, Y. (Michael) Yang, T.-B. Song, C.-C. Chen, H. Zhao, Z. Hong, H. Zhou, Y. Yang, *Nano Today* **2015**, *10*, 355.

[25] European Commission -- Joint Research Centre -- Institute for Environment and Sustainability, *International Reference Life Cycle Data System (ILCD) Handbook -- General Guide for Life Cycle Assessment -- Detailed Guidance*, **2010**.

[26] E. Drury, P. Denholm, R. Margolis, *National Renewable Energy Laboratory Technical Report*, **2011**, NREL/TP-6A20-52197.

[27] Levelized Cost and Levelized Avoided Cost of New Generation Resources. In US Annual Energy Outlook; U.S. Energy Information Administration: Washington, DC, 2015; https://www.eia.gov/forecasts/aeo/electricity_generation.cfm (accessed Nov 1, 2015).

[28] I. Clover, "Buffett Strikes Cheapest Electricity Price in US with Nevada Solar Farm," can be found under http://www.pv-magazine.com/news/details/beitrag/buffett-strikes-cheapest-electricity-price-in-us-with-nevada-

solar-farm_100020120/#axzz3qP7ENAFM, **2015**.

[29] J. Gong, S. B. Darling, F. You, *Energy Environ. Sci.* **2015**, *8*, 1953.

[30] B. Hailegnaw, S. Kirmayer, E. Edri, G. Hodes, D. Cahen, *J. Phys. Chem. Lett.* **2015**, *6*, 1543.

[31] L. Serrano-Lujan, N. Espinosa, T. T. Larsen-Olsen, J. Abad, A. Urbina, F. C. Krebs, *Adv. Energy Mater.* **2015**, *5*, 1501119.

[32] T. A. Berhe, W. Su, C.-H. Chen, C.-J. Pan, J.-H. Cheng, H.-M. Chen, M.-C. Tsai, L.-Y. Chen, A. A. Dubale, B.-J. Hwang, *Energy Environ. Sci.* **2016**, *9*, 323.

[33] Y.-Y. Zhang, S. Chen, P. Xu, H. Xiang, X.-G. Gong, A. Walsh, S. Wei, "Intrinsic Instability of the Hybrid Halide Perovskite $CH_3NH_3PbI_3$," can be found under http://arxiv.org/abs/1506.01301, **2015**.

[34] W. S. Yang, J. H. Noh, N. J. Jeon, Y. C. Kim, S. Ryu, J. Seo, S. I. Seok, *Science* **2015**, *348*, 1234.

[35] Y. Deng, Q. Wang, Y. Yuan, J. Huang, *Mater. Horiz.* **2015**, *2*, 578.

[36] S. Lizin, S. Van Passel, E. De Schepper, L. Vranken, *Sol. Energy Mater. Sol. Cells* **2012**, *103*, 1.

[37] F. C. Krebs, M. Hösel, *ChemSusChem* **2015**, *8*, 966.

[38] G. E. Eperon, V. M. Burlakov, A. Goriely, H. J. Snaith, *ACS Nano* **2014**, *8*, 591.

[39] P. Heinstein, C. Ballif, L.-E. Perret-Aebi, *Green* **2013**, *3*, 125.

[40] I. R. Benmessaoud, A.-L. Mahul-Mellier, E. Horváth, B. Maco, M. Spina, H. A. Lashuel, L. Forró, *Toxicol. Res.* **2016**, *5*, 407.

[41] Y. Sun, J. Shi, J. Lian, W. Gao, M. L. Agiorgousis, P. Zhang, S. Zhang, *Nanoscale* **2016**, *8*, 6284.

[42] H. J. Snaith, A. Abate, J. M. Ball, G. E. W. Eperon, T. Leijtens, N. K. Noel, S. D. Stranks, J. T. T.-W. Wang, K. Wojciechowski, W. Zhang, T. Leigtens, *J. Phys. Chem. Lett.* **2014**, *5*, 1511.

[43] C. Eames, J. M. Frost, P. R. F. Barnes, B. C. O'Regan, A. Walsh, M. S. Islam, *Nat. Commun.* **2015**, *6*, 7497.

[44] Z. Xiao, Y. Yuan, Y. Shao, Q. Wang, Q. Dong, C. Bi, P. Sharma, A. Gruverman, J. Huang, *Nat. Mater.* **2015**, *14*, 193.

[45] T. Leijtens, E. T. Hoke, G. Grancini, D. J. Slotcavage, G. E. Eperon, J. M. Ball, M. De Bastiani, A. R. Bowring, N. Martino, K. Wojciechowski, M. D. McGehee, H. J. Snaith, A. Petrozza, *Adv. Energy Mater.* **2015**, 1500962.

[46] J. You, L. Meng, T.-B. Song, T.-F. Guo, Y. (Michael) Yang, W.-H. Chang, Z. Hong, H. Chen, H. Zhou, Q. Chen, Y. Liu, N. De Marco, Y. Yang, *Nat. Nanotechnol.* **2015**, *11*, 75.

[47] T. Leijtens, G. E. Eperon, N. K. Noel, S. N. Habisreutinger, A. Petrozza, H. J. Snaith, *Adv. Energy Mater.* **2015**, *5*, 1500963.

[48] F. C. Krebs, T. Tromholt, M. Jørgensen, *Nanoscale* **2010**, *2*, 873.

[49] Y. Li, X. Wang, S. Wu, H. Ci, H. Xu, X. Li, H. Sun, Z. Zhang, A. Cao, X. Guo, Y. Li, *J. Mater. Chem. A* **2015**, *3*, 18847.

[50] Z. Yang, C.-C. Chueh, F. Zuo, J. H. Kim, P.-W. Liang, A. K.-Y. Jen, *Adv. Energy Mater.* **2015**, *5*, 1500328.

[51] K. Yan, M. Long, T. Zhang, Z. Wei, H. Chen, S. Yang, J. Xu, *J. Am. Chem. Soc.* **2015**, *137*, 4460.

[52] T. M. Schmidt, T. T. Larsen-Olsen, J. E. Carlé, D. Angmo, F. C. Krebs, *Adv. Energy Mater.* **2015**, *5*, 1500569.

[53] P. Pistor, J. Borchert, W. Fra, R. Csuk, R. Scheer, *J. Phys. Chem. Lett.* **2014**, *5*, 3308.

[54] D. W. de Quilettes, S. M. Vorpahl, S. D. Stranks, H. Nagaoka, G. E. Eperon, M. E. Ziffer, H. J. Snaith, D. S. Ginger, *Science* **2015**, *348*, 683.

[55] M. Bag, L. A. Renna, R. Adhikari, S. Karak, F. Liu, P. M. Lahti, T. P. Russell, M. T. Tuominen, D. Venkataraman, *J. Am. Chem. Soc.* **2015**, *137*, 13130.

[56] M. I. Saidaminov, A. L. Abdelhady, B. Murali, E. Alarousu, V. M. Burlakov, W. Peng, I. Dursun, L. Wang, Y. He, G. Maculan, A. Goriely, T. Wu, O. F. Mohammed, O. M. Bakr, *Nat. Commun.* **2015**, *6*, 7586.

[57] N. K. Noel, A. Abate, S. D. Stranks, E. S. Parrott, V. M. Burlakov, A. Goriely, H. J. Snaith, *ACS Nano* **2014**, *8*, 9815.

[58] Z. Gu, L. Zuo, T. T. Larsen-Olsen, T. Ye, G. Wu, F. C. Krebs, H. Chen, *J. Mater. Chem. A* **2015**, *3*, 24254.

[59] K.-C. Wang, J.-Y. Jeng, P.-S. Shen, Y.-C. Chang, E. W.-G. Diau, C.-H. Tsai, T.-Y. Chao, H.-C. Hsu, P.-Y. Lin, P. Chen, T.-F. Guo, T.-C. Wen, *Sci. Rep.* **2014**, *4*, 4756.

[60] Y. Ogomi, K. Kukihara, S. Qing, T. Toyoda, K. Yoshino, S. Pandey, H. Momose, S. Hayase, *Chem. Phys. Chem.* **2014**, *15*, 1062.

[61] H. Kim, S. H. Im, N. Park, *J. Phys. Chem. C* **2014**, *118*, 5615.

[62] C. Roldan-Carmona, O. Malinkiewicz, A. Soriano, G. M. Espallargas, A. Garcia, P. Reinecke, T. Kroyer, M. I. Dar, M. K. Nazeeruddin, H. J. Bolink, *Energy Environ. Sci.* **2014**, *7*, 994.

[63] D. Liu, T. L. Kelly, *Nat. Photonics* **2013**, *8*, 133.

[64] M. He, D. J. Zheng, M. Y. Wang, C. J. Lin, Z. Q. Lin, *J. Mater. Chem. A* **2014**, *2*, 5994.

[65] M. M. Lee, J. Teuscher, T. Miyasaka, T. N. Murakami, H. J. Snaith, *Science* **2012**, *338*, 643.

[66] J. Burschka, N. Pellet, S.-J. Moon, R. Humphry-Baker, P. Gao, M. K. Nazeeruddin, M. Grätzel, *Nature* **2013**, *499*, 316.

[67] Q. Chen, H. Zhou, Z. Hong, S. Luo, H.-S. Duan, H.-H. Wang, Y. Liu, G. Li, Y. Yang, *J. Am. Chem. Soc.* **2014**, *136*, 622.

[68] P.-W. Liang, C.-Y. Liao, C.-C. Chueh, F. Zuo, S. T. Williams, X.-K. Xin, J. Lin, A. K.-Y. Jen, *Adv. Mater.* **2014**,

26, 3748.

[69] J. M. Ball, M. M. Lee, A. Hey, H. J. Snaith, *Energy Environ. Sci.* **2013**, *6*, 1739.

[70] M. J. Carnie, C. Charbonneau, M. L. Davies, J. Troughton, T. M. Watson, K. Wojciechowski, H. Snaith, D. A. Worsley, *Chem. Commun.* **2013**, *49*, 7893.

[71] A. Dualeh, N. Tétreault, T. Moehl, P. Gao, M. K. Nazeeruddin, M. Grätzel, *Adv. Funct. Mater.* **2014**, *24*, 3250.

[72] K. W. Tan, D. T. Moore, M. Saliba, H. Sai, L. A. Estroff, T. Hanrath, H. J. Snaith, U. Wiesner, *ACS Nano* **2014**, *8*, 4730.

[73] M. Saliba, K. W. Tan, H. Sai, D. T. Moore, T. Scott, W. Zhang, L. a. Estroff, U. Wiesner, H. J. Snaith, L. A. Estro, *J. Phys. Chem. C* **2014**, *118*, 17171.

[74] G. E. Eperon, V. M. Burlakov, P. Docampo, A. Goriely, H. J. Snaith, *Adv. Funct. Mater.* **2014**, *24*, 151.

[75] V. M. Burlakov, G. E. Eperon, H. J. Snaith, S. J. Chapman, A. Goriely, *Appl. Phys. Lett.* **2014**, *104*, 91602.

[76] J. H. Heo, S. H. Im, J. H. Noh, T. N. Mandal, C.-S. Lim, J. A. Chang, Y. H. Lee, H. Kim, A. Sarkar, M. K. Nazeeruddin, M. Grätzel, S. Il Seok, *Nat. Photonics* **2013**, *7*, 486.

[77] M. Liu, M. B. Johnston, H. J. Snaith, *Nature* **2013**, *501*, 395.

[78] G. Xing, N. Mathews, S. Sun, S. S. Lim, Y. M. Lam, M. Grätzel, S. Mhaisalkar, T. C. Sum, *Science* **2013**, *342*, 344.

[79] S. D. Stranks, G. E. Eperon, G. Grancini, C. Menelaou, M. J. P. Alcocer, T. Leijtens, L. M. Herz, A. Petrozza, H. J. Snaith, *Science* **2013**, *342*, 341.

[80] Y. Zhao, K. Zhu, *J. Phys. Chem. C* **2014**, *118*, 9412.

[81] M. Olszak-Humienik, *Thermochim. Acta* **2001**, *378*, 107.

[82] O. Yamamuro, M. Oguni, T. Matsuo, H. Suga, *Thermochim. Acta* **1986**, *98*, 327.

[83] G. Niu, W. Li, F. Meng, L. Wang, H. Dong, Y. Qiu, *J. Mater. Chem. A* **2014**, *2*, 705.

[84] O. Horvath, I. Miko, *J. Photochem. Photobiol. A Chem.* **1998**, *114*, 95.

[85] C. C. Stoumpos, C. D. Malliakas, M. G. Kanatzidis, *Inorg. Chem.* **2013**, *52*, 9019.

[86] A. Poglitsch, D. Weber, *J. Chem. Phys.* **1987**, *87*, 6373.

[87] M. Otonicar, S. D. Skapin, B. Jancar, R. Ubic, D. Suvorov, *J. Am. Ceram. Soc.* **2010**, *93*, 4168.

[88] D. I. Woodward, I. M. Reaney, *Acta Crystallogr. B.* **2005**, *61*, 387.

[89] L. P. Keller, P. R. Buseck, *Am. Minteralogist* **1994**, *79*, 73.

[90] B.-W. Park, E. M. J. Johansson, B. Philippe, T. Gustafsson, K. Sveinbjörnsson, A. Hagfeldt, G. Boschloo, *Chem. Mater.* **2014**, *26*, 4466.

[91] D. T. Moore, H. Sai, K. Wee Tan, L. A. Estroff, U. Wiesner, *APL Mater.* **2014**, *2*, 081802.

[92] H.-B. Kim, H. Choi, J. Jeong, S. Kim, B. Walker, S. Song, J. Y. Kim, *Nanoscale* **2014**, *6*, 6679.

[93] E. Edri, S. Kirmayer, D. Cahen, G. Hodes, *J. Phys. Chem. Lett.* **2013**, *4*, 897.

[94] F. Hao, C. C. Stoumpos, D. H. Cao, R. P. H. Chang, M. G. Kanatzidis, *Nat. Photonics* **2014**, *8*, 489.

[95] T. Salim, S. Sun, Y. Abe, A. Krishna, A. C. Grimsdale, Y. M. Lam, *J. Mater. Chem. A* **2015**, *3*, 8943.

[96] C. Zuo, H. J. Bolink, H. Han, J. Huang, D. Cahen, L. Ding, *Adv. Sci.* **2016**, *3*, 1500324.

[97] Z. Xiao, C. Bi, Y. Shao, Q. Dong, Q. Wang, Y. Yuan, C. Wang, Y. Gao, J. Huang, *Energy Environ. Sci.* **2014**, *7*, 2619.

[98] W. Nie, H. Tsai, R. Asadpour, A. J. Neukirch, G. Gupta, J. J. Crochet, M. Chhowalla, S. Tretiak, M. A. Alam, H. Wang, *Science* **2015**, *347*, 522.

[99] W. Zhang, M. Saliba, D. T. Moore, S. K. Pathak, M. T. Hörantner, T. Stergiopoulos, S. D. Stranks, G. E. Eperon, J. A. Alexander-Webber, A. Abate, A. Sadhanala, S. Yao, Y. Chen, R. H. Friend, L. A. Estroff, U. Wiesner, H. J. Snaith, *Nat. Commun.* **2015**, *6*, 6142.

[100] C. T. Zuo, L. M. Ding, *Nanoscale* **2014**, *6*, 9935.

[101] N. J. Jeon, J. H. Noh, Y. C. Kim, W. S. Yang, S. Ryu, S. Il Seok, *Nat. Mater.* **2014**, *13*, 897.

[102] Z. Xiao, Q. Dong, C. Bi, Y. Shao, Y. Yuan, J. Huang, *Adv. Mater.* **2014**, *26*, 6503.

[103] W. Zhu, T. Yu, F. Li, C. Bao, H. Gao, Y. Yi, J. Yang, G. Fu, X. Zhou, Z. Zou, *Nanoscale* **2015**, *7*, 5427.

[104] J. Xiao, Y. Yang, X. Xu, J. Shi, L. Zhu, S. Lv, H. Wu, Y. Luo, D. Li, Q. Meng, *J. Mater. Chem. A* **2015**, *3*, 5289.

[105] Y. Zhao, K. Zhu, *Chem. Commun.* **2014**, *50*, 1605.

[106] Z. Zhou, Z. Wang, Y. Zhou, S. Pang, D. Wang, H. Xu, Z. Liu, N. P. Padture, G. Cui, *Angew. Chemie Int. Ed.* **2015**, *54*, 9705.

[107] F. Hao, C. C. Stoumpos, R. P. H. Chang, M. G. Kanatzidis, *J. Am. Chem. Soc.* **2014**, *136*, 8094.

[108] J. J. Choi, X. Yang, Z. M. Norman, S. J. L. Billinge, J. S. Owen, *Nano Lett.* **2014**, *14*, 127.

[109] D. Damjanovic, *Reports Prog. Phys.* **1999**, *61*, 1267.

[110] W. Yongzhen, A. Islam, X. Yang, C. Qin, J. Liu, K. Zhang, W. Peng, L. Han, Y. Wu, A. Islam, X. Yang, C. Qin, J. Liu, K. Zhang, W. Peng, L. Han, W. Yongzhen, A. Islam, X. Yang, C. Qin, J. Liu, K. Zhang, W. Peng, L. Han, *Energy Environ. Sci.* **2014**, *7*, 2934.

[111] A. Leguy, Y. Hu, M. Campoy-Quiles, M. I. Alonso, O. J. Weber, P. Azarhoosh, M. van Schilfgaarde, M. T. Weller, T. Bein, J. Nelson, P. Docampo, P. R. F. Barnes, *Chem. Mater.* **2015**, *27*, 3397.

[112] Y. Wu, A. Islam, X. Yang, C. Qin, J. Liu, K. Zhang, W. Peng, L. Han, *Energy Environ. Sci.* **2014**, *7*, 2934.

[113] N. Ahn, D.-Y. Son, I.-H. Jang, S. M. Kang, M. Choi, N.-G. Park, *J. Am. Chem. Soc.* **2015**, *137*, 8696.

[114] D. B. Mitzi, *Prog. Inorg. Chem.* **1999**, *30*, 1.

[115] J. Kim, S.-H. Lee, J. H. Lee, K.-H. Hong, *J. Phys. Chem. Lett.* **2014**, *5*, 1312.

[116] S. Yang, Y. C. Zheng, Y. Hou, X. Chen, Y. Chen, Y. Wang, H. Zhao, H. G. Yang, *Chem. Mater.* **2014**, *26*, 6705.

[117] K. Liang, D. B. Mitzi, M. T. Prikas, *Chem. Mater.* **1998**, *10*, 403.

[118] H.-S. Kim, C.-R. Lee, J.-H. Im, K.-B. Lee, T. Moehl, A. Marchioro, S.-J. Moon, R. Humphry-Baker, J.-H. Yum, J. E. Moser, M. Grätzel, N.-G. Park, *Sci. Rep.* **2012**, *2*, 591.

[119] H. Yu, F. Wang, F. Xie, W. Li, J. Chen, N. Zhao, *Adv. Funct. Mater.* **2014**, *45*, 7102.

[120] Y. Tidhar, E. Edri, H. Weissman, D. Zohar, G. Hodes, D. Cahen, B. Rybtchinski, S. Kirmayer, *J. Am. Chem. Soc.* **2014**, *136*, 13249.

[121] M. I. Dar, N. Arora, P. Gao, S. Ahmad, M. Gra, *Nano Lett.* **2014**, *14*, 6991.

[122] H. Zhou, Q. Chen, G. Li, S. Luo, T.-B. Song, H.-S. Duan, Z. Hong, J. You, Y. Liu, Y. Yang, *Science* **2014**, *345*, 542.

[123] M. A. Green, K. Emery, Y. Hishikawa, W. Warta, E. D. Dunlop, *Prog. Photovolt Res. Appl.* **2014**, *22*, 701.

[124] B. L. Bramfitt, B. S. Corporation, *Structure / Property Relationships in Irons and Steels*, ASM International, **1998**.

[125] R. S. Sanchez, V. Gonzalez-Pedro, J.-W. Lee, N.-G. Park, Y. S. Kang, I. Mora-Sero, J. Bisquert, *J. Phys. Chem. Lett.* **2014**, *5*, 2357.

[126] J. M. Frost, K. T. Butler, A. Walsh, *arXiv:1405.5810 [cond-mat.mes-hall]* **2014**, DOI 10.1063/1.4890246.

[127] R. Gottesman, E. Haltzi, L. Gouda, S. Tirosh, Y. Bouhadana, A. Zaban, E. Mosconi, F. De Angelis, *J. Phys. Chem. Lett.* **2014**, *5*, 2662.

[128] J. M. Frost, K. T. Butler, F. Brivio, C. H. Hendon, M. van Schilfgaarde, A. Walsh, *Nano Lett.* **2014**, *14*, 2584.

[129] J. Kreisel, M. Alexe, P. A. Thomas, *Nat. Mater.* **2012**, *11*, 260.

[130] P. Docampo, F. C. Hanusch, N. Giesbrecht, P. Angloher, A. Ivanova, T. Bein, *Apl Mater.* **2014**, *2*, 081508.

[131] J. Haruyama, K. Sodeyama, L. Han, Y. Tateyama, *J. Phys. Chem. Lett.* **2014**, *5*, 2903.

[132] H.-S. Kim, N.-G. Park, *J. Phys. Chem. Lett.* **2014**, *5*, 2927.

[133] V. D'Innocenzo, G. Grancini, M. J. P. Alcocer, A. R. S. Kandada, S. D. Stranks, M. M. Lee, G. Lanzani, H. J. Snaith, A. Petrozza, *Nat. Commun.* **2014**, *5*, 3586.

[134] D. Shen, X. Yu, X. Cai, M. Peng, Y. Ma, X. Su, L. Xiao, D. Zou, *J. Mater. Chem. A* **2014**, *2*, 20454.

[135] Q. Chen, H. Zhou, T.-B. Song, S. Luo, Z. Hong, H.-S. Duan, L. Dou, Y. Liu, Y. Yang, *Nano Lett.* **2014**, *14*, 4158.

[136] Y. Ma, L. Zheng, Y.-H. Chung, S. Chu, L. Xiao, Z. Chen, S. Wang, B. Qu, Q. Gong, Z. Wu, X. Hou, *Chem. Commun.* **2014**, *50*, 12458.

[137] P. Docampo, F. C. Hanusch, S. D. Stranks, M. Döblinger, J. M. Feckl, M. Ehrensperger, N. K. Minar, M. B. Johnston, H. J. Snaith, T. Bein, *Adv. Energy Mater.* **2014**, *4*, 1400355.

[138] H. Hu, D. Wang, Y. Zhou, J. Zhang, S. Lv, S. Pang, X. Chen, Z. Liu, N. P. Padture, G. Cui, *RSC Adv.* **2014**, *4*, 28964.

[139] O. Malinkiewicz, A. Yella, Y. H. Lee, G. M. Espallargas, M. Graetzel, M. K. Nazeeruddin, H. J. Bolink, *Nat. Photon.* **2013**, *8*, 128.

[140] D. J. Lewis, P. O'Brien, *Chem. Commun.* **2014**, *50*, 6319.

[141] M. K. Kang, D. M. Chen, S. P. Yang, G. L. Hu, *Metall. Trans. A.* **1992**, *23*, 785.

[142] F. H. Pollak, M. Cardona, *J. Phys. Chem Solids* **1966**, *27*, 423.

[143] S. Dharani, H. A. Dewi, R. R. Prabhakar, T. Baikie, S. Chen, Y. Du, N. Mathews, P. P. Boix, S. G. Mhaisalkar, *Nanoscale* **2014**, *6*, 13854.

[144] J. W. Jung, S. T. Williams, A. K.-Y. Jen, *RSC Adv.* **2014**, *4*, 62971.

[145] K. G. Stamplecoskie, J. S. Manser, P. V Kamat, *Energy Environ. Sci.* **2015**, *8*, 208.

[146] C.-C. Chueh, C.-Y. Liao, F. Zuo, S. T. Williams, P.-W. Liang, A. K.-Y. Jen, *J. Mater. Chem. A* **2015**, *3*, 9058.

[147] Y. Zhao, K. Zhu, *J. Phys. Chem. Lett.* **2013**, *4*, 2880.

[148] M. De Bastiani, V. D'Innocenzo, S. D. Stranks, H. J. Snaith, A. Petrozza, *Apl Mater.* **2014**, *2*, 81509.

[149] V. Roiati, E. Mosconi, A. Listorti, S. Colella, G. Gigli, F. De Angelis, *Nano Lett.* **2014**, *14*, 2168.

[150] L. Wang, C. McCleese, A. Kovalsky, Y. Zhao, C. Burda, *J. Am. Chem. Soc.* **2014**, *136*, 12205.

[151] E. Mosconi, E. Ronca, F. De Angelis, *J. Phys. Chem. Lett.* **2014**, *5*, 2619.

[152] Y. Kutes, L. Ye, Y. Zhou, S. Pang, B. D. Huey, N. P. Padture, *J. Phys. Chem. Lett.* **2014**, *5*, 3335.

[153] J. M. Frost, K. T. Butler, A. Walsh, *APL Mat.* **2014**, *2*, 81506.

[154] X. R. Huang, S. S. Jiang, X. B. Hu, W. J. Liu, *J. Phys. Condens. Matter* **1997**, *9*, 4467.

[155] H. Oga, A. Saeki, Y. Ogomi, S. Hayase, S. Seki, *J. Am. Chem. Soc.* **2014**, *136*, 13818.

[156] Q. Wang, Y. Shao, H. Xie, L. Lyu, X. Liu, Y. Gao, J. Huang, *Appl. Phys. Lett.* **2014**, *105*, 163508.

[157] C. Wehrenfennig, G. E. Eperon, M. B. Johnston, H. J. Snaith, L. M. Herz, *Adv. Mater.* **2014**, *26*, 1584.

[158] H.-S. Duan, H. Zhou, Q. Chen, P. Sun, S. Luo, T.-B. Song, B. Bob, Y. Yang, *Phys. Chem. Chem. Phys.* **2014**, *17*, 112.

[159] M. L. Agiorgousis, Y. Sun, H. Zeng, S. Zhang, *J. Am. Chem. Soc.* **2014**, *136*, 14570.

[160] Q. Wang, Y. Shao, Q. Dong, Z. Xiao, Y. Yuan, J. Huang, *Energy Environ. Sci.* **2014**, *7*, 2359.

[161] S. Bai, Z. Wu, X. Wu, Y. Jin, N. Zhao, Z. Chen, Q. Mei, X. Wang, Z. Ye, T. Song, R. Liu, S. Lee, B. Sun, *Nano*

Res. **2014**, *7*, 1749.

[162] A. Guerrero, E. J. Juarez-Perez, J. Bisquert, I. Mora-Sero, G. Garcia-Belmonte, *Appl. Phys. Lett.* **2014**, *105*, 133902.

[163] Z. Song, S. C. Watthage, A. B. Phillips, B. L. Tompkins, R. J. Ellingson, M. J. Heben, *Chem. Mater.* **2015**, *27*, 4612.

[164] L. Katzin, *J. lnorg. Nucl. Chem.* **1957**, *4*, 187.

[165] W. Depmeier, J. Felsche, G. Wildermuth, *J. Solid State Chem.* **1977**, *21*, 57.

[166] Z. L. Xiao, H. Z. Chen, M. M. Shi, G. Wu, R. J. Zhou, Z. S. Yang, M. Wang, B. Z. Tang, *Mater. Sci. Eng. B Solid-State Mater. Adv. Technol.* **2005**, *117*, 313.

[167] B.-W. Park, B. Philippe, X. Zhang, H. Rensmo, G. Boschloo, E. M. J. Johansson, *Adv. Mater.* **2015**, *27*, 6806.

[168] A. Molla-abbassi, M. Skripkin, M. Kritikos, I. Persson, M. Sandström, *Dalt. Trans.* **2003**, 1746.

[169] A. L. Abdelhady, M. I. Saidaminov, B. Murali, V. Adinolfi, O. Voznyy, K. Katsiev, E. Alarousu, R. Comin, I. Dursun, L. Sinatra, E. H. Sargent, O. F. Mohammed, O. M. Bakr, *J. Phys. Chem. Lett.* **2016**, *7*, 295.

[170] Z. Yang, A. Rajagopal, S. B. Jo, C.-C. Chueh, S. T. Williams, C. C. Huang, J. K. Katahara, H. W. Hillhouse, A. K.-Y. Jen, *Nano Lett* **2016**, *16*, 7739.

[171] M. Kulbak, D. Cahen, G. Hodes, *J. Phys. Chem. Lett.* **2015**, *6*, 2452.

[172] M. Saliba, T. Matsui, K. Domanski, J.-Y. Seo, A. Ummadisingu, S. M. Zakeeruddin, J.-P. Correa-Baena, W. R. Tress, A. Abate, A. Hagfeldt, M. Gratzel, *Science* **2016**, *354*, 206.

[173] X. Liu, Z. Yang, C.-C. Chueh, A. Rajagopal, S. T. Williams, Y. Sun, A. K.-Y. Jen, *J. Mater. Chem. A.* **2016**, *4*, 17939.

[174] M. Grätzel, *Acc. Chem. Res.* **2017**, *50*, 487.

[175] D. P. McMeekin, G. Sadoughi, W. Rehman, G. E. Eperon, M. Saliba, M. T. Horantner, A. Haghighirad, N. Sakai, L. Korte, B. Rech, M. B. Johnston, L. M. Herz, H. J. Snaith, *Science* **2016**, *351*, 151.

[176] D. Pérez-del-Rey, D. Forgács, E. M. Hutter, T. J. Savenije, D. Nordlund, P. Schulz, J. J. Berry, M. Sessolo, H. J. Bolink, *Adv. Mater.* **2016**, *28*, 9839.

[177] J. Navas, A. Sánchez-Coronilla, J. J. Gallardo, J. C. Piñero, D. De los Santos, E. I. Martín, N. C. Hernández, R. Alcántara, C. Fernández-Lorenzo, J. Martín-Calleja, *Nano Energy* **2017**, *34*, 141.

[178] M. T. Klug, A. Osherov, A. A. Haghighirad, S. D. Stranks, P. R. Brown, S. Bai, J. T.-W. Wang, X. Dang, V. Bulović, H. J. Snaith, A. M. Belcher, *Energy Environ. Sci.* **2017**, *10*, 236.

[179] L. A. Frolova, D. V Anokhin, K. L. Gerasimov, N. N. Dremova, P. A. Troshin, *J. Phys. Chem. Lett.* **2016**, *7*, 4353.

[180] Q. Chen, L. Chen, F. Ye, T. Zhao, F. Tang, A. Rajagopal, Z. Jiang, S. Jiang, A. K.-Y. Jen, Y. Xie, J. Cai, L. Chen,

Nano Lett. **2017**, *17*, 3231.

[181] M. Yuan, L. N. Quan, R. Comin, G. Walters, R. Sabatini, O. Voznyy, S. Hoogland, Y. Zhao, E. M. Beauregard, P. Kanjanaboos, Z. Lu, D. H. Kim, E. H. Sargent, *Nat. Nanotechnol.* **2016**, *11*, 872.

[182] S. Ito, S. Tanaka, H. Nishino, *J. Phys. Chem. Lett.* **2015**, *6*, 881.

[183] Y. Guo, K. Shoyama, W. Sato, Y. Matsuo, K. Inoue, K. Harano, C. Liu, H. Tanaka, E. Nakamura, *J. Am. Chem. Soc.* **2015**, *137*, 15907.

[184] A. Wakamiya, M. Endo, T. Sasamori, N. Tokitoh, Y. Ogomi, S. Hayase, Y. Murata, *Chem. Lett.* **2014**, *43*, 711.

[185] H. Yu, H. Lu, F. Xie, S. Zhou, N. Zhao, *Adv. Funct. Mater.* **2016**, *26*, 1411.

[186] X. Ke, J. Yan, A. Zhang, B. Zhang, Y. Chen, *Appl. Phys. Lett.* **2015**, *107*, 91904.

[187] Y. Tian, I. G. Scheblykin, *J. Phys. Chem. Lett.* **2015**, *6*, 3466.

[188] Q. Lin, A. Armin, R. Chandra, R. Nagiri, P. L. Burn, P. Meredith, *Nat. Photonics* **2014**, *9*, 106.

[189] G. Catalan, A. Lubk, A. H. G. Vlooswijk, E. Snoeck, C. Magen, A. Janssens, G. Rispens, G. Rijnders, D. H. A. Blank, B. Noheda, *Nat. Mater.* **2011**, *10*, 963.

[190] I. M. Hermes, S. A. Bretschneider, V. W. Bergmann, D. Li, A. Klasen, J. Mars, W. Tremel, F. Laquai, H.-J. Butt, M. Mezger, R. Berger, B. J. Rodriguez, S. A. L. Weber, *J. Phys. Chem. C* **2016**, *120*, 5724.

[191] M. U. Rothmann, W. Li, Y. Zhu, U. Bach, L. Spiccia, J. Etheridge, Y.-B. Cheng, *Nat. Commun.* **2017**, *8*, 14547.

[192] B. Náfrádi, P. Szirmai, M. Spina, H. Lee, O. V. Yazyev, A. Arakcheeva, D. Chernyshov, M. Gibert, L. Forró, E. Horváth, *Nat. Commun.* **2016**, *7*, 13406.

[193] W. J. Mir, M. Jagadeeswararao, S. Das, A. Nag, *ACS Energy Lett.* **2017**, *2*, 537.

[194] H. Liu, Z. Wu, J. Shao, D. Yao, H. Gao, Y. Liu, W. Yu, H. Zhang, B. Yang, *ACS Nano* **2017**, *11*, 2239.

[195] G. A. H. Wetzelaer, M. Scheepers, A. M. Sempere, C. Momblona, J. Ávila, H. J. Bolink, *Adv. Mater.* **2015**, *27*, 1837.

[196] T. M. Brenner, D. A. Egger, L. Kronik, G. Hodes, D. Cahen, *Nat. Rev. Mater.* **2016**, *1*, 15007.

[197] A. Pockett, G. E. Eperon, T. Peltola, H. J. Snaith, A. Walker, L. M. Peter, P. J. Cameron, *J. Phys. Chem. C* **2015**, *119*, 3456.

[198] L. Gouda, R. Gottesman, A. Ginsburg, D. A. Keller, E. Haltzi, J. Hu, S. Tirosh, A. Y. Anderson, A. Zaban, P. P. Boix, *J. Phys. Chem. Lett.* **2015**, *6*, 4640.

[199] A. Dualeh, T. Moehl, N. Tetreault, J. Teuscher, P. Gao, M. K. Nazeeruddin, M. Graetzel, *ACS Nano* **2014**, *8*, 362.

[200] S. van Reenen, M. Kemerink, H. J. Snaith, *J. Phys. Chem. Lett.* **2015**, *6*, 3808.

[201] A. Rajagopal, S. T. Williams, C.-C. Chueh, A. K.-Y. Jen, *J. Phys. Chem. Lett.* **2016**, *7*, 995.

[202] C. Momblona, O. Malinkiewicz, C. Roldán-Carmona, A. Soriano, L. Gil-Escrig, E. Bandiello, M. Scheepers, E. Edri, H. J. Bolink, *APL Mater.* **2014**, *2*, 81504.

[203] C.-H. Chiang, C.-G. Wu, *Nat. Photonics* **2016**, *10*, 196.

[204] J. H. Heo, H. J. Han, D. Kim, T. K. Ahn, S. H. Im, *Energy Environ. Sci.* **2015**, *8*, 1602.

[205] I. Levine, P. K. Nayak, J. T.-W. Wang, N. Sakai, S. Van Reenen, T. M. Brenner, S. Mukhopadhyay, H. J. Snaith, G. Hodes, D. Cahen, *J. Phys. Chem. C* **2016**, *120*, 16399.

[206] Y. Yamada, T. Nakamura, M. Endo, A. Wakamiya, Y. Kanemitsu, *J. Am. Chem. Soc.* **2014**, *136*, 11610.

[207] L. Ma, F. Hao, C. C. Stoumpos, B. T. Phelan, M. R. Wasielewski, M. G. Kanatzidis, *J. Am. Chem. Soc.* **2016**, *138*, 14750.

[208] B. Chen, M. Yang, S. Priya, K. Zhu, *J. Phys. Chem. Lett.* **2016**, *7*, 905.

[209] C.-Z. Li, C.-C. Chueh, H.-L. Yip, K. M. O'Malley, W.-C. Chen, A. K.-Y. Jen, *J. Mater. Chem.* **2012**, *22*, 8574.

[210] P.-W. Liang, C.-C. Chueh, S. T. Williams, A. K.-Y. Jen, *Adv. Energy Mater.* **2015**, *5*, 1402321.

[211] T. Kirchartz, F. Deledalle, P. S. Tuladhar, J. R. Durrant, J. Nelson, *J. Phys. Chem. Lett.* **2013**, *4*, 2371.

[212] J. Nelson, *The Physics of Solar Cells*, Imperial College Press, **2003**.

[213] S. S. Hegedus, W. N. Shafarman, *Prog. Photovoltaics Res. Appl.* **2004**, *12*, 155.

[214] V. D. Mihailetchi, J. Wildeman, P. W. M. Blom, *Phys. Rev. Lett.* **2005**, *94*, 126602.

[215] L. J. A. Koster, V. D. Mihailetchi, R. Ramaker, P. W. M. Blom, *Appl. Phys. Lett.* **2005**, *86*, 123509.

[216] L. J. A. Koster, V. D. Mihailetchi, H. Xie, P. W. M. Blom, *Appl. Phys. Lett.* **2005**, *87*, 203502.

[217] S. R. Cowan, A. Roy, A. J. Heeger, *Phys. Rev. B* **2010**, *82*, 245207.

[218] K.-W. Tsai, C.-C. Chueh, S. T. Williams, T.-C. Wen, A. K. Y. Jen, *J. Mater. Chem. A* **2015**, *3*, 9128.

[219] J. H. Kim, C.-C. Chueh, S. T. Williams, A. K.-Y. Jen, *Nanoscale* **2015**, *7*, 17343.

[220] J. H. Kim, P.-W. Liang, S. T. Williams, N. Cho, C.-C. Chueh, M. S. Glaz, D. S. Ginger, A. K.-Y. Jen, *Adv. Mater.* **2015**, *4*, 695.

[221] J. H. Kim, S. T. Williams, N. Cho, C.-C. Chueh, A. K.-Y. Jen, *Adv. Energy Mater.* **2015**, *5*, 1401229.

[222] J. H. Kim, J. W. Jung, S. T. Williams, F. Liu, T. P. Russell, A. K.-Y. Jen, *Nanoscale* **2015**, *7*, 10936.

[223] D. B. Sulas, K. Yao, J. J. Intemann, S. T. Williams, C.-Z. Li, C.-C. Chueh, J. J. Richards, Y. Xi, L. D. Pozzo, C. W. Schlenker, A. K.-Y. Jen, D. S. Ginger, *Chem. Mater.* **2015**, *27*, 6583.

[224] Y. Zang, C.-Z. Li, C.-C. Chueh, S. T. Williams, W. Jiang, Z.-H. Wang, J.-S. Yu, A. K.-Y. Jen, *Adv. Mater.* **2014**, *26*, 5708.

[225] J. Zhang, C.-Z. Li, S. T. Williams, S. Liu, T. Zhao, A. K.-Y. Jen, *J. Am. Chem. Soc.* **2015**, *137*, 2167.

[226] P.-W. Liang, C.-C. Chueh, X.-K. Xin, F. Zuo, S. T. Williams, C.-Y. Liao, A. K.-Y. Jen, *Adv. Energy Mater.* **2015**, *5*, 1400960.

[227] H. Zhang, H. Wang, S. T. Williams, D. Xiong, W. Zhang, C.-C. Chueh, W. Chen, A. K. Y. Jen, *Adv. Mater.* **2017**, *29*, 1606608.

[228] F. Zuo, S. T. Williams, P.-W. Liang, C.-C. Chueh, C.-Y. Liao, A. K.-Y. Jen, *Adv. Mater.* **2014**, *26*, 6454.